Pi-bracket sensor for crack detection monitoring near stiffeners in bridge girders

by

Boris Telehanic

A Thesis submitted to the Faculty of Graduate and Postdoctoral Studies of

The University of Manitoba

in partial fulfilment of the requirements of the degree of

DOCTOR OF PHILOSOPHY

Department of Civil Engineering

University of Manitoba

Winnipeg, MB, Canada

ABSTRACT

This study investigates the design, validation, and performance of a pi-bracket sensor system for structural health monitoring of fatigue cracks in steel bridge girders through fiber optic sensors (FOSs), with a focus on detecting cracks near stiffeners, areas traditionally not monitored due to bending limitations of FOSs. Combining experimental testing, Finite Element Analysis, and theoretical validation, the research demonstrates that the pi-bracket configuration overcomes the limitations of FOSs by enabling non-invasive strain measurements in critical, hard-to-access regions. Laboratory experiments confirmed the system's sensitivity to crack openings as small as 0.2mm, with measurable strain magnitudes (129 με) captured by fiber optic sensor on the pi-bracket. FEA simulations isolated strain variations attributable solely to crack formation near stiffeners, revealing distinct strain differences at the pi-bracket crown (-2.37 με for 0.1mm cracks and -4.74 με for 0.2mm cracks) and contact point (-29.52 με and -59.04 με, respectively). The strain subtraction methodology effectively distinguished crack-induced strains from load-related effects, enabling targeted assessments of structural integrity. Integration with Brillouin Optical Time Domain Analysis technology ensured reliable distributed strain measurements while protecting sensors from mechanical damage. The system's crack detection ability was confirmed through Finite Element Analysis simulations on full-scale girder models, demonstrating its adaptability for the field applications. These findings collectively validate the pi-bracket sensor system as a robust addition for detecting cracks in traditionally undetectable areas near stiffeners, overcoming fiber optic sensor bending limitations and enhancing infrastructure resilience through precise, localized monitoring.

A comprehensive case study on a steel bridge in Manitoba, Canada, further demonstrated the capability of the pi-bracket sensor system for continuous, high-resolution strain measurement, specifically in fatigue-critical stiffened regions. A conservative crack detection threshold of 37με was established from controlled laboratory repeatability tests and validated through extensive field instrumentation. The proposed crack detection procedure, grounded in finite element simulations and enhanced by signal processing techniques to compensate for temperature and environmental noise, was successfully validated against field data. Although no active cracks were detected during monitoring, the system showed sensitivity and robustness in differentiating crack-related

strain signals from normal structural and environmental variations. These results provide a strong foundation for future deployments aimed at early crack detection, promising improvements in structural safety, maintenance prioritization, and longevity of steel bridges.

ACKNOWLEDGEMENT

Finishing this thesis feels like closing a chapter I've poured my heart into-one I couldn't have written without the incredible people who stood by me.

First, I want to thank Prof. Aftab Mufti, my advisor, for always believing in my work. Your guidance kept me grounded, and your endless patience helped me push through every obstacle. I'm so grateful for the way you challenged me to think deeper and aim higher.

To Prof. Douglas J. Thomson, my co-advisor, thank you for being more than a mentor. Your feedback was like a compass, steering me in the right direction whenever I felt lost. The time and energy you gave to this project meant the world to me.

A huge thanks to my committee members, Prof. Dagmar Svecova and Prof. Baidar Bakht, for your insightful comments and thoughtful advice. Your questions made this work stronger, and I'm lucky to have had your expertise shaping it.

I am also thankful to the team at the McQuade Structures Laboratory. Without your assistance in setting up experiments and troubleshooting late-night issues, this work would not have come together.

I would like to express my sincere gratitude to SIMTReC, Research Manitoba and Vector Construction for providing the financial support that made this research possible.

I also deeply appreciate Charleen Choboter for her invaluable support throughout my research.

Most of all, I want to thank my family. To my parents, thank you for teaching me to never give up, no matter how tough things got. To my wife, Ivana, you have been my rock. You listened to my rants, celebrated my small wins, and kept our home filled with love even when I was buried in work. And to my boys, Kamil and Boris, your endless energy reminded me to find joy in every moment, even during the most difficult days. This thesis is for you, too.

Thank you all for making this possible.

Boris Telehanic

DEDICATION

To my parents, for your steadfast love and belief in me.
To my wife, Ivana, whose support and patience have been my anchor.
And to my boys, Kamil and Boris, who fill my life with joy and wonder.

ORIGINAL CONTRIBUTION

The foundation for this research was established by Dr. Aftab Mufti and Dr. Douglas J. Thomson, who first proposed the idea of developing a new sensor system for detecting fatigue cracks in steel bridge girders, with a particular focus on the difficult-to-monitor regions near stiffeners. The initial geometric configurations for the sensor system were conceived by Dr. Mufti (Concept A), Dr. Thomson (Concept B), and Dr. Baidar Bakht (Concept C), whose combined expertise and vision shaped the direction of this work from the outset.

Building on these foundational ideas, my original contribution lies in advancing the concepts into a fully realized and validated pi-bracket sensor system. I undertook the detailed design, numerical modeling, fabrication, laboratory validation, comprehensive analysis of the system, and simulation of field conditions using Abaqus. Through controlled experiments and finite element simulations, I demonstrated that the pi-bracket sensor can reliably detect crack openings as small as 0.1 mm in both simulation and physical testing, even in regions where traditional fiber optic sensors are limited by bending constraints.

In addition, I developed and implemented a strain subtraction methodology to isolate crack-induced strain from load-induced effects, thereby significantly improving detection accuracy. I also integrated the pi-bracket with distributed fiber optic sensing, specifically through Brillouin Optical Time Domain Analysis, and validated its capability for non-invasive, distributed strain measurement in previously inaccessible areas.

Beyond simulation and experimental validation, I proposed a novel methodology for translating the pi-bracket sensor system into field applications. This methodology establishes practical procedures for identifying critical monitoring locations, optimizing sensor installation configurations, and interpreting sensor data to detect and anticipate fatigue crack initiation in real bridge environments. A key component of this work is the proposal of a crack detection threshold based on empirical data, which serves as a critical parameter for distinguishing crack-related strain signals from normal structural variations. By directly linking predictive simulation results to in-situ applications, this work bridges the gap between laboratory research and practical field deployment.

This thesis provides comprehensive guidelines for the implementation of the pi-bracket sensor system in structural health monitoring. It offers a robust and scalable solution for early crack detection in steel bridges, thereby advancing the state of practice in infrastructure monitoring. By transforming the initial conceptual ideas of Dr. Mufti, Dr. Thomson, and Dr. Bakht into a validated, field-ready system, this work makes a substantive contribution to the field of structural health monitoring and provides new tools to enhance infrastructure safety, resilience, and longevity.

TABLE OF CONTENTS

LIST OF TABLES

LIST OF FIGURES

ABBREVIATIONS

AI	Artificial Intelligence
AR	Average Resolution
ASTM	American Society for Testing and Materials
BIM	Building Information Modeling
BOTDA	Brillouin Optical Time Domain Analysis
BOTDR	Brillouin Optical Time Domain Reflectometry
BWIM	Bridge Weight-in-Motion
CAD	Computer-Aided Design
CHBDC	Canadian Highway and Bridge Design Code
CSHM	Civil Structural Health Monitoring
DAQ	Data Acquisition System
FEA	Finite Element Analysis
FOS	Fiber Optic Sensor
GFRP	Glass Fiber Reinforced Polymer
IASC	International Annealed Copper Standard
IoT	Internet of Things
ML	Machine Learning
NDE	Non-destructive Evaluation
SHM	Structural Health Monitoring
S/N	Signal-to-Noise
SR	Sampling Resolution
UAV	Unmanned Aerial Vehicle

CHAPTER 1: INTRODUCTION

1.1. GENERAL BACKGROUND

Bridges are critical infrastructure components, serving as vital arteries in a nation's transportation network and economic system. They facilitate the efficient movement of goods and people, playing an essential role in connecting communities and supporting commerce. Among the diverse types of bridge structures, steel girder bridges stand out as particularly common, constituting approximately 40% of all short and medium span bridges worldwide. A significant number of these structures were constructed during the extensive construction boom of the 1950s-70s, which saw rapid infrastructure development across North America and many other regions globally. Consequently, many of these bridges are now approaching or exceeding their originally intended service life (Mufti et al. 2011; Raeisi et al. 2018).

The aging process of bridges leads to a variety of potential deficiencies. These can appear as inadequate structural strength, damage resulting from accidents, corrosion of materials, the formation of fatigue cracks, and deficiencies in foundation integrity. Among these issues, the formation and propagation of cracks in steel bridges is particularly critical. Steel girders, formed of web plates with welded flanges, are key elements in bridge structures but are especially susceptible to fatigue fracture crack formation. These cracks often result from environmental stresses and cyclic loading caused by truck traffic, particularly in regions where tensile stresses prevail. The timely detection of such cracks is paramount to prevent unexpected service disruptions and mitigate the associated economic impacts (Raeisi et al. 2019).

A particularly problematic area in steel bridges is the region near vertical stiffeners, which are frequently a source of cracks due to the welding processes used during fabrication. Welded connections at stiffeners introduce residual stresses and create geometric discontinuities, both of which can serve as initiation points for fatigue cracks. Furthermore, constraint-induced fractures are common in these areas because the stiffeners restrict deformation, concentrating stresses and increasing the likelihood of crack formation and propagation under repeated loading cycles. This makes the monitoring of stiffener regions especially important for maintaining the structural integrity of steel bridges (Russo et al. 2016).

Traditionally, bridge condition assessments have relied heavily on visual inspections, a method codified in standards such as the Canadian Highway Bridge Design Code (CHBDC), section 14. However, this approach is fraught with limitations. These include variations in inspector expertise, restricted access to certain structural components, extended intervals between inspections, and the inherent difficulty in identifying small fatigue cracks visually. Moreover, the time between two visual inspections leaves bridge structures unmonitored, during which cracks may propagate to unwanted conditions. To address these shortcomings, the industry has developed various non-destructive evaluation techniques, including acoustic emission analysis, eddy current testing, and ultrasonic inspections. While these methods offer enhanced detection capabilities, they are often costly and are typically performed at discrete intervals, potentially allowing cracks to form and grow undetected between inspection periods (Raeisi et al. 2019).

In response to these challenges, periodic or continuous Structural Health Monitoring (SHM) techniques have emerged as a promising alternative. These advanced methods provide more quantitative and real-time assessments of structural integrity. SHM techniques can be broadly categorized into discrete monitoring systems, which utilize strain gauges or short/long gauge sensors, and distributed monitoring systems, employing technologies such as FOSs (Mufti et al. 2011).

Recent research has made significant strides in improving the effectiveness of health monitoring for bridge structures. A successful experimental program undertaken at the University of Manitoba explored the use of various sensor monitoring systems to detect fatigue cracks in steel girders. The study found that continuous monitoring systems using distributed fiber optic sensors (DFOS) are among the most effective ways to detect fatigue-induced cracks in girders. However, it's important to note that this method has a limitation in detecting cracks formed near vertical stiffeners (Mufti et al. 2011).

The timely detection of cracks is paramount to prevent unexpected service disruptions and mitigate associated economic impacts. As such, the development and implementation of advanced monitoring techniques represent a critical area of research in civil engineering, with the potential to significantly enhance the safety, longevity, and cost-effectiveness of bridge infrastructure management (Mufti 2002).

This thesis aims to contribute to this field by exploring innovative approaches to bridge health monitoring, with a particular focus on steel girder bridges. Through a combination of theoretical analysis and experimental work, this work seeks to advance the state-of-the-art in crack detection and structural health assessment, ultimately contributing to the development of more resilient and sustainable transportation infrastructure. Specifically, it is proposed that the Pi-Bracket system can be used as a harness for the DiTest SMARTape DFOS, aimed at reducing the undetectable regions near vertical stiffeners where crack detection is limited. Additionally, this research investigates the potential of the PI-Bracket crack sensor to achieve similar performance to the DiTest SMARTape, which can reliably detect cracks smaller than 0.2mm wide. These innovations address critical limitations in current monitoring techniques and promise to enhance the comprehensive assessment of bridge structural health.

Figure 1.1: Steel girder with welded stiffener and FOS in a current monitoring system

1.2. PROBLEM DEFINITION

The monitoring of bridge structures has advanced with the adoption of DFOS systems, which are effective in detecting fatigue-induced cracks in steel girders. However, a critical limitation of this technology is its inability to detect reliably cracks that form near vertical stiffeners, the ends of which are particularly prone to crack initiation and propagation due to residual stresses, geometric discontinuities from welding, and stress concentrations caused by restricted deformation under repeated loading cycles (Russo et al. 2016). Furthermore, because the FOS is unattached near stiffeners, it creates unmonitored zones extending 5"-10" to each side of the stiffener, as illustrated in Figure 1.1. In addition, the unattached portions of the FOS are not supported or protected by the surrounding structure in these regions, making them more susceptible to mechanical damage. These limitations raise concerns about the reliability of current monitoring systems in ensuring the safety and structural integrity of steel bridges.

1.3. METHODOLOGY

The Bracket Fatigue Sensor will undergo a comprehensive multi-stage testing process to ensure its effectiveness and reliability. The main stages include initial design concept selection, experimental validation, finite element analysis (FEA) bracket sensor optimization, laboratory validation, and final FEA simulations to predict sensor behaviour in the presence of a crack on a large-scale girder. Each stage is designed to progressively evaluate and refine the sensor's performance, beginning with collaborative decision making and consideration of practical constraints, advancing through digital modeling, laboratory testing and culminating in real-world FEA simulations. This systematic approach allows for a thorough assessment and optimization of the sensor's capabilities.

An additional chapter will present a case study of a bridge in Manitoba, Canada, outlining the instrumentation procedure, data collection methods, and the development of the crack detection methodology, providing essential understanding of practical field deployment and performance evaluation.

1.3.1. Design Concept Selection

In the initial phase of this research, the selection of the bracket geometry was guided by collaborative discussions with the project team, leading to the choice of the Pi-bracket as the most promising concept for the Bracket Crack Sensor. This decision was based on a combination of theoretical considerations and practical input from the team regarding manufacturability and anticipated performance. Material selection was primarily influenced by the limitations of hand-made manufacturing capabilities. Aluminum was chosen for the initial prototypes due to its availability, ease of fabrication, and suitability for the resources at hand. While steel was also considered for its superior mechanical and thermal properties, the practical constraints of the available manufacturing setup necessitated the use of aluminum for the early stages of development and testing.

At this stage, three geometric concepts, illustrated in Figures 1.2, 1.3, and 1.4, were reviewed.

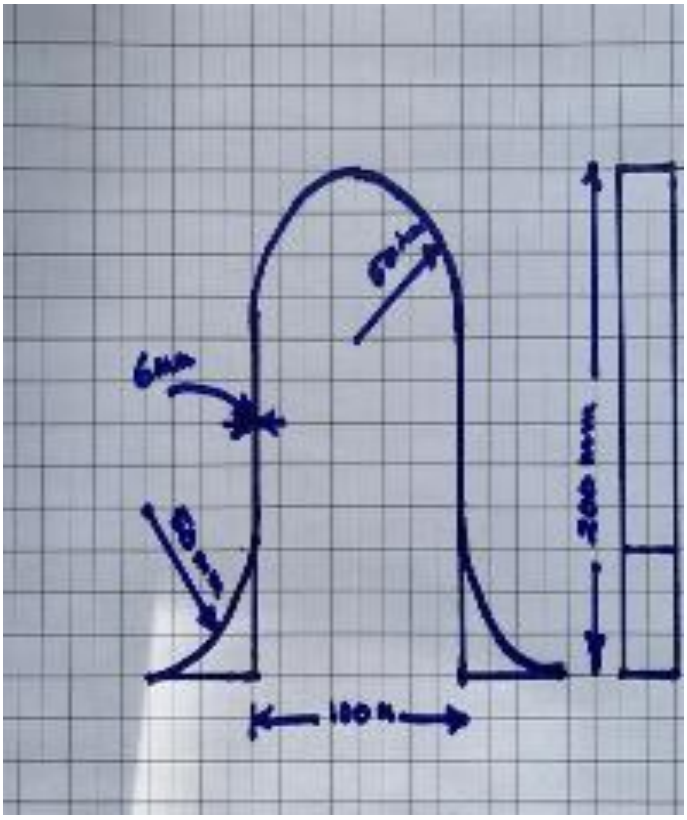

Figure 1.2: Bracket crack sensor - Concept A

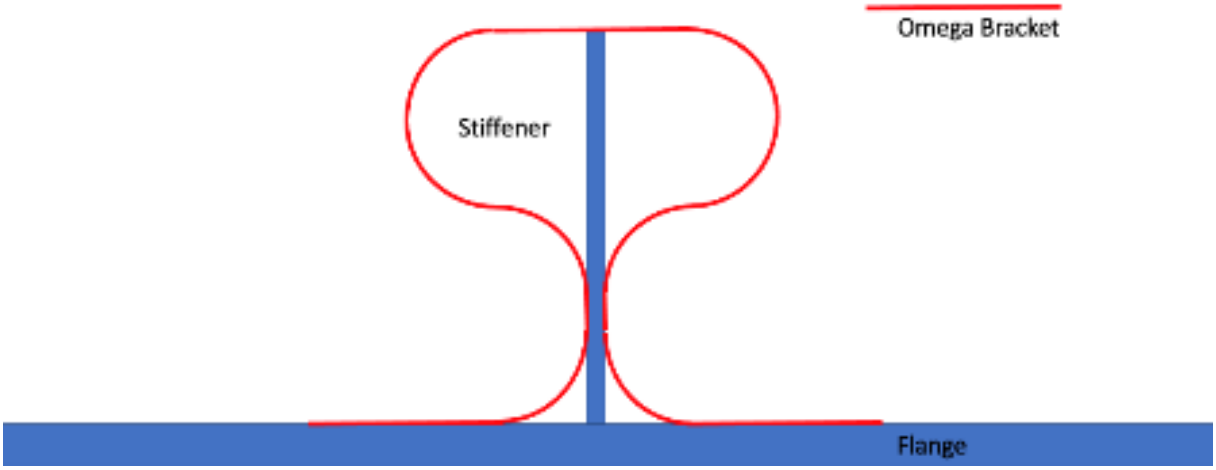

Figure 1.3: Bracket crack sensor - Concept B

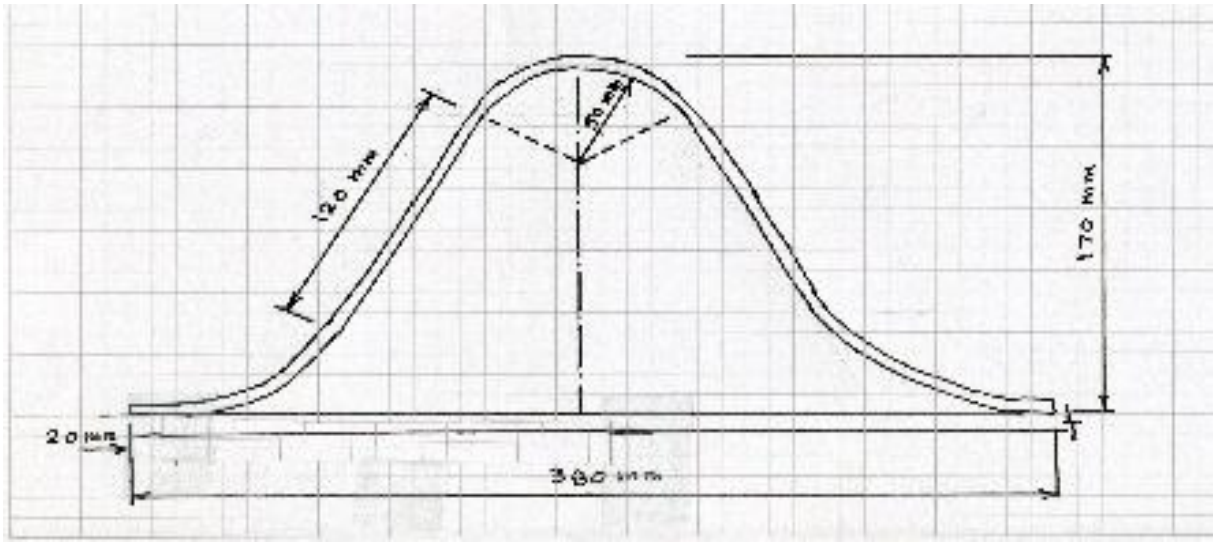

Figure 1.4: Bracket crack sensor - Concept C

The Pi-bracket was advanced to experimental testing based on consensus during these early discussions. The subsequent stages of the research focus on validating this selection through experimental investigation using a specialized apparatus, FEA modeling to evaluate whether the chosen bracket geometry and material are optimal, laboratory-scale testing, and finally, FEA simulation to predict the sensor's performance on a full-scale steel girder with a simulated crack.

1.3.2. Experimental Validation

The most promising concept was selected for manufacturing and subsequent experimental testing using specialized apparatus. This experimental setup consists of two hinged steel plates, a Pi gauge sensor (PI-5-200, Tokyo Sokki Kenkyujo), and a micrometer. The Pi gauge will measure the crack opening signal simulated by the micrometer. Using the micrometer, a controlled force can be applied to split the hinged plates at the hinge, allowing for precise adjustment of the investigated crack width.

This experimental setup offers several advantages for crack sensor research. The inclusion of a micrometer enables precise control over crack width, allowing researchers to finely adjust and test sensor performance across a range of crack sizes. The controlled environment ensures that experiments are highly reproducible, making it possible to obtain consistent results across multiple trials. Additionally, the versatility of the apparatus allows for the evaluation of various types of crack sensors, such as strain gauges, making it a valuable tool for comprehensive sensor assessment.

1.3.3. Laboratory Validation

The laboratory validation involves a 3-meter steel beam with a pre-existing crack at mid-span, created by cutting through the flange into the web 40 mm above the bottom flange and subsequently rewelding. A point load is applied to the top flange at mid-span to induce a new crack in the rewelded region. The actuator load is incrementally increased at 1 mm/min to widen the crack, monitored in real-time using a PI Gauge readout unit mounted on the beam's opposite side.

Concurrently, a Brillouin Optical Time Domain Analysis (BOTDA) fiber optic interrogator is calibrated to capture distributed strain data, while strain gauges installed at critical locations record localized strains for comparison with both FOS readings and FEA predictions. Beam deflection is continuously monitored throughout the test.

1.3.4. FEA Simulations

FEA is employed at two key stages in the research. First, FEA modeling is used to evaluate whether the chosen Pi-bracket geometry and aluminum material are optimal by analyzing key properties such as elasticity, thermal expansion, and corrosion resistance, as well as the interaction between the aluminum bracket and steel girders. This analysis provides a theoretical basis for justifying the initial design choices, assesses their impact on sensor sensitivity, strain transfer efficiency, and long-term durability, and identifies potential opportunities for further optimization, such as modifications to bracket thickness or the consideration of alternative materials for future iterations.

Second, after laboratory-scale testing, FEA simulations are used to predict how the optimized Pi-bracket sensor would perform when installed on a full-scale steel girder with a simulated crack. These simulations allow for detailed analysis of the sensor's response to crack initiation and propagation under realistic loading scenarios, providing critical information on strain distribution, crack opening displacement, and the overall effectiveness of the Pi-bracket design in practical structural health monitoring applications.

By combining digital modeling with physical testing using both specialized apparatus and large-scale laboratory experiments, this methodology ensures a thorough assessment of the sensor's design, sensitivity, and reliability under various simulated crack conditions, contributing to the development of more accurate and dependable structural health monitoring systems.

1.3.5. Case Study

This case study focuses on the deployment and validation of the pi-bracket sensor system integrated with distributed fiber optic sensing technology on a steel bridge in Manitoba, Canada. The purpose is to bridge the gap between laboratory testing and practical field application by assessing how the sensor system performs under real-world conditions and operational variability. A key objective of the field trial is to establish a reliable threshold for crack detection by thoroughly evaluating the pi-bracket sensor system's installation and performance on the actual bridge.

The field trial systematically evaluates the installation methods of the pi-bracket sensor system, focusing on the practical challenges of mounting and maintaining sensors on a large steel bridge

under operational conditions. Sensor signal quality and stability are monitored continuously during normal bridge use, enabling the establishment of baseline strain profiles in critical fatigue-prone regions. These baseline measurements serve as essential reference points for identifying deviations indicative of incipient cracking. Furthermore, the study tests evaluate the crack detection methodology by analyzing real-time data collected from the bridge. This process ensures the sensor system's effectiveness in detecting crack activity under the dynamic and complex loading and environmental conditions experienced in the field, thereby bridging the gap between theoretical models and practical application.

1.4. SCOPE OF RESEARCH

This research proposes the use of the Bracket Crack Sensor as a harness for the DFOS to address current limitations in crack detection near stiffeners in bridge girders. By integrating the Bracket Crack Sensor with the DFOS, the study aims to minimize undetectable regions near stiffeners, where conventional crack detection methods are limited. Furthermore, the research will assess whether the Bracket Crack Sensor, when used with DFOS, can achieve performance comparable to that of the DiTest SMARTape II Strain sensor, which is capable of reliably detecting cracks as small as 0.2 mm in width (Roctest n.d.). Overall, this investigation focuses on evaluating the effectiveness of this combined approach in enhancing crack detection capabilities and advancing SHM systems to improve bridge safety.

1.5. RESEARCH OBJECTIVES

Proposed study investigates and evaluates the following research objectives:

- To develop and validate an innovative Bracket Crack Sensor through a comprehensive multi-stage testing process.
- To manufacture and test the most promising sensor concept using a specialized experimental apparatus.
- To conduct large-scale laboratory validation tests on a 3-meter span steel beam, assessing the sensor's performance under realistic loading conditions.

- To compare and correlate data from multiple measurement systems, including the Bracket Crack Sensor, Pi-gauge, FOS, and Strain Gauges, validating the sensor's accuracy and reliability.
- To analyze the relationship between applied load, crack width, and sensor's sensitivity and range of detection.
- To evaluate the reproducibility and consistency of the Bracket Crack Sensor's performance across repeated tests and varying conditions.
- To employ FEA simulations both to predict sensor behavior on large-scale girders in the presence of cracks and to retrospectively evaluate whether the selection of the Pi-bracket geometry and aluminum material was optimal, identifying opportunities for further design and material optimization.
- To assess the potential for integrating the Bracket Crack Sensor into SHM systems, considering its practical applicability, durability and ability to enhance crack detection near stiffeners.
- To develop a crack detection methodology that can be deployed in the field, enabling objective, automated detection and monitoring of cracks under operational conditions through the establishment and validation of a reliable detection threshold.
- To contribute to the development of more accurate, reliable and dependable SHM technologies through the comprehensive evaluation and refinement of the Bracket Crack Sensor design.

CHAPTER 2: LITERATURE REVIEW

2.1. INTRODUCTION

This chapter presents a comprehensive review of the literature pertaining to SHM, with a particular focus on its application in bridge structures. The review aims to provide a solid foundation for understanding the current state of SHM technology, while also addressing the critical need for new methods to monitor cracks in steel girders.

The chapter begins by exploring the fundamental concepts of SHM, including its core processes and key principles. It then delves into the technological evolution of SHM, tracing its historical development and examining emerging technologies that are driving advancements in the field.

A significant portion of the review is dedicated to the methods and techniques employed in SHM, with a special emphasis on sensor technologies, particularly FOS. The review critically examines the capabilities and limitations of various sensor types, providing a comparative analysis that highlights the unique advantages and challenges associated with each.

The chapter also explores different methods of data collection, including the application of advanced technologies such as artificial intelligence and internet of things. Recent advances and trends in SHM are discussed, encompassing technological innovations, policy developments, and sustainability considerations.

Special attention is given to BOTDA, a key technology in distributed fiber optic sensing. The review examines the principles of BOTDA, its applications in SHM, and recent advancements in this area.

Furthermore, this chapter includes an investigation into various FEA software packages to determine the most appropriate tool for our research needs. This evaluation will consider factors such as accuracy, computational efficiency, user-friendliness, and compatibility with SHM data integration. By assessing popular FEA software used in civil engineering, such as SAP2000, ETABS, STAAD Pro, Abaqus, ANSYS, and others, it is aimed to guide researchers in navigating these options and making informed decisions when selecting software for different applications.

Finally, the chapter concludes with an overview of FEA and its role in SHM, including a discussion of various software tools used in civil engineering for design, structural analysis, and FEA.

By synthesizing current knowledge, identifying trends, and highlighting gaps in the literature, this review aims to contextualize the research questions addressed in this thesis and provide a robust framework for the subsequent chapters.

2.2. CIVIL STRUCTURAL HEALTH MONITORING

2.2.1. Definition and Distinction of Civil Structural Health Monitoring

Civil Structural Health Monitoring (CSHM) is the systematic process of observing, assessing, and analyzing the integrity and performance of civil infrastructure, such as bridges, buildings, dams, and tunnels, over their service life. The primary objective of CSHM is to ensure safety, optimize maintenance, and extend the lifespan of these critical structures by providing timely information on damage, deterioration, or abnormal behavior (Mufti and Thomson 2024).

While the core principles of SHM apply across various engineering fields, CSHM is distinct in several important ways.

Aerospace SHM is tailored to aircraft and spacecraft, where structures are lightweight, highly dynamic, and subject to extreme operational and environmental conditions. Monitoring in aerospace emphasizes real-time diagnostics, fatigue crack detection, and minimal sensor weight (Farrar and Worden 2006).

Mechanical SHM focuses on machinery and rotating equipment, targeting faults such as misalignment, imbalance, and wear. Monitoring methods often involve vibration analysis and lubricant monitoring, with an emphasis on predictive maintenance and minimizing operational downtime (Farrar and Worden 2006).

Civil SHM, in contrast, addresses large-scale, stationary structures exposed to environmental loads and long-term degradation processes like corrosion and fatigue. CSHM must account for the complexity and scale of civil infrastructure, the diversity of construction materials, and the challenges of sensor deployment and maintenance in harsh or inaccessible locations. The societal

consequences of failure, including public safety and economic impacts, are often significant (Mufti and Thomson 2024).

In summary, CSHM is uniquely characterized by its focus on large, long-lived, and safety-critical infrastructure, requiring robust, scalable, and distributed monitoring solutions tailored to the civil engineering context.

2.2.2. Fundamentals of SHM

SHM is a comprehensive process that involves continuous assessment of a structure's integrity over time. The SHM process can be broken down into four main components: sensing, data acquisition, processing, and decision-making.

2.2.2.1. Overview of the SHM Process

Sensing: The first step in SHM involves the deployment of sensors to monitor various structural parameters. These sensors can include accelerometers, strain gauges, FOS, and other devices capable of measuring physical quantities related to structural health (Farrar and Worden 2006). The selection and placement of sensors are fundamental for effective monitoring.

Data acquisition: Once sensors are in place, data acquisition systems collect and store the measured data. This involves converting analog signals from sensors into digital format, often using data acquisition hardware and software (Lynch and Loh 2006). The data acquisition process must be reliable and capable of handling large volumes of data over extended periods.

Processing: The acquired data undergoes processing to extract meaningful information. This stage often involves signal processing techniques, feature extraction, and the application of various algorithms to identify changes in structural behavior (Worden and Manson 2007). Processing may include noise reduction, data normalization, and the application of statistical or machine learning methods.

Decision-making: The final stage involves interpreting the processed data to make informed decisions about the structure's health. This may include automated alerts for potential issues, recommendations for maintenance, or more complex prognostic assessments (Brownjohn 2007).

2.2.2.2. Key Principles of SHM

The key principles of structural health monitoring (SHM) revolve around a systematic approach to ensuring the safety and longevity of critical infrastructure. The primary objective is damage detection, which entails identifying any damage or degradation within a structure by monitoring deviations from its normal behavior, often through changes in dynamic properties or response patterns (Sohn et al. 2003). Once damage is detected, the next principle is localization, where SHM systems work to pinpoint the precise location of the damage within the structure, typically using sensor data fusion and advanced signal processing techniques (Balageas et al. 2006). Quantification is equally important, as it involves estimating the size, severity, or extent of the detected damage to assess its impact on the structure's integrity (Rytter 1993). The final principle is prognosis, which focuses on predicting the future state of the structure, estimating its remaining useful life, and forecasting potential failure modes by leveraging historical data, current condition assessments, and predictive modeling (Farrar and Lieven 2007). By integrating these components and principles, SHM provides a comprehensive approach to maintaining structural integrity, enhancing safety, and optimizing maintenance strategies for critical infrastructure.

2.2.3. Technological Evolution

The technological evolution of SHM has been characterized by remarkable progress over recent decades. Initially, SHM systems relied primarily on periodic visual inspections and manual data collection, as described by Mufti et al. (2022). Early implementations involved basic sensors and data loggers that provided only fundamental structural information. As technology advanced, more sophisticated sensing devices such as strain gauges, accelerometers, and FOS were introduced, greatly enhancing the accuracy and comprehensiveness of data collection (Lynch and Loh 2006; Mufti et al. 2011).

A major milestone occurred in the early 2000s with the advent of wireless sensor networks, which enabled real-time data collection and transmission, thereby increasing the efficiency and coverage of monitoring systems. The integration of Internet of Things (IoT) technologies further improved these capabilities by allowing seamless connectivity and robust data management (Azimi et al. 2020).

In recent years, the field has experienced rapid advancements driven by several emerging technologies. Artificial intelligence (AI) and machine learning (ML) are now utilized to analyze large volumes of structural data, facilitating more accurate damage detection and predictive maintenance (Pulse IoT Technologies 2024). IoT devices, including concrete sensors and wireless strain gauges, provide continuous monitoring and enable early detection of issues such as corroded rebar or cracks in concrete (Ye et al. 2014). Modern sensor technologies have evolved to offer greater precision, reduced size, enhanced durability, and improved energy efficiency, with fiber optic sensors becoming essential due to their high sensitivity and resistance to electromagnetic interference (Rakha and Gorodetsky 2018).

The adoption of drone and robotic inspections has revolutionized data collection, making it safer and more efficient, especially in hard-to-reach areas (Seo et al. 2016). The development of smart materials and self-sensing structures is expanding the possibilities for integrated SHM solutions (Smart Structures 2024; National Instruments 2024). Additionally, the use of digital twins, virtual models continuously updated with real-time data, provides engineers with powerful tools for simulation and scenario analysis (Lai et al. 2023).

The convergence of these emerging technologies is paving the way for more comprehensive and efficient SHM systems. As the discipline continues to evolve, advanced data analytics, IoT integration, and AI-driven decision-making are expected to play increasingly vital roles in safeguarding and extending the lifespan of critical infrastructure (Pulse IoT Technologies 2024; Smart Structures 2024).

2.3. METHODS AND TECHNIQUES IN SHM

2.3.1. Sensor Technologies

SHM employs a variety of sensor technologies to assess the integrity and performance of structures. The most used sensors include strain gauges, accelerometers, and FOS. Each type of sensor has unique capabilities and limitations, making them suitable for different applications in SHM.

2.3.1.1. The Most Common Sensors in SHM

The most common sensors used in SHM offer distinct advantages and limitations. Strain gauges are widely utilized to measure the deformation or strain experienced by materials under stress, making them ideal for static applications that require precise stress and strain measurements. While strain gauges provide accurate localized data, their performance can be affected by environmental conditions such as temperature changes and moisture, which may impact their adhesion to surfaces (Glisic 2022).

Accelerometers, on the other hand, are essential for dynamic monitoring as they measure acceleration forces acting on a structure. These sensors are particularly valuable for assessing vibrations resulting from traffic, wind, or seismic events. While accelerometers provide valuable understanding of a structure's dynamic behaviour, they can be prone to noise and must be carefully calibrated for specific monitoring scenarios (Wang et al. 2023).

Acoustic and ultrasonic sensors detect structural damage through wave propagation analysis, making them valuable for both surface and subsurface flaw detection in SHM (Wang et al. 2023). Ultrasonic sensors emit high-frequency sound waves that reflect off internal defects such as cracks, voids, and delamination, providing precise thickness measurements and flaw sizing in concrete and steel elements. Acoustic emission sensors passively monitor high-frequency stress waves generated by active crack growth, corrosion, or material failure, enabling real-time detection of damage initiation and progression. These sensors excel at identifying active damage processes but require sophisticated signal processing to distinguish structural noise from genuine damage signals

and are typically limited to localized monitoring rather than large-area coverage (Wang et al. 2003).

Fiber optic sensors have gained popularity in SHM due to their resistance to electromagnetic interference, their lightweight, and their ability to be embedded directly within structures. Although FOS are still relatively rare in practical applications, their use is steadily increasing as their advantages become more widely recognized in the field of structural health monitoring. FOS can detect a range of parameters, including strain, temperature, and vibration, with high sensitivity and spatial resolution. Their distributed sensing capabilities enable continuous monitoring over long distances, offering comprehensive data that enhances the understanding of structural health (Roctest n.d.).

Video and camera-based systems, including infrared thermography, are increasingly common for non-contact, real-time visual inspection and crack detection in SHM (Wang et al. 2023; Yoon et al. 2022). These systems are widely paired with machine learning algorithms, such as convolutional neural networks and deep learning, for automated image processing, enabling real-time detection, localization, and quantification of surface cracks, corrosion, and other visible damage across large areas. High-resolution cameras capture surface defects while IR cameras identify subsurface issues like delamination and moisture ingress through thermal signatures. These vision-based approaches enable remote, automated bridge inspections but require good lighting, clear line-of-sight, and computational resources for model training and inference. (Yoon et al. 2022).

The Pi-gauge is a Pi-shaped displacement or strain transducer (Figure 2.1) that measures crack-opening width or small relative displacements between two points on a structure by converting mechanical movement into an electrical signal via strain-gauge elements mounted on a spring-type arch. In bridge applications, the gauge is typically surface-bonded or mechanically fixed across a crack or joint line on concrete or steel elements, where it records variations in crack width or panel-to-panel gap under service loading, including traffic and environmental effects. The device is widely used in field and load-test campaigns on concrete bridge structures such as prestressed concrete girders, segmental box girders, and precast bridge-deck joints, providing quantitative, repeatable measurements that link visible cracking with structural performance

indicators (Tokyo Measuring Instruments Laboratory Co., Ltd. 2019; Tokyo Electric Power Services Co., Ltd. 2021, Tokyo Measuring Instruments Laboratory Co., Ltd. 2025).

Figure 2.1: Pi-gauge

Within SHM, the Pi-gauge is commonly adopted to monitor crack development and movement in concrete bridge components, especially in prestressed concrete and precast concrete systems, where small crack openings and panel to panel gaps can indicate loss of continuity, debonding, or early fatigue related deterioration (Tokyo Electric Power Services Co., Ltd. 2021). Tokyo Electric Power Services Co., Ltd. reports that a pi shaped displacement gauge, combined with strain gauges, is used to monitor crack openings perpendicular to the bridge axis in prestressed concrete road bridges, enabling engineers to estimate residual tensile force in the prestressed concrete steel

and track aging related deterioration without inducing new damage (Tokyo Electric Power Services Co., Ltd. 2021). The Pi-gauge is similarly applicable to steel bridge components, where it can be mounted across welds, joints, or crack like gaps to capture small displacements under cyclic or fatigue loading, although its use in steel tends to be less documented than in concrete. In both material types, the Pi-gauge serves as a practical, field verified SHM device for targeted crack and joint monitoring, particularly in controlled experiments, load test campaigns, and periodic condition assessment programs.

Compared with the pi-bracket sensor system developed in this research, an important distinction is that the Pi-gauge itself functions as the primary sensor, whereas the pi-bracket is a mechanical harness that hosts a FOS to measure strain and crack related response. In the pi-bracket configuration, the bracket transfers localized strain and crack related deformations from the girder to the FOS, which records a distributed strain profile along its length, enabling higher resolution spatial information over a continuous segment of the structure, such as girder. In contrast, the Pi-gauge provides only a local, point based displacement reading at the specific crack or joint where it is installed and does not supply continuous or distributed strain coverage along the member. Additionally, typical Pi-gauge installations in bridge health monitoring applications are oriented toward intermittent or semi continuous monitoring (e.g., during load test campaigns or periodic inspections), and the data acquisition is often limited to discrete measurement intervals rather than true, long term continuous streaming. Many practical deployments rely on manual or semi automated read outs, whereas modern FOS based systems such as the pi bracket can be integrated with distributed fiber optic sensing (e.g., BOTDA) to enable permanent, automated, continuous monitoring with high temporal and spatial resolution. Therefore, while the Pi-gauge is a well established, field verified tool for crack width and gap measurements in concrete and steel bridges, it is fundamentally a local, point based sensor that is less suitable for fully distributed, continuous SHM, whereas the pi-bracket - FOS configuration is explicitly designed to support distributed, long term monitoring of crack related strain in bridge girders.

2.3.1.2. Comparative Analysis of Sensor Capabilities and Limitations

A comparative analysis reveals that while strain gauges offer high accuracy for localized measurements, they are limited in their ability to provide distributed sensing over large areas.

Accelerometers excel in dynamic monitoring but may not capture subtle changes in static conditions and require excessive sensor density for girder-scale coverage (Farrar and Worden 2006). Fiber optic sensors represent the optimal technology for continuous monitoring of steel bridge girders in medium-span bridges due to their unique combination of distributed sensing capability spanning the full girder length using just 1-2 cables, manageable data processing via established Brillouin and Rayleigh scattering analysis on standard infrastructure rather than GPU-intensive AI/ML pipelines required for video systems, and superior environmental resilience without the thermal compensation errors common in strain gauges (Yoon et al. 2022; Roctest n.d.). Unlike short-gauge alternatives that demand hundreds of units, FOS provides continuous 24/7 strain profiles detecting fatigue cracks and yielding patterns while matching steel's thermal expansion characteristics, offering global structural insights with minimal sensor density as confirmed by Table 2.1 (Farrar and Worden 2006). FOS provide extensive coverage with the ability to monitor multiple parameters along a single fiber, making them particularly advantageous for large-scale infrastructures (Roctest n.d.), though they face challenges such as installation complexity and sensitivity to bending constraints (Mufti et al. 2011; Ye et al. 2014).

Table 2.1: Comparison of common SHM sensors

Sensor Type	Monitoring Type	Spatial Coverage	Coverage Scale	Data Processing complexity
Strain Gauges	Continuous	Local (mm-cm)	Short Gauge	Simple
Accelerometers	Continuous	Local/Global	Short Gauge	Moderate
FOS (Distributed)	Continuous / Distributed	Distributed (cm-km)	Long Gauge / Distributed	Advanced
Video / Cameras	Continuous	Local (cm-m)	Area based	AI / ML Heavy
Acoustic / Ultrasonic	Triggered / Event	Local (cm-m)	Short Gauge	Advanced
Pi-Gauge	Periodic	Local (mm-cm)	Short Gauge	Simple

2.3.2. Fiber Optic Sensors

FOS represent a cutting-edge technology in the field of SHM. These sensors leverage the properties of light traveling through optical fibers to detect changes in physical parameters such as temperature and strain.

2.3.2.1. Overview of FOS Technology and its Advantages

FOS provide numerous significant benefits compare to conventional sensing technologies. Their small size and lightweight nature allow for easy embedding into structures without adding significant mass or altering structural integrity. Additionally, FOS are immune to electromagnetic interference, making them suitable for use in environments where electrical noise could compromise sensor performance (Roctest n.d.). The ability of FOS to provide distributed sensing capabilities enables continuous monitoring along the entire length of the fiber, allowing for real-time assessment of structural conditions over vast distances.

The SMARTape II sensor system, developed by Roctest, represents a significant advancement in distributed strain sensing technology for SHM applications. The sensing architecture incorporates single-mode optical fiber within a Glass Fiber Reinforced Polymer (GFRP)/epoxy composite matrix, providing superior mechanical durability and environmental resistance characteristics. This sensor platform enables both surface-mounted and embedded deployment configurations, demonstrating exceptional measurement stability under adverse environmental conditions. The optimized form factor and robust mechanical properties facilitate long-term deployment in civil and geotechnical engineering applications, particularly in extreme operational environments where conventional sensing methodologies demonstrate limited efficacy (Roctest n.d.).

2.3.2.2. Limitations of FOS

Despite their advantages, FOS also have certain limitations. One significant challenge is related to bending constraints; excessive bending can lead to signal loss or inaccurate readings (Mufti et al. 2011). Additionally, while FOS technology is versatile, its application in specific areas may be

hindered by practical issues such as installation complexity and sensitivity to surrounding materials that can affect performance (Wang et al. 2023).

In conclusion, while FOS present remarkable opportunities for advanced SHM applications due to their unique capabilities, addressing their limitations is essential for optimizing their effectiveness in various structural monitoring scenarios.

2.3.3. Methods of Data Collection

SHM entails observing and analysing a system continuously over time by intermittently measuring its performance. These measurements help monitor any changes to the material and geometric characteristics of infrastructure including bridges.

Predominant method of the performance measurement of bridges all over the world is through visual inspections. Comprehensive non-destructive testing and analysis are typically carried out when necessary to assess specific local or component level data, with the goal of gaining a deeper insight into the structure. Moreover, continuous monitoring of structural health is limited to exceptional cases where the necessity for such data is evident, typically for complex structural systems or structures with known issues. In scenarios where repairs could be prohibitively costly or unfeasible in the immediate future, monitoring is utilized to closely observe the performance of the structure (Ettouney and Alampalli 2012).

Visual inspection has served as the primary method for assessing the condition of bridges. However, in recent years, there has been a growing adoption of additional non-destructive evaluation (NDE) techniques to supplement visual inspections. When a crack forms in a bridge girder, it induces a change in the local strain. Furthermore, the process of crack formation and propagation can generate an acoustic wave. NDE methods capitalize on these phenomena, employing various types of devices and sensors including strain gauges, FOS, etc. SHM can be categorized as periodic monitoring or continuous monitoring (Raeisi et al. 2018).

2.3.3.1. Periodic Monitoring

Periodic inspection can be utilized through several methods such as Visual Inspections, Ultrasound Testing, Acoustic Emission, etc.

The health of a bridge is usually monitored by visual inspections (Ettouney and Alampalli 2012). Visual inspection is a very economical solution to assess performance of the bridge since it does not require any specific testing equipment (Raeisi et al. 2018).

Damage assessment using SHM techniques are used to calculate remaining life of the bridges and their elements (Ettouney and Alampalli 2012). Several limitations which may in some cases result in bridge failure were identified. Some of the limitations are inspection intervals, interpretability, and accessibility (Raeisi et al. 2018).

The most traditional performance assessment ratings are inaccurate due to the high variability in traffic loading. Inspection levels of outdated visual method as specified in Canadian Highway Bridge Design Code are not adequate in estimations of remaining life of the bridges and their elements. That can lead to recommendations for unnecessary and in most cases extensively costly repairs if condition is under-estimated, or in contrast if condition is over-estimated it can lead to dangerous safety issues. Modern SHM systems, can overcome issues with inaccurate assessment of bridge condition. Moreover, inexpensive, and portable methods of obtaining traffic data can serve both, to monitor structural health of the infrastructure and to collect very much wanted larger amount of site-specific data that can be used for other purposes (Mufti et al. 2018).

According to Section 14 of the Canadian Highway Bridge Design Code (CHBDC), the interval between visual inspections must not exceed 24 months. The CHBDC outlines three distinct levels of inspection. The first level, INSP1, pertains to components that cannot be inspected due to accessibility challenges, such as hidden structural members or interior parts that are not reachable, including internal webs or voided slabs. The second level, INSP2, involves inspections that fulfill the evaluator's requirements, with all findings thoroughly documented and made available for the evaluator's review. The third and most comprehensive level, INSP3, requires the evaluator to specifically direct the inspection of all critical components as well as any elements considered substandard, ensuring a thorough assessment of the bridge's condition (CSA 2014).

While the code mandates that periods between visual checks cannot exceed 24 months, it is important to note that this alone may not adequately ensure the bridge's safety, which remains a primary objective of performance assessment. Mufti, Bakht, Raeisi, Algohi & Faraz built a strong case proposing addition of new INSP4 inspection level through SHM to current three inspection levels of the bridge condition assessment arguing that would significantly increase safety of the bridges. Researchers concluded that the current concept is unreliable. The reliability index calibration methodology is significantly influenced by inspection protocol efficacy, wherein the manual inspection procedures conducted by field personnel constitute a critical determinant in the assessment framework. New INSP4 inspection level would require bridges to be instrumented with electronic sensors, continuously monitoring structural health (Mufti et al. 2018).

2.3.3.2. Continuous Monitoring

There are several methods that can be deployed for continuous SHM, including vibration-based damage detection or strain-based sensing detection using different types of sensors.

One of the most common methods utilized to monitor steel girders bridges is with strain gauges. This method offers two approaches, direct and indirect sensing. Direct approach is when the strain gauge is applied directly to the girder surface containing the crack, measuring the strain. Formation or propagation of the crack will result in change in strain, which can be detected via data acquisition readout unit. While this approach offers the benefit of straightforward interpretation of measurements for crack detection, it requires a considerable number of sensors to monitor larger areas. This can lead to intricate wiring, a high volume of data acquisition channels, and ultimately drives up the overall cost of monitoring (Raeisi et al. 2018).

The indirect sensing method relies on strain measurements taken at locations distant from the surface where the crack is present. In this technique, strain gauges are affixed to the let's say flanges of the girder, monitoring crack in a girder web. Given that these strain gauges are not directly applied to the surface with the crack, algorithms become essential to predict damage within the girder (Raeisi et al. 2018).

While strain gauges have proven reliability in crack detection, researchers have been seeking alternative solutions due to their limitations as discussed above. Since the 1990s, FOS have been

utilized for SHM. The principle of FOS relies on the transmission of light through optical fibers to measure physical quantities such as displacement, temperature or strain. There are different mechanisms by which FOS operate, including intensity-based, phase-based and wavelength-based methods. FOS can be intrinsic or extrinsic, with intrinsic sensors further categorized into short gauge, long gauge, and distributed sensors. DFOS, employing different methods of sensing are practical for detecting damage in steel bridge girders, monitoring strain along the entire girder length. Some of the most used methods of sensing includes Bragg Grating Optical Time Domain Reflectometry and BOTDA (Ettouney and Alampalli 2012).

2.3.4. Data Processing Techniques

Data processing techniques are essential in Structural Health Monitoring by enabling the extraction of meaningful information from vast amounts of sensor data. Modern SHM systems generate large volumes of heterogeneous data that require sophisticated processing techniques for effective interpretation and decision support. This section examines the primary data processing techniques employed in contemporary SHM data analysis:

Statistical analysis: Statistical analysis forms the foundation of SHM data processing. It involves methods such as Principal Component Analysis, Fast Fourier Transform, and time-series analysis to process vibration data and assess structural health (Wang et al. 2023). These techniques are particularly useful for long-term monitoring, where historical data can be analyzed to identify patterns and anomalies in structural behavior. For instance, frequency-response functions and principal component analysis have been widely used for feature extraction in bridge SHM applications, enhancing system efficiency by reducing computational demand for damage recognition (Wang et al. 2023).

Machine learning: Machine learning has revolutionized SHM by enabling the automated processing of large datasets to uncover complex relationships that traditional methods may overlook. In SHM applications, machine learning is primarily used for pattern recognition and data-driven damage diagnostics. Support Vector Machines, Neural Networks, and Random Forest classifiers are examples of machine learning algorithms that serve as key computational frameworks for detecting structural damage, identifying anomalies, and implementing predictive

maintenance in infrastructure monitoring systems. Deep learning models have demonstrated high accuracy in detecting structural damage using limited sensor data. The proposed methodology integrates a deep neural network with Principal Component Analysis to enhance crack detection and localization, using a reduced strain gauge sensor array to reconstruct strain fields through dimensionality reduction and predictive modeling techniques (Yoon et al. 2022).

Artificial intelligence: Artificial Intelligence methodologies in Structural Health Monitoring extend beyond conventional machine learning frameworks by incorporating advanced decision-making architectures capable of processing heterogeneous sensor data streams for comprehensive structural assessment. Recent AI-driven SHM systems integrate machine learning, deep learning, and transfer learning paradigms, enabling improved performance in complex structural systems through large-scale data analytics and digital transformation frameworks (Wang et al. 2023). These algorithmic implementations encompass the complete SHM operational spectrum, incorporating advanced sensing technologies, sophisticated data preprocessing protocols, feature extraction methodologies, and decision-making frameworks. Together, these elements establish a comprehensive structural assessment paradigm based on computational intelligence techniques.

Digital twin: Digital twins offer an innovative approach to Structural Health Monitoring by generating virtual models of physical structures that are dynamically updated with real-time data. This technology enables engineers to simulate various scenarios, predict future performance, and make informed decisions about maintenance or retrofitting needs (Wang et al. 2023). Digital twins integrate sensor data with deep learning models to provide real-time diagnostics and forecasting of potential structural issues, enhancing overall efficiency and safety. For example, researchers at Newcastle University are developing a digital twin framework for real-time structural damage identification, using a virtual replica to support continuous monitoring and performance prediction with high accuracy (Wang et al. 2023).

These data processing techniques are transforming SHM practices worldwide. Their integration enables more accurate assessments of structural health, proactive maintenance planning, and improved safety for critical infrastructure.

2.4. RECENT ADVANCES AND TRENDS

2.4.1. Technological Innovations

SHM has experienced substantial progress with the incorporation of Artificial Intelligence (AI), the Internet of Things (IoT), and big data analytics, alongside the emergence of autonomous systems utilizing drones and robots. The combination of AI, IoT, and big data analytics has transformed SHM methodologies, facilitating more efficient and precise monitoring of civil infrastructure. With AI and IoT, SHM systems can now collect and analyze data in real time, allowing for immediate assessment of structural conditions. Enhanced pattern recognition and anomaly detection are made possible through sophisticated algorithms, improving the identification of potential issues before they become critical. Predictive maintenance strategies are also facilitated by these innovations, enabling infrastructure managers to address problems proactively. Furthermore, the development of autonomous SHM systems using drones and robots has expanded the reach and safety of inspections, allowing for the monitoring of hard-to-access or hazardous areas without putting personnel at risk.

Distributed fiber optic sensors have played a transformative role in these technological innovations. Their ability to provide continuous, distributed measurements of strain, temperature, and vibration along the entire length of a fiber allows for unprecedented spatial coverage and resolution in monitoring civil infrastructure. Unlike traditional point sensors, DFOS can detect subtle changes and emerging issues over vast areas, which is especially valuable for large-scale structures like bridges and tunnels. As DFOS technology becomes more integrated with AI, IoT, and autonomous inspection systems, it enables more comprehensive and automated monitoring solutions that significantly enhance the safety and reliability of critical infrastructure.

2.4.1.1. Real-time Data Collection and Analysis

IoT-enabled sensors embedded in structures continuously monitor critical parameters such as strain, temperature, and vibration, generating vast amounts of data for real-time analysis using advanced AI algorithms (Wang et al. 2023). The synergy between IoT and AI has greatly enhanced the effectiveness of SHM systems, enabling more precise and efficient assessments of structural integrity. Strategically placed sensors provide a constant stream of data that offers a comprehensive

understanding of a structure's condition. This continuous monitoring in real-time is essential for maintaining operational reliability, optimal performance, and safety (Scuro et al. 2023). The real-time nature of this data collection facilitates timely decision-making. Once captured, sensor data is transmitted to central processing units where AI algorithms analyze the information immediately. This rapid processing allows for prompt responses to detected anomalies, preventing minor issues from escalating into significant structural failures (Mazhandu 2024).

Distributed fiber optic sensors have revolutionized real-time data collection and analysis in SHM by enabling continuous monitoring over long distances with high spatial resolution. These sensors generate large volumes of data that can be transmitted in real time to central processing units, where advanced AI algorithms analyze the information for immediate assessment. The distributed nature of DFOS ensures that even minor anomalies or localized changes in structural behavior are captured, providing a more comprehensive and accurate assessment of a structure’s health. This capability supports timely decision-making and rapid response to detected issues, greatly improving the effectiveness of real-time SHM systems (Wang et al. 2023; Scuro et al. 2023).

AI algorithms, particularly those based on machine learning models, are pivotal in interpreting the extensive datasets generated by IoT sensors. These algorithms excel at identifying patterns and trends that may not be apparent to human analysts, offering understanding into the health and performance of structures. Over time, as these AI systems process more data, they refine their predictive capabilities, further enhancing the overall efficiency and reliability of SHM systems (Abruzzese et al. 2024).

2.4.1.2. Enhanced Pattern Recognition and Anomaly Detection

Machine learning algorithms detecting subtle changes in structural behavior that could signal potential problems, facilitating early intervention (Presno Vélez et al. 2024). This capability marks a significant improvement in SHM, enabling more proactive and accurate maintenance strategies. Deep learning models within machine learning frameworks excel at analyzing vast amounts of data from numerous sensors and recognizing complex patterns that may not be noticeable to human observers. These algorithms can be trained using historical data to establish a baseline of normal structural behavior, allowing them to identify deviations from this norm. This method enables the

detection of anomalies that may indicate the emergence of structural issues, such as fatigue cracks, corrosion, or alterations in load distribution (Khaloo et al. 2018).

The early detection of potential problems is essential for maintaining the integrity and longevity of structures. By identifying issues in their nascent stages, engineers and maintenance teams can intervene before minor problems escalate into major structural failures. This not only enhances safety but also can lead to significant cost savings by avoiding extensive repairs or premature replacement of infrastructure (Muttillo et al. 2024).

Moreover, as these machine learning models continue to process data over time, they can refine their predictive capabilities, becoming increasingly accurate in distinguishing between normal variations and genuine anomalies. This adaptive learning process enhances the overall reliability and effectiveness of SHM systems, providing stakeholders with increasingly valuable knowledge for making decisions regarding infrastructure management and maintenance planning (Scuro et al. 2023).

The continuous and high-density data provided by distributed fiber optic sensors significantly improves pattern recognition and anomaly detection in SHM. Machine learning algorithms can leverage the detailed datasets from DFOS to identify subtle changes and complex patterns that may indicate early-stage damage, such as crack initiation or propagation. The distributed sensing capability ensures that no critical area is left unmonitored, making it easier for AI models to establish accurate baselines and detect deviations. This enhances the reliability of early warning systems and supports proactive maintenance interventions before issues escalate (Khaloo et al. 2018; Presno Vélez et al. 2024).

2.4.1.3. Predictive Maintenance

AI-powered systems can forecast potential failures by examining historical data in combination with real-time conditions, facilitating the adoption of proactive maintenance strategies (Wang et al. 2023). This innovative maintenance approach utilizes machine learning algorithms and artificial intelligence to analyze extensive sensor and monitoring device data gathered from instrumented structures.

By continuously analyzing real-time data and comparing it to historical trends, AI systems can detect subtle signs of potential structural problems well before they escalate. This capability facilitates a transition from reactive or scheduled maintenance to a more efficient and cost-effective proactive maintenance model. Predictive algorithms are particularly effective at identifying early warning signs of equipment failure or structural deterioration, such as shifts in vibration patterns, temperature anomalies, or stress variations indicators that might go unnoticed during traditional inspections (Muttillo et al. 2024).

The implementation of AI-driven predictive maintenance has shown significant benefits across various industries. Studies have demonstrated that this approach can lead to a remarkable reduction in operational expenditures related to maintenance activities. Moreover, by preventing unexpected failures and optimizing maintenance schedules, predictive maintenance contributes to extending the lifespan of critical infrastructure assets, promoting long-term sustainability and safety (Scuro et al. 2023).

Distributed fiber optic sensors contribute to predictive maintenance by supplying continuous, high-resolution data that allows AI-powered systems to identify early signs of structural deterioration. By monitoring parameters such as strain and temperature over time, DFOS enable predictive algorithms to detect trends and forecast potential failures with greater accuracy. This supports a shift from reactive or scheduled maintenance to a proactive approach, optimizing maintenance schedules and reducing costs. The integration of DFOS data into predictive maintenance frameworks extends asset life and enhances the safety and sustainability of infrastructure systems (Scuro et al. 2023; Muttillo et al. 2024).

As these machine learning models continue to process data over time, they can refine their predictive capabilities, becoming increasingly accurate in distinguishing between normal variations and genuine anomalies. This adaptive learning process enhances the overall reliability and effectiveness of SHM systems, providing stakeholders with increasingly valuable insights for decision-making regarding infrastructure management and maintenance planning (Presno Vélez et al. 2024).

2.4.2. Policy and Standards Development

In Canada, the development of policies and standards for SHM systems is critical for ensuring effective implementation and integration into infrastructure management practices. The "Guidelines for Structural Health Monitoring," published by SIMTReC (formerly ISIS Canada) in 2001, provides a foundational framework for SHM practices across the country. These guidelines outline best practices for the design, installation, operation, and maintenance of SHM systems, ensuring that stakeholders can effectively monitor structural integrity (Kim et al. 2010).

The emergence of these standards has had a significant impact on the implementation of SHM technologies. By establishing clear protocols and methodologies, the guidelines facilitate uniformity in monitoring practices across various sectors, including transportation and civil infrastructure. This consistency not only enhances the reliability of SHM systems but also builds public confidence in the safety and longevity of critical infrastructure assets (Kim et al. 2010). Furthermore, the guidelines encourage the adoption of innovative technologies such as wireless sensor networks and advanced data analytics. The integration of these technologies allows for real-time monitoring and data collection, which is essential for proactive maintenance strategies (ISIS Canada 2001). As a result, stakeholders can identify potential issues before they escalate into significant problems, thereby improving overall infrastructure resilience.

The development of the "Guidelines for Structural Health Monitoring" was a collaborative effort involving researchers from across Canada under the leadership of Dr. Aftab Mufti, a prominent figure in SHM research and Director of SIMTReC. This nationwide collaboration ensured that the guidelines addressed diverse regional challenges and incorporated expertise from multiple disciplines within civil engineering.

The "Guidelines for Structural Health Monitoring" have played a pivotal role in shaping SHM practices within Canada. They emphasize the use of FOS and advanced materials to improve the durability and accuracy of monitoring systems (ISIS Canada 2001). By standardizing methodologies for sensor placement, data collection, and interpretation, these guidelines facilitate widespread adoption of SHM technologies across Canadian provinces.

The impact extends beyond technical implementation; these guidelines have also influenced policy development by encouraging collaboration between academia, industry stakeholders, and

government agencies. This collaborative approach ensures that SHM practices align with national infrastructure priorities while addressing region-specific challenges such as extreme weather conditions common in Canada.

Moreover, Mufti et al. (2018) proposed adding a new inspection level related to SHM to the existing three inspection levels outlined in the Canadian Highway Bridge Design Code Section 14. This proposed INSP4 inspection level emphasizes continuous monitoring through SHM technologies, significantly enhancing bridge safety by providing more comprehensive assessments of bridge conditions. The authors argue that this addition would improve infrastructure safety by addressing limitations in current bridge evaluation practices.

Additionally, the Canadian Highway Bridge Design Code (CSA S6-19) includes provisions for structural monitoring and maintenance of bridges, providing a comprehensive framework that guides the design, evaluation, and rehabilitation of highway bridges across the country (CSA 2019). The CSA S6-19 code emphasizes integrating SHM practices into bridge design to enhance safety and reliability.

2.4.3. Sustainability Considerations

SHM is essential for promoting sustainable infrastructure management by improving the longevity of structures, optimizing maintenance strategies, and minimizing environmental impacts. Incorporating SHM systems into infrastructure management helps organizations meet worldwide sustainability objectives, including United Nations Sustainable Development Goals (SDGs) (Encardio Rite 2024). SHM systems deliver real-time data on structural integrity, facilitating proactive maintenance that optimizes resource use and prevents catastrophic failures, thereby reducing the need for costly replacements.

2.4.3.1. Lifecycle Management and Resource Optimization

A significant contribution of SHM to sustainability is its capacity to enhance lifecycle management of infrastructure. SHM systems facilitate ongoing monitoring throughout a structure's lifecycle, from design and construction to operation and decommissioning, enabling data-driven decision-

making at each phase. This integration minimizes the need for invasive inspections and unnecessary repairs, thereby conserving materials and energy while promoting long-term reliability (Atamturktur et al. 2014). As an example, bridges and buildings equipped with FOS provide immediate feedback about their structural performance without compromising their aesthetic or structural integrity, ensuring minimal environmental impact during monitoring processes (Smart Structures 2024).

2.4.3.2. Extending Service Life and Reducing Environmental Impact

Another critical aspect of SHM's role in sustainability is its ability to mitigate environmental impacts by extending the service life of infrastructure. By detecting early signs of damage or deterioration, SHM systems allow engineers to address issues before they escalate into major problems, reducing the need for extensive reconstruction or material-intensive repairs. This not only lowers greenhouse gas emissions associated with construction activities but also preserves natural resources (Limongelli et al. 2019). Additionally, advancements in renewable energy technologies have enabled SHM systems to harness power from solar, wind, or structural vibrations, ensuring a sustainable energy supply for sensor networks while reducing dependence on conventional energy sources (Encardio Rite 2024).

Recent studies have quantified the environmental benefits of applying SHM to bridge management. Raeisi et al. (2021) demonstrated that the use of SHM instrumentation and analysis techniques on steel girder bridges can significantly reduce carbon dioxide (CO_2) emissions by extending the service life of aging infrastructure. Their research showed that if SHM is used to extend the service life of a bridge by 5 to 10 years, the average annual CO_2 emissions associated with bridge reconstruction can be reduced by 9–17%. Furthermore, a broader implementation of SHM across a fleet of structurally deficient bridges could result in substantial cumulative emission reductions. For example, in the state of Iowa, it was estimated that if SHM were used to extend the service life of 80% of deficient bridges by 5–10 years, total CO_2 emissions from bridge replacements over a 20-year period could be reduced by up to 60%. These findings underscore the important role of SHM not only in infrastructure resilience but also in advancing environmental sustainability by minimizing the carbon footprint of bridge maintenance and replacement (Raeisi et al. 2021).

2.5. BRILLOUIN OPTICAL TIME DOMAIN ANALYSIS

2.5.1. Principles of BOTDA

BOTDA is a sophisticated distributed sensing method that measures strain and temperature variations throughout an optical fiber by using stimulated Brillouin scattering. The principle of BOTDA is based on the Brillouin effect, where light interacts with acoustic phonons within the fiber material (Ettouney and Alampalli 2012).

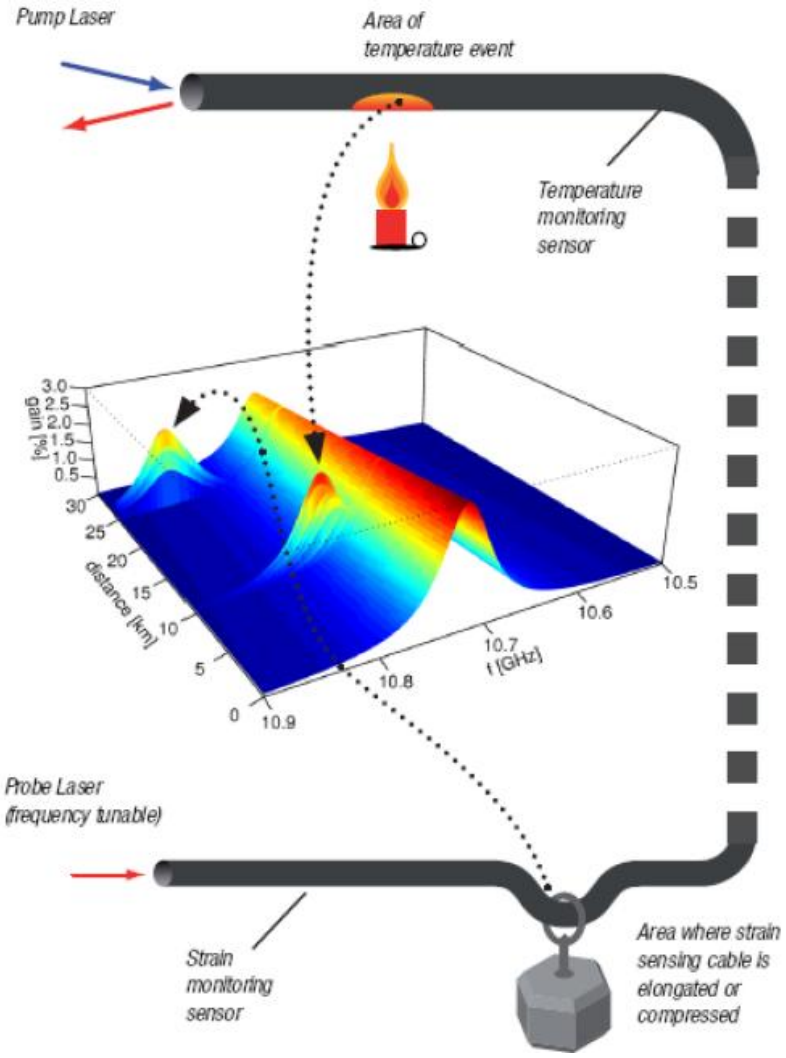

Figure 2.2: BOTDA sensing method (Omnisens 2009)

Ettouney and Alampalli (2012) explained that BOTDA operates based on the Brillouin effect, where light interacts with the vibrational waves known as acoustic phonons within a material. Sending a laser pulse through an optical fiber induces Brillouin scattering, which is sensitive to local temperature fluctuations or mechanical stresses along its span. This strain prompts a change in the frequency of the Brillouin-scattered light, which is subsequently captured and examined to ascertain the temperature or strain at distinct location along the fiber. BOTDA sensing method is shown in the Figure 2.2.

According to Omnisens (2009) Brillouin frequency shift v_b can be expressed as:

$$v_b = \frac{2nv_a}{\lambda_{pump}}$$

where n is refractive index, λ_{pump} is the wavelength of the pump and v_a is the local acoustic wave velocity, which changes due to the compressive or tensile strains within a material as a result of stresses. Abovementioned equation can be simplified as

$$v_b = A_\varepsilon \times \varepsilon$$

where A_ε is factor of strain proportionality and ε is normal local strain.

Because of direct relationship between Brillouin shift and temperature, the Brillouin frequency shift v_b can be generalized to:

$$v_b = A_\varepsilon \times \varepsilon + A_T \times T$$

where A_T is factor of temperature proportionality and T is local temperature.

Through examining the frequency shift of the Brillouin scattered light, strain at various points along the length of the fiber can be determined. This information is used to create a distributed strain profile of the fiber (Omnisens 2009).

The BOTDA method offers several advantages over other distributed sensing techniques. Compared to Brillouin Optical Time Domain Reflectometry (BOTDR), BOTDA achieves higher spatial resolution and greater measurement accuracy, making it particularly suitable for applications requiring precise localization of strain events. Additionally, BOTDA offers a longer measurement range, attributed to the strong signal strength inherent in the technique. Another

significant benefit is its ability to simultaneously measure both temperature and strain, allowing for comprehensive monitoring in environments where both parameters may fluctuate.

The spatial resolution achievable with BOTDA is governed by the pulse width of the pump beam, which typically ranges from 0.1 meters to 2 meters. This flexibility allows the system to be tailored to the specific requirements of different SHM applications (Omnisens 2009).

2.5.2. Technical Capabilities and Performance of BOTDA

The effectiveness of BOTDA in SHM depends on several critical technical parameters. Among these, accurate peak frequency determination is fundamental, as it directly governs the reliability of strain and temperature measurements along the fiber. Additionally, the reproducibility of measurements ensures BOTDA's suitability for long-term monitoring, while high strain and spatial resolution enable the detection of subtle and localized structural changes. Together, these capabilities define the precision, reliability, and practical value of BOTDA for civil engineering applications.

A fundamental aspect of BOTDA is the accurate determination of the Brillouin frequency shift, which encodes the local strain and temperature information along the optical fiber. This frequency shift is extracted by scanning the frequency of a probe wave relative to a pump pulse and recording the Brillouin gain spectrum at each point along the fiber. The peak of the Brillouin gain spectrum, corresponding to the local Brillouin frequency, is typically identified using Lorentzian curve fitting or advanced signal processing techniques such as cross-correlation. The precision of this peak frequency determination is crucial, as it directly impacts the reliability of distributed strain and temperature measurements, allowing even small changes in the structural state to be detected and quantified (Nikles et al. 1997).

Another critical performance parameter is reproducibility. BOTDA systems are recognized for their excellent measurement stability and repeatability, with strain measurement repeatability typically within ±5 με and Brillouin frequency shift reproducibility within ±2 MHz under controlled conditions. This high level of reproducibility is essential for long-term monitoring applications, ensuring that BOTDA can consistently deliver reliable data over extended periods,

which is vital for tracking gradual structural changes and maintaining the credibility of the monitoring system (Inaudi and Glisic 2006; Barrias et al. 2016).

Strain resolution is also a defining strength of BOTDA. Modern systems can resolve strain changes as small as 10 με, with some advanced laboratory setups achieving even finer resolutions below 5 με. Such high sensitivity enables the early detection of microcracks, localized yielding, or other subtle deformations, providing engineers with timely information to address potential problems before they escalate into major structural damage (Inaudi and Glisic 2006; Barrias et al. 2016).

Spatial resolution, determined primarily by the width of the pump pulse, defines how finely BOTDA can localize changes along the fiber. Standard commercial systems offer spatial resolutions ranging from 0.1 m to 2 m, while recent advances, such as the differential pulse-width pair technique, have pushed spatial resolution down to just a few centimeters. Such fine spatial resolution is particularly valuable for detecting localized phenomena, such as cracks, weld defects, or stress concentrations, especially in large and complex civil structures (Omnisens 2009).

In summary, the technical strengths of BOTDA, including precise peak frequency determination, excellent reproducibility, high strain resolution, and fine spatial resolution, make it a powerful and reliable tool for distributed structural health monitoring. These capabilities ensure that BOTDA can provide actionable, long-term insights into the integrity and safety of civil infrastructure.

2.5.3. Applications in SHM

BOTDA technology has become widely adopted in SHM because of its ability to provide distributed measurements over long distances. In bridge monitoring, BOTDA enables continuous, real-time strain measurements along the entire span, offering a more comprehensive assessment than traditional point sensors and making it particularly suitable for large-scale infrastructure monitoring programs (Mufti et al. 2011). The technology is also used in pipeline monitoring, where it facilitates the continuous detection of strain and temperature changes, allowing for the early identification of leaks or structural issues (Zhang et al. 2019). In geotechnical applications, BOTDA systems are employed to monitor slope stability and detect ground movements (Zhu et al. 2015). High-rise building monitoring is another area where BOTDA has proven valuable, as it can

measure differential shortenings in columns and structural walls, helping to track shrinkage and creep-induced deformations across multiple floors (Glisic et al. 2013; Barrias et al. 2016).

The benefits of BOTDA in SHM applications include its capacity for continuous, real-time monitoring, high spatial resolution, and measurement accuracy, as well as its suitability for long-range sensing and ability to detect and localize multiple events along the fiber length. However, BOTDA systems do have some limitations, such as the requirement for access to both ends of the fiber, increased system complexity compared to other techniques, and the potential for measurement errors due to cross-sensitivity between strain and temperature.

These applications demonstrate the versatility and effectiveness of BOTDA technology in various SHM scenarios. As the technology evolves, addressing current limitations and improving performance, BOTDA is poised to play an increasingly important role in ensuring the safety, longevity, and efficiency of critical infrastructure. The integration of BOTDA with other sensing techniques and advanced data analysis methods promises to further enhance its capabilities in SHM applications, underscoring its importance as a key tool in the future of infrastructure management and maintenance.

2.6. SUMMARY

This chapter has presented a comprehensive review of the literature on SHM, with a particular focus on its application to bridge structures. Fundamental concepts and key principles of SHM were outlined, emphasizing the importance of damage detection, localization, quantification, and prognosis in maintaining the safety and longevity of civil infrastructure. Special attention was given to the use of FOS, which are becoming an increasingly recognized technology in SHM due to their ability to provide distributed, high-resolution strain measurements and their suitability for long-term monitoring in challenging environments.

By synthesizing current knowledge, identifying recent trends, and highlighting existing gaps, particularly in the area of crack detection near stiffeners, this literature review establishes the context and rationale for the development and evaluation of the Bracket Crack Sensor proposed in this thesis. The findings underscore the growing importance of FOS in modern SHM systems and

the need for innovative sensing solutions and robust modeling approaches to advance the state of SHM for bridge safety and reliability.

CHAPTER 3: EXPERIMENTAL APPARATUS

3.1. INTRODUCTION

This chapter describes a series of experiments conducted using a dedicated experimental apparatus to validate the performance of the hand-made Pi-bracket and to optimize the data acquisition system settings for the FOS. The primary objective is to determine whether the homemade Pi-bracket functions effectively as a sensor harness and to establish optimal DAQ parameters for the FOS, ensuring accurate and reliable crack detection in subsequent laboratory testing. The experimental methodology integrates theoretical modeling, precise instrumentation, and empirical validation. Through these experiments, the research lays the groundwork for robust and sensitive SHM applications in later stages of the project.

3.2. APPARATUS EXPERIMENT WITH STRAIN GAUGES

The first section focuses on the apparatus experiment using strain gauges, aimed to measure strain along the bracket validating the FEA simulation results. In this experiment, strain gauges will be attached to the Pi-bracket, and it will be subjected to controlled loads, allowing for a comprehensive assessment of its mechanical properties, sensitivity to strain, and how well the experimental results align with computational predictions.

Several pi-brackets were hand made in two sizes, 12” (304.8 mm) and 8” (203.2 mm), for use throughout the research. In the apparatus experiment described here, the 12" pi-bracket was selected because its larger size made it easier to instrument with strain gauges compared to the 8" version. The additional space allowed for a more comprehensive and accurate strain measurement setup, enabling a thorough assessment of the bracket’s mechanical properties, sensitivity to strain, and the correlation between experimental results and FEA simulation predictions.

3.2.1. Experimental Setup

The experimental apparatus setup was specifically designed to simulate crack opening and measure the strain response of the Pi-bracket under controlled conditions.

The Pi-bracket, made of aluminum, was bonded to the experimental apparatus using epoxy adhesive (Araldite 2021-1). The apparatus consisted of a pair of steel plates interconnected by a flexural hinge, a micrometer to induce controlled crack openings, and a Pi-gauge sensor (PI-5-100, Tokyo Sokki Kenkyujo) to monitor and quantify the crack opening width. The experimental apparatus arrangement is shown in Figure 3.1.

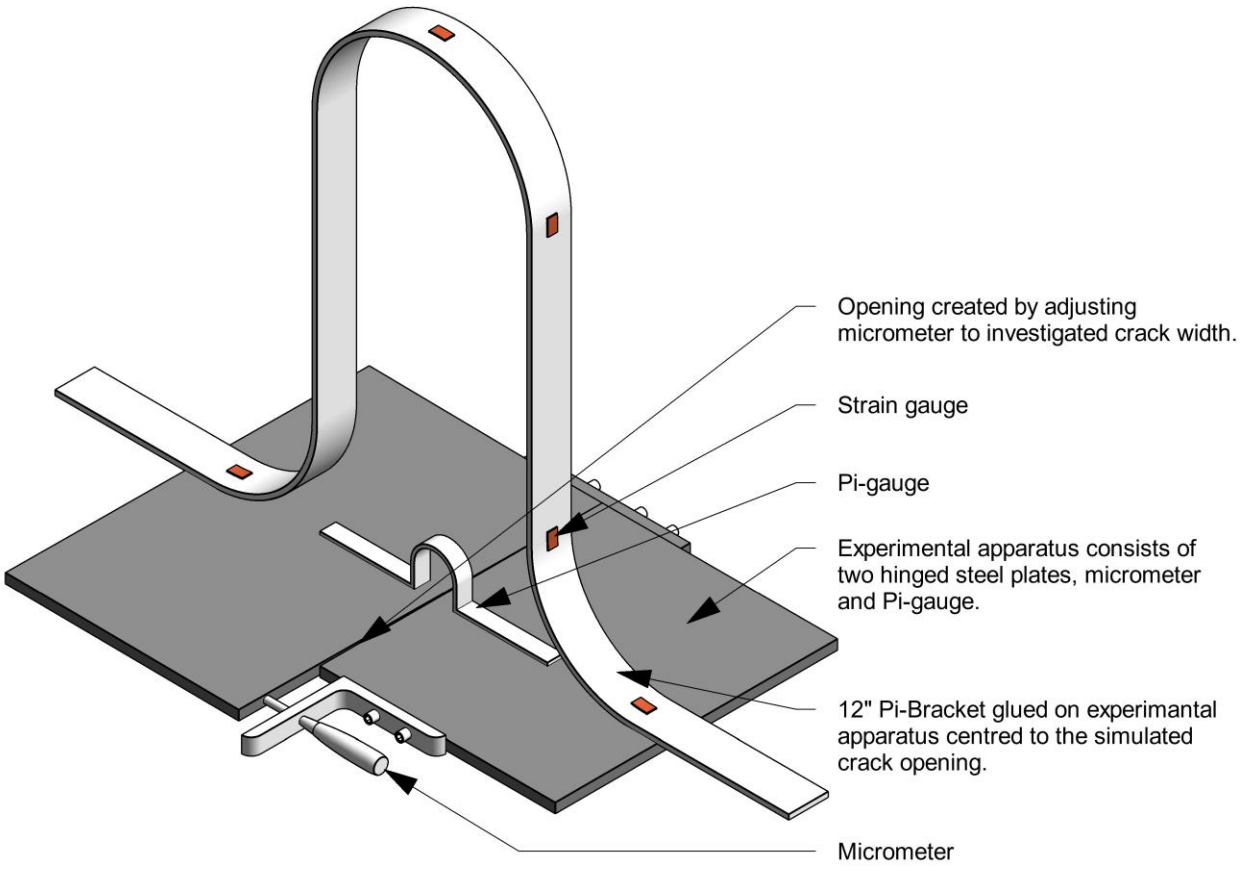

Figure 3.1: Experimental apparatus arrangement with strain gauges

The strain gauges were connected via wires to a National Instruments NI SCXI-1001 data acquisition system, which recorded strain measurements during the experiment. This DAQ system

ensured data collection for subsequent analysis. The complete experimental setup, including the pi-bracket, micrometer, pi-gauge, and DAQ system, is shown in Figure 3.2.

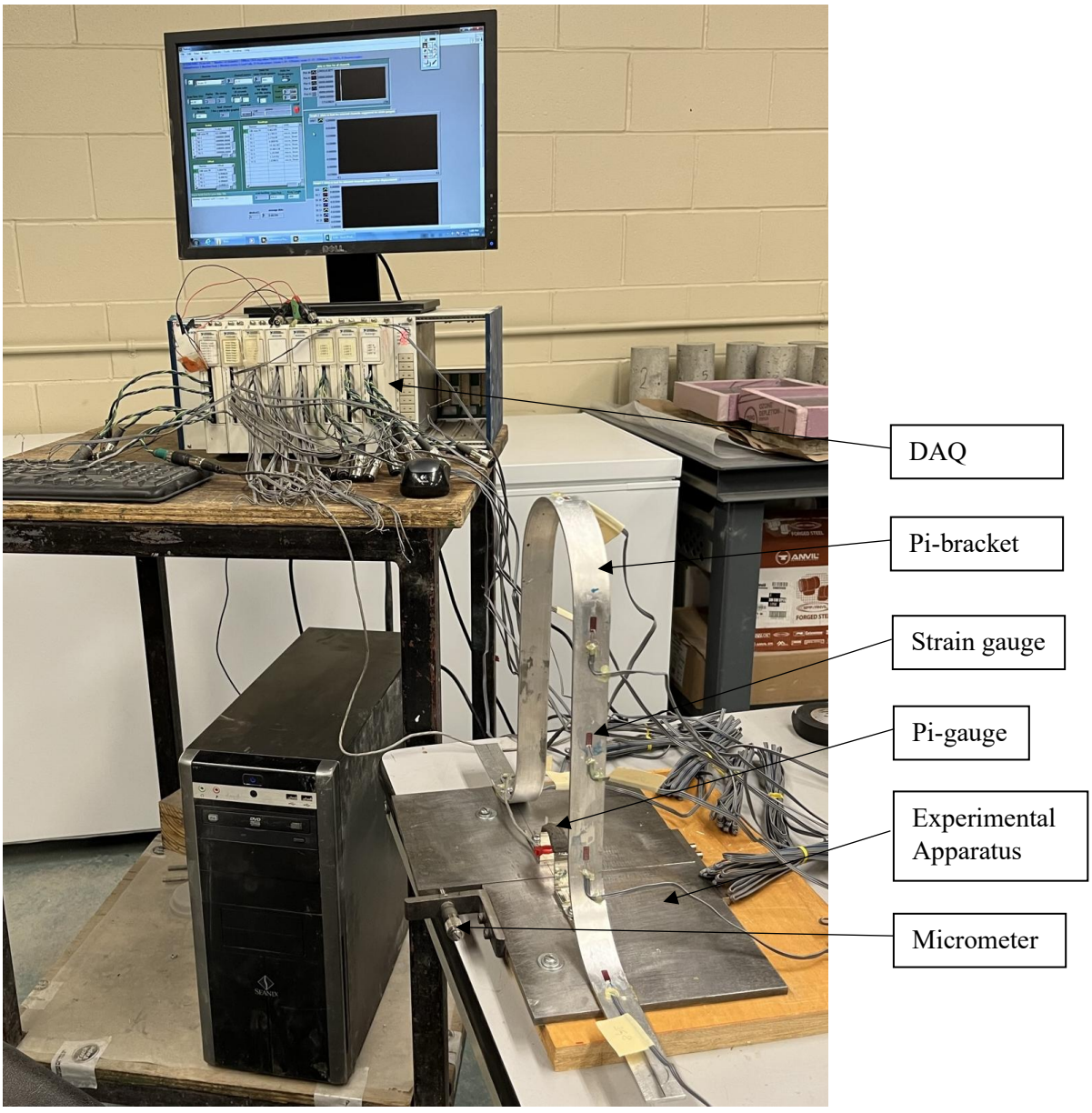

Figure 3.2: Complete experimental setup with strain gauges

Several strain gauges were attached to the pi-bracket to measure the strain response to increasing crack opening width. This setup allowed controlled adjustment of crack opening widths ranging from an initial 0mm up to 0.3mm, in increments of 0.1mm.

3.2.1.1. FEA Model

The model comprises a single part created as a 3D deformable wire, representing half of the symmetrical pi-bracket, as illustrated in Figure 3.3. The model utilized aluminum material properties, with a Young's modulus of 69000MPa and Poisson's Ratio of 0.33. A rectangular profile beam section with dimensions of 25.4 mm x 3.175 mm was assigned to the wire part.

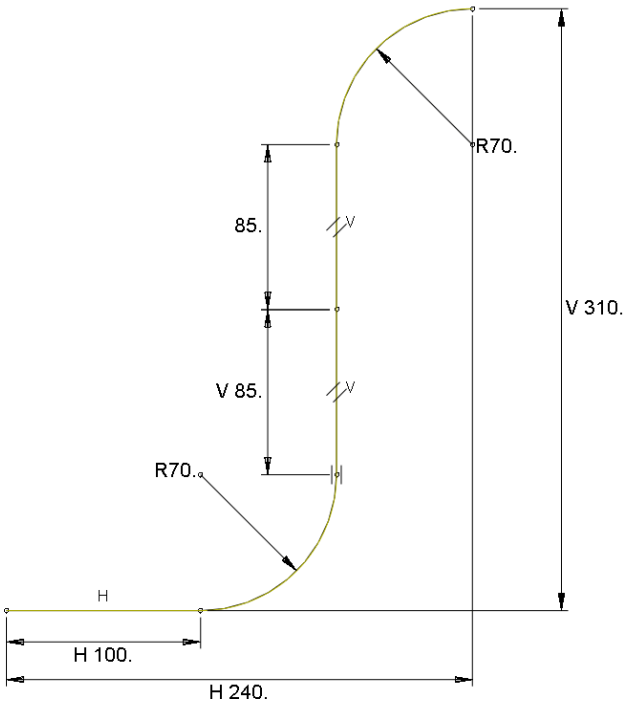

Figure 3.3: Pi-bracket geometry dimensions (shown in mm)

The simulation consisted of four "static, general analysis" steps: an initial condition without crack opening, followed by three steps corresponding to crack openings of 0.1mm, 0.2mm, and 0.3mm.

Boundary conditions were implemented at two locations, as shown in Figure 3.4. At the base of the 100mm foot, a "Displacement boundary condition" restrained all displacements and rotations except for x-direction displacement. At the crown, a "Symmetry boundary condition - XSYMM" restricted displacement along the x-direction as well as rotations about y-direction and z-direction. Loading conditions were represented by displacements ranging from 0mm to 0.3mm in 0.1mm increments.

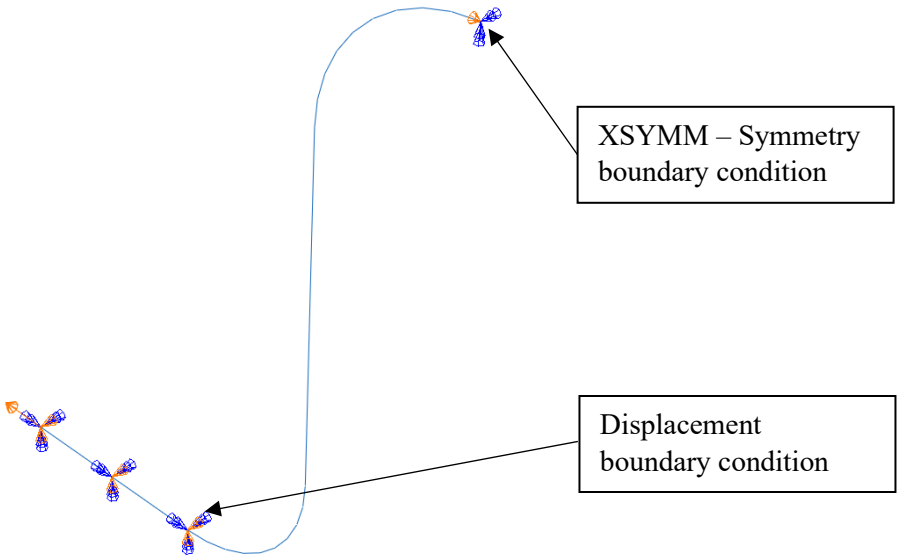

Figure 3.4: Boundary conditions

The model was meshed with optimal part seeding at 25mm, utilizing B31 beam elements, resulting in 19 nodes. These B31 elements in Abaqus assume linear elastic behavior for Timoshenko beams with a constant modulus, regardless of the beam section's response to axial tension and bending (Dasault Systemes 2012).

3.2.1.2. Pi-Bracket Geometry

The Pi-bracket geometry was specifically designed to address challenges associated with using continuous fiber optic SMARTape sensors near stiffeners. The bracket serves as a harness for the SMARTape sensor, effectively mitigating the extent of undetectable areas due to the FOS limitations for bending.

While the initial design proposed a 12" (304.8mm) deep bracket, the actual manufactured depth was 310mm due to limitations in the home-made production process. Initially, each bend in the geometry was proposed to have a radius of 50mm. However, the actual bracket's bends have a radius of 70mm, resulting in a width of 140mm between the two parallel legs. It's important to

note that the shape of the bracket may not be as precise as it would be if manufactured commercially, which could introduce some variations in performance compared to the idealized model.

The Pi-bracket's unique shape, as illustrated in Figure 3.5, allows for strategic placement of the sensor, enabling more comprehensive monitoring of potential crack formations. This design is particularly critical for areas near stiffeners, which are prone to high stress concentrations and, consequently, crack initiation.

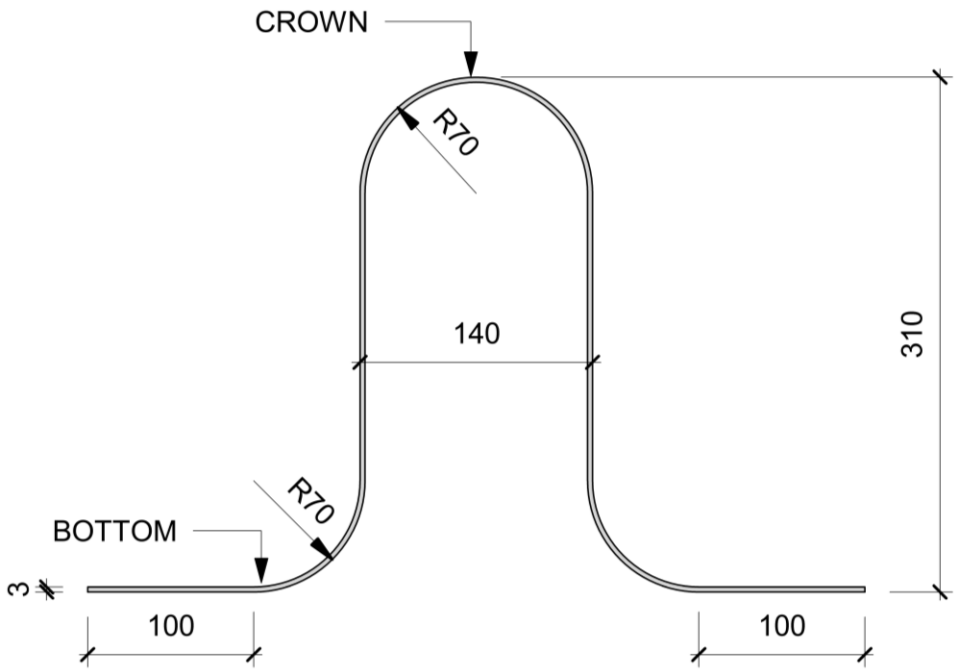

Figure 3.5: Pi-bracket geometry

To support clear discussion and precise evaluation of the pi-bracket's performance, two critical reference points, Crown and Bottom, are established and used throughout this work. As illustrated in Figure 3.5, the Crown refers to the uppermost curved section of the pi-bracket, marking the apex where the sensor transitions from one leg to the other. The Bottom indicates the transition point where the bracket curves into the flat surface intended for attachment to the beam. These locations are of particular significance, as they represent key areas where strain measurements are most indicative of the bracket's effectiveness in mitigating undetectable regions and monitoring crack activity.

This geometry enhances the overall effectiveness of the SHM system for steel bridge girders, potentially improving early detection of cracks and other structural deficiencies.

3.2.1.3. Strain Gauge Instrumentation

To measure strain response of the Pi-bracket, seven strain gauges (FLA-6-11-5LT, Tokyo Sokki Kenkyujo) were affixed at specific locations on the bracket, as shown in Figure 3.6. The placement of these strain gauges was determined based on data obtained from the Abaqus simulation, ensuring optimal positioning for capturing the bracket's strain behavior under various loading conditions.

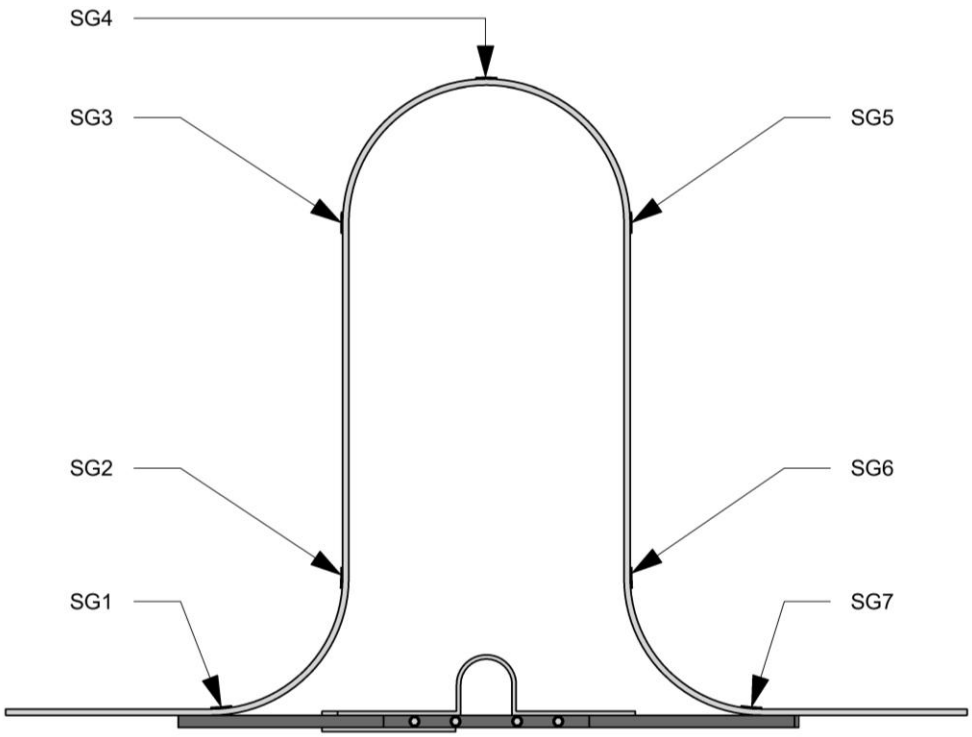

Figure 3.6: Strain gauge locations

The instrumentation process began with surface preparation in accordance with the strain gauge manufacturer’s recommendations (Figure 3.7). The Pi-bracket surface was sanded at the intended gauge locations to create a smooth, clean area, followed by cleaning with alcohol to remove any contaminants. A conditioner was then applied to the surface, and a neutralizer was used to ensure optimal adhesion for the strain gauges.

Figure 3.7: Surface preparation

Figure 3.8: Strain gauge affixation

Next, the strain gauges were carefully affixed to the predetermined locations on the Pi-bracket (Figure 3.8). M-BOND 200 KIT adhesive was used to bond the strain gauges to the bracket, and the adhesive was allowed to dry completely to ensure secure attachment. Following installation, the Pi-gauge (PI-5-100, Tokyo Sokki Kenkyujo) was calibrated (Figure 3.9) to ensure accurate measurement of crack opening width.

The calibration process involved incrementally adjusting the micrometer on a digital gauge calibrator to known displacements and recording the corresponding Pi-gauge readings. This procedure established correlation between the Pi-gauge output and the actual crack opening, allowing for reliable conversion of sensor readings into physical displacement values. The Pi-gauge was capable of measuring crack openings with a resolution of 0.001 mm and an accuracy within ±1% of the measured value, ensuring highly accurate and reliable monitoring of even the smallest crack width changes during testing (Tokyo Sokki Kenkyujo 2024).

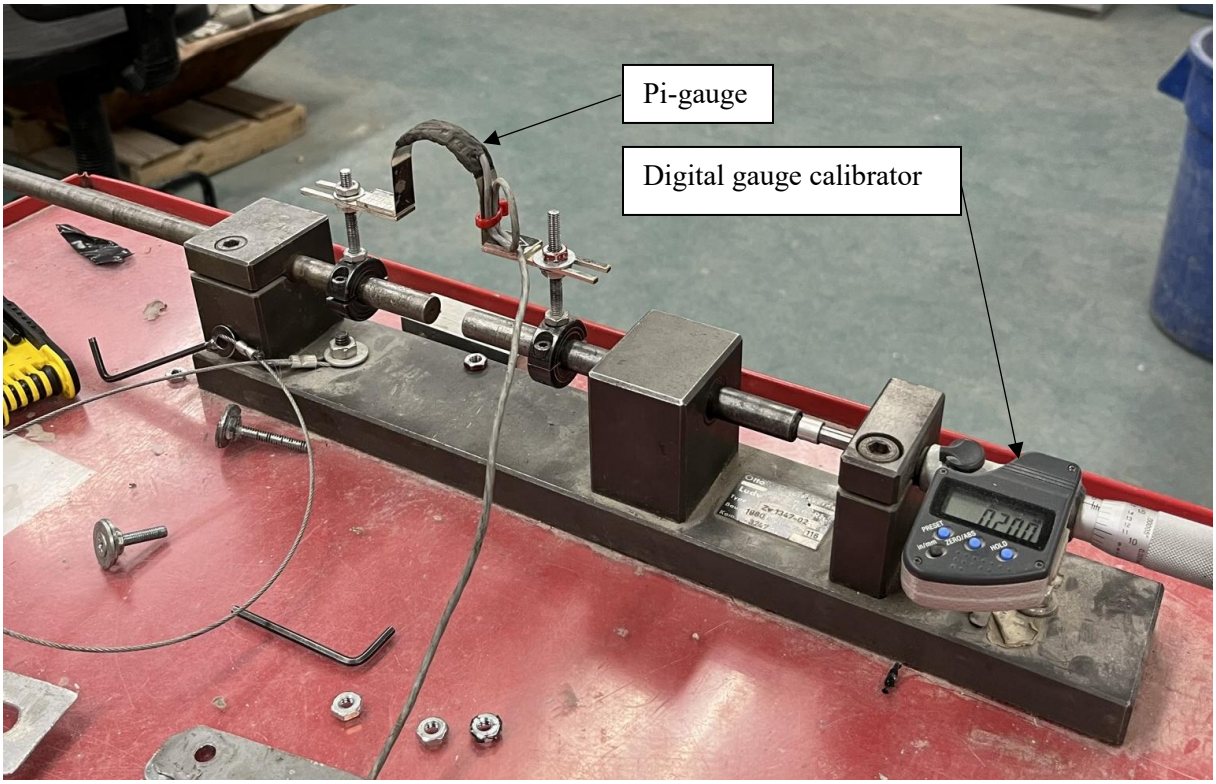

Figure 3.9: Pi-gauge calibration

Finally, the strain gauges were connected by wire to the National Instruments NI SCXI-1001 data acquisition readout unit (Figure 3.2). The strategic placement and installation of these strain gauges, combined with data acquisition system, enable a detailed comparison between the experimental results and the FEA predictions. This approach validates the accuracy and reliability of the Pi-bracket sensor system for crack detection in steel bridge girders.

3.2.2. Experiment Procedure

Prior to each experiment, a comprehensive system recalibration was performed to ensure accuracy, with both the strain and initial crack opening artificially reset to zero. During testing, strain measurements were recorded as the crack opening was incrementally increased from 0 mm to 0.3 mm in steps of 0.1 mm. A micrometer was used to apply force and control the widening of the crack, while the crack opening width was continuously monitored and quantified using a Pi-gauge, which offers a resolution of 0.001mm and an accuracy within ±1% of the measured value. Upon reaching each target crack opening widths, specifically 0.1 mm, 0.2 mm, and 0.3 mm, the operation was temporarily paused to allow for stable data collection. At each interval, precise readings of both the crack opening width and the strain from the seven strain gauges were recorded over a period of approximately 30 seconds, with a sampling rate of one reading per second. This entire experiment was repeated six times to ensure readout consistency and reliability of the results. Throughout the process, strain gauge readings were collected using a National Instruments NI SCXI-1001 data acquisition readout unit. This procedure enabled the systematic collection of strain data under controlled crack opening conditions, providing a robust dataset for comparison with the FEA simulation results and for evaluating the performance of the Pi-bracket sensor.

3.2.3. Results and Analysis

3.2.3.1. FEA Results

The Abaqus model was analyzed under three displacement-controlled loading conditions of 0.1 mm, 0.2 mm, and 0.3 mm. The resulting strain distributions are shown in Figures 3.10 through 3.12, where the numbers 1-19 on the bracket indicate specific node locations.

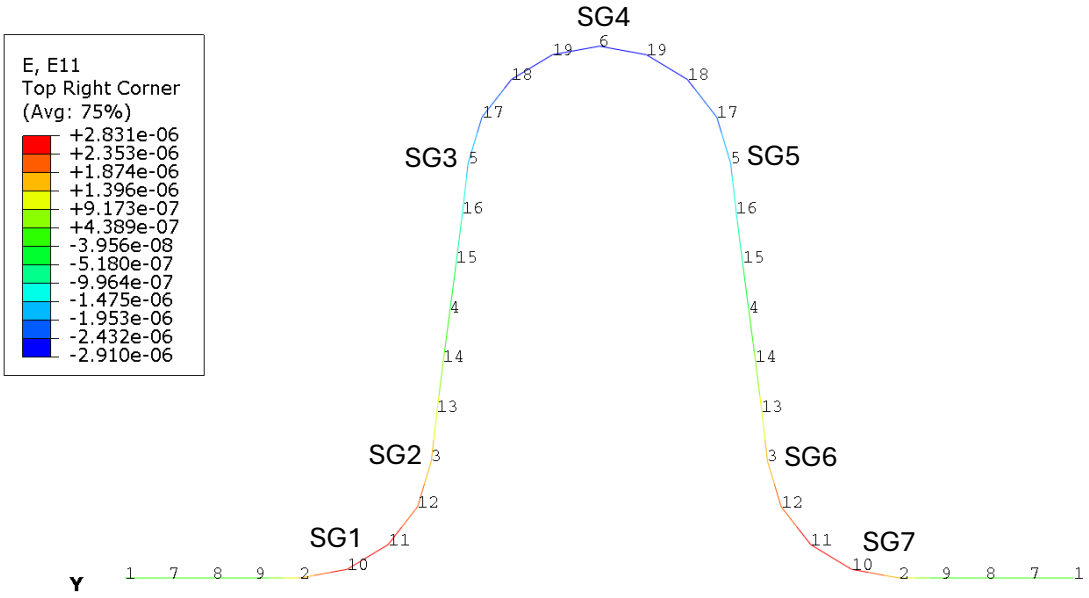

Figure 3.10: Strain distribution at 0.1mm crack width

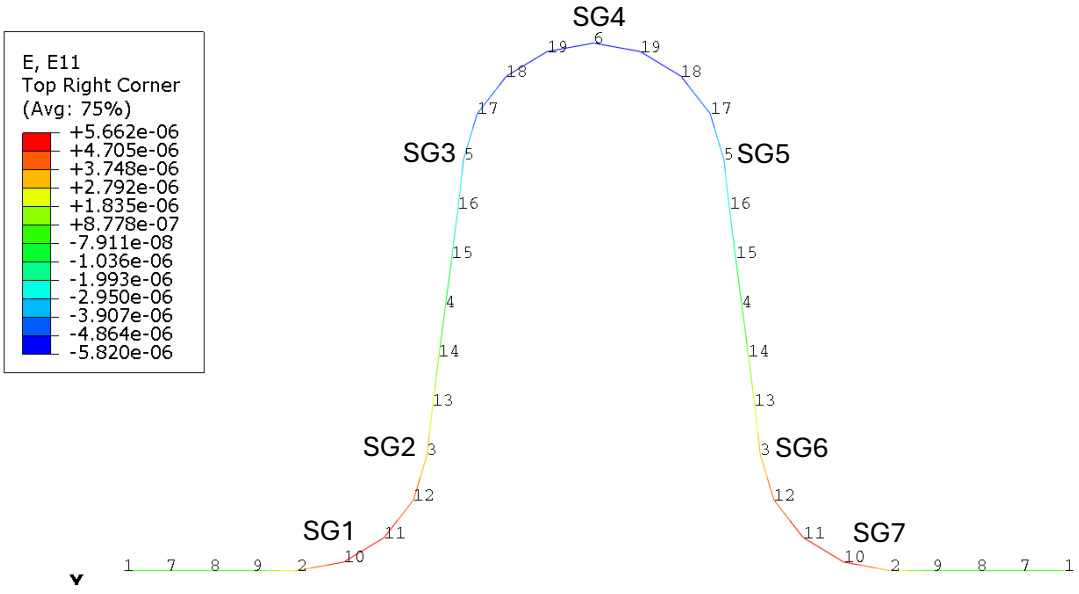

Figure 3.11: Strain distribution at 0.2mm crack width

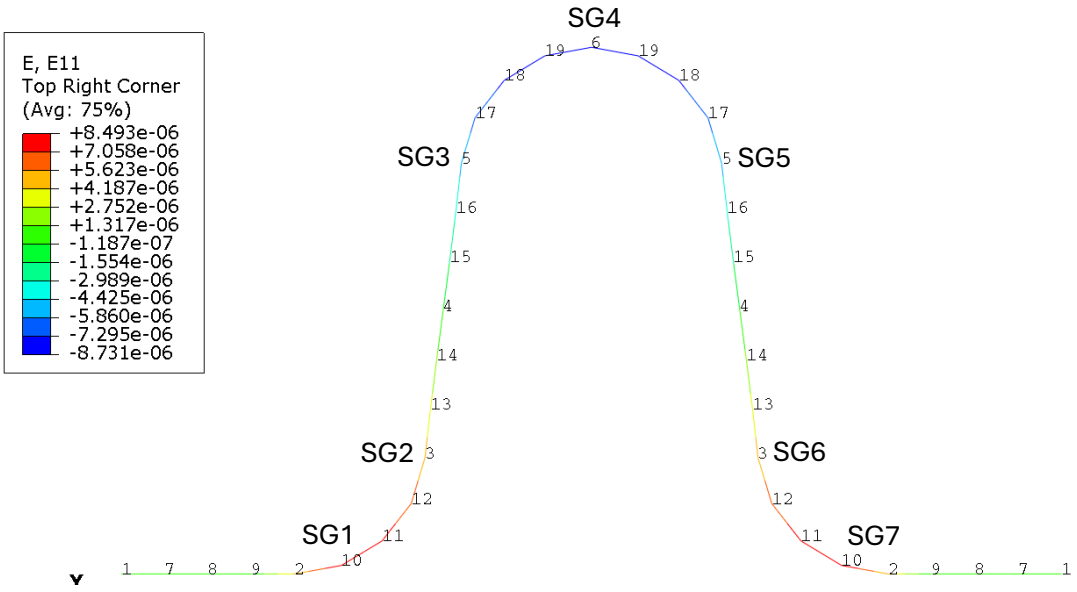

Figure 3.12: Strain distribution at 0.3mm crack width

However, to enable direct comparison with the laboratory strain gauge measurements, strain values were specifically obtained, using a query command, from the nodes that correspond to the actual strain gauge placements on the Pi-bracket used in the experiment, as illustrated in Figure 3.6. These extracted nodal strain values are presented in Table 3.1.

Table 3.1: Abaqus strain at strain gauge locations

Crack [mm]	SG1 [με]	SG2 [με]	SG3 [με]	SG4 [με]	SG5 [με]	SG6 [με]	SG7 [με]
0.1	2.8	1.6	-1.6	-2.9	-1.6	1.6	2.8
0.2	5.7	3.2	-3.2	-5.8	-3.2	3.2	5.7
0.3	8.5	4.9	-4.9	-8.7	-4.9	4.9	8.5

Only half of the Pi-bracket was modeled, utilizing a symmetry approach to take advantage of its geometric symmetry. In Table 3.1, each strain gauge (SG) location is matched to a specific node. SG1 corresponds to node 10, SG2 to node 3, SG3 to node 5, and SG4 to node 6. Because of the

symmetric shape of the bracket, it is expected that the strain values at mirrored positions will be identical under symmetric loading conditions. For example, the strain at node 10 on the left half of the Pi-bracket, which corresponds to SG1, will be the same as the strain for SG7, which corresponds to node 10 on the right half of the bracket. Similarly, node 3 represents both SG2 on the left half and SG6 on the right half, while node 5 represents both SG3 on the left and SG5 on the right. Therefore, the results from the half-model accurately represent the strain distribution for the entire bracket, and the relevant nodal strain values.

Figure 3.13 provides a graphical representation of the strain values at each strain gauge location for the different crack openings.

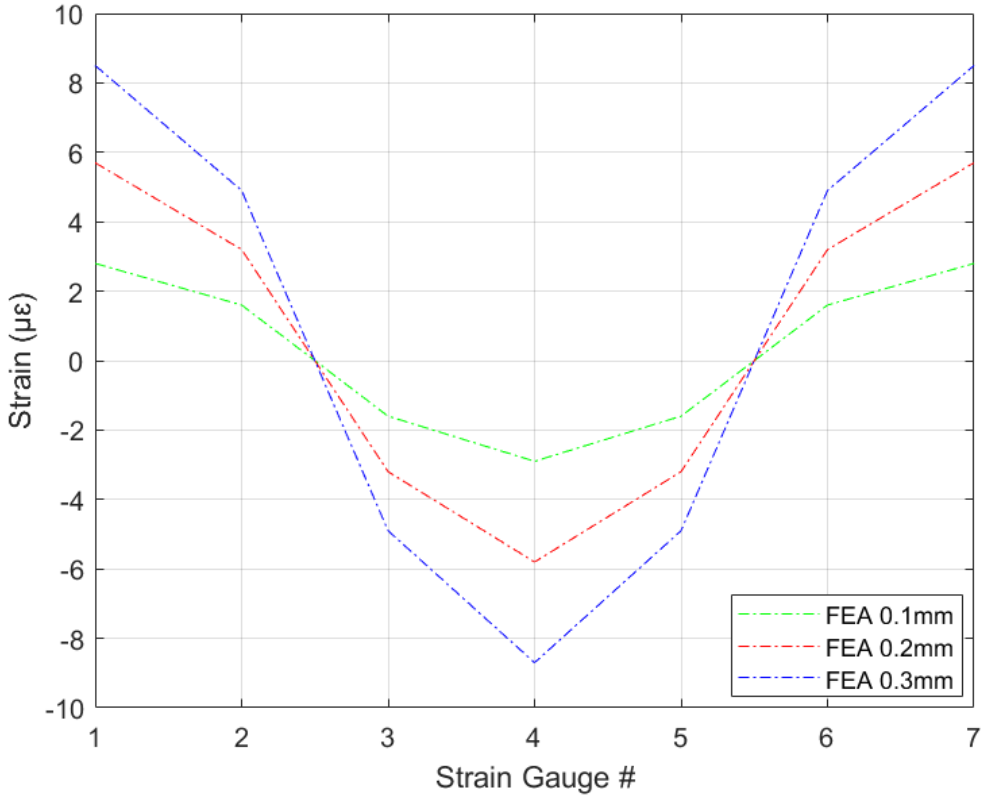

Figure 3.13: Predicted Abaqus strain at nodes corresponding to strain gauge locations

3.2.3.2. Experiment Results

The laboratory experiment was performed at an ambient temperature of 19.8°C. Strain measurements were collected as the crack opening was gradually increased from no crack to 0.3 mm, in increments of 0.1 mm. To process the data, the mean value of the strain readings was first calculated for each crack opening within each experiment, as detailed in Appendix B, Figure B.1. Next, the baseline strain measured in the initial state without the crack was subtracted from the strain values recorded at 0.1 mm, 0.2 mm, and 0.3 mm. This adjustment was essential, as the research was focused on the changes in strain resulting from crack propagation rather than the initial state of the crack. The resulting means were then averaged to obtain the final strain values for each strain gauge across the range of crack openings. Figure 3.14 presents a graphical summary of these measured strain values, illustrating how strain varies with crack opening at each gauge location.

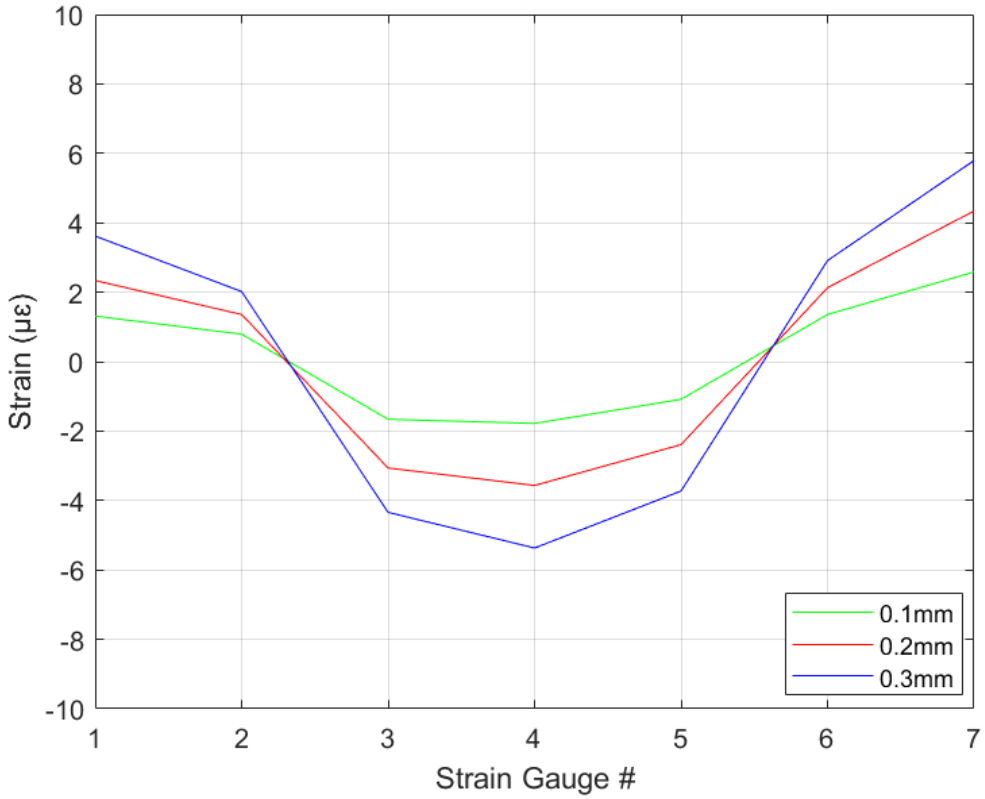

Figure 3.14: Average measured strain on Pi-bracket at strain gauge locations for crack width of 0.1, 0.2 and 0.3mm

This graph reveals strain distribution patterns across the Pi-bracket as crack width increases. The ultimate strain values are presented in Table 3.2, providing a comprehensive overview of the strain behavior at each gauge location for different crack opening widths.

Table 3.2: Average measured strain at strain gauge locations for crack width of 0.1, 0.2 and 0.3mm

Crack [mm]	SG1 [με]	SG2 [με]	SG3 [με]	SG4 [με]	SG5 [με]	SG6 [με]	SG7 [με]
0.1	1.3	0.8	-1.7	-1.8	-1.1	1.4	2.6
0.2	2.3	1.4	-3.1	-3.6	-2.4	2.1	4.3
0.3	3.6	2.0	-4.3	-5.4	-3.7	2.9	5.8

3.2.3.3. Comparison

Figure 3.15 illustrates a comparative analysis of strains between the Abaqus model and experimental data concerning the varying width of crack opening induced by incremental load.

To quantify the extent of the disparity, strain difference was calculated using the equation:

$$Strain\ Difference = |\text{Strain Abaqus} - \text{Strain Experiment}|$$

Table 3.3 presents these calculated values, revealing a range of strain difference spanning from 0.1με to 4.9με.

Table 3.3: Strain difference

Crack [mm]	SG1 [με]	SG2 [με]	SG3 [με]	SG4 [με]	SG5 [με]	SG6 [με]	SG7 [με]
0.1	1.5	0.8	0.1	1.1	0.5	0.2	0.2
0.2	3.4	1.8	0.1	2.2	0.8	1.1	1.4
0.3	4.9	2.9	0.6	3.3	1.2	2.0	2.7

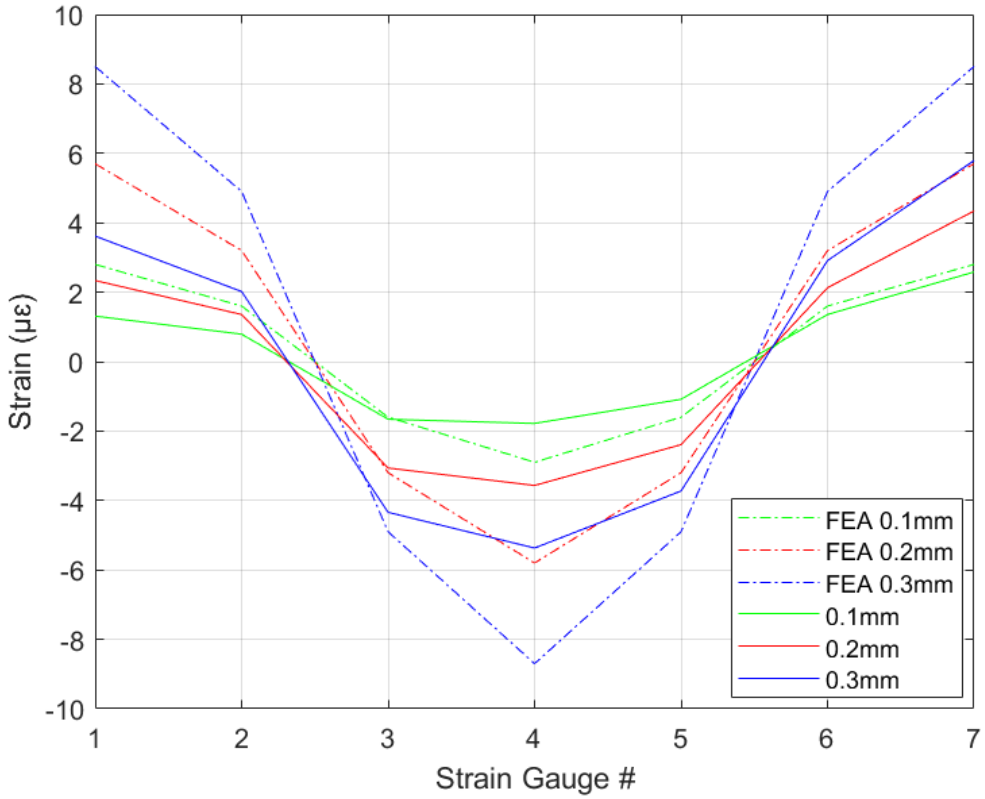

Figure 3.15: Strain comparison predicted (dashed lines), measured (solid lines)

To further contextualize these differences, the percent error was calculated using the following equation:

$$\% \, Error = \left| \frac{\text{Strain Abaqus} \; - \; \text{Strain Experiment}}{\text{Strain Abaqus}} \right| \times 100\%$$

Table 3.4 displays the percent error for each strain gauge and crack width, providing a normalized measure of the discrepancy between simulation and experiment.

Table 3.4: Strain difference - percentage

Crack [mm]	SG1 [%]	SG2 [%]	SG3 [%]	SG4 [%]	SG5 [%]	SG6 [%]	SG7 [%]
0.1	53.57	50.00	6.25	37.93	31.25	12.5	7.14
0.2	59.65	56.25	3.13	37.93	25.00	34.38	24.56
0.3	57.65	59.18	12.24	37.93	24.49	40.82	31.76

The Abaqus model predictions are depicted as dot-dashed lines, while the laboratory experiment measurements are represented by solid lines. Discrepancies between the Abaqus model and the experimental results arise from several sources. Laboratory experiments are inherently susceptible to measurement errors and noise, which can affect the accuracy of the recorded data. In contrast, Abaqus simulations are deterministic and consistently produce the same results under identical conditions, whereas strain readings in laboratory experiments can vary from one measurement to another.

Another important factor is the difference between idealized and actual conditions. The Abaqus model operates under idealized assumptions, with perfect geometry and material properties, while the experimental setup is designed to replicate real-life conditions, which naturally include imperfections. The Pi-bracket used in the experiments was hand-made by bending it to shape, a process that can introduce subtle manufacturing imperfections not accounted for in the computational model.

The precise positioning of strain gauges also contributes to the observed discrepancies. Even small variations in placement can lead to differences in strain readings. For example, SG1 and SG7, which should theoretically yield similar values due to their symmetric positions, show different levels of agreement with the Abaqus model. At a crack width of 0.3 mm, SG1 differs from the Abaqus prediction by 4.9 με, corresponding to a percent error of 57.65%, while SG7 differs by only 2.7 με, with a percent error of 31.76%. Similarly, SG3 shows a 0.6 με difference from the simulation at 0.3 mm crack width, with a percent error of 12.24%, while SG5 shows a difference of 1.2 με and a percent error of 24.49% at the same crack width.

Temperature effects further complicate the comparison. Even over short time periods, small changes in temperature can induce significant variations in strain readings. For strain gauges on aluminum, the temperature compensation factor is approximately 23.4 με per degree Celsius, and for steel, it is about 11.7 με per degree Celsius (ASM International 1990). Therefore, a temperature change of just 1°C can result in an error of about 23.4 με for aluminum, which is realistic even in a temperature-controlled environment. In this context, the maximum observed difference of 4.9 με between the experimental and Abaqus results (57.65% error for SG1 at 0.3 mm crack width) could be explained by a temperature fluctuation of only about 0.2°C.

These factors underscore the challenges in achieving perfect alignment between simulation and experimental results, highlighting the importance of considering real-world variables in interpreting and applying model predictions.

3.2.4. Conclusions

The integration of FEA with experimental data from strain gauge measurements provided a comprehensive understanding of the mechanical behavior and performance of the Pi-bracket. The results revealed a considerable level of agreement between the Abaqus simulations and the laboratory experiments, with discrepancies generally falling within an acceptable margin of error. The observed strain differences ranged from 0.1 με to 4.9 με, corresponding to percent errors between 3.13% and 59.65%, as detailed in Table 3.4. For example, at a crack width of 0.3 mm, the largest observed difference was 4.9 με for SG1, which corresponds to a percent error of 57.65%,

while other gauges such as SG3 at the same crack width showed much smaller differences, such as 0.6 με (12.24% error).

While the Abaqus simulations consistently produced identical results under the same conditions, the laboratory experiments exhibited some variability in the strain readings, reflecting the natural fluctuations and unpredictability inherent in physical testing. Several factors contributed to the observed differences between simulation and experiment. Measurement errors and noise are inevitable in laboratory settings and can influence the recorded data. The deterministic nature of Abaqus simulations, which always yield the same outcome for a given input, contrasts with the variability seen in actual experiments. Additionally, the simulations operate under idealized conditions, whereas the experimental setup is subject to the complexities and imperfections of actual materials and fabrication methods. The hand-made nature of the Pi-bracket introduces potential manufacturing imperfections that are not accounted for in the computational model. Finally, the precise positioning of the strain gauges can be challenging to achieve, and even slight misalignments may lead to further discrepancies between measured and simulated strain values.

Temperature effects also played a significant role in the observed discrepancies. Even in a temperature-controlled environment, small fluctuations can have a noticeable impact on strain measurements. For example, the largest observed difference of 4.9 με (57.65% error for SG1 at 0.3 mm crack width) could be attributed to a temperature change of only about 0.2°C, which is quite realistic under laboratory conditions.

These findings underscore the importance of considering both simulated and experimental data when evaluating SHM systems. The study not only demonstrates the value of integrating FEA and experimental approaches but also provides a solid foundation for further refinement of the pi-bracket sensor system and its field application.

3.3. OPTIMIZATION OF DAQ SETTINGS FOR FOS MEASUREMENTS

The optimization of the DAQ system for the FOS was focused on investigating the best DAQ settings for fiber optic sensor measurements, with particular emphasis on sampling resolution and averaging resolution as the primary factors studied. This process is a critical step in enhancing the performance of the pi-bracket sensor system, as it aims to determine the optimal DAQ

configurations for achieving high-resolution and reliable measurements in subsequent experiments. Importantly, the reason for evaluating different configurations is rooted in the practical demands of real-world applications: if this system is deployed for continuous, 24/7 monitoring, it will generate an enormous volume of data over time. Therefore, it is essential to select a configuration that not only manages data storage and processing efficiently but also maintains sufficient sensitivity to detect significant changes in strain, large enough to indicate the potential formation of a crack. It should be emphasized that the objective of this study is not to measure the precise size of the cracks, but rather to reliably detect their presence. The aim was to identify the most effective DAQ settings for use in the full-scale beam experiment employing the fiber optic sensor, which is presented in the next chapter.

3.3.1. Experimental Setup

For the DAQ settings optimization, the experimental apparatus was modified from the previous strain gauge experiment to specifically investigate the effects of sampling resolution and averaging resolution on FOS measurements. In this phase, the pi-gauge was omitted, as precise crack width measurements were not the primary focus. Instead, a micrometer was used to control and replicate consistent crack width openings, referred to as width 1, and width 2, for all measurements. While exact width measurements were not critical for the DAQ optimization itself, maintaining consistent crack widths across all measurements was important for comparing DAQ performance under different configurations. The micrometer allowed for precise control: turning its dial one full rotation opened the crack by about 1 mm, ensuring the crack width remained stable between measurements. This approach guaranteed that any observed changes in the strain data could be attributed to adjustments in the DAQ settings, rather than variations in crack width. The experimental apparatus arrangement with fibre optic sensor is shown in Figure 3.16.

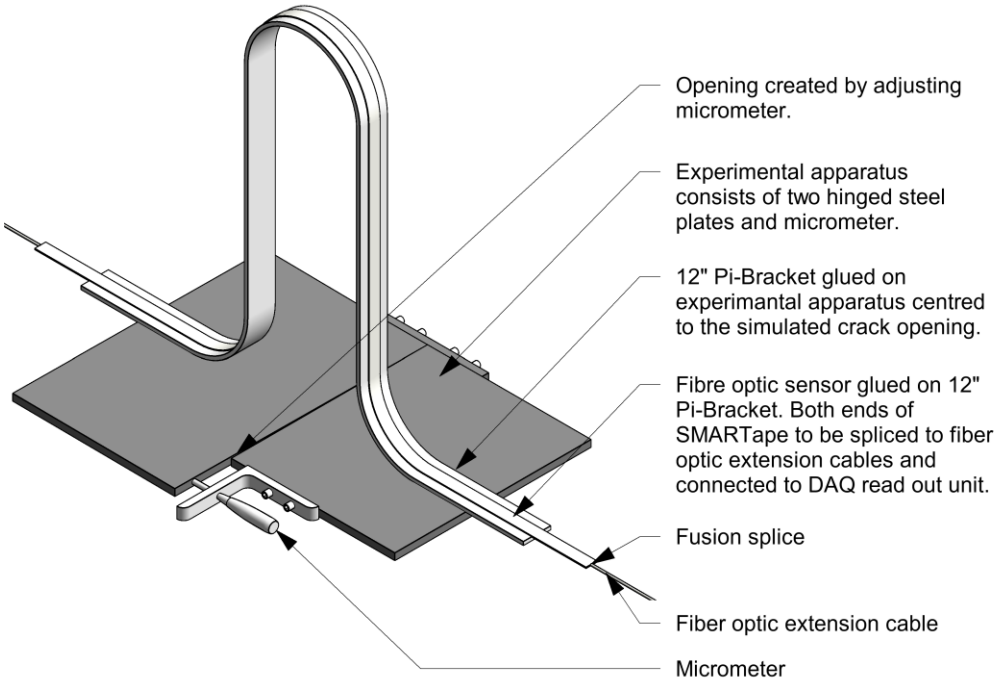

Figure 3.16: Experimental setup arrangement with fibre optic sensor

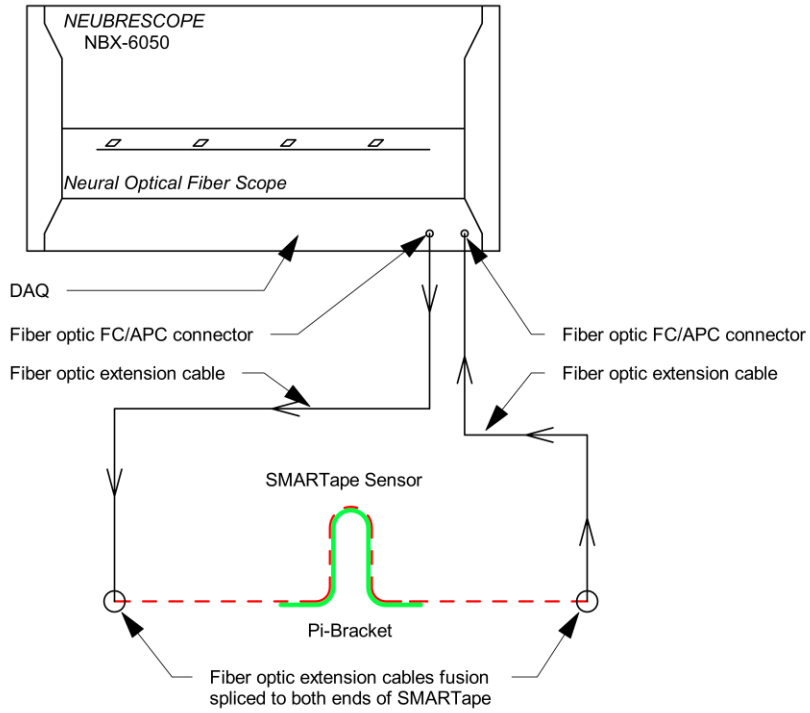

Figure 3.17: Diagram of the experimental setup

The FOS was connected to a Neubrescope NBX-6050 data acquisition system via optical extension cables using FC/APC single mode fiber optic connectors, as shown in Figure 3.17. This DAQ system was configured with various settings to determine the optimal parameters, and it recorded strain measurements throughout the experiment. Figure 3.18 illustrates the complete experimental setup, including the Pi-bracket, fibre optic sensor, the apparatus with the micrometer, and the DAQ system.

This method ensured that our experimental results would be reliable and comparable. The micrometer's ability to create uniform crack widths provided a consistent baseline for evaluating the effects of different DAQ configurations (Table 3.4), thereby isolating the impact of DAQ settings on the quality and resolution of the strain profile obtained from the fiber optic sensor.

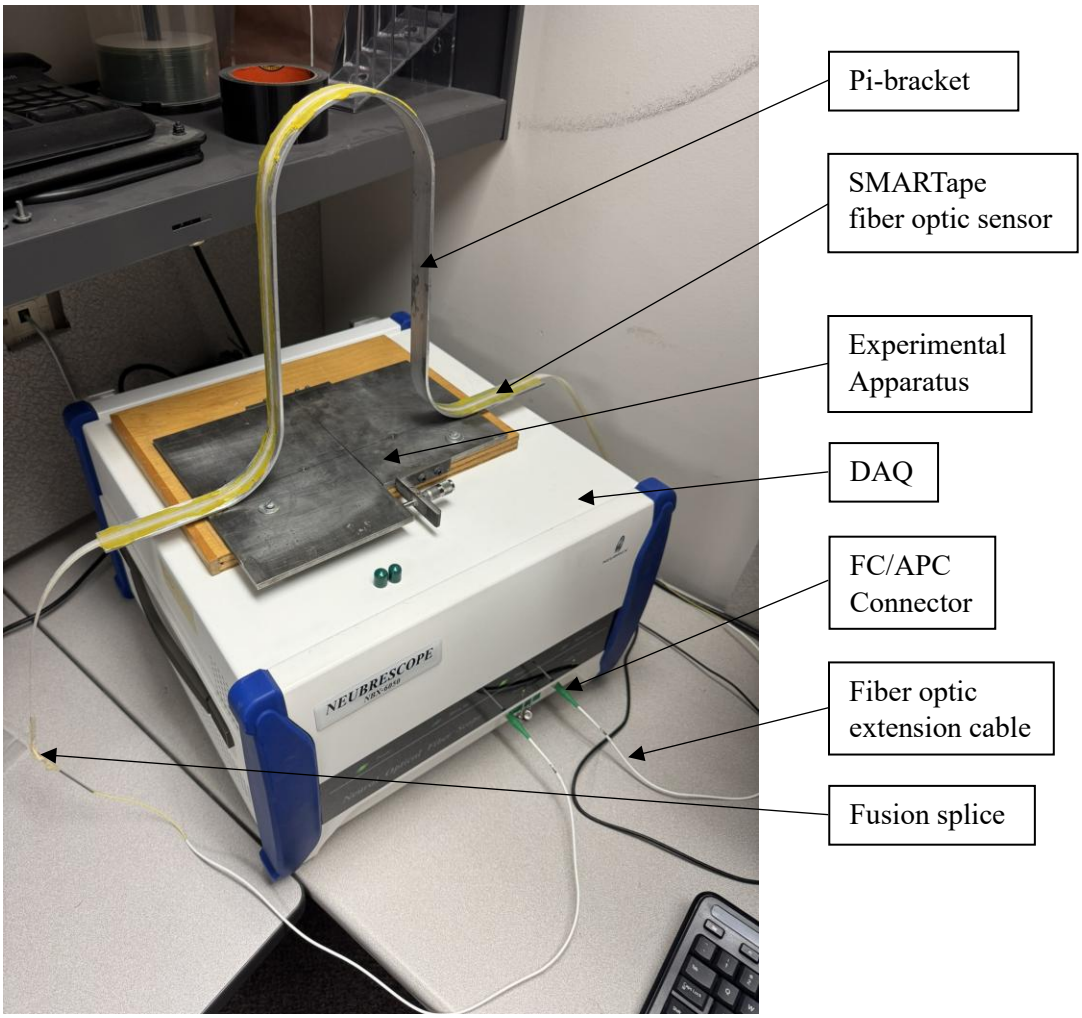

Figure 3.18: Complete experimental setup with fibre optic sensor

3.3.1.1. Pi-Bracket Instrumentation with FOS

To measure the strain response of the Pi-bracket, a ribbon-type fiber optic sensor, specifically, the DiTeSt SMARTape 2 Strain Sensor manufactured by Smartec, was carefully affixed along its length. The instrumentation process involved several detailed steps to ensure accurate and reliable strain measurements.

First, the fiber optic sensor preparation was undertaken (Figure 3.19). Since the DiTeSt SMARTape 2 does not come pre-prepared with connectors, fiber optic extension cables were fusion spliced to the sensor using a Fujikura FSM-50s fusion splicer. This precise splicing process ensured low-loss, high-quality connections between the sensor and the extension cables. Given the fragile nature of the splice points, these locations were carefully protected to prevent breakage during handling and installation.

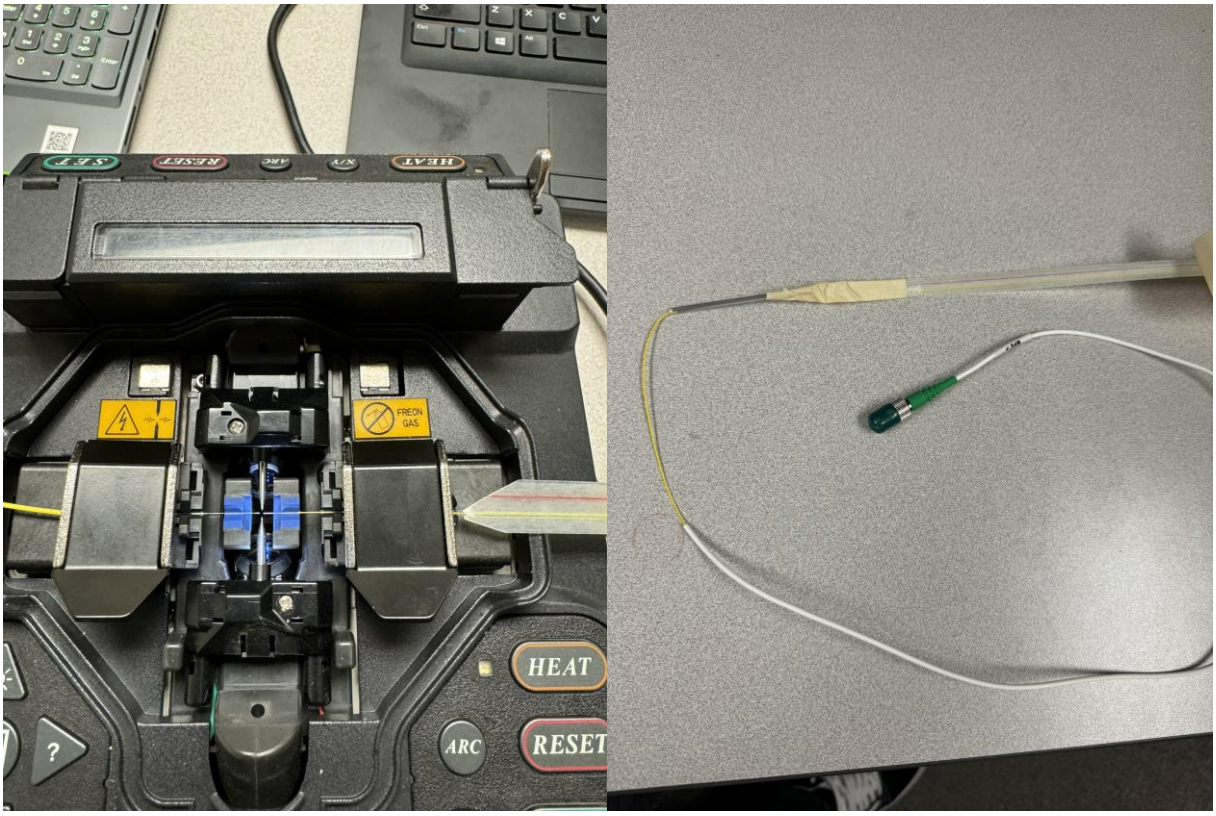

Figure 3.19: Fibre optic sensor fusion splicing

Next, the surface preparation of the Pi-bracket followed the same procedure previously used for strain gauge installation. The entire length of the Pi-bracket was thoroughly sanded with sandpaper to create a smooth and clean surface. This was followed by cleaning with alcohol to remove any dust, oils, or contaminants that could interfere with adhesive bonding.

The fiber optic sensor was then affixed to the Pi-bracket. Using Araldite 2021-1 adhesive, the DiTeSt SMARTape 2 sensor was precisely bonded along the full length of the bracket. To maintain proper positioning during curing, paper tape was applied over the bracket, securing the sensor firmly in place. After allowing sufficient time for the adhesive to fully cure, the tape was carefully removed, leaving the fiber optic sensor securely attached to the Pi-bracket.

Finally, the data acquisition system connection was established (Figure 3.18). The sensor, now bonded to the Pi-bracket, was connected via the prepared extension cables to the Neubrescope NBX-6050 DAQ unit. This careful and methodical installation process ensured the proper functioning of the DiTeSt SMARTape 2 Strain Sensor.

3.3.1.2. DAQ System Configuration

A Neubrescope NBX-6050 data acquisition unit with enhanced sampling and averaging capabilities was utilized to determine optimal settings for subsequent experiments. Four distinct DAQ configurations were systematically evaluated, as summarized in Table 3.5. These configurations were designed to evaluate the trade-offs between spatial resolution, signal-to-noise (S/N) ratio, and data processing requirements.

The FOS was configured to a total length of 50 meters, including the extension FOS, which represents the minimum allowable length for the system.

Beyond sampling and averaging resolutions, other key parameters of the Neubrescope NBX-6050 were also optimized for each configuration. Specifically, the averaging count and frequency range were set to values appropriate for each test scenario. One of the most critical settings was the selection of the measurement mode. Based on the manufacturer's recommendations, the Progressive mode was selected, as it is known to enhance the S/N ratio and typically provides improved resolution for strain measurements, even it requires twice the time than the normal mode

measurement (Neubrex 2023). Selecting Progressive mode was particularly important for this study, as it reduces noise and enables the accurate capture of subtle strain variations along the pi-bracket. This ensures high measurement precision and reliability, which are essential for effective crack detection and monitoring using the fiber optic sensor system.

Table 3.5: Summary of DAQ configurations for FOS

Configuration Name	Sampling Resolution (SR)	Averaging Resolution (AR)	Description
5-10	0.05m (5cm)	0.1m (10cm)	High Sampling with Light Averaging
5-20	0.05m (5cm)	0.2m (20cm)	High Sampling with Moderate Averaging
10-20	0.1m (10cm)	0.2m (20cm)	Moderate Sampling with Light Averaging
10-50	0.1m (10cm)	0.5m (50cm)	Moderate Sampling with Extended Averaging

The careful selection and adjustment of these parameters, particularly the use of Progressive measurement mode, were fundamental to optimizing the DAQ system's performance. The overall objective was to identify the configuration that would deliver the most reliable and accurate strain measurements for crack detection and monitoring using the pi-bracket sensor system in this study.

3.3.2. Experiment Procedure

The experiment to optimize the DAQ settings for the FOS on the pi-bracket followed a systematic and structured approach. First, the pi-bracket instrumented with the attached FOS was connected to the experimental apparatus, ensuring all components were securely in place and ready for testing.

The Neubrescope NBX-6050 DAQ unit was then set to Progressive mode, and for each of the four DAQ configurations, the appropriate sampling and averaging settings were applied. For each configuration, crack widths were simulated using the micrometer-controlled apparatus. Three different states were established for each test: the initial state (with no load applied by the micrometer, serving as the baseline), Width 1 (a smaller opening, corresponding to one revolution of the micrometer, approximately 1 mm), and Width 2 (a larger opening, corresponding to two revolutions, approximately 2 mm).

At each crack width, the micrometer was adjusted to the desired position, and a single strain profile was recorded from the FOS. To ensure data reliability and repeatability, three separate measurements were taken for each DAQ configuration and crack width, resulting in a total of 36 measurements (4 configurations × 3 widths × 3 measurements).

This process, adjusting the crack width, recording the strain profile, and repeating for each DAQ configuration, was carried out systematically for all four tested configurations (5-10, 5-20, 10-20, and 10-50). The initial measurement, taken with no applied load, provided a baseline for comparison against the subsequent measurements at increased crack widths.

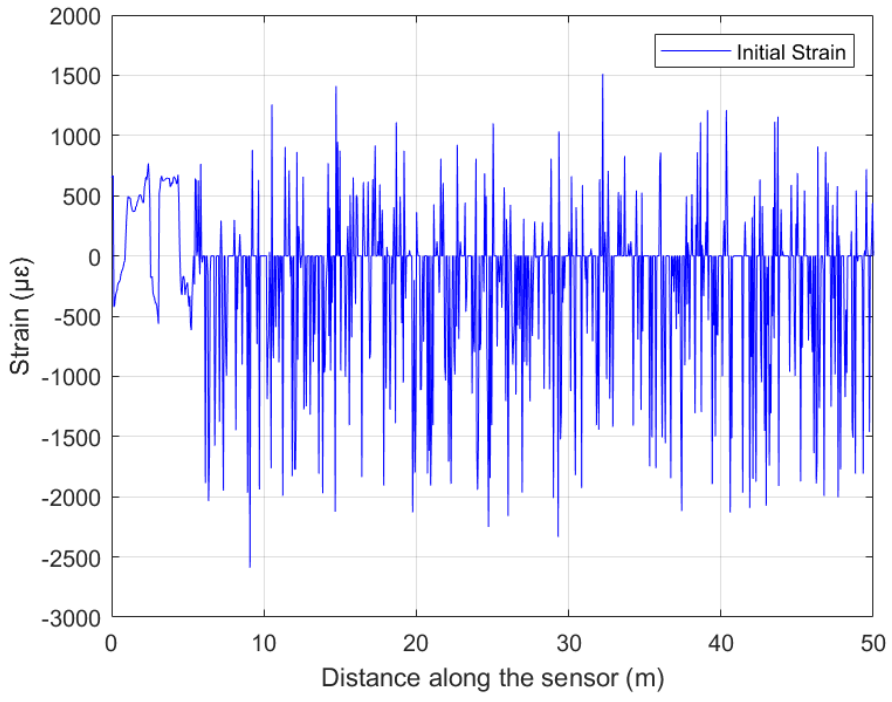

Figure 3.20: Initial strain measurement

When the initial measurement was taken, it was not immediately clear where the pi-bracket was located along the length of the fiber optic sensor, as most of the recorded signal appeared to be electronic noise (Figure 3.20). However, from the initial strain profile, it was evident that meaningful signal was only present within the first 6 meters of the sensor length, suggesting that the pi-bracket was located in this region, while the signal beyond 6 meters consisted solely of noise.

It is important to note that the initial strain profile measured by the fiber optic sensor is often not zero, even when no external load is applied. This is due to residual or pre-built strains that can arise from the manufacturing process, handling, installation, and environmental effects such as temperature changes. Such baseline strain offsets are a well-recognized phenomenon in distributed fiber optic sensing and must be accounted for during analysis (Bao and Chen 2012).

The Neubrescope calculates strain at each point along the fiber using the formula:

$$\varepsilon = \frac{(center\ frequency) - (zero\ frequency\ shift)}{c_{11}} + reference\ strain$$

Here, the center frequency is the measured Brillouin frequency at each location, zero frequency shift is the baseline frequency, c_{11} is the strain calibration constant, and reference strain is an offset. Any differences in temperature or handling between the baseline and measurement, or slight pre-strain during installation, will result in a non-zero initial strain reading. For this reason, all subsequent measurements are compared to this initial profile, and changes in strain are interpreted relative to this baseline (Neubrex 2023).

To accurately localize the pi-bracket, a heat gun was used to apply thermal stimulation to the crown of the pi-bracket. By comparing the resulting strain profile with the initial measurement, the most pronounced change in strain was observed at approximately 1.6 meters along the sensor (Figure 3.21), confirming the location of the pi-bracket. In the figure, the green dashed vertical lines indicate the identified location of the pi-bracket.

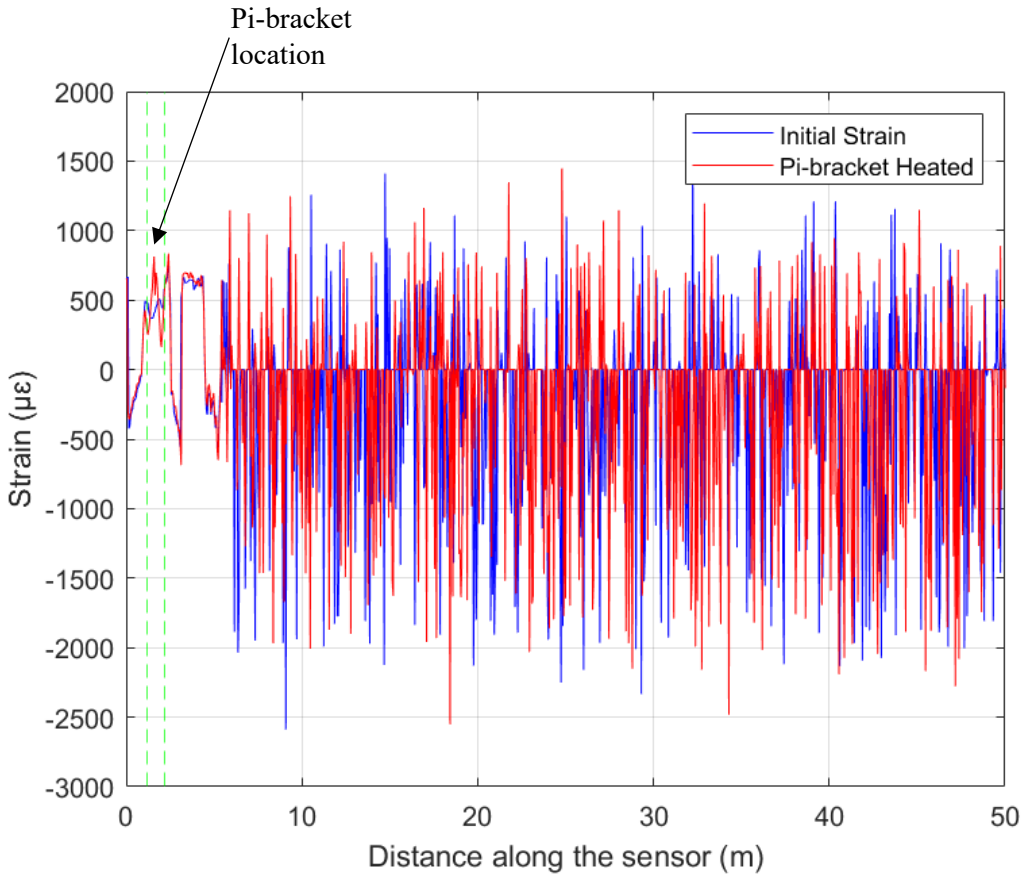

Figure 3.21: Pi-bracket thermal localization

The SMARTape fiber optic sensor itself measured approximately 1.5 meters in length, with an additional 1 meter of extension fiber on each side.

The signal observed between 6 meters and 50 meters corresponds to random noise, as the actual physical length of the SMARTape fiber optic sensor was only approximately 1.5m slightly extending beyond the pi-bracket on either side. Because the Neubrescope NBX-6050 was set to its minimum allowable sensor length of 50 meters, any data recorded beyond the true sensor length represent only electronic noise and do not reflect real strain measurements. To improve clarity, Figure 3.22 displays the strain profiles limited to the first 5 meters, excluding the noise data beyond this range as it is irrelevant to the analysis.

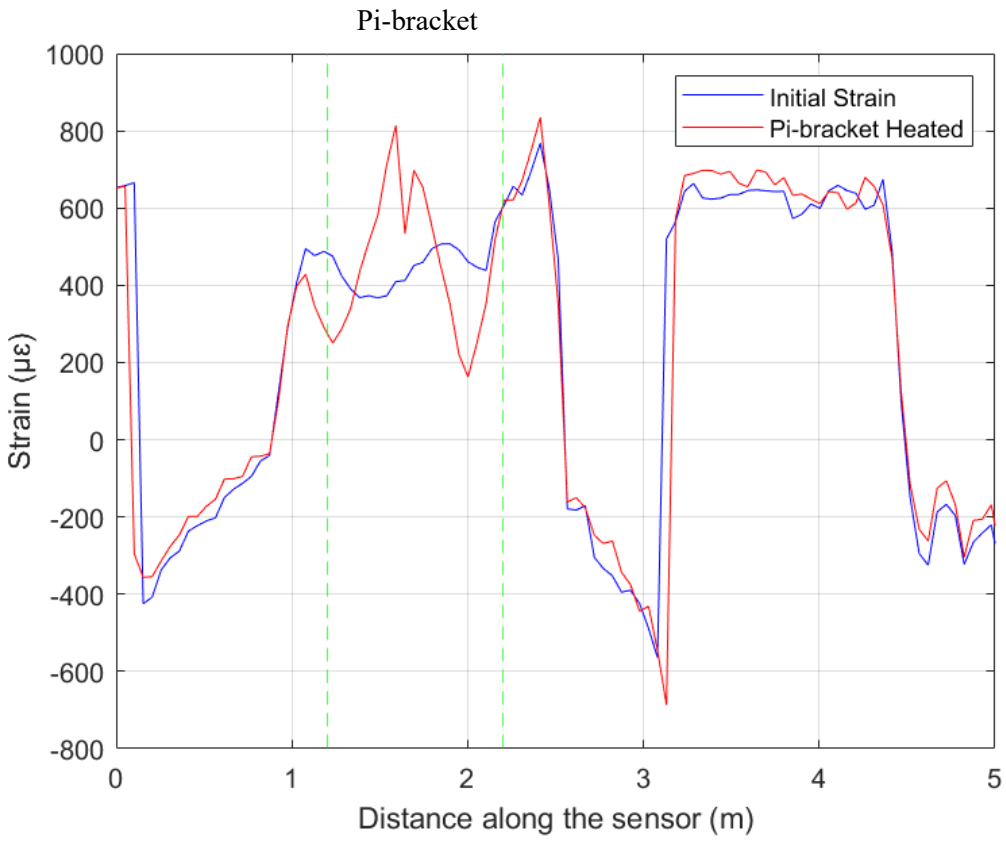

Figure 3.22: Pi-bracket thermal localization – detail

Following data collection, the recorded strain profiles were analyzed to evaluate the trade-offs between spatial resolution, S/N ratio, and data processing requirements for each DAQ configuration. This comprehensive methodology, with multiple measurements at each configuration and crack width, enabled a robust assessment of the DAQ settings. Ultimately, this approach facilitated the identification of the optimal configuration for accurate crack detection and monitoring using the pi-bracket sensor, while ensuring consistency across all tested crack widths.

3.3.3. Results and Analysis

3.3.3.1. Signal Analysis

The signal processing methodology described in this section was applied consistently throughout the thesis, with MATLAB serving as the primary tool for data analysis and visualization. This

standardized approach ensured consistency across all experiments, while also allowing for the flexibility needed to address the unique requirements of each specific application. Signal processing was essential in this research, as it enabled the extraction of meaningful information from raw data and facilitated accurate comparisons between different DAQ settings.

For the experimental program, strain measurements were recorded for three distinct crack opening states: the initial state (no crack), a 1 mm crack, and a 2 mm crack. MATLAB was used both to process the raw data and to plot the resulting strain profiles.

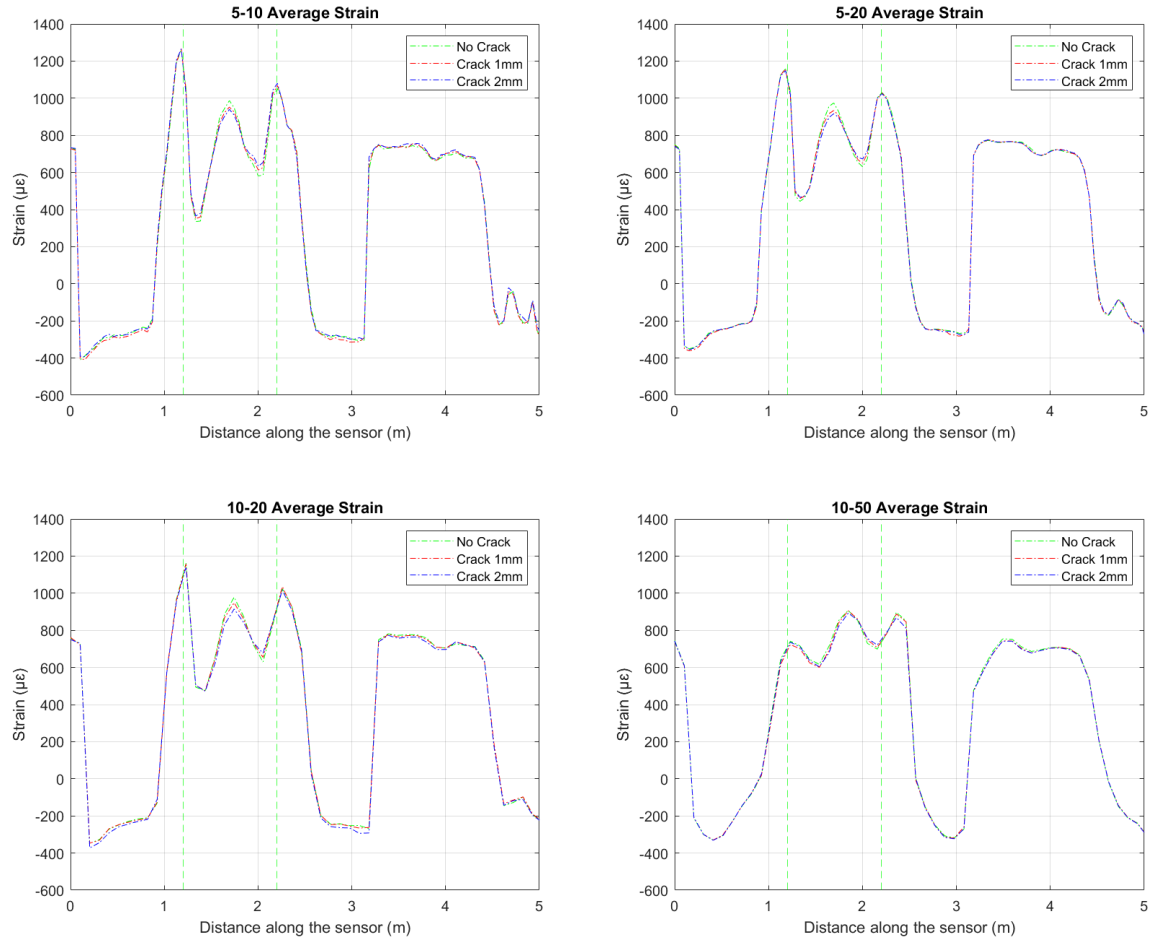

Figure 3.23: Average strain profiles for different DAQ configurations and crack widths

The first step in the data analysis involved averaging all readings for each DAQ configuration (5-10, 5-20, 10-20, and 10-50). These averaged strain profiles were plotted in Figure 3.23. The characteristic wavy shape of the strain profile results from residual strain imposed by the geometry

of the pi-bracket itself. Because the fiber optic sensor is bonded to the bracket's surface, the intrinsic curvature of the pi-bracket induces a residual strain pattern: the two bottom curvatures experience residual compression, while the crown curvature retains residual tension. This geometric constraint, not external loading, creates the observed wavy strain profile, directly mirroring the contours of the pi-bracket. Averaging helped to reduce random noise in the data, but the effect of crack opening on the strain profiles was not immediately obvious. While some visible differences could be seen between the most distinct DAQ settings, such as 5-10 and 10-50, the intermediate configurations (for example, 5-20 and 10-20) showed minimal recognizable differences. This observation highlighted the need for further data processing to better understand the impact of crack opening across the different DAQ configurations.

Subsequently, the averaged strain profiles for each crack state were compared across the various DAQ configurations, as illustrated in Figure 3.24. This comparison was important for identifying the influence of DAQ configuration on the measured strain profiles. However, these plots reflected the total strain profile of the sensor, not just the strain resulting from crack widening. The distinction between the comparison plots for 1 mm and 2 mm crack openings was also not readily apparent, as these plots used the same averaged data as in Figure 3.23, simply presented in a different format for comparison across DAQ settings.

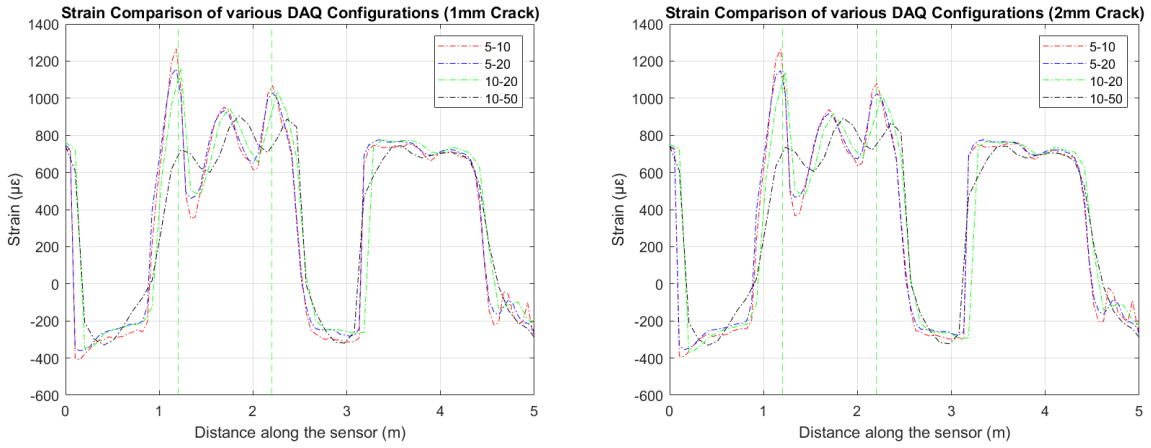

Figure 3.24: Comparison of average strain profiles of various DAQ configurations for 1mm and 2mm crack widths

To isolate the strain changes specifically due to crack widening, the averaged baseline strain profile corresponding to no crack was subtracted from the averaged profiles at 1 mm and 2 mm crack openings. This step was crucial, as the main research focus was on the change in strain resulting from crack opening. Figure 3.25 presents the isolated strain profiles for the 1 mm and 2 mm crack openings, from which the baseline strain has been subtracted.

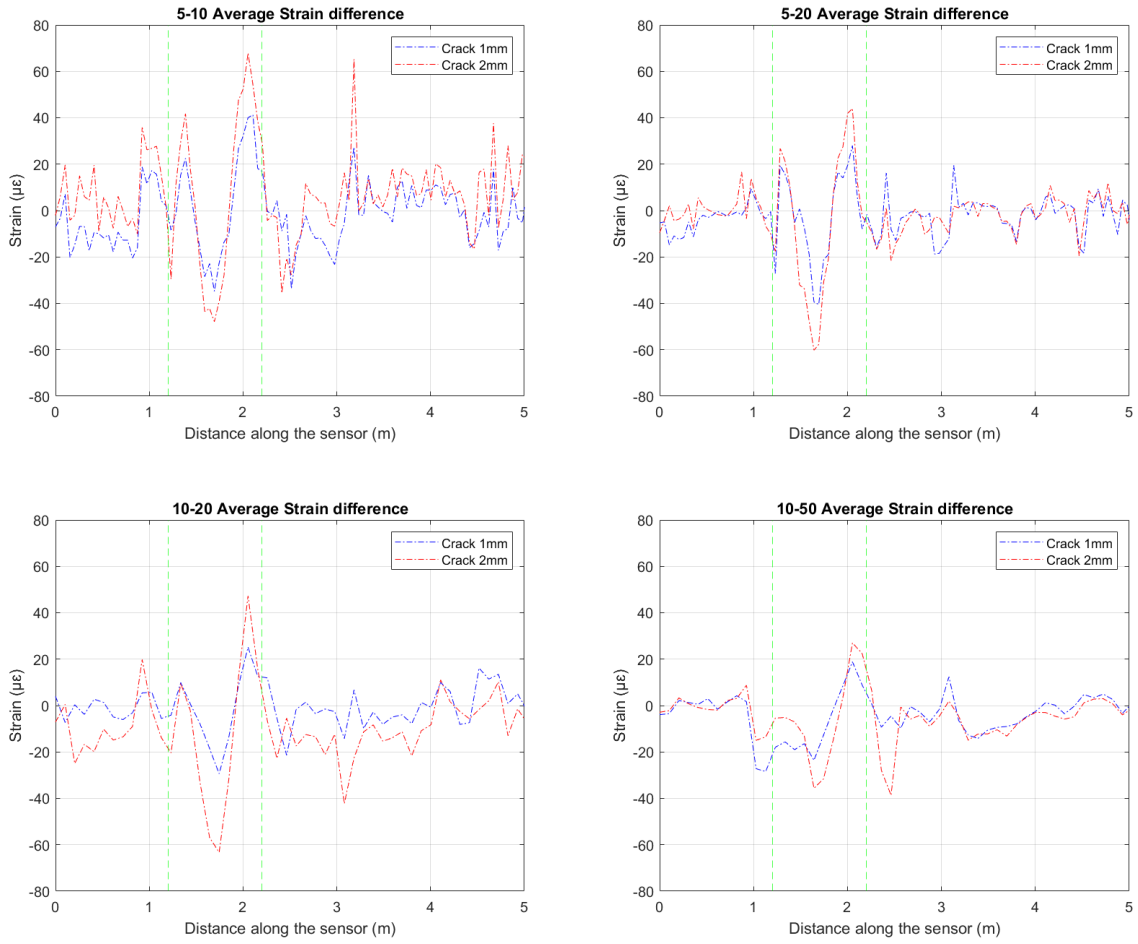

Figure 3.25: Baseline subtracted average strain profiles for different DAQ configurations

The subtracted strain profiles for each crack width were then compared across all DAQ configurations, as shown in Figure 3.26. This comparison revealed more pronounced differences in the strain response of the sensor system to crack widening. However, the resulting graphs still lacked clarity due to residual noise and measurement variations, and the data at this stage were not

sufficiently refined to draw clear conclusions. It became apparent that further smoothing of the strain profiles was necessary to enhance interpretability and enable more meaningful analysis.

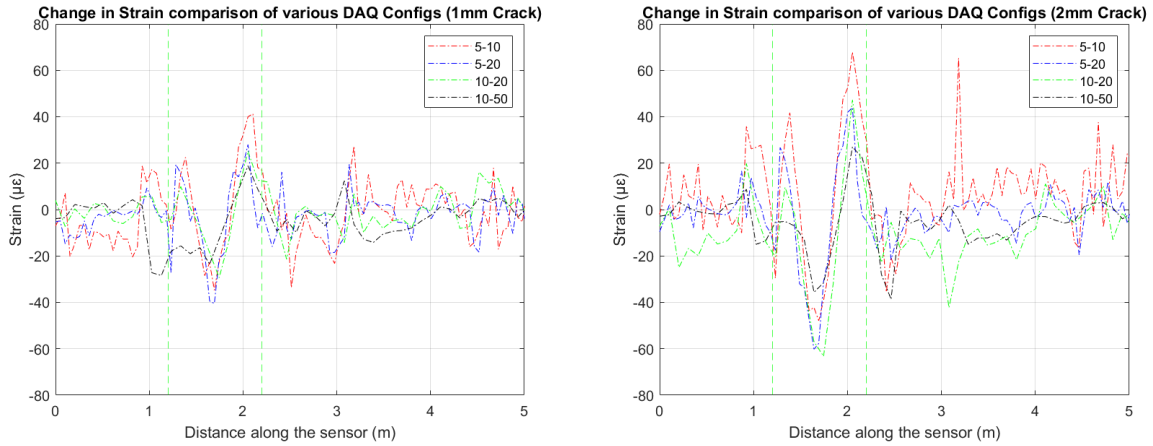

Figure 3.26: Comparison of subtracted strain profiles across DAQ configurations for 1mm and 2mm crack widths

To address this, a moving average filter was applied to each of the processed datasets. This smoothing technique was chosen for its simplicity and effectiveness in reducing random noise while preserving the underlying trends in the data. The moving average filter was implemented in MATLAB, and various window sizes, corresponding to the number of data points being averaged, were investigated to determine the most suitable option.

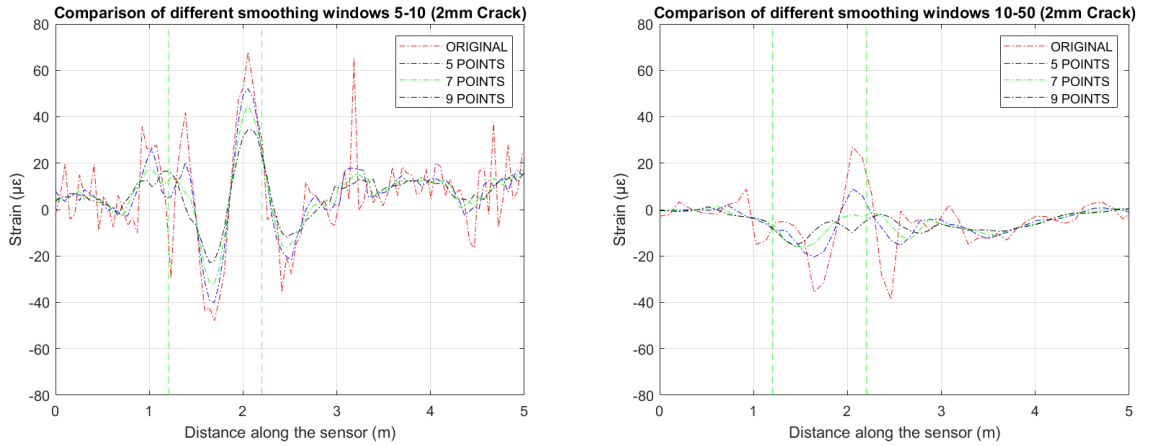

Figure 3.27: Effect of moving average window size on isolated strain profiles for 2 mm crack opening: comparison of 5-10 and 10-50 DAQ configurations

Specifically, window sizes of 5, 7, and 9 were tested on two different DAQ configurations, 5-10 and 10-50, for the isolated strain profiles corresponding to a 2 mm crack opening, as shown in Figure 3.27. In addition to the smoothed profiles, the figure also includes the initial, unsmoothed strain profile for direct comparison. It is important to note that DAQ configurations 5-10 and 5-20 have strain readings sampled every 5 cm, while DAQ configurations 10-20 and 10-50 have strain readings sampled every 10 cm. From the figure, it is evident that for the 5-10 DAQ configuration, applying a moving average filter over 9 points yields the best results, still preserving an acceptable value for the maximum strain. However, for the 10-50 DAQ configuration, a 9-point moving average is too aggressive, smoothing out the data to the extent that the maximum strain value is no longer accurately represented. In this case, a 5-point moving average provides the most reliable results. Given this limitation in the 10-50 DAQ configuration, the moving average filter with a window size of 5 points was ultimately selected as the best compromise for all data sets.

The resulting smoothened strain profiles, which illustrate the change in strain for 1 mm and 2 mm crack widening across different DAQ settings, are presented in Figure 3.28 and discussed in the subsequent section. These refined plots provide a much clearer visualization of how the pi-bracket sensor system responds to different crack widths, thereby allowing for more meaningful analysis and comparison of the various DAQ configurations.

Overall, this systematic approach to signal processing enabled a comprehensive analysis of the pi-bracket sensor performance under different DAQ configurations and simulated crack widths.

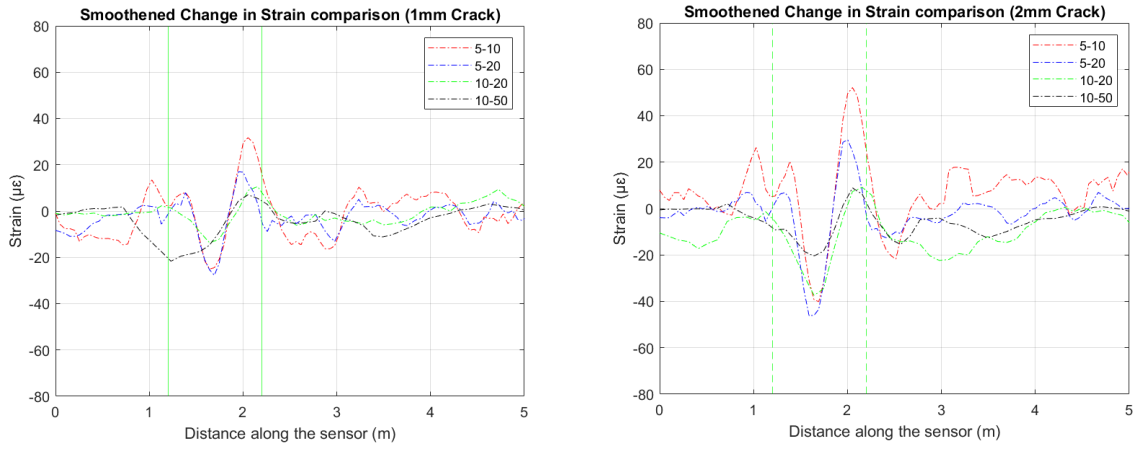

Figure 3.28: Comparison of smoothened strain profiles across DAQ configurations for 1mm and 2mm crack widths

3.3.3.2. Comparison

The smoothened strain profiles corresponding to 1 mm and 2 mm crack widening for each DAQ configuration are shown in Figure 3.28. This figure provides a clear basis for comparing the response of the pi-bracket sensor system to different crack widths under varying DAQ configurations.

Across all DAQ configurations, the system demonstrates a distinct sensitivity to crack width, as evidenced by the consistently larger strain changes observed for the 2 mm crack compared to the 1 mm crack as expected. Notably, the 5-10 and 5-20 DAQ settings yield highly detailed strain profiles, with the 5-10 configuration (featuring 0.05 m sampling and 0.1 m averaging) exhibiting the greatest sensitivity to changes in crack width. Importantly, even the lowest resolution DAQ setting (10-50) is capable of detecting both 1 mm and 2 mm cracks, indicating that all tested configurations are viable for identifying crack openings of this magnitude. It should be emphasized that the objective of this study is not to measure the precise size of the cracks, but rather to reliably detect their presence and to select the most suitable DAQ configuration for use in subsequent full-scale beam testing.

The shape of the strain profile remains consistent across all configurations, with peak strains typically occurring near the crown or base of the pi-bracket. This is the region where the bracket transitions from being adhesively bonded to the apparatus to being unattached. This pattern is in agreement with the expected mechanical behavior and supports the reliability of the sensor system.

The influence of DAQ settings on signal quality is also evident. Higher sampling resolutions, such as the 0.05 m interval used in the 5-10 and 5-20 configurations, produce more detailed strain profiles, capturing finer variations that are critical for early crack detection. However, this increased detail comes at the cost of significantly larger datasets, which demand more processing time and storage, an important consideration for long-term or real-time monitoring applications. Lighter averaging windows (0.1 m and 0.2 m) preserve more localized strain information, making it easier to identify subtle changes near the crack. In contrast, extended averaging (such as the 0.5 m window in the 10-50 configuration) results in smoother strain profiles and improved signal-to-noise ratios, particularly for larger cracks, but can mask small, localized strain events and reduce sensitivity to initial crack formation.

Despite these differences, all DAQ configurations tested in this study were able to detect strain changes associated with both 1 mm and 2 mm simulated crack openings. The configuration with the highest sampling and lightest averaging (5-10) demonstrated the greatest sensitivity, as evidenced by the highest maximum strain values for both crack widths. This suggests that, especially for early-stage crack detection where strain changes are subtle, high-resolution settings are most effective. For larger cracks, the difference in detection capability between the 0.05 m and 0.1 m sampling intervals becomes less pronounced, indicating that a moderate sampling resolution may be sufficient for identifying more developed cracks while also reducing data management demands.

The strain responses observed in this experiment were significantly higher than those anticipated for the full-scale beam laboratory experiment, where maximum bracket strains are expected to be around 10με. Therefore, the primary considerations in selecting the optimal DAQ setting are the maximum strain values observed and the clarity with which the measurements can be interpreted. The maximum strain values for each DAQ configuration and crack width, as measured using the FOS, are summarized in Table 3.6.

Table 3.6: Maximum strain values for different DAQ configurations and crack widths (measured using FOS)

DAQ Settings	1mm	2mm
	Strain max [με]	Strain max [με]
5-10	31.69	52.16
5-20	27.74	46.20
10-20	13.72	37.42
10-50	21.66	20.44

This comparison demonstrates that while higher sampling and lighter averaging (5-10 setting) offer the most detailed strain profiles and highest sensitivity, all tested DAQ configurations can effectively detect and differentiate between different crack widths. The choice of optimal DAQ

setting will depend on the specific requirements of the monitoring system, balancing factors such as detection sensitivity, data processing capabilities, and the expected range of crack sizes to be monitored.

3.3.4. Identification of Optimal Configuration

Based on the comparative analysis of the four DAQ configurations and their effects on signal quality, several conclusions can be drawn regarding the optimal setup for crack detection. The 5-10 configuration, which uses a 0.05 m sampling interval and a 0.1 m averaging window, provides the highest sensitivity to crack detection, particularly for smaller crack widths. This makes it the most suitable choice when early detection and high precision are priorities. However, this configuration also generates the largest datasets, which may present challenges for data processing and storage, especially in continuous or long-term monitoring scenarios.

On the other hand, configurations such as 10-20 and 10-50, which use lower sampling resolutions and larger averaging windows, produce smoother strain profiles with improved noise characteristics but at the expense of spatial resolution and sensitivity. For applications where long-term monitoring and efficient data management are more critical than the earliest possible crack detection, these settings may be more appropriate. The 5-20 configuration offers a balanced compromise, providing good sensitivity with more manageable data volumes.

Ultimately, the selection of the optimal DAQ configuration should be guided by the specific requirements of the intended monitoring application. For the upcoming full-scale beam experiment, where the expected maximum strain is around 10με, the 5-10 setting is recommended to ensure reliable detection of small strain changes. However, if data management constraints are a significant concern, the 5-20 configuration may offer an effective alternative. These recommendations are made with the understanding that the primary objective of this study is not to measure the precise size of cracks, but rather to reliably detect their presence and to identify the most suitable DAQ configuration for practical, real-world deployment.

3.3.5. Conclusions

The results clearly indicate that the 5-10 DAQ setting is the most suitable configuration for the laboratory beam experiment. This setting consistently demonstrated the highest sensitivity to crack detection, which is particularly important for identifying the small strains and narrow crack widths anticipated in the beam test. The detailed strain profiles produced by the 5-10 configuration allow for precise localization and characterization of strain changes along the pi-bracket, a crucial capability when monitoring for early-stage damage or microcracking. This approach ensures the highest possible resolution and sensitivity for detecting small strains and crack openings, thereby advancing the development of a robust and effective fiber optic sensor system for structural health monitoring applications.

Notably, the 5-10 setting yielded the highest maximum strain values for both 1 mm and 2 mm crack openings, with recorded peaks of 31.69 με and 52.16 με, respectively. This high level of sensitivity is especially relevant given that the expected maximum strains in the beam experiment are on the order of 10 με. By selecting this configuration, the experiment will be well-equipped to detect even subtle changes, maximizing the reliability of crack detection under realistic laboratory conditions.

The findings from the DAQ optimization provide a robust foundation for these future investigations, ensuring that the most effective data acquisition strategy is in place as the experimental program progresses.

CHAPTER 4: PI-BRACKET OPTIMIZATION

4.1. INTRODUCTION

FEA modeling plays a pivotal role in the development and optimization of the Bracket Crack Sensor. This chapter outlines the approach to creating FEA models of multiple geometric concepts to investigate whether the selection of aluminum and the Pi-bracket concept represent the optimal solution. This transition sets the stage for a detailed exploration of sensor design, simulation, and performance evaluation, bridging the gap between research insights and engineering implementation. The bracket concept design was selected through collaborative discussions, while the choice of aluminum as the material was driven by practical constrains of in-house manufacturing. Using FEA, this chapter explores how the selected design and material combination responds to operational stresses, with the goal of validating its suitability and identifying opportunities for further optimization.

4.2. MATERIAL SELECTION

The material selection process is critical in determining the Bracket Crack Sensor's performance and manufacturability. Although both steel and aluminum are widely used engineering metals, each possesses distinct properties that influence their suitability for different applications and manufacturing constraints. In this study, aluminum was chosen primarily due to the limitations of the home-made production process, which favored material that is easier to work with. However, to ensure that this selection is optimal, FEA modeling will also compare the performance of aluminum to steel. This comparative analysis will help determine whether aluminum was the best choice or if steel should be recommended for mass manufacturing, considering factors such as strength, durability, cost, and ease of production. By examining both materials in detail, this section aims to provide a well-founded recommendation for large-scale implementation of the Bracket Crack Sensor.

4.2.1. Steel Properties

Structural steel, particularly American Society for Testing and Materials (ASTM) A992 grade, offers a combination of properties that make it highly suitable for sensor applications in SHM. This steel grade is widely recognized for its excellent mechanical performance. Its specified yield strength ranges from 345 to 448 MPa and a minimum ultimate tensile strength of 448 MPa (Bartlett and Dexter 2001). These strength characteristics ensure that the material can maintain its integrity under a variety of loading conditions, which is essential for sensors that must function reliably in demanding structural environments. Additionally, ASTM A992 steel demonstrates notable ductility, with a minimum elongation at failure of 21% in a 50 mm gauge length. This ductility allows the material to deform under stress without immediate failure, an important feature for sensors intended to detect and respond to structural changes.

The thermal properties of structural steel further enhance its suitability for sensor applications. Carbon steel, such as ASTM A992, has a thermal conductivity in the range of 45 to 60 W/m·K, which influences heat transfer within the sensor and can affect its sensitivity to temperature variations. The high melting point of steel, typically between 1370 and 1510°C, ensures that the material can withstand elevated temperatures without losing its structural integrity. Moreover, the specific heat capacity of structural alloy steel, which ranges from 452 to 1499 J/kg-K, contributes to the thermal stability of sensors, helping them maintain consistent performance even as environmental temperatures fluctuate (Bartlett and Dexter 2001).

Elastic properties are also critical for sensor performance. Structural steel exhibits a high elastic modulus, with ASTM A992 having a value of 200,000 MPa based on extensive testing (Dexter et al. 2000). This high modulus ensures predictable and consistent elastic behavior, which is vital for the accurate detection of strain and deformation in SHM applications.

Altogether, the combination of high strength, good ductility, favorable thermal characteristics, and reliable elastic properties make ASTM A992 structural steel an excellent choice for use in devices such as the Bracket Crack Sensor. These attributes ensure that the material can provide both the durability, and the precision required for effective long-term monitoring of structural health.

4.2.2. Aluminum Properties

Aluminum, and particularly the 6061 alloy, possesses a range of properties that make it an attractive material for sensors in SHM applications. One of its most notable attributes is its light weight. With a density of approximately 2.7 g/cm³, about one-third that of steel, aluminum allows for the creation of sensors that add minimal additional mass to the structures. This is beneficial in applications where weight reduction is a priority (Bartlett and Dexter 2001).

Corrosion resistance is another significant advantage of aluminum. The material naturally forms a protective oxide film on its surface, which provides excellent resistance to corrosion in a wide variety of environments. This inherent durability is particularly valuable for sensors that are exposed to fluctuating atmospheric conditions, as it can enhance both the lifespan and reliability of the sensor system (Diler et al. 2021).

Aluminum 6061 also exhibits high thermal conductivity, measured at approximately 167 W/m-K, which is considerably higher than that of many other structural materials (ASM International 1990). For sensors mounted on steel girders, this property enables rapid heat transfer, ensuring that the sensor and the girder maintain similar temperatures and reducing the risk of thermal stresses at their interface. The high thermal responsiveness can also improve the accuracy of temperature-related measurements or compensations within the sensor system.

Mechanically, aluminum 6061-T6 offers a well-balanced combination of strength and ductility, with a tensile strength of 310 MPa, a yield strength of 276 MPa, and an elongation of 12% over a 50 mm gauge length. These mechanical properties ensure sufficient stability for sensor applications while allowing for some flexibility under load.

The elastic modulus, or Young's modulus, of aluminum 6061 is approximately 68.9 GPa. While this is lower than that of steel, resulting in greater deformation under the same stress, it is an important consideration in sensor design, particularly for applications where some flexibility is desirable (ASM International 1990).

Finally, aluminum's high malleability and formability enable the fabrication of complex sensor geometries, giving designers the freedom to optimize sensor shapes for specific monitoring needs (Bartlett and Dexter 2001).

Collectively, these properties make aluminum 6061 a highly versatile choice for sensor design, offering a unique combination of lightweight construction, corrosion resistance, thermal and electrical responsiveness, and durability that can be applied in a wide range of SHM applications.

4.2.3. FEA Simulations for Material Selection

This section presents two simple simulations in Abaqus comparing the behavior of steel and aluminum beams under different loading conditions. The results are used to evaluate whether the initial choice of aluminum for the Bracket Crack Sensor was optimal, providing justification for the selected material.

4.2.3.1. Displacement-Controlled Simulation

In the first simulation, a bar measuring 1 meter in length with a cross-section of 1" x 1/8" was analyzed. These dimensions were chosen to reflect aluminum profiles commonly available from commercial retailers. The simulation involved subjecting one end of the beam to a prescribed longitudinal displacement of 0.2 mm, while the opposite end was fully fixed. This setup was used to evaluate and compare the mechanical response of both steel and aluminum materials under identical geometric and loading conditions.

The modeling process was carried out in Abaqus/CAE. A three-dimensional deformable wire part, representing the bar, was created with a length of 1000 mm. In the Property module, material definitions were established for both steel and aluminum. For steel, a Young's modulus of 200,000 MPa and a Poisson's ratio of 0.3 were used, while for aluminum, the values were 69,000 MPa and 0.33, respectively. A rectangular beam section with dimensions of 25.4 mm by 3.175 mm was assigned to the part. The step-by-step process of how the bar was modeled in Abaqus/CAE, including key settings and selections, is illustrated in Appendix C, Figures C.1 through C.11.

The assembly process involved creating an instance of the bar, after which a static general step was defined to simulate the displacement-controlled loading. Boundary conditions were applied such that one end of the beam was fully constrained, and a displacement of 0.2 mm was imposed at the free end. The bar was then meshed using an appropriate element type and mesh size.

Resulting displacement, strain, and stress distributions were extracted for both steel and aluminum. It is important to note that Abaqus does not enforce a specific unit system, so all input values must be entered consistently to maintain accuracy. This simulation approach enabled a direct comparison of the two materials' performance under identical conditions.

4.2.3.2. Force-Controlled Simulation

In the second simulation, the same bar geometry was used, but instead of applying a prescribed displacement, a concentrated force of 100 N was applied in the longitudinal direction at one end of the beam, while the opposite end remained fully fixed. This force-controlled scenario was modeled for both steel and aluminum materials to allow for a direct comparison of their mechanical responses under identical conditions.

The modeling process in Abaqus/CAE closely followed the steps outlined for the displacement-controlled simulation. The bar was defined as a 1-meter long, 1" x 1/8" cross-section wire part, with material properties assigned for steel and aluminum as previously described. After assembling the part, a static general analysis step was created specifically for the force-controlled case (as shown in Appendix C, Figure C.12). The boundary conditions were set so that one end of the beam was fully constrained, and a concentrated force of 100 N was applied at the free end in the longitudinal direction (see Appendix C, Figure C.13 for the application of the concentrated load).

The model was then meshed and submitted for analysis. Upon completion, the resulting displacement, strain, and stress distributions were extracted for both materials. This force-controlled simulation provided valuable insights into how steel and aluminum beams behave under direct loading, further informing the material selection process for the Bracket Crack Sensor by highlighting differences in mechanical performance under practical loading scenarios.

4.2.4. Comparison of Steel vs Aluminum

This section compares the performance of steel and aluminum in two simulations: a displacement-controlled test and a force-controlled test. The results offer a comprehensive understanding of the

behavior of these materials under various loading conditions, which is essential for identifying the optimal material for the Bracket Crack Sensor.

4.2.4.1. Displacement-Controlled Simulation Results

In this simulation, both steel and aluminum bars were subjected to a 0.2mm displacement at one end while fixed at another end. The material responses were recorded for the fundamental parameters describing how materials respond to applied forces (displacement) or deformations as shown in Appendix C, Figures C.14 and C.15, including Strain (Appendix C, Figures C.16 and C.17) and Stress (Appendix C, Figures C.18 and C.19). The results are summarized in Table 4.1.

Table 4.1: Displacement-controlled simulation results comparison

Material	Displacement [mm]	Strain [με]	Stress [MPa]
Steel	0.2	200	40
Aluminum	0.2	200	13.8

4.2.4.2. Force-Controlled Simulation Results

In this simulation, a 100N force was applied to one end of the bar instead of the 0.2mm displacement. The displacement results are shown in Appendix C, Figures C.20 and C.21; the strain results are presented in Figures C.22 and C.23; and the stress results are provided in Figures C.24 and C.25.The results are summarized in Table 4.2.

Table 4.2: Force-controlled simulation results comparison

Material	Displacement [mm]	Strain [με]	Stress [MPa]
Steel	0.0062	6.2	1.24
Aluminum	0.01797	17.97	1.24

The primary function of the bracket is to serve as a harness for the FOS, thereby supporting the main objective of the sensor system detecting crack formation in steel girders near vertical stiffeners. Due to the sensor's installation parallel to the girder's length, it effectively monitors crack width. In this context, the displacement-controlled simulation results are more relevant to our application, as they better represent the sensor's response to crack opening. In this simulation, both materials exhibited the same displacements and strains, as expected for a fixed displacement. Aluminum experienced lower stress (13.8 MPa) compared to steel (40 MPa) under the same displacement, which initially appeared advantageous for sensitivity.

However, a critical factor in the Canadian context is the extreme temperature range that bridge structures experience, from -40°C to +40°C. Aluminum's high thermal conductivity, while beneficial for rapid heat dissipation, can introduce measurement inaccuracies due to thermal gradients and differential expansion between the aluminum bracket and the steel girder (ASM International 1990). This mismatch may cause the bracket and girder to respond differently to temperature changes, potentially compromising strain measurement accuracy.

In contrast, using steel for the bracket ensures thermal compatibility and consistent behavior with the steel girder across fluctuating temperatures. This consistency is crucial for reliable, long-term monitoring in harsh climates. Additionally, material uniformity minimizes the risk of galvanic corrosion, which can occur when dissimilar metals are in contact in moist environments (Diler et al. 2021).

While aluminum's lighter weight and ease of fabrication were initially appealing for prototype development, these advantages are outweighed by the benefits of using steel for mass manufacturing. Steel brackets not only align with the material properties of the girders but also provide greater durability and measurement reliability over the lifespan of the sensor system.

The proposed method for mounting the bracket to the steel girder is adhesive bonding, a technique widely utilized by researchers in similar applications (Kralovec and Shagerl 2020). Given the precedent and the decision to use adhesive for mounting the FOS to both the girder and the bracket, adhesive bonding will also be employed to mount the bracket to the steel girder. This mounting method further emphasizes the importance of the results from the displacement-controlled simulation. Figure 4.1 illustrates the proposed bracket system, highlighting the relationship between the bracket, FOS, steel girder, and stiffener.

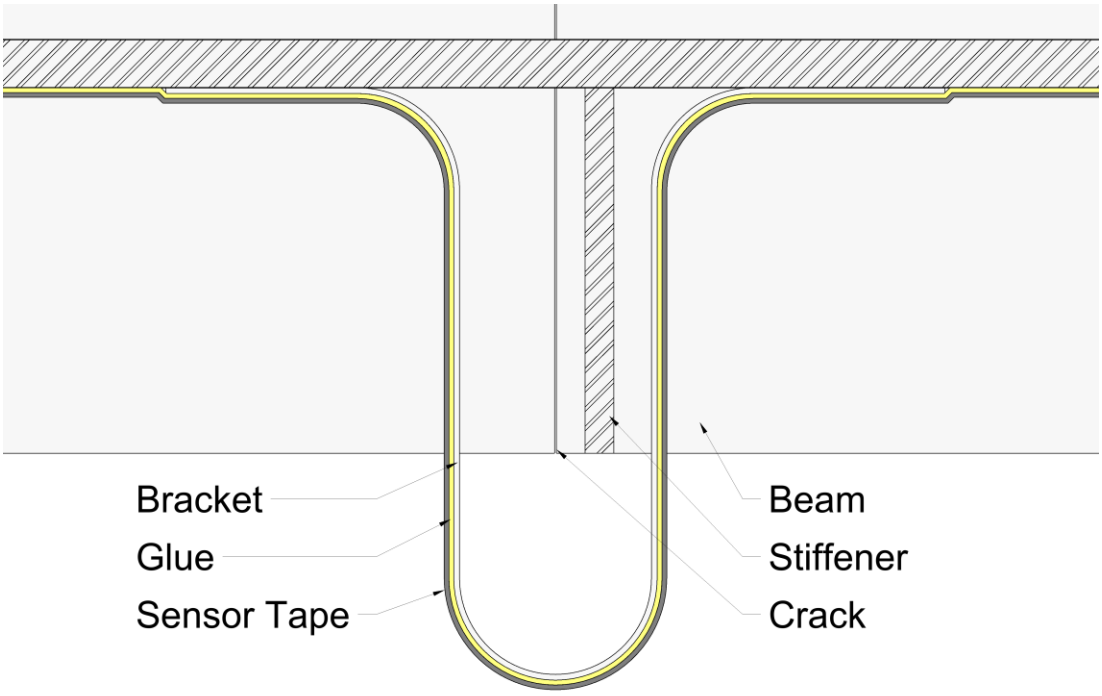

Figure 4.1: Proposed bracket system

The use of adhesive bonding in this context aligns with current trends in SHM where non-invasive and easily installable sensor systems are preferred (Kralovec and Shagerl 2020). This approach not only simplifies the installation process but also minimizes potential damage to the existing structure, which is vital in bridge monitoring applications.

The higher stress experienced by the steel bracket (40 MPa compared to aluminum's 13.8 MPa) could potentially lead to premature failure of the adhesive bond between the bracket and the girder. The lower stress experienced by the aluminum bracket suggests that it would be less likely to induce high stresses at the adhesive interface, contributing to a more durable and reliable mounting solution.

In summary, although aluminum was suitable for initial prototyping due to its workability, our comparative analysis demonstrates that steel is the superior choice for large-scale deployment. Steel brackets offer improved thermal compatibility, enhanced measurement accuracy in extreme temperature environments, and material consistency with the bridge structure, making them the recommended option for the Bracket Crack Sensor. Nevertheless, due to the limitations of in-house

manufacturing capabilities, the experimental investigations presented in the subsequent Chapters will employ aluminum Pi-brackets. It should be noted, however, that steel is recommended as the preferred material for mass production applications.

4.3. BRACKET CRACK SENSOR GEOMETRY SELECTION

4.3.1. Geometric Concepts

The selection of the optimal bracket geometry for the Bracket Crack Sensor was made through collaborative discussions among the research project team. Three candidate designs were considered: the Pi bracket (Figure 4.2), Omega bracket (Figure 4.3), and Lambda bracket (Figure 4.4). Each concept was developed using aluminum strips with cross-sectional dimensions of 1" x 1/8" and a uniform depth of 200 mm, as established in the material selection section. Initial sketches of these designs are presented in Section 1.3.1.

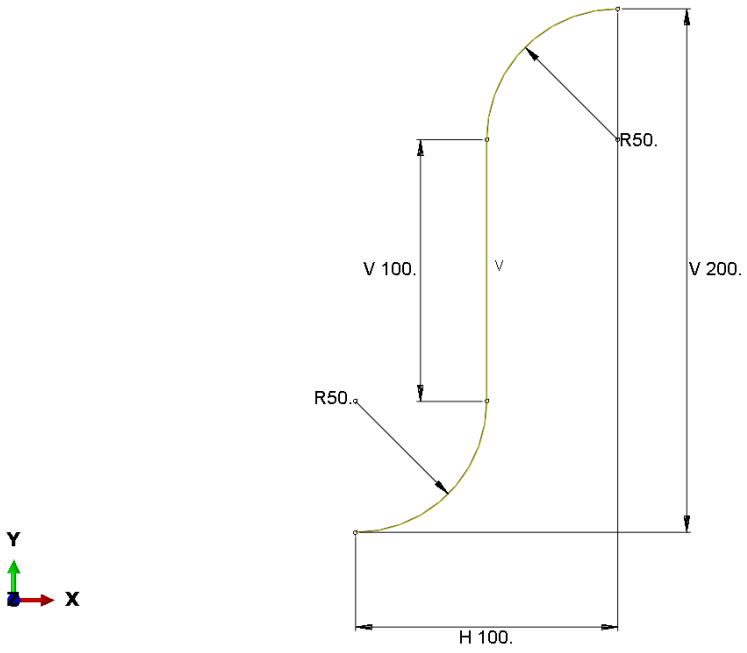

Figure 4.2: Pi-bracket model dimensions

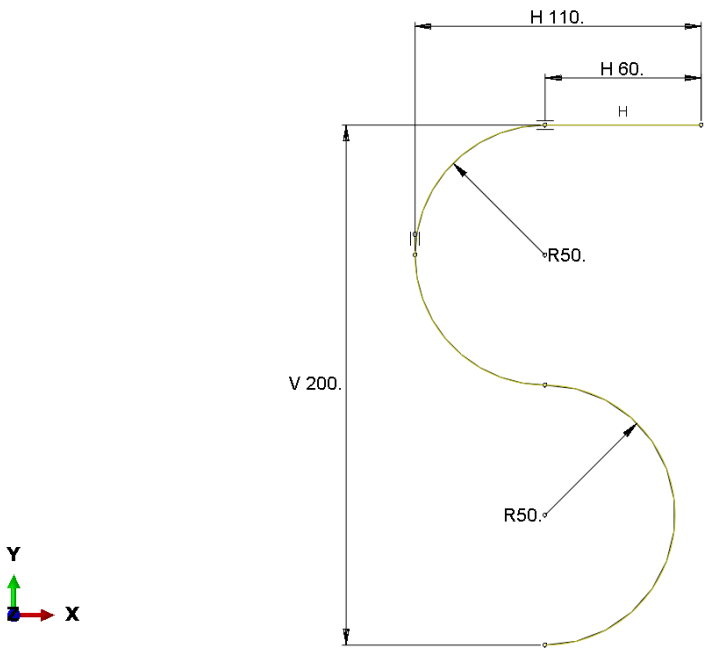

Figure 4.3: Omega bracket model dimensions

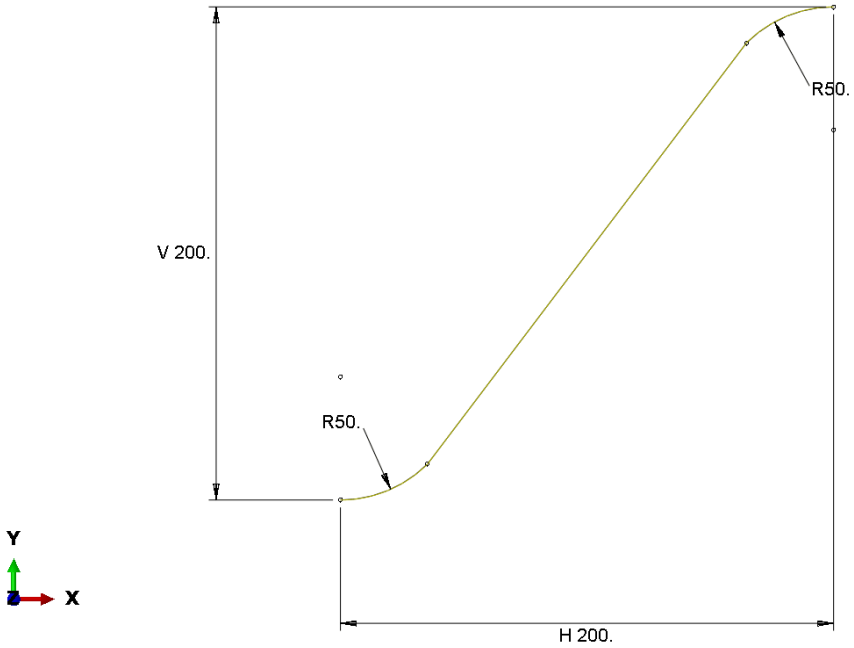

Figure 4.4: Lambda bracket model dimensions

4.3.2. FEA Modeling of Geometric Concepts

Having selected the Pi-bracket as the preferred design through team consensus, the next step was to rigorously investigate whether this choice was indeed optimal. To this end, FEA simulations were performed for all three bracket geometries under identical, displacement-controlled loading conditions. This approach, consistent with best practices in strain-based structural health monitoring (Kralovec and Shagerl 2020), involved applying a 0.2 mm displacement to represent crack opening. Symmetry was utilized in the models to enhance computational efficiency while preserving accuracy.

The boundary conditions were carefully defined to reflect realistic constraints and loading scenarios. A symmetry boundary condition, labeled "XSYMM," was applied to the crown of the bracket (the top right end in Figure 4.5).

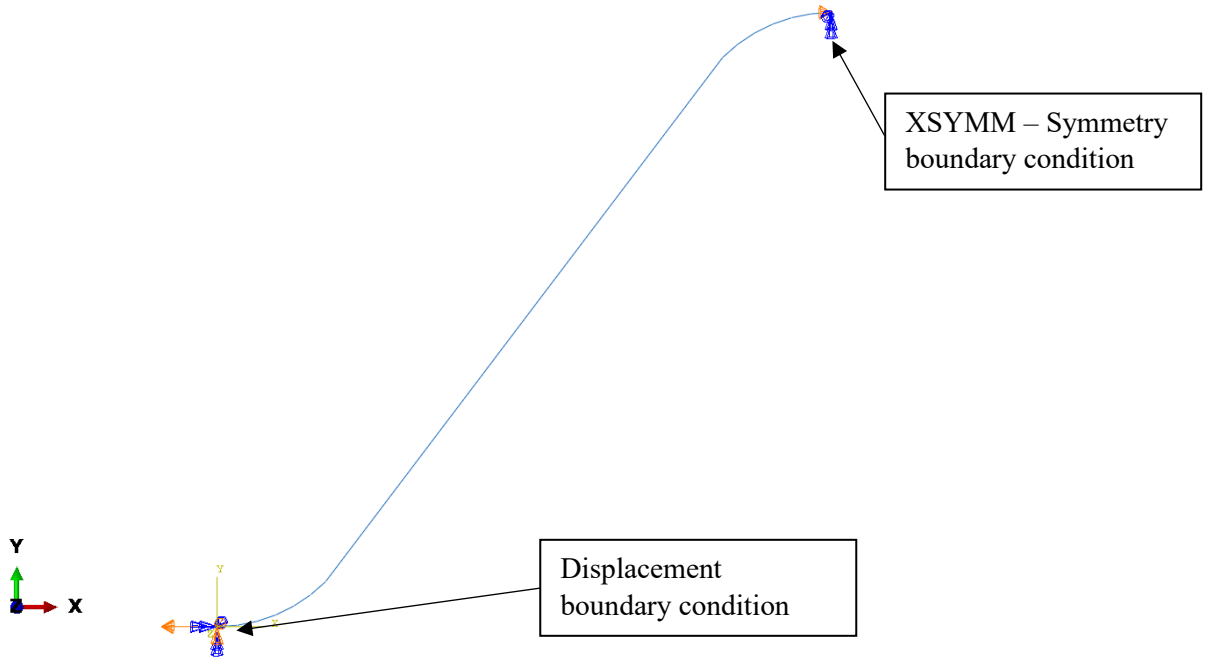

Figure 4.5: Lambda bracket - boundary conditions

This condition restricts displacement in the X direction (U1=0) and prevents rotations about the Y and Z axes (UR2=UR3=0), while allowing free movement in the Y and Z directions and rotation about the X-axis. At the bottom left end of the model, a displacement/rotation boundary condition

was introduced, permitting translation only in the X direction (U1), which simulates a sliding support. A prescribed displacement of 0.1 mm was then applied at this location, representing the bracket's opening movement in response to the simulated crack.

The primary focus of the analysis is on the maximum strain, as the data acquisition system (DAQ) will be reading strain values. This approach is consistent with the strain-based crack monitoring techniques discussed by Kralovec and Shagerl (2020), which have been extensively researched.

4.3.3. Performance Analysis

The performance analysis of the three bracket concepts (Pi, Omega, and Lambda) was conducted based on the displacement-controlled simulation results. For this test, a displacement of 0.1mm was applied to the bottom left end of the bracket, as explained in the previous section, which represents displacement of 0.2mm of a whole bracket. The key parameters evaluated were the maximum strains (E11) at the top (Crown) and bottom of the brackets, as well as the maximum displacement of the crown in Y-direction (U2). The results are summarized in Table 4.3.

Table 4.3: Bracket geometry selection simulation results comparison (under a horizontal displacement of 01.mm)

Concept	Strain E11 Crown [με]	Strain E11 Bottom [με]	Displacement U2 Max [mm]
Pi bracket	-13.41	13.55	-0.024
Omega bracket	-8.02	10.09	0.051
Lambda bracket	-12.73	12.87	-0.082

The Omega bracket demonstrated the lowest performance in terms of strain sensitivity, which is important for crack detection as emphasized by Kralovec and Shagerl (2020). The Lambda and Pi bracket concepts showed similar results, with the Pi bracket yielding slightly higher strains and smaller displacement in the U2 direction.

In addition to its favorable mechanical performance, the Pi-bracket's narrower profile provides practical advantages for installation. This geometry allows for direct and efficient bonding of the fiber optic sensor to the girder, minimizing the area of the girder covered by the sensor and potentially enhancing the overall sensitivity and accuracy of the structural health monitoring system.

Overall, these findings validate the collaborative selection of the Pi-bracket as the optimal geometry for the Bracket Crack Sensor.

4.3.4. Optimization Process

The results of the comparative performance analysis have confirmed that the Pi-bracket, originally selected through collaborative team discussions, is indeed the optimal geometry for the Bracket Crack Sensor. With this validation established, the focus shifts to optimizing the Pi-bracket's dimensions to maximize its effectiveness while accommodating practical installation constraints.

For both the depth and thickness optimization processes, displacement-controlled FEA simulations were performed. In each case, the simulation applied a load represented by a 0.2 mm displacement, corresponding to the target crack opening displacement for reliable detection.

The first aspect of optimization considered was bracket depth, to ensure that the bracket could clear stiffeners or other obstacles on a variety of girder configurations. FEA simulations were conducted for two Pi-bracket depths, and the results are summarized in Table 4.4.

Table 4.4: Depth optimization results comparison

Pi-Bracket Depth [mm]	Strain E11 Crown [με]	Strain E11 Bottom [με]	Displacement U2 Max [mm]
200	-13.41	13.55	-0.024
300	-6.89	6.94	-0.012

The comparison between the initial 200 mm deep Pi-bracket and the 300 mm deep Pi-bracket reveals that increasing the bracket depth significantly reduces both strain and displacement values. The 300 mm bracket exhibited approximately half the strain (-6.89 με at the crown and 6.94 με at the bottom) compared to the 200 mm bracket (-13.41 με at the crown and 13.55 με at the bottom). Similarly, the displacement at the crown decreased from -0.024 mm for the 200 mm bracket to -0.012 mm for the 300 mm bracket.

These results suggest that a deeper bracket reduces strain and deformation under the same applied displacement. However, this reduction in strain may impact the sensitivity of crack monitoring, which relies on strain measurements. Therefore, a balance between bracket depth and strain sensitivity needs to be considered during optimization.

Further optimization could involve fine-tuning the bracket thickness to balance between sensitivity and durability. The results are summarized in Table 4.5.

Table 4.5: Thickness optimization results comparison

Pi-Bracket Thickness	Strain E11 Crown [με]	Strain E11 Bottom [με]	Displacement U2 Max [mm]
1/8” (3.175 mm)	-13.41	13.55	-0.024
1/4” (6.35 mm)	-26.63	27.2	-0.024
3/8” (9.525 mm)	-39.64	40.92	-0.024

The thickness optimization simulation for the Pi-bracket reveals a significant impact on strain values while maintaining consistent displacement. As the bracket thickness increased from 3.175mm to 6.35mm and 9.525mm, the strain values (E11) at both crown and bottom increased proportionally. The 6.35mm thick bracket showed approximately double the strain of the 3.175mm bracket, while the 9.525mm thick bracket exhibited about triple the strain. The displacement at the crown remained constant at -0.024mm for all three thicknesses. This behavior is explained by the fact that all simulations were conducted within the linear elastic range of the materials, where Hooke’s Law applies. Since the same displacement (0.2 mm) was imposed in each case, the change

in length was equal for all brackets, resulting in identical crown displacements. However, increasing the bracket thickness led to higher stresses and, consequently, proportionally higher strain values under the same applied load. These results suggest that increasing the bracket thickness enhances strain sensitivity without affecting overall displacement, potentially improving the bracket's ability to detect small changes in crack width.

Due to current material availability, only 1/8" (3.175 mm) thick aluminum is being used for the experimental phase. However, should the bracket progress to mass production, thicker materials will be considered to potentially enhance strain sensitivity. This consideration is consistent with research indicating that material thickness can influence strain rate sensitivity in metallic materials.

The depth and thickness optimization, guided by FEA simulations, provides robust support for the Pi-bracket's superior performance and informs practical adjustments for real-world application. To further validate these findings, two Pi-bracket depths, 8" (203.2 mm) and 12" (304.8 mm), will be fabricated and tested, both with a thickness of 1/8" (3.175 mm). This experimental work will help identify any unforeseen factors affecting performance and will be instrumental in finalizing the optimal design for the Bracket Crack Sensor before proceeding to full-scale beam experiments and potential mass production.

4.4. CONCLUSIONS

The comprehensive analysis and optimization confirm that the Pi-bracket is the optimal geometry for the Bracket Crack Sensor. Among the three concepts evaluated, the Pi-bracket consistently exhibited the highest strain sensitivity and lowest displacement, both critical for effective crack detection in structural health monitoring applications. Its narrower profile also allows for more direct and efficient bonding of the fiber optic sensor to the girder, enhancing the sensitivity and accuracy of the monitoring system.

Dimension optimization revealed that the smaller 8" (203.2 mm) bracket measured higher strains than the larger 12" (304.8 mm) version. Therefore, the 8-inch bracket will be used for the laboratory experiment to maximize strain sensitivity. Increasing bracket thickness also resulted in proportionally higher strain values while maintaining consistent displacement, indicating that thicker brackets could further enhance sensitivity.

Aluminum was used for prototype fabrication due to in-house manufacturing limitations, offering advantages such as light weight, corrosion resistance, and ease of fabrication. However, its high thermal conductivity can introduce measurement inaccuracies in environments with significant temperature fluctuations. For mass production and long-term application, steel is recommended as the preferred material due to its superior thermal compatibility with steel girders and its durability in demanding environments.

For the purposes of this research, aluminum Pi-brackets will continue to be used in experimental investigations due to current manufacturing constraints. However, for future prototypes and large-scale implementation, steel and increased thickness should be considered to further enhance strain sensitivity.

In the next chapter, the optimized 8-inch Pi-bracket will undergo laboratory testing to further evaluate its performance under realistic loading and cracking conditions, building on the findings established through FEA optimization.

CHAPTER 5: EXPERIMENTAL STUDY

5.1. INTRODUCTION

The laboratory experiment marks a key phase in evaluating the performance of the pi-bracket sensor system for crack detection in steel bridge girders. This experiment builds upon the findings gained from previous chapters, particularly the DAQ optimization study conducted with the 300mm bracket and FOS. In this chapter, we transition to using the 200mm pi-bracket, which is expected to offer higher strain sensitivity.

The main components of the laboratory experimental setup include a W10x45 (W250x67) steel I-beam measuring 3.2 meters in length, arranged in a simply supported configuration with the supports spaced 3 meters apart. The setup also incorporates the pi-bracket, a SMARTape II fiber optic sensor, and the Neubrescope NBX-6050 data acquisition system, as illustrated in the schematic diagram in Figure 5.1. This arrangement provides a realistic simulation of a bridge girder environment for assessing the sensor system's crack detection capabilities.

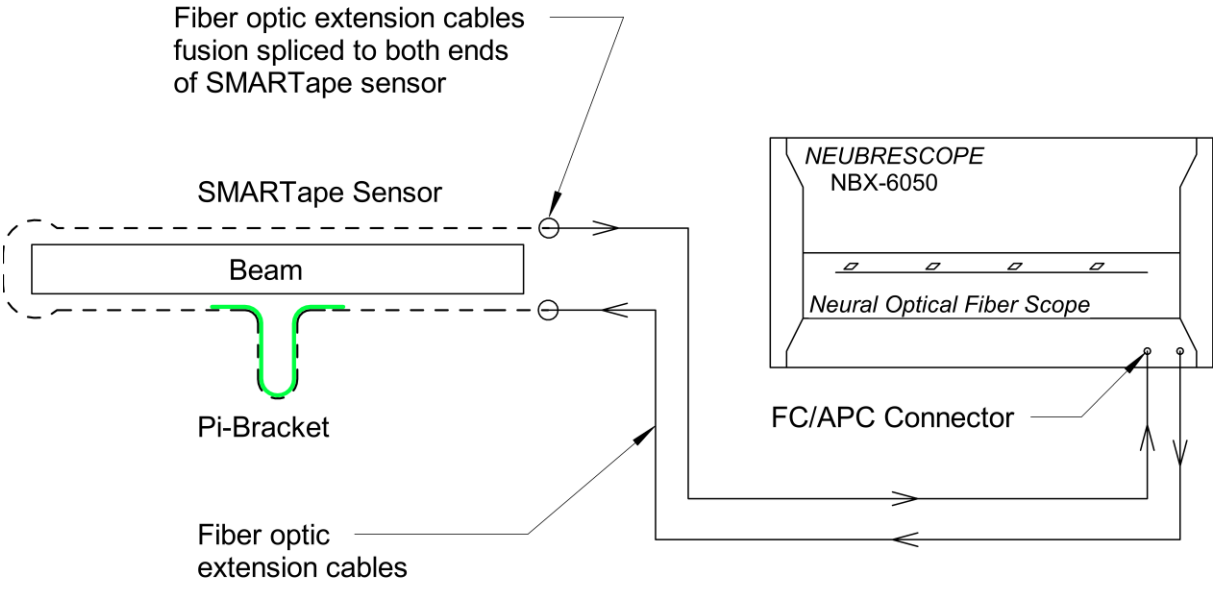

Figure 5.1: I-beam experiment - schematic diagram

A central focus of this chapter is the use of laboratory experiments to validate the predictions made by FEA simulations performed using Abaqus. This combined approach enables a thorough assessment of the pi-bracket sensor system's capabilities. The experiment is designed to evaluate the system's ability to detect and monitor cracks within a simulated bridge girder environment, while also validating the effectiveness of the optimized DAQ settings under realistic testing conditions.

Furthermore, the experimental results obtained from the fiber optic sensor are compared directly with FEA simulations, providing a robust validation of the sensor system's performance. This comparison also offers valuable insight into the relationship between experimental measurements and computational predictions, shedding light on strain distributions that may not be directly observed during physical testing.

By conducting this experiment and comparing it with FEA simulations, we aim to bridge the gap between theoretical predictions and practical applications. The integration of FEA simulations allows for a more in-depth understanding of the system's behavior, potentially revealing nuances in stress distribution and crack propagation that complement the experimental observations. This dual approach of laboratory testing and computational modeling offers a robust framework for validating the pi-bracket sensor system's efficacy in real-world applications.

5.2. FEA MODEL

A computational model was constructed using Abaqus software to replicate the experimental setup components: the steel girder, aluminum pi-bracket, and steel stiffener, each modeled as deformable planar shell elements with thicknesses matching experimental dimensions (8.9mm for girder web, 15.7mm for girder flanges, and 3.175mm for pi-bracket). Material properties were assigned to reflect the actual materials: aluminum was modeled with a Young's modulus of 69,000 MPa and a Poisson's ratio of 0.33, while steel was assigned a Young's modulus of 210,000 MPa and a Poisson's ratio of 0.3. Only the linear elastic portion of the material's behaviour was considered in the simulation.

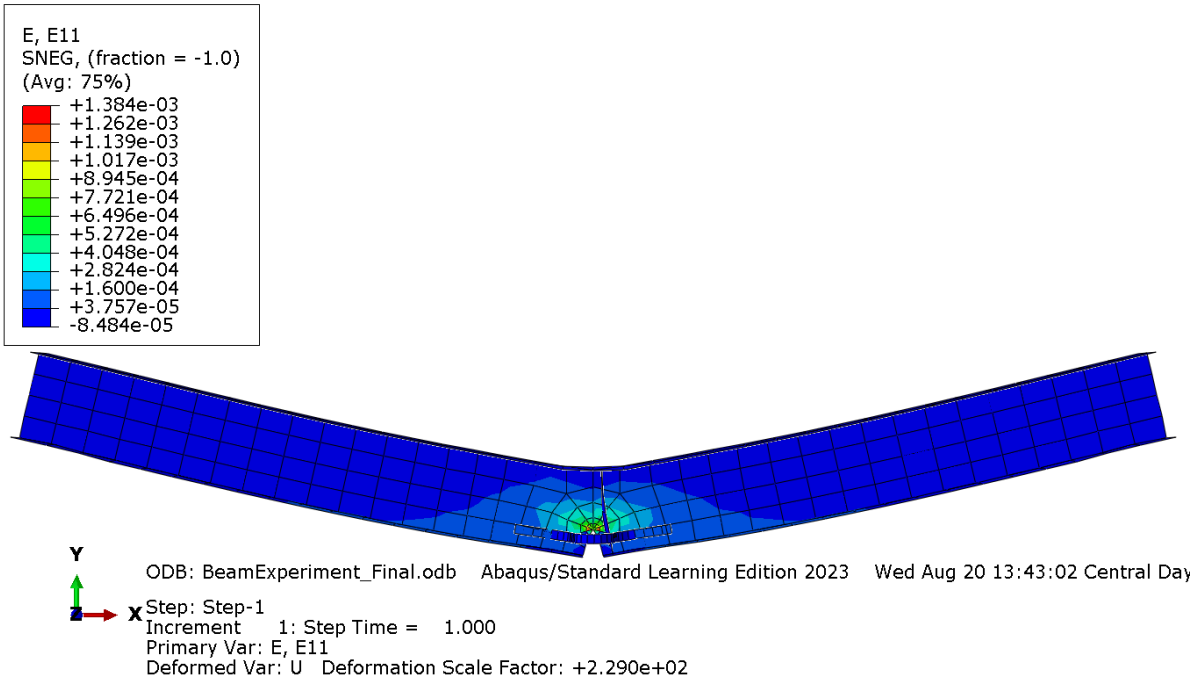

Figure 5.2: FEA model

To accurately simulate the simply supported steel girder, the beam was modeled with a total length of 3.2 meters and supports spaced 3 meters apart, reflecting the experimental setup (Figure 5.2).

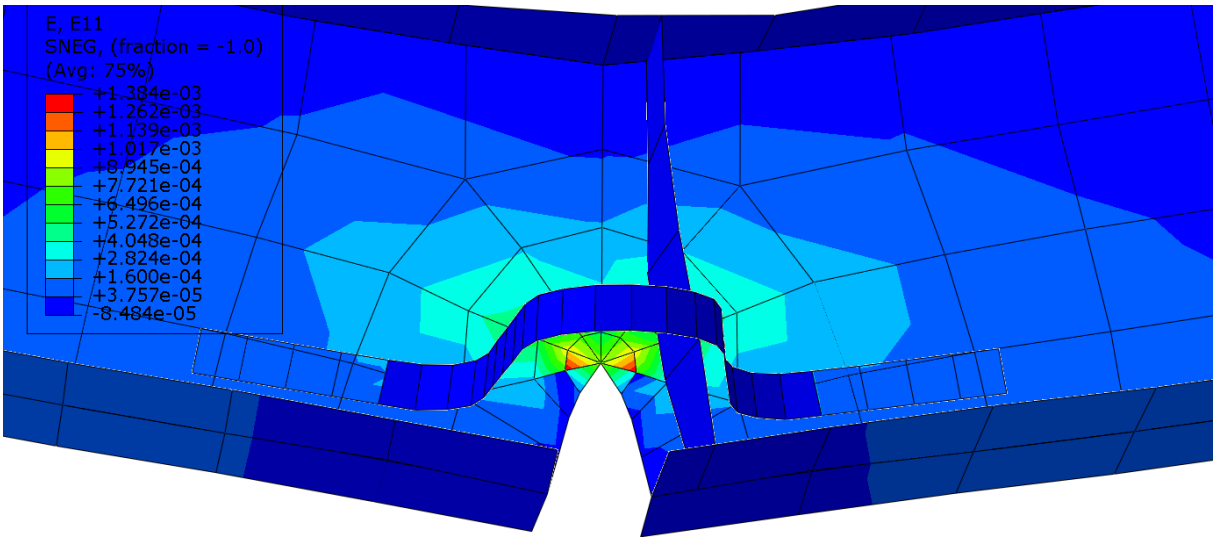

Figure 5.3: Detail of the FEA model around the Pi-bracket

Figure 5.3 shows a detailed close-up of the FEA model around the pi-bracket. At one end, a pinned support was applied, restricting all translational degrees of freedom (U1, U2, U3) as well as rotations about the local axes UR1 and UR2, effectively preventing movement in all directions except axial displacement. The opposite end was modeled as a roller support, where displacements in the U2 and U3 directions were restrained while allowing other movements, thereby replicating the realistic support conditions of the experimental beam. The crack was explicitly introduced as a stationary geometric discontinuity at the midspan of the web, created by partitioning the face of the beam. This crack extended vertically 57 mm from the bottom edge of the web, representing a pre-existing flaw rather than simulating crack propagation.

The connections between the FOS, pi-bracket, and beam were modeled as rigid interfaces using tie constraints. This approach enforces identical displacements and rotations at the interface, effectively simulating a completely rigid bond between the connected components. Although this represents an idealized scenario, it is sufficient for the purposes of this study, which focuses on the ability to detect the initiation of cracks.

The crack was explicitly introduced as a stationary geometric discontinuity at the midspan of the web, created by partitioning the face of the beam. This crack extended vertically 57 mm from the bottom edge of the web, representing a pre-existing flaw rather than simulating crack propagation. The crack was further defined as a contour integral, with the region and crack tip selected to specify the extension direction using q-vectors. To accurately model the stress singularity at the crack tip, a collapsed element side with a single node was implemented, and the mid-side node parameter was set to 0.3.

The mesh was primarily composed of four-node quadrilateral shell elements (S4R), which are well-suited for general-purpose analyses and capable of handling large strains. In the immediate vicinity of the crack, three-node triangular shell elements (S3) were used to better capture the geometric complexity. The S4R elements provided six degrees of freedom per node and utilized bilinear interpolation for accuracy.

Loading in the simulation was displacement-controlled, with concentrated forces applied at the midspan to produce crack opening widths of 0.1 mm and 0.2 mm, mirroring the experimental conditions. The applied displacement was defined as the relative movement between two nodes located at the same height as the pi-bracket, on either side of the crack. This approach does not

imply that the entire crack opens uniformly by the prescribed amount; instead, the displacement at the crack tip remains zero, while the maximum opening occurs at the bottom of the web, between the flanges. For example, when a 0.2 mm displacement is specified, the actual opening at the crack tip is zero, and the opening at the bottom of the web is larger.

This FEA model configuration enabled a detailed simulation of the beam's response under the specified loading conditions, allowing for in-depth analysis of stress and strain distributions, particularly in the regions surrounding the crack and the pi-bracket. The primary aim of the model was to assess the influence of the pi-bracket on strain distribution and to facilitate direct comparison with experimental strain measurements obtained from the fiber optic sensor. Rather than investigating crack propagation, the focus was on determining whether the pi-bracket sensor system could reliably detect changes in strain associated with crack formation, regardless of the crack's size or the presence of multiple cracks. The comparison between FEA results and experimental data is essential for validating the effectiveness of the pi-bracket sensor system in enhancing crack detection, supporting the broader goal of evaluating sensor performance for structural health monitoring applications rather than conducting a full fracture mechanics analysis.

5.3. EXPERIMENTAL SETUP

5.3.1. Beam Specimen

The experiment utilized a W10x45 (W250x67) steel beam specimen designed to simulate a section of a bridge girder. This wide flange beam, with total length of 3.2 meters, was arranged in a simply supported configuration with supports positioned 3 meters apart. This arrangement, illustrated in Figures 5.4 and 5.5, effectively replicates the structural behavior of a bridge girder segment under loading conditions relevant to the study.

To simulate realistic bridge girder geometry and operational damage scenarios, a transverse stiffener was welded to the beam 25 mm from the edge of the artificial crack on one side. This asymmetric design was intentionally chosen to generate non-uniform stress distributions characteristic of in-service bridge environments and to enable a comparative assessment between stiffened and non-stiffened regions. The geometry of the stiffener, crack location, and pi-bracket

placement were all carefully designed to emulate common failure scenarios observed in aging bridge infrastructure.

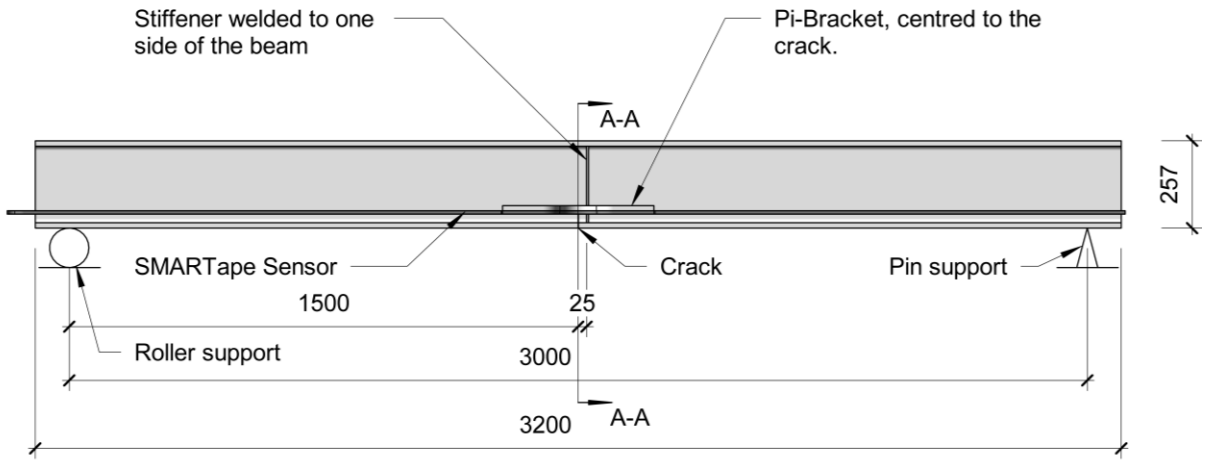

Figure 5.4: Beam – front elevation

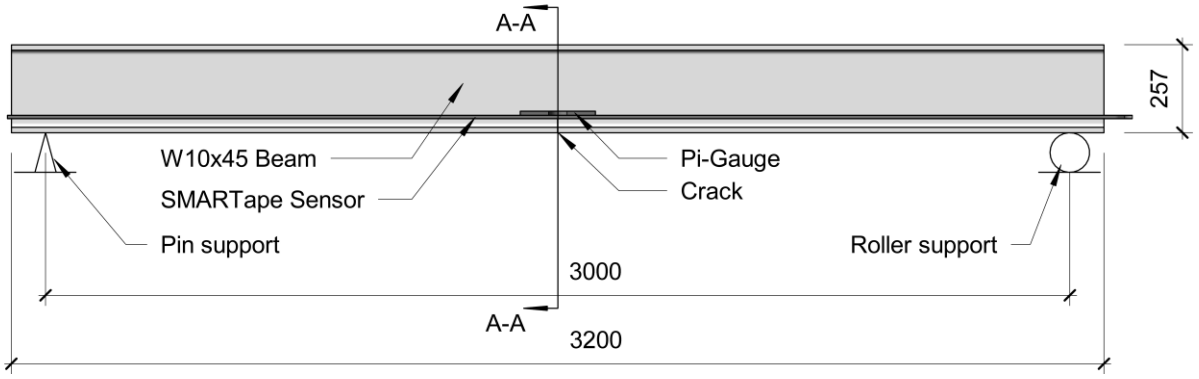

Figure 5.5: Beam – rear elevation

Structural damage was represented by introducing an artificial crack at the midspan of the beam. This crack was created by cutting through the bottom flange and extending it 57 mm vertically into the web from the underside of the beam, as depicted in the cross-sectional view in Figure 5.6.

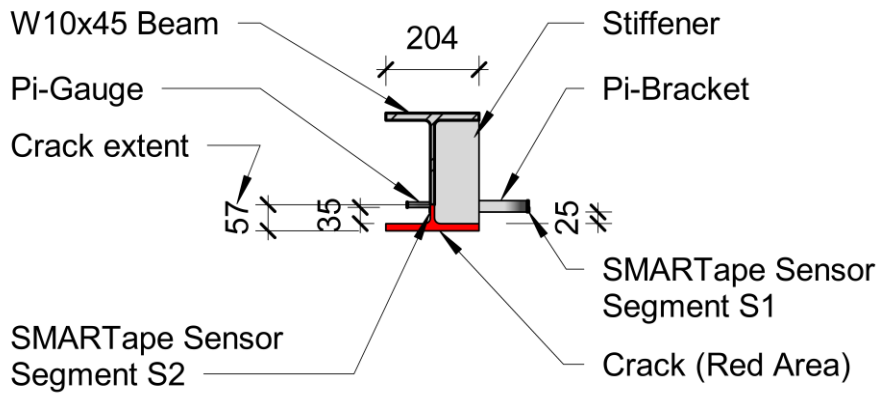

Figure 5.6: Beam – section A-A

The pi-bracket assembly was positioned 35 mm above the upper edge of the bottom flange, with its central axis aligned to the crack position. This configuration optimized sensor routing and maintained proximity to critical stress zones, enhancing detection sensitivity to crack-induced strain fields.

On the stiffened side of the beam, a FOS mounted on the pi-bracket was used for crack detection, while on the unstiffened side, the FOS was directly bonded over the crack. This configuration not only enabled a direct comparison of detection methods under different structural conditions but also provided valuable insight into the influence of local stiffening on sensor performance. By emulating the complex and asymmetric stress distributions typically encountered in real bridge structures, particularly near stiffeners where crack detection is especially challenging, the experimental setup offered a robust framework for evaluating sensor efficacy in practical applications.

5.3.2. Pi-Bracket

Based on the results of previous experiments, the laboratory setup transitioned from a 12” (300mm) Pi-Bracket to an 8” (200mm) version. This change was implemented to enhance the sensor's sensitivity and improve its overall performance in detecting smaller crack widths.

However, its dimensions have been optimized to provide better strain magnification and crack detection capabilities.

The geometry of the 200mm Pi-Bracket is illustrated in Figure 5.7, which shows the refined design used in the laboratory experiment and replicated in the FEA model.

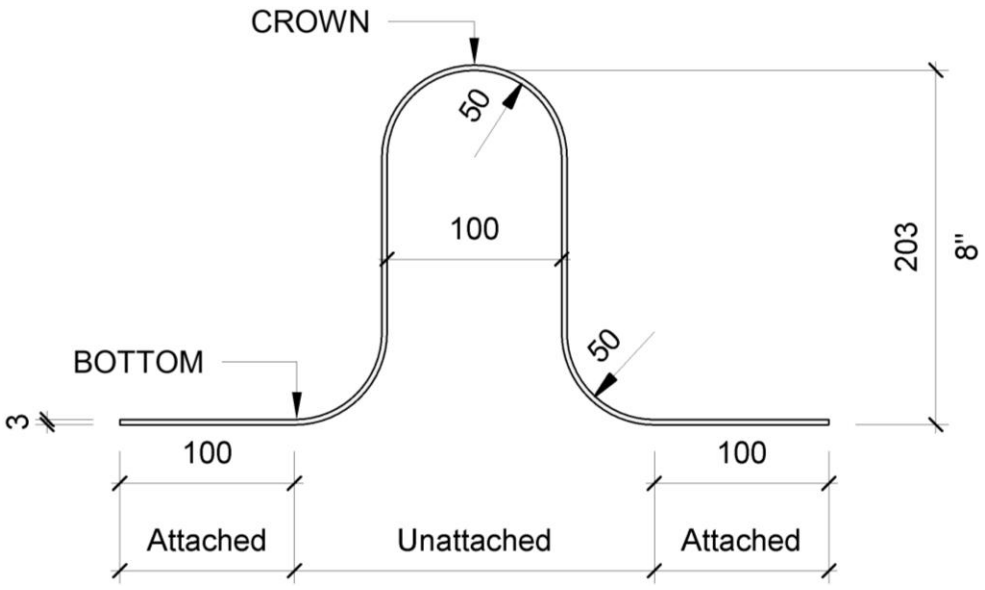

Figure 5.7: 8” Pi-bracket

This transition to a smaller bracket size represents an important step in the ongoing optimization process, aiming to achieve more accurate and reliable crack width measurements in steel bridge girders, both experimentally and computationally.

5.3.3. Instrumentation

The laboratory experiment employed a comprehensive instrumentation setup to accurately measure and monitor crack formation and propagation in the steel beam specimen. The primary sensing technology utilized was the DiTeSt SMARTape II distributed fiber optic sensor, developed by Smartec. This sensor consists of a single continuous optical fiber and was selected for its ability to provide detailed strain measurements along the entire length of the beam.

The instrumentation process began with the beam positioned beneath the hydraulic actuator, centered at midspan. The beam was configured with simple support conditions with supports spaced 3 meters apart. Prior to testing, the beam surface was carefully prepared by cleaning and sanding to ensure optimal adhesion of the sensors. Both the beam and pi-bracket surfaces were thoroughly sanded at the designated sensor locations and then cleaned with alcohol to remove any contaminants. This meticulous surface preparation was essential for achieving reliable sensor bonding.

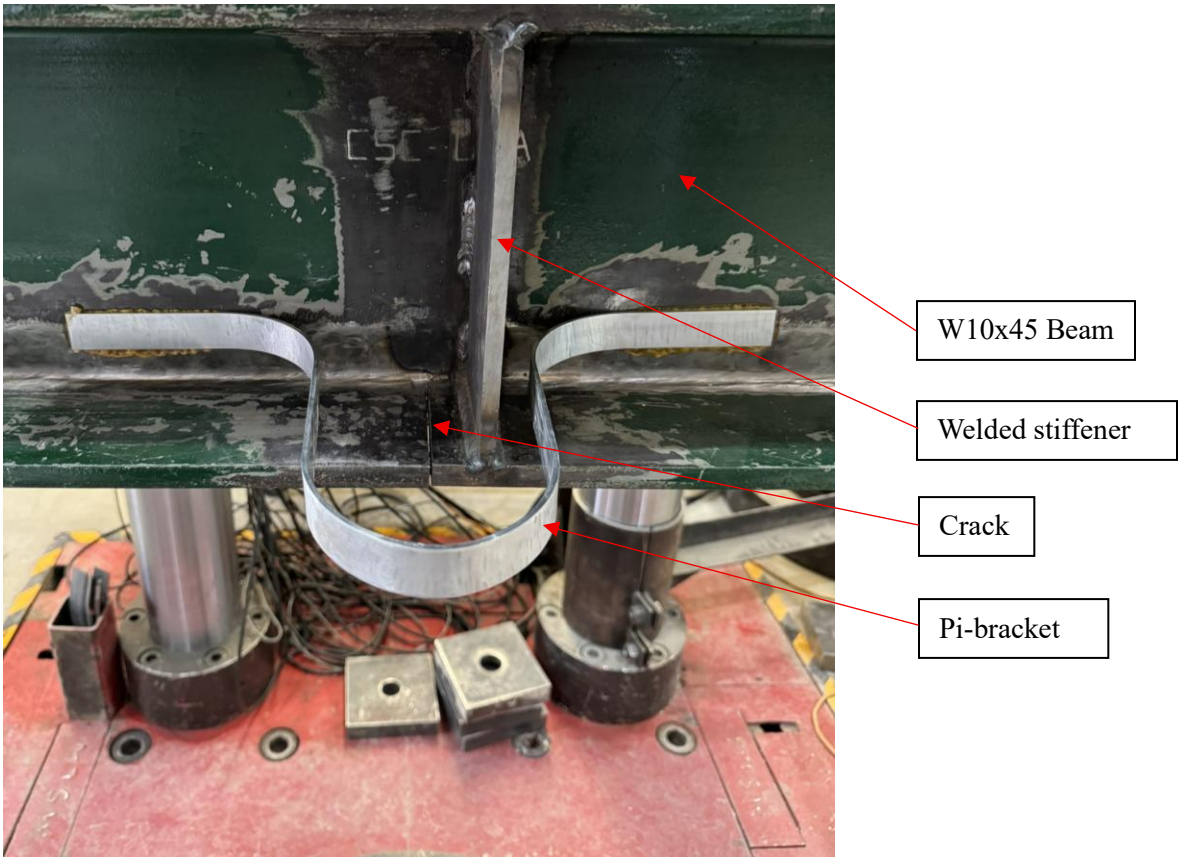

Figure 5.8: Pi-bracket location

The pi-bracket was then installed 25 mm above the upper edge of the bottom flange, with its central axis aligned precisely with the crack location. This placement was selected to facilitate efficient sensor routing and to maximize sensitivity to crack-induced strain fields, as depicted in Figure 5.8.

Installation of the FOS involved splicing extension cables to the sensor, with all splicing locations carefully protected to prevent damage. The sensor was affixed to the pi-bracket and to both sides of the beam using Araldite 2021-1 adhesive. On the front face of the beam, the SMARTape II strain sensor was routed over the simulated crack using the pi-bracket as a guide, which also acted as a protective harness. Figure 5.9 illustrates the complete experimental setup, showing the front face of the beam.

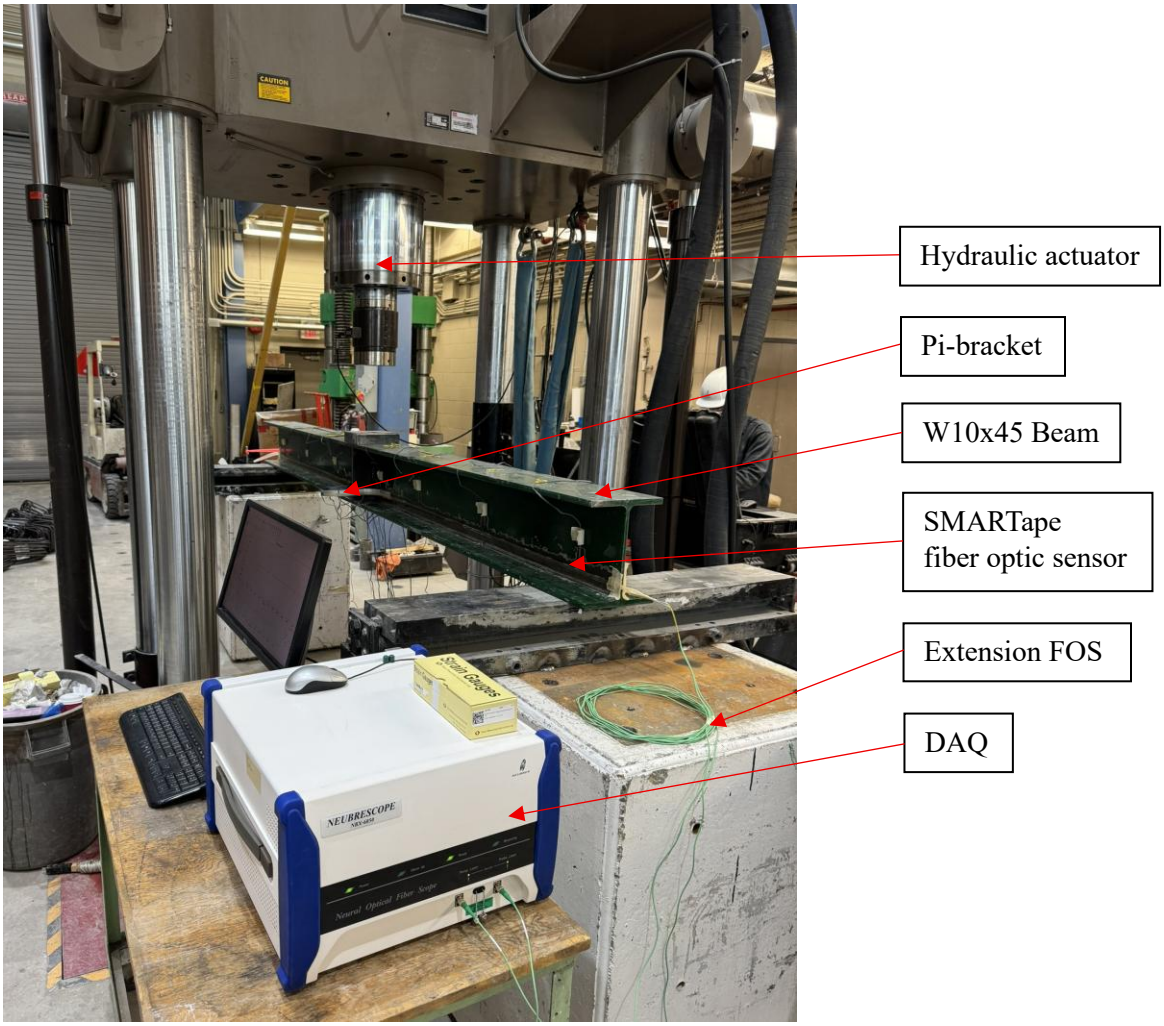

Figure 5.9: Experimental setup showing the front face of the beam

As illustrated in Figure 5.10, the sensor on the rear face was directly bonded to the beam surface across the crack region. Fiber continuity was ensured by routing the fiber from the front to the rear

face at one end of the beam. During bonding, paper tape was used to hold the FOS in place and was removed after the adhesive had fully cured.

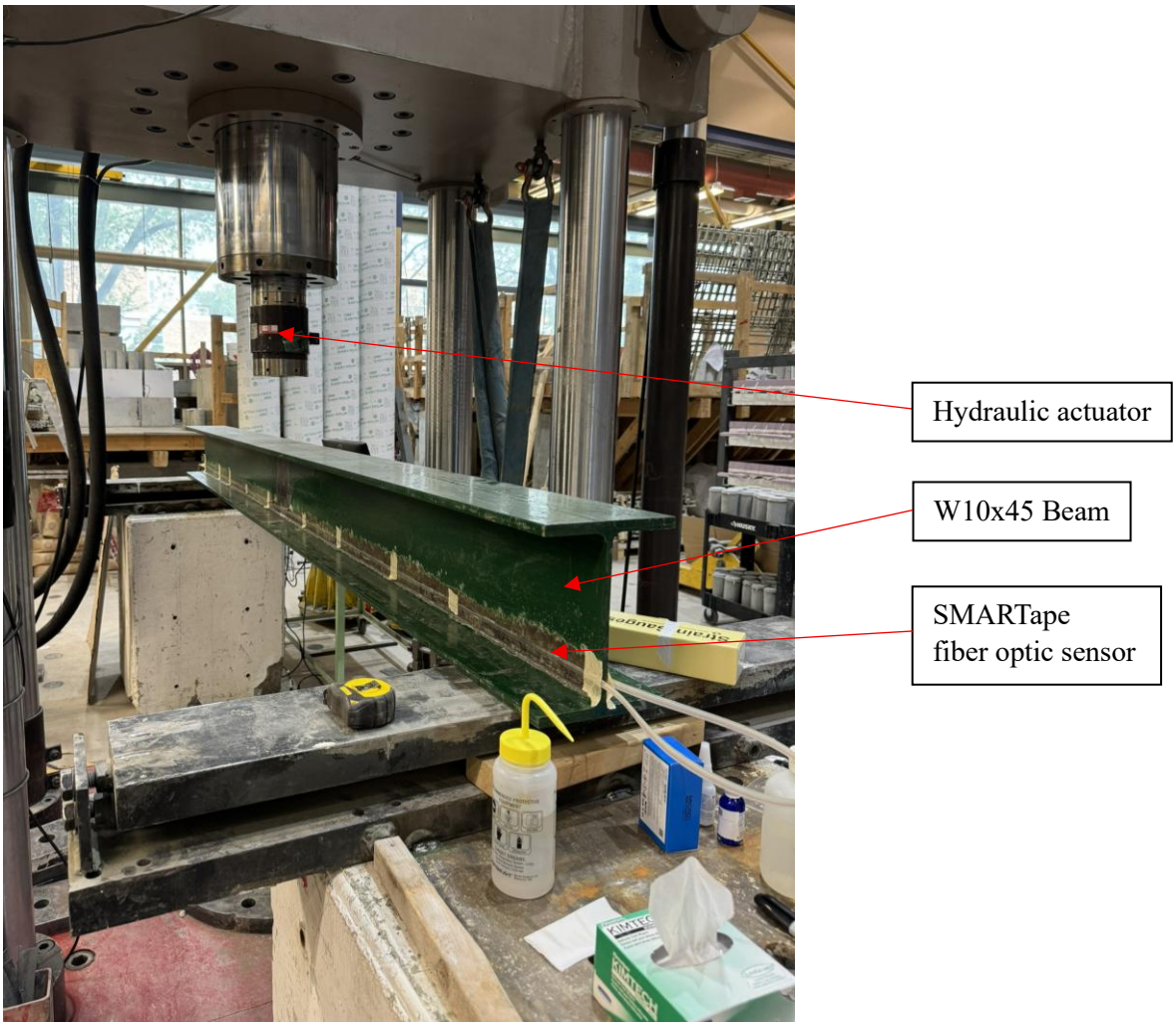

Figure 5.10: Experimental setup showing the rear face of the beam

The termini of the SMARTape sensor were fusion-spliced to extension fiber optic cables and connected to a DAQ system, enabling real-time monitoring and data collection throughout the experiment. Various configurations of the Neubrescope NBX-6050 DAQ system were tested prior to the experiment to identify optimal parameters. The final configuration utilized a 5 cm sampling interval and a 10 cm spatial resolution, leveraging BOTDA technology to achieve high-resolution strain distribution measurements along the fiber. For data acquisition, the FOS was connected to the Neubrescope NBX-6050 unit, as illustrated in. In addition, the pi-gauge and load actuator were

connected to a National Instruments DAQ readout unit, enabling synchronized measurement of mechanical loading and strain responses.

Prior to installation, the PI-5-200 (Tokyo Sokki Kenkyujo) pi-gauge underwent a thorough calibration to ensure accurate crack width measurements. This process involved incrementally adjusting the micrometer on a digital gauge calibrator to predetermined displacements while recording the corresponding pi-gauge readings. By establishing a direct relationship between the pi-gauge output and the actual crack opening, this procedure enabled reliable conversion of sensor readings into precise physical displacement values. The pi-gauge offers a resolution of 0.001 mm and maintains an accuracy within ±1% of the measured value, providing highly reliable monitoring of even the smallest changes in crack width during testing (Tokyo Sokki Kenkyujo 2024). After calibration, the pi-gauge was centered over the induced crack and positioned directly above the DFOS, allowing for direct correlation between measured crack width and strain readings obtained from the fiber optic sensor. Figure 5.11 shows a close-up of the pi-gauge and FOS position on the rear face of the beam.

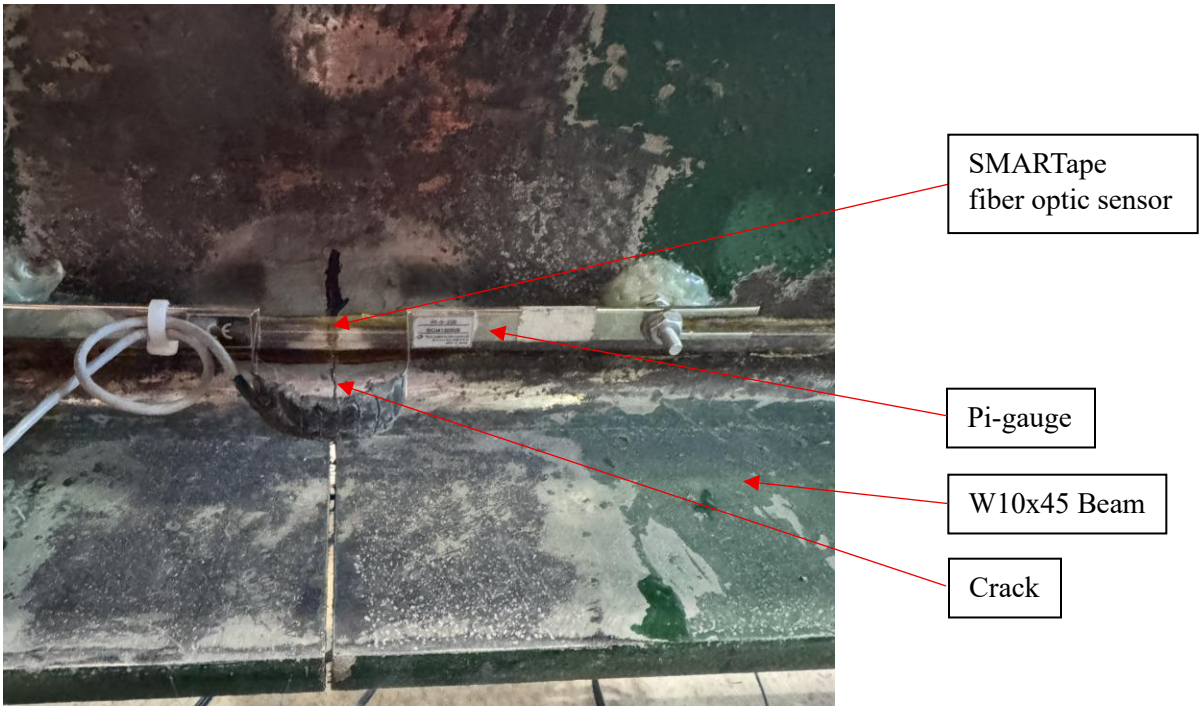

Figure 5.11: Detail of the pi-gauge and SMARTape position relative to crack

In the context of steel bridges, critical fatigue cracks are typically considered to be those with widths in the range of 0.1 mm to 0.3 mm, as cracks within this interval are generally regarded as significant for early intervention and maintenance (FHWA 2012). According to the manufacturer's specifications, the DiTest SMARTape II fiber optic sensor can detect cracks as small as 0.2 mm, and it was anticipated that the proposed pi-bracket system would achieve comparable performance. It is important to note that the objective of this study is to evaluate the ability of the pi-bracket sensor system to accurately detect and monitor the presence of cracks, rather than to quantify their exact widths. The primary goal is to determine whether the system can reliably detect the initiation of a crack and thereby enable immediate intervention by an inspector for further evaluation. This approach supports proactive maintenance and timely intervention, which are critical for ensuring the safety and longevity of bridge infrastructure (Mufti et al. 2018).

This instrumentation process, encompassing precise sensor placement, robust bonding procedures, and reliable data acquisition, ensured the accuracy and repeatability of experimental measurements throughout the study.

5.3.4. Neubrescope NBX-6050 Settings

The DAQ system configuration for FOS is a pivotal aspect of the experimental setup, as it directly influences the accuracy and reliability of the measurements obtained from the FOS integrated with the pi-bracket. Based on the findings from Chapter 3, the optimal settings for the laboratory experiment were determined to be the 5-10 configuration.

The DAQ reading unit was configured to following settings:

Distance Range:	50m
Sampling Interval:	5cm
Spatial Resolution:	10cm
Averaging Count:	2^15 (32768)
Frequency Range Start:	10.700 GHz
Frequency Range Stop:	11.400 GHz

Step:	5 MHz
Span - Count:	141
Puls Adjustment:	On
Auto Frequency Adjustment:	On
Measurement Mode:	Progressive

5.3.5. FOS Calibration

Accurate calibration of the FOS is critical to ensure precise strain measurements and reliable monitoring of crack development in the steel beam specimen. This section details the calibration methodology employed to localize the sensor along the beam and pi-bracket, enabling effective correlation between experimental data and structural features for subsequent analysis.

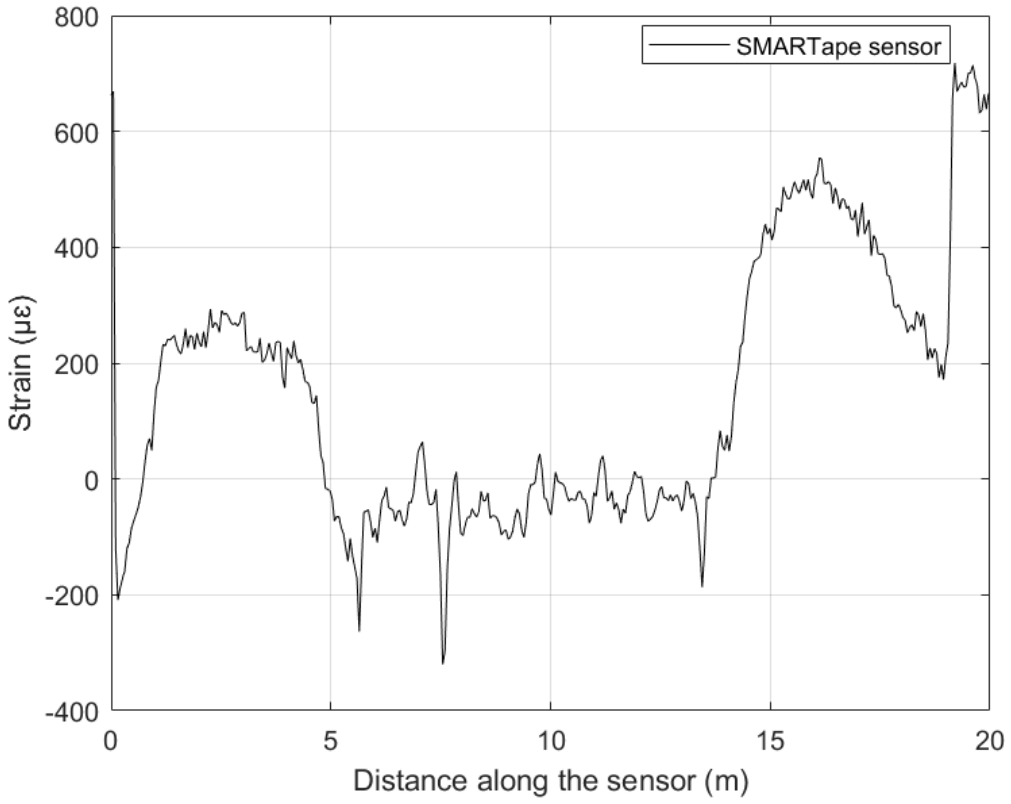

Figure 5.12: Initial calibration measurement of the fiber optic sensor

Initial strain measurements did not clearly reveal the locations of the beam and pi-bracket along the fiber optic sensor, as shown in Figure 5.12. To resolve this, a heat gun was used as a localization tool to accurately identify key positions along the FOS. The calibration procedure involved heating one end of the beam with the heat gun and recording the resulting strain response as shown in Figure 5.13.

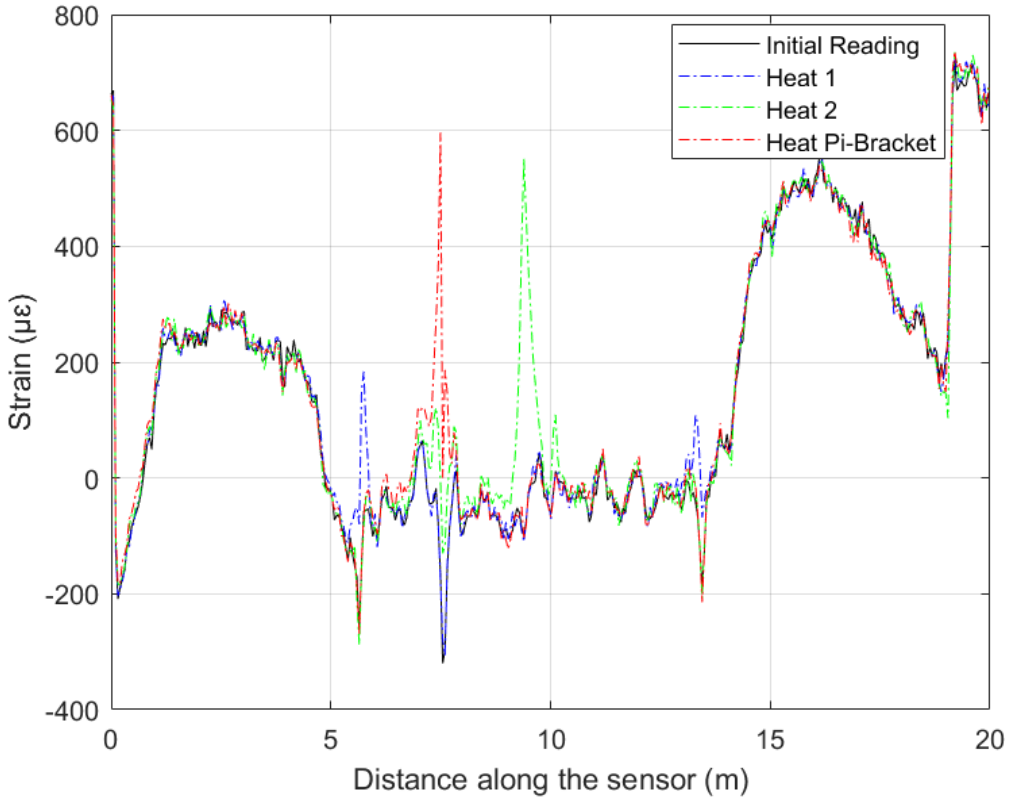

Figure 5.13: Thermal localization of fiber optic sensor

This process was then repeated for the opposite end of the beam and for the crown of the pi-bracket. By subtracting the initial, unheated strain reading from the measurement obtained during heating, the thermal response could be isolated. Utilizing thermal localization enabled identification of the positions of both the beam and the pi-bracket along the sensor strain profile. This methodology is essential for establishing an accurate spatial reference, thereby facilitating meaningful comparison between experimental measurements and FEA predictions.

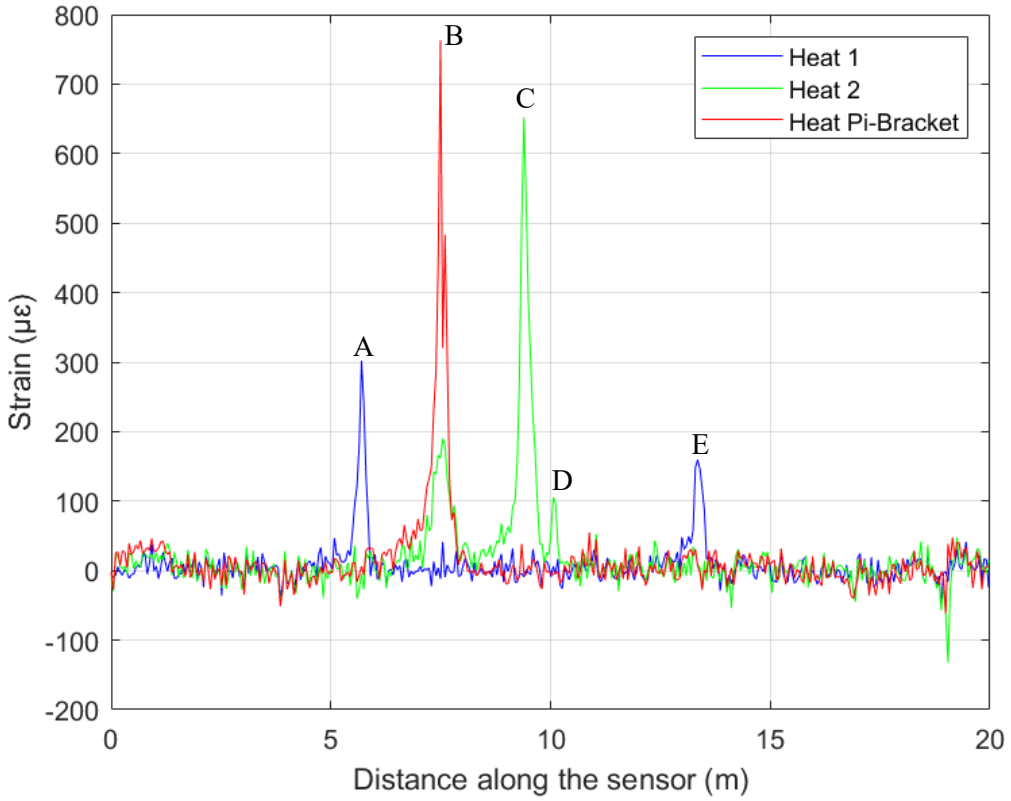

Figure 5.14: Thermal localization of fiber optic sensor after initial strain subtracted

The experimental setup utilized a single, continuous SMARTape sensor, routed from the front to the back of the beam at one end. This configuration enabled simultaneous strain measurements on both sides of the beam, facilitating comprehensive monitoring of the specimen. The thermal localization technique allowed for the identification of distinct sensor segments, as depicted in Figure 5.14. Points A through E in this figure identify significant locations along the sensor. Specifically, Sensor S1 corresponded to the portion attached to the front of the beam, spanning from 5.7 meters (A) to 9.4 meters (C) along the sensor length, with the pi-bracket located at 7.55 meters (B). Sensor S2 referred to the segment affixed to the rear of the beam, extending from 10.1 meters (D) to 13.3 meters (E), with the crack opening situated at 11.75 meters. This approach enabled precise mapping of the sensor positions relative to key structural features, ensuring accurate interpretation of subsequent strain measurements during crack propagation testing.

Figure 5.15 presents a comprehensive schematic diagram of the entire FOS setup, illustrating the spatial relationships between the SMARTape II sensor and the pi-bracket. Following the completion of sensor installation and system integration, the beam was fully prepared for testing.

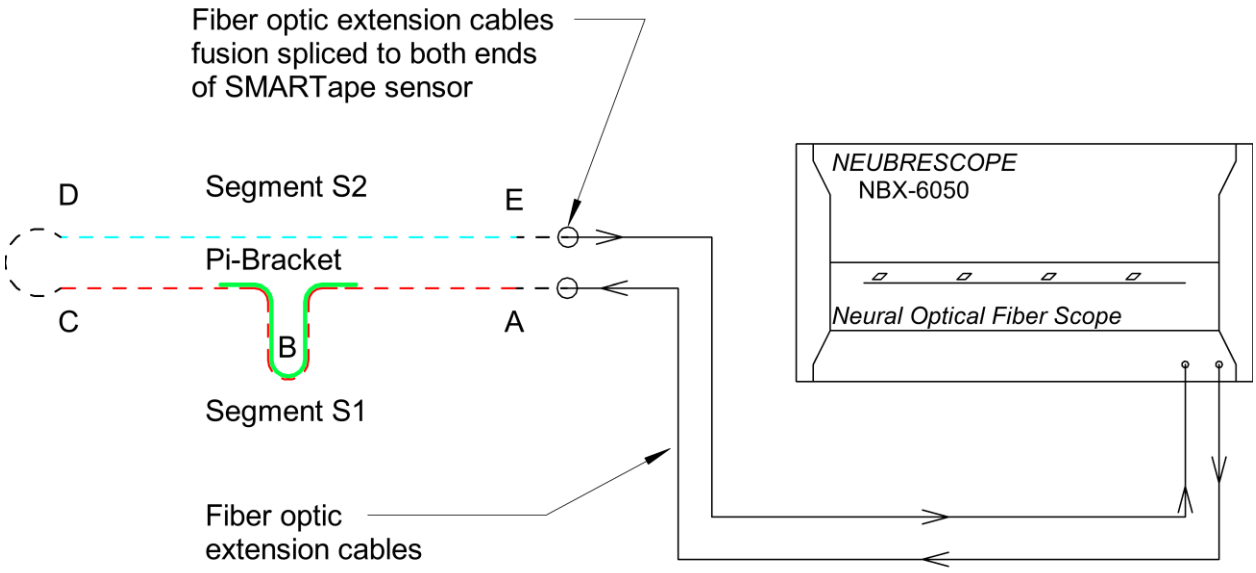

Figure 5.15: Schematic diagram of fiber optic sensor setup

5.4. EXPERIMENTAL PROCEDURE

The experimental procedure was designed to systematically evaluate the performance of the FOS integrated with the pi-bracket in detecting and monitoring crack propagation. To ensure repeatability and statistical significance, the entire experiment was repeated four times. Prior to each repetition, a comprehensive system recalibration was performed, and both the strain measurements and initial crack opening were artificially reset to zero. This approach guaranteed consistent baseline conditions for each experimental run.

The initial setup involved connecting the beam assembly, including the pi-bracket with the attached FOS and the pi-gauge, to the data acquisition readout unit. The Neubrescope NBX-6050 was configured following the parameters outlined in section 5.3.4, and the FOS was calibrated as described in section 5.3.5. Once the system was prepared, loading and measurement protocols were executed using an MTS 311.51 hydraulic actuator capable of applying loads up to 5450 kN

at the beam's midspan. The actuator facilitated controlled crack widening at a rate of 0.1 mm every 30 seconds.

Strain measurements were recorded for crack openings ranging from 0 mm to 0.2 mm, with increments of 0.1 mm, matching the crack widths simulated in the FEA. Throughout the loading process, the crack opening width was continuously monitored and quantified using the pi-gauge, which was connected to a National Instruments DAQ readout unit equipped with LabVIEW software. Data were collected at a sampling rate of one reading per second to ensure detailed temporal resolution.

For each target crack width increment, a baseline strain reading was first taken before applying any static load. The actuator was then paused once the desired crack opening was reached, as monitored by the pi-gauge. At this stage, the actual load applied, and the corresponding beam displacement were recorded (as detailed in Table 5.1). Subsequently, single strain profiles from the FOS were collected using the Neubrescope NBX-6050. During this period, precise crack opening measurements continued to be recorded over approximately 30 seconds, maintaining the one reading per second sampling rate.

This procedure ensured the collection of consistent and reliable data, enabling a comprehensive comparison between experimental results and FEA simulations. The alignment of experimental parameters with the numerical model validates the pi-bracket and FOS system's capability for early crack detection and monitoring.

5.5. RESULTS AND ANALYSIS

5.5.1. FEA Results

FEA conducted using Abaqus provided an assessment of the strain behavior exhibited by the pi-bracket sensor system under simulated crack conditions. By replicating the experimental configuration within a computational environment, the analysis enabled an investigation of strain patterns along the length of the beam. The FEA model assumed an idealized bond between the pi-bracket and the beam.

Initially, the strain distribution originating from the beam with the crack, but without the presence of the pi-bracket was examined, as illustrated in Figures 5.16 and 5.17 for the 0.1 mm and 0.2 mm crack conditions, respectively. For reference and comparison, the magenta line represents the theoretical strain profile expected for an uncracked beam subjected to identical loading conditions.

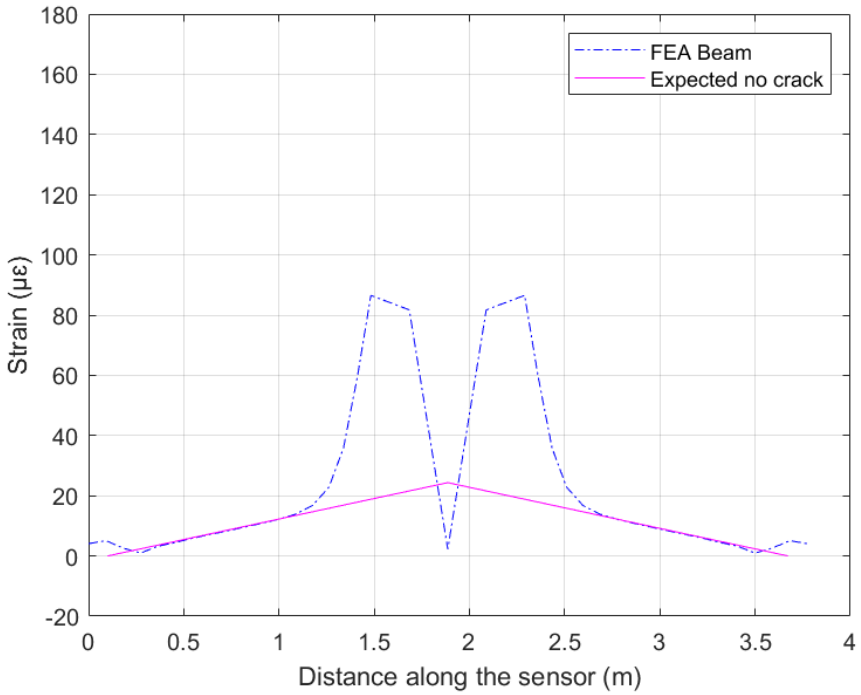

Figure 5.16: Strain profile for “FEA Beam” scenario (0.1mm crack)

The strain in a cracked beam is higher than in an uncracked beam under the same load primarily because the presence of cracks reduces the effective stiffness and load-carrying capacity of the beam section. When the beam is cracked, the tensile forces that were previously carried uniformly are now redistributed, causing localized increases in strain near the cracks. This is due to the cracked section behaving less rigidly, resulting in a greater deformation (strain) under the same applied load.

However, at the location of the crack, the strain drops to zero because the crack creates a physical discontinuity where the material can no longer transfer tensile force. The crack opens, breaking the continuity of the strain field so the surfaces on either side of the crack move relative to each other rather than deforming uniformly. While strain values increase in regions adjacent to the crack

due to load redistribution and stiffness reduction, the crack plane exhibits zero tensile strain, effectively behaving as an open gap under tension.

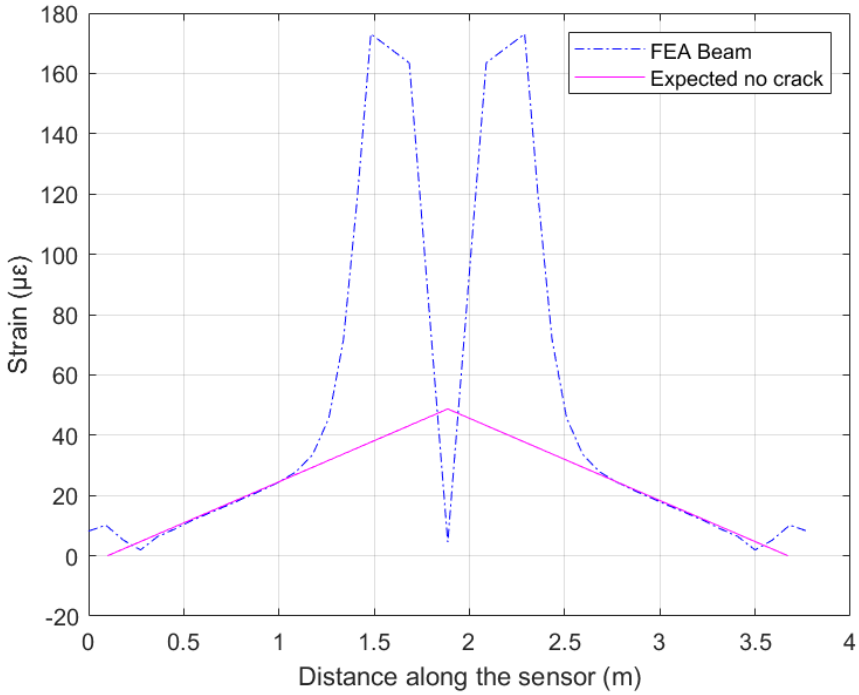

Figure 5.17: Strain profile for "FEA Beam" scenario (0.2mm crack)

The study focused on two distinct strain scenarios. The first scenario, derived from the initial condition of the beam with the crack but without the presence of the pi-bracket, is designated as "FEA Beam" This scenario reflects typical conditions in current SHM practices, where a continuous FOS is left unattached to the girder near stiffeners, creating a gap of about 10 centimeters on each side. As shown in Figures 5.18 and 5.19 for the 0.1 mm and 0.2 mm crack conditions respectively, this gap does not correspond to the direct distance along the beam itself. Instead, it represents the length along the sensor, which must pass over the stiffener, resulting in a longer sensor path compared to the straight beam length.

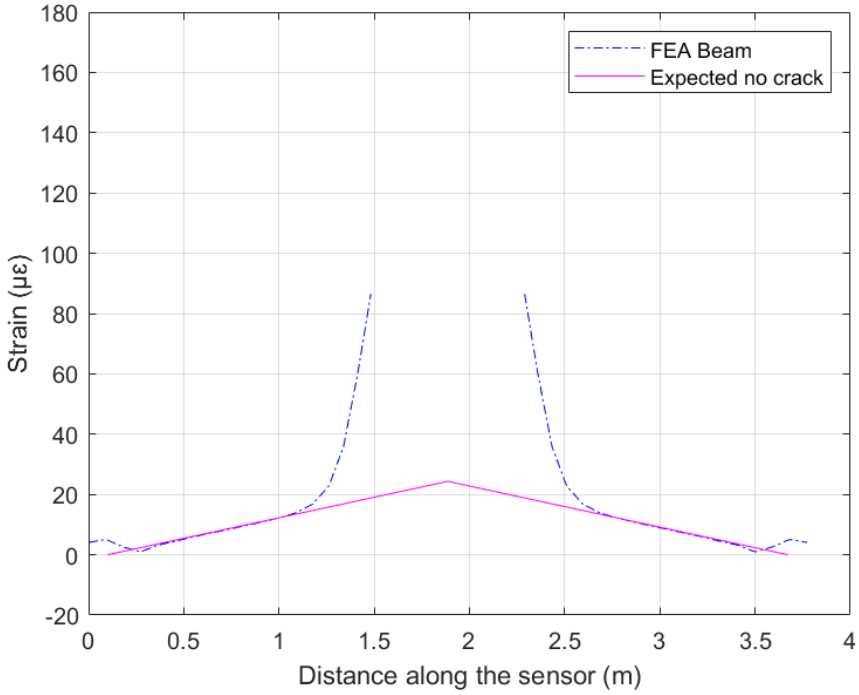

Figure 5.18: Strain profile for “FEA Beam” scenario (0.1mm crack)

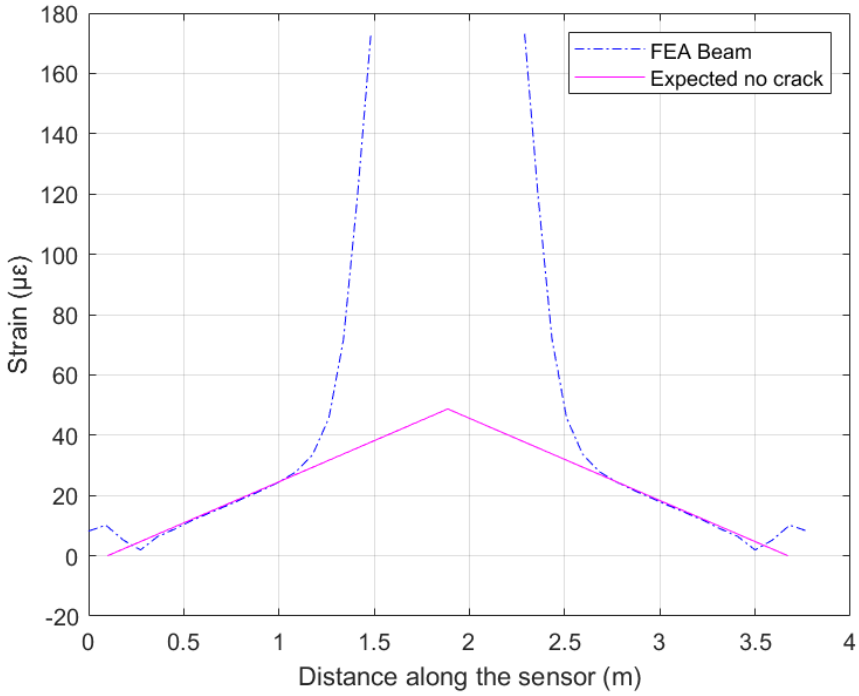

Figure 5.19: Strain profile for “FEA Beam” scenario (0.2mm crack)

This arrangement is generally due to practical limitations, such as the sensor's minimum bending radius and challenges associated with installation around stiffeners. This strain profile thus served as a baseline, illustrating the strain distribution in the absence of the pi-bracket and highlighting the challenges associated with monitoring in this critical region.

The second scenario, designated as "FEA Beam + Pi-bracket," incorporated the pi-bracket into the model. In this case, the strain was plotted continuously along the entire sensor path, which includes both the beam and the pi-bracket as it passes over the stiffener. The inclusion of the pi-bracket enables an uninterrupted sensor path by overcoming the installation challenges posed by the stiffener, thereby bridging the gap present in the baseline scenario and ensuring continuous strain monitoring across this critical region. This allowed for a direct comparison with the baseline scenario and demonstrated the bracket's effectiveness in bridging the previously undetectable region near stiffeners. The strain results for the 0.1 mm and 0.2 mm crack conditions are shown in Figures 5.20 and 5.21, respectively.

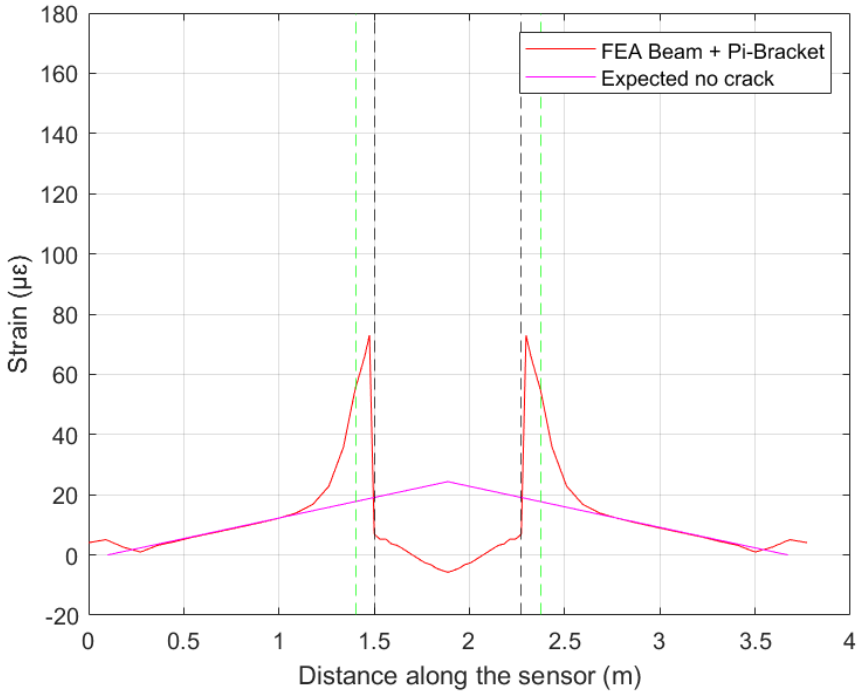

Figure 5.20: Simulated strain profile for "FEA Beam+Pi-Bracket" scenario (0.1mm crack)

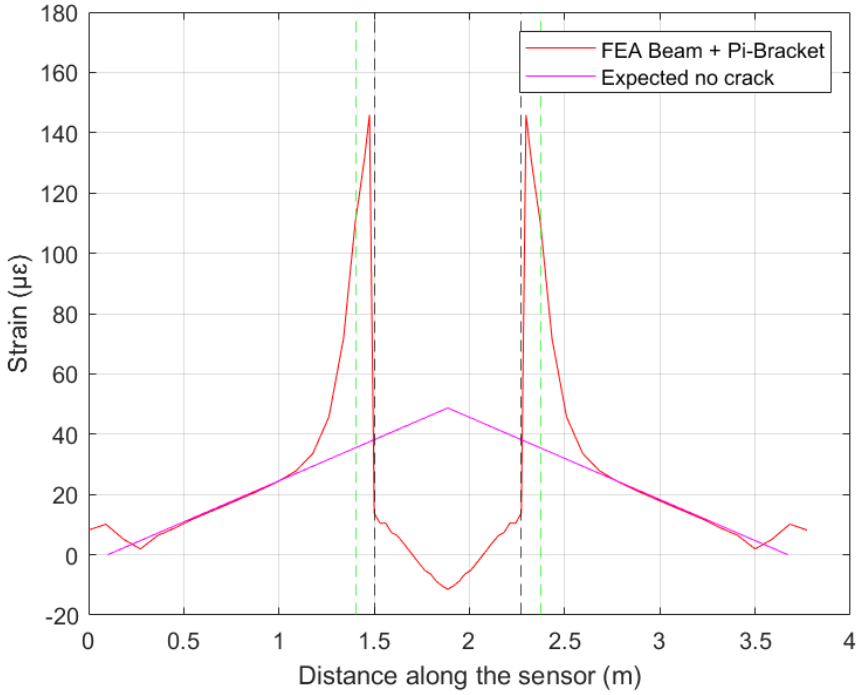

Figure 5.21: Simulated strain profile for “FEA Beam+Pi-Bracket” scenario (0.2mm crack)

In these figures, green dashed vertical lines identify the position of the pi-bracket along the strain profile, providing spatial reference points for interpreting the sensor configuration, while black dashed vertical lines separate the attached and unattached portions of the pi-bracket to the beam. This distinction is important for interpreting the strain distribution, as the attached and unattached regions of the pi-bracket exhibit different mechanical behaviors due to their interaction with the beam. Please see Figure 5.7, highlighting the attached and unattached portions of the pi-bracket to the beam.

Figures 5.22 and 5.23 present a comparative analysis of the two strain scenarios “Beam” and “Beam + Pi-bracket” under crack conditions of 0.1 mm and 0.2 mm, respectively. To ensure the computational results matched the experimental FOS results, the strain profiles obtained from the FEA were averaged between two points along the defined sensor path, emulating the averaging performed by the DAQ system during the physical tests.

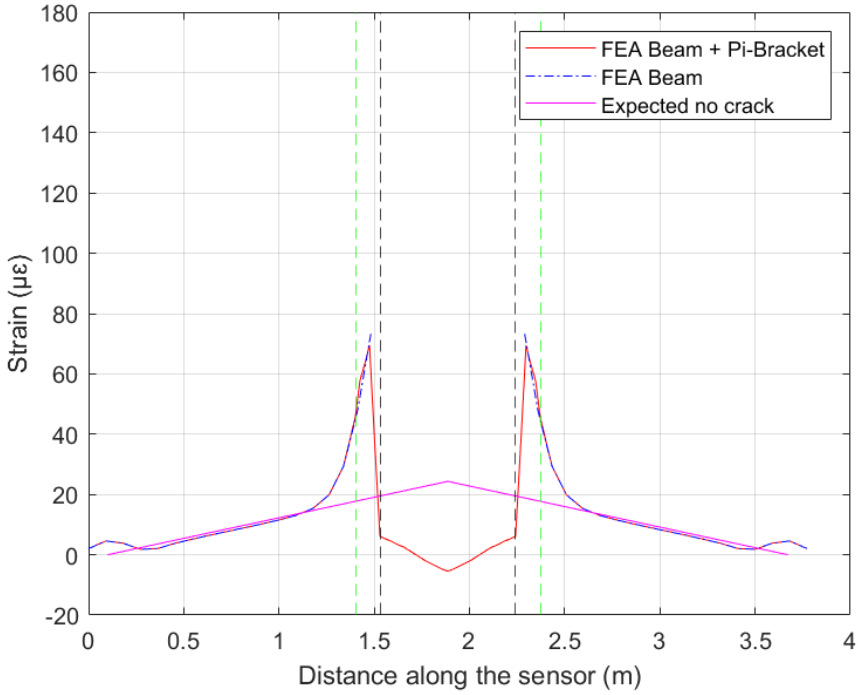

Figure 5.22: Strain comparison of Beam with and without Pi-Bracket (0.1mm crack)

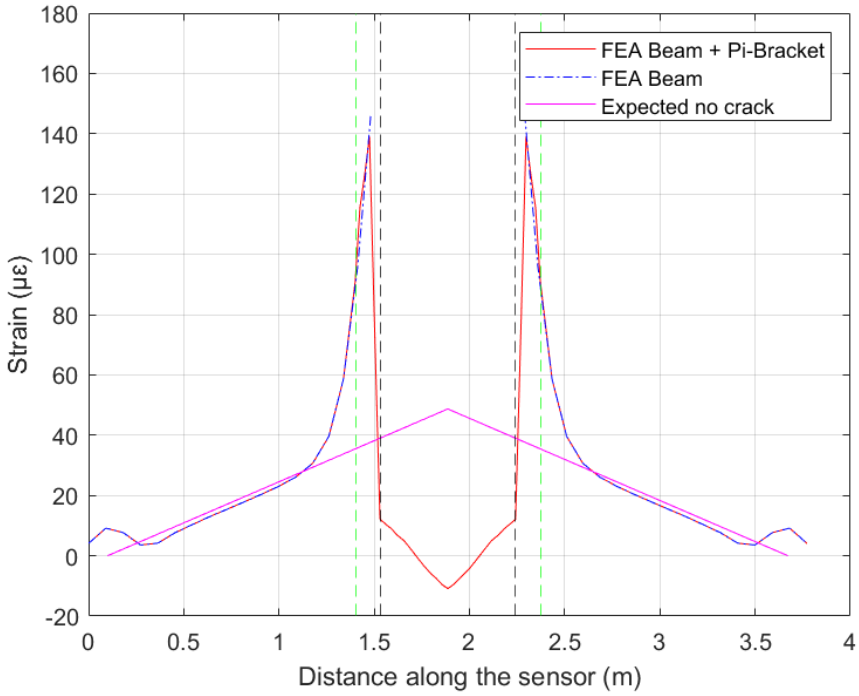

Figure 5.23: Strain comparison of Beam with and without Pi-Bracket (0.2mm crack)

These FEA-predicted strain profiles will be compared to the experimental strain measurements obtained from the FOS to assess the accuracy of the FEA model and the effectiveness of the pi-bracket sensor system.

5.5.2. Experiment Results

The experimental phase of this study yielded comprehensive strain data captured by the SMARTape DFOS system, that can be used to evaluate the effectiveness of the pi-bracket sensor configuration under controlled crack propagation conditions.

Figure 5.24 presents the averaged raw strain profiles obtained from multiple measurements, illustrating the sensor's response to incremental crack opening widths of 0.1mm, and 0.2mm. In this figure, the baseline strain, representing the condition without a crack, is also shown, enabling direct comparison of the sensor's response before and after crack formation.

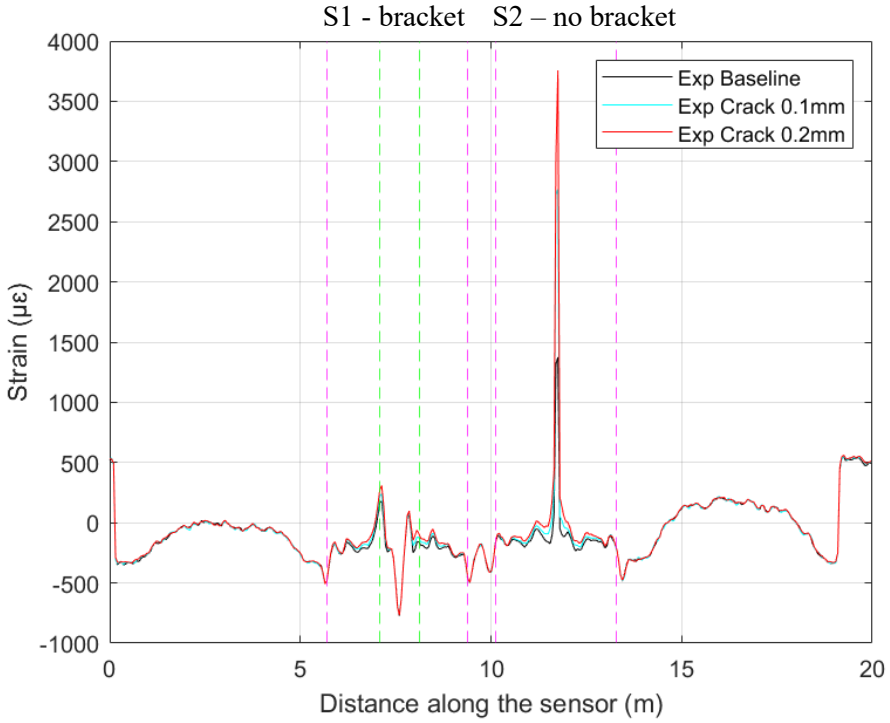

Figure 5.24: SMARTape averaged strain profiles

These profiles demonstrate the system's ability to detect and quantify strain changes associated with crack formation and propagation. Magenta dashed vertical lines delineate the locations of sensor segments S1 and S2, whereas green dashed vertical lines denote the position of the pi-bracket along the sensor path.

In actual use the strain will always be compared to the strain prior to a crack forming. This is simulated in the Figure 5.25, which presents the change in strain relative to baseline resulting from crack widening, as measured by the SMARTape sensor system. These strain change profiles, corresponding to crack openings of 0.1mm and 0.2mm, were derived by subtracting the baseline strain profile (i.e., the strain profile for condition with no applied load) from the strain profiles obtained at each crack opening.

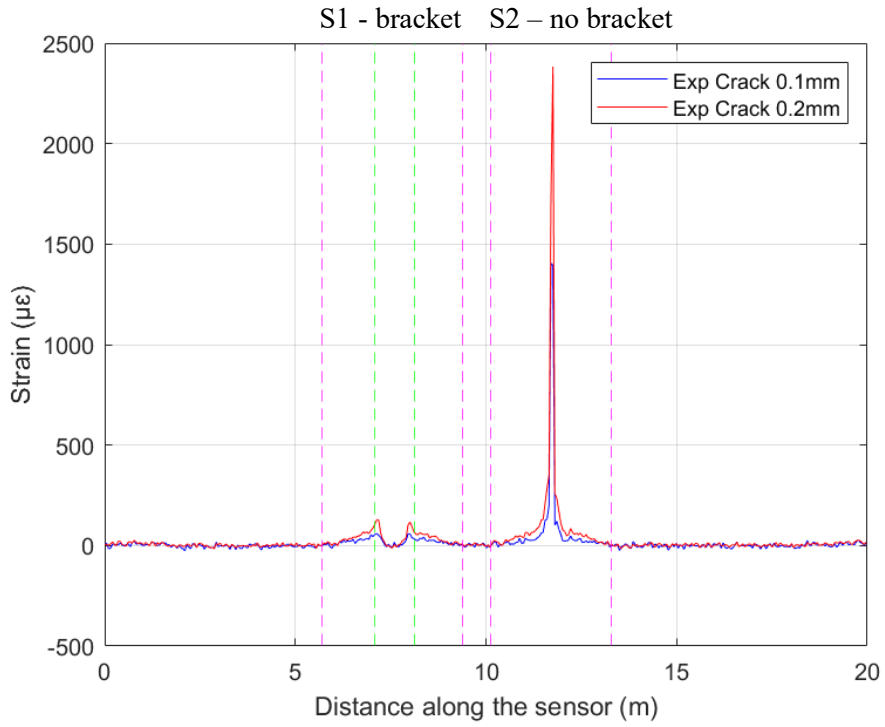

Figure 5.25: SMARTape change in strain profiles relative to baseline

This approach isolates the strain response resulting specifically from crack widening, eliminating any residual or pre-existing strains within the FOS. Analysis of the resulting data reveals a distinct contrast in strain magnitudes between the two sensor sections. Specifically, the maximum strain change observed within sensor section S1, which is positioned over the pi-bracket, reached 129.1

με. In contrast, sensor section S2, which is directly bonded across the crack, exhibited a substantially higher maximum strain change of 2382.1 με. This significant difference in strain values indicates a substantial strain concentration at the crack location, as detected by the directly bonded sensor segment (S2). This magnitude of strain change would be easily detectable even in the presence of environmentally induced changes.

Figure 5.26 presents a detailed analysis of the change in strain profiles for section S1, which includes the pi-bracket at the center, specifically showing the data obtained for crack openings of 0.1mm and 0.2mm. Despite the presence of some residual noise in the data, the overall trends in the strain profiles clearly demonstrate the sensor's ability to capture strain changes induced by the crack opening, even when these changes are mediated by the presence of the pi-bracket. The presence of the pi-bracket does not stop the coupling of the strain information to the sensor, allowing for crack detection even in locations away from the immediate vicinity of the crack.

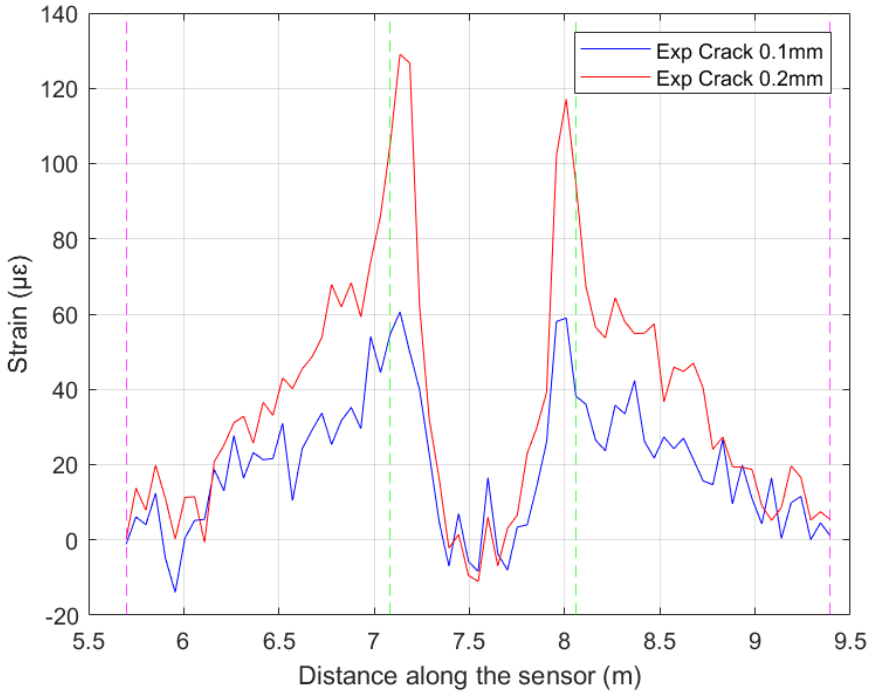

Figure 5.26: Strain profiles in the vicinity of the Pi-bracket (section S1)

Figure 5.27 focuses on the section S2 change in strain profiles for crack openings of 0.1mm and 0.2mm. In this configuration, the FOS is directly attached to the beam over the crack, allowing for

a direct measurement of the localized strain in that region. As expected, the strain values are significantly higher compared to section S1, where the strain is distributed through the pi-bracket. Specifically, for a crack opening of 0.2mm, the local strain around the crack reaches 2382.1 με, indicating a substantial strain concentration in the immediate vicinity of the crack. This direct measurement highlights the sensitivity of the FOS when directly bonded to the structure and provides a valuable reference point for evaluating the performance of the pi-bracket in section S1. It is important to note that while the strain for the 0.2mm crack opening in section S2 reaches 2382.1 με, the corresponding strain recorded by sensor S1 is only 129.1 με. Although significantly lower in magnitude, this distributed strain is readily detectable by the SMARTape system. Even in the presence of the pi-bracket, sufficient strain is coupled to the FOS sensor for crack detection.

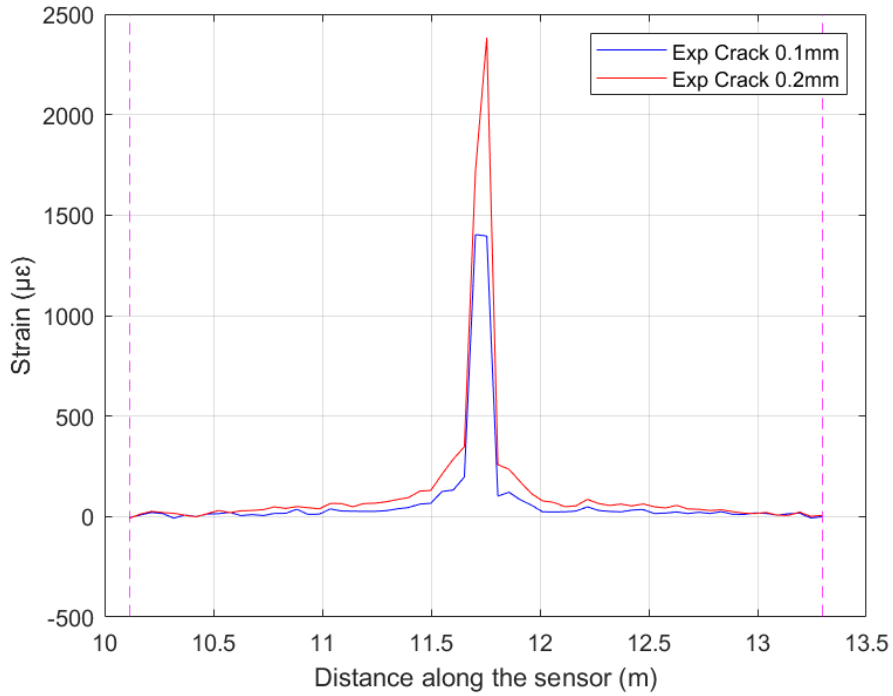

Figure 5.27: Strain profiles for section S2 without Pi-bracket

The presence of noise in the strain measurements can be attributed to several contributing factors, including environmental vibrations, temperature fluctuations, etc. Analysis of the results from sensor section S1 elucidated the influence of the pi-bracket on strain distribution, revealing notable differences compared to the strain data collected from sensor section S2, where the fiber optic

sensor was directly bonded over the crack. This comparative assessment underscores the pi-bracket's significant role in modulating and redistributing strain along the sensor path, suggesting that its inclusion may improve the system's capability to detect cracks in structurally complex regions, such as areas adjacent to stiffeners.

5.5.3. Comparison of Experiment and FEA Results

This section presents a comparative analysis of the experimental results obtained from the laboratory experiment and the corresponding FEA simulations. The primary objective of this comparison is to evaluate the efficacy of the pi-bracket sensor system for crack detection in the vicinity of stiffeners. The analysis focuses on strain measurements at key locations within the system, specifically the pi-bracket itself and the region directly over the crack near stiffener.

Figures 5.28 and 5.29 present a visual comparison of the overall strain profiles obtained from the laboratory experiment and the FEA simulation for crack openings of 0.1mm and 0.2mm, respectively.

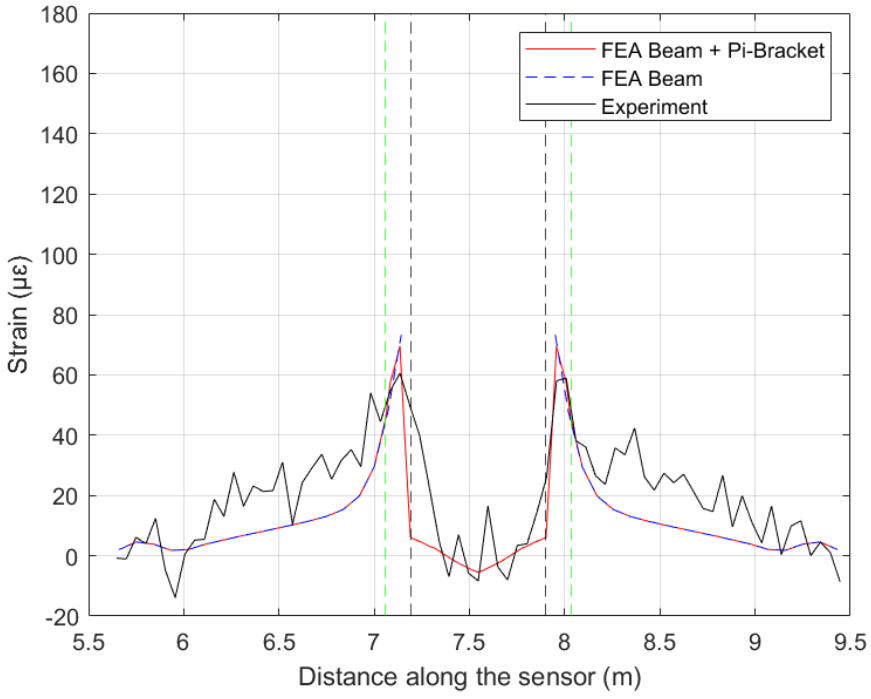

Figure 5.28: Comparison of experimental and FEA strain profiles for 0.1mm crack

Green dashed vertical lines indicate the position of the pi-bracket along the strain profile, providing clear spatial markers to facilitate interpretation of the sensor arrangement. Black dashed vertical lines demarcate the transitions between the attached and unattached regions of the pi-bracket on the beam. This consistent identification scheme aligns with that used in previous figures for clarity and continuity.

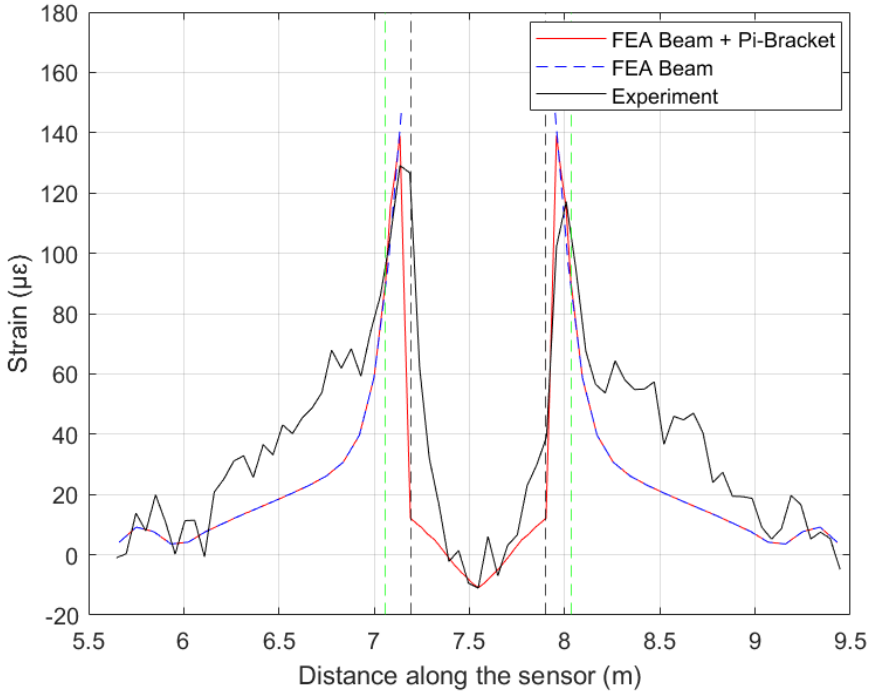

Figure 5.29: Comparison of experimental and FEA strain profiles for 0.2mm crack

Figures 5.30 and 5.31 present a detailed view of the longitudinal strain profiles specifically within the pi-bracket region for crack openings of 0.1 mm and 0.2 mm, respectively. These figures facilitate a focused analysis of strain distribution within this critical sensing area, highlighting the localized strain behavior of the pi-bracket under varying crack conditions.

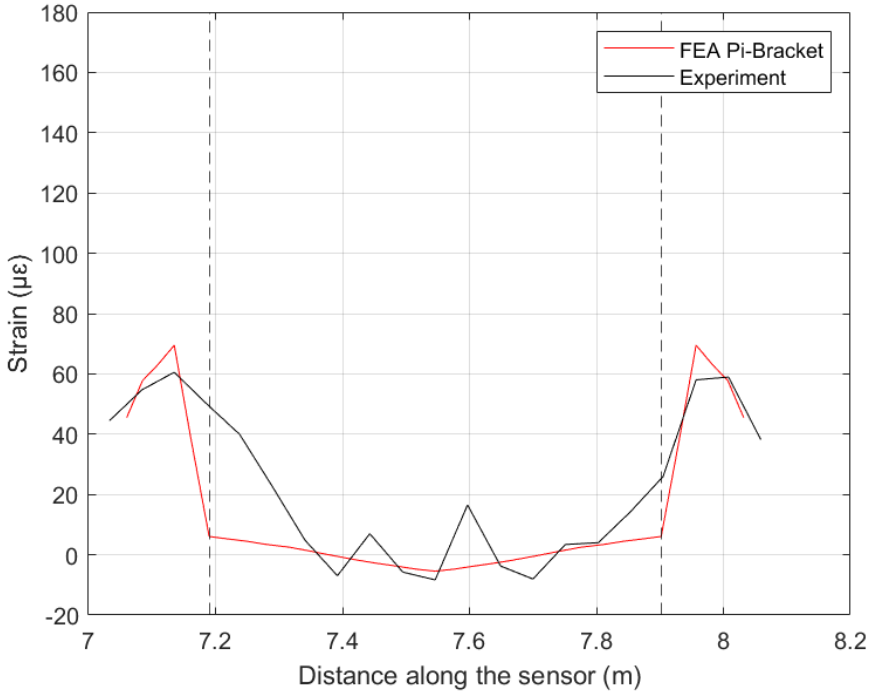

Figure 5.30: Experiment vs FEA Pi-bracket strain comparison for 0.1mm crack

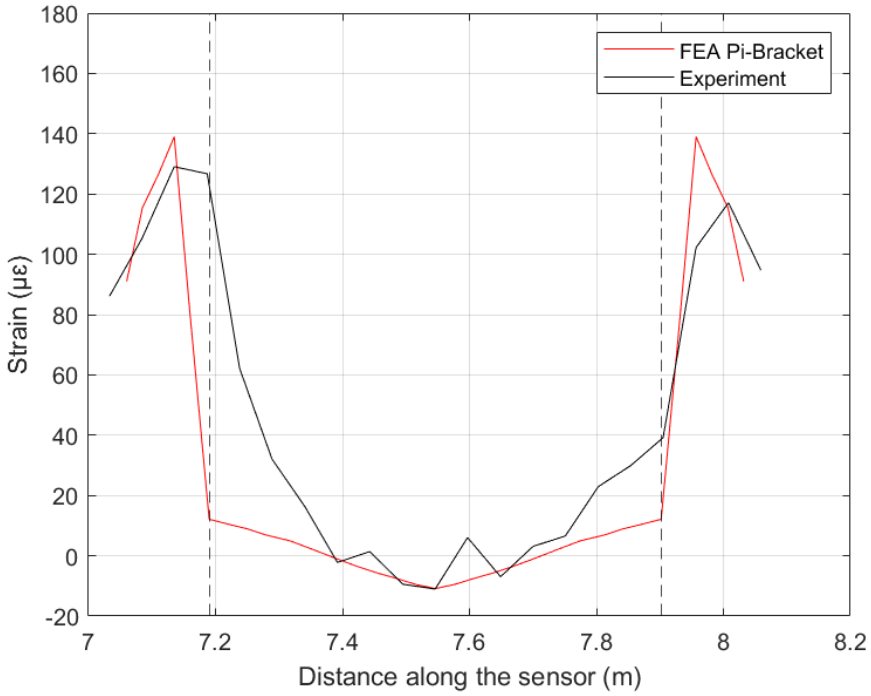

Figure 5.31: Experiment vs FEA Pi-bracket strain comparison for 0.2mm crack

Table 5.1: Experiment and FEA results

Laboratory Experiment						FEA Simulation		
Crack width [mm]	Load [kN]	Beam displacement [mm]	Strain S2 max. [με]	Strain S1 Pi-bracket Crown [με]	Strain S1 max. [με]	Strain Pi-bracket Crown [με]	Strain Pi-bracket max. [με]	Strain Beam no bracket max. [με]
0.1	15.9	-1.26	1402.9	-8.3	60.6	-5.4	69.5	73.3
0.2	31.9	-2.38	2383.1	-11.04	129.1	-10.9	139.0	146.6

The FEA simulations predicted a maximum strain of 69.5 με for a crack opening of 0.1 mm, while the corresponding experimental measurement yielded a maximum strain of 60.6 με. This amounts to a discrepancy of 12.8% between the simulation and experimental results. For a 0.2 mm crack opening, the FEA simulations predicted a maximum strain of 139.0 με in the pi-bracket at the location of direct contact with the beam for a 0.2mm crack opening. Experimentally, the maximum strain recorded by sensor section S1, distributed over the pi-bracket, was 129.1 με for a similar crack opening (Table 5.1). This represents 7% discrepancy between the FEA prediction and the experimental measurement. Reasons for this discrepancy can be attributed to various factors discussed in Section 5.6.1.

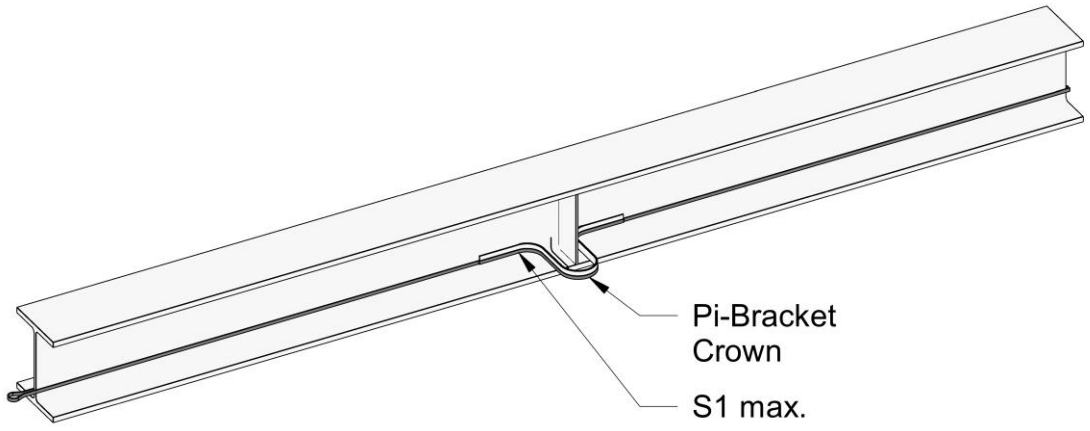

Figure 5.32: Measurement locations of maximum strain values as presented in Table 5.1

For better understanding and visual clarity, Figure 5.32 identifies the exact locations of the points where these maximum strain values were measured, with the corresponding values tabulated in Table 5.1. The colors used in Table 5.1 further assist the reader in comparing the FEA and experimental results effectively. This level of agreement suggests that the numerical model can adequately predict the strain behavior of the pi-bracket under the applied loading conditions. However, it also highlights the presence of real-world factors not fully captured by the simulation, which is discussed further below.

Furthermore, the FEA model predicted a maximum strain of -10.9 με at the pi-bracket crown for a 0.2mm crack opening. Experimentally, the SMARTape sensor section S1 measured a strain of -11.04 με at the crown of the pi-bracket, demonstrating close agreement with the FEA result. While the magnitudes of both the simulated and experimental strains at the pi-bracket crown were small in comparison to the strains observed when the SMARTape was directly attached over the crack (2383.1 με), the SMARTape, when attached to the parts of the pi-bracket bonded to the beam, successfully detected the crack. The observed strains reached 129.1 με compared to FEA simulations of 139.0 με, representing the aforementioned 7% discrepancy.

The experimental strain measurements on the pi-bracket generally show strong agreement with the FEA predictions across different crack opening sizes. For a crack opening of 0.1 mm, the measured maximum strain was 60.6 με, representing a 12.8% difference compared to the FEA value of 69.5 με. At a crack opening of 0.2 mm, the experimental strain of 129 με was about 7% lower than the FEA's 139 με. These similarities affirm the FEA model’s ability to reliably simulate the strain behavior of the pi-bracket under various crack widths, reinforcing its utility for predictive structural health monitoring.

Strain measurements further demonstrate that strain concentrates at the location of the crack, with section S2 (directly above the crack) showing significantly higher strain than section S1 (over the pi-bracket). Nevertheless, the pi-bracket sensor system remains capable of crack detection, as confirmed by the adequately high strain value of 129 με observed in S1. These findings underscore the pi-bracket’s effectiveness in capturing and transferring strain from a crack to the sensing system, even in challenging locations such as near a stiffener, while also protecting the sensor from mechanical damage.

The observed discrepancy in strain measurements for both 0.1mm and 0.2mm wide crack on the pi-bracket (FOS at the pi-bracket location) between FEA and experimental results can be attributed to several factors. The FEA simulation employed idealized model, representing simplifications of real-world conditions. The experiment, conversely, inherently accounts for real condition which may be subjected to different kinds of error, including DAQ error, human error, sensor error, etc. Furthermore, the FEA simulations were performed using a student version of Abaqus, which limited the mesh density to a maximum of 1000 nodes. This mesh limitation may have constrained the accuracy of the FEA results, particularly in critical areas around the crack tip and pi-bracket.

Despite these discrepancies, the overall agreement between the FEA and experimental results supports the effectiveness of the pi-bracket sensor system for crack detection in bridge girders. The observed discrepancy indicates that the experiment is well captured by the simulation as expected. Future research should focus on refining the FEA model with more accurate material properties, boundary conditions, and a higher-resolution mesh (if the software limitations are addressed) to further improve the correlation between simulation and experimental results. Furthermore, investigating the sensitivity of the system to varying environmental conditions and validating its performance under dynamic loading scenarios would provide a more comprehensive understanding of its capabilities and limitations. This would enhance the potential for real-world implementation in SHM applications.

5.6. DISCUSSION

This study introduced and evaluated a novel pi-bracket sensor system designed to address the challenges of crack detection in bridge girders, particularly in the proximity of stiffeners where conventional monitoring methods face limitations. The experimental and numerical results presented herein demonstrate the potential of this system for enhancing SHM capabilities in critical infrastructure. It is important to reiterate that this study's primary objective was not to investigate the complex fracture mechanics or crack interaction phenomena within the instrumented beams. Rather, the focus was to evaluate the capability of the pi-bracket sensor system to detect the presence of cracks in their early stages, thereby facilitating preventative measures against potential structural failures in bridge infrastructure.

5.6.1. Discrepancies Between Experiment and FEA Results

Discrepancies between FEA models and experimental results arise from a combination of factors related to modeling approaches, material characteristics, experimental practices, and environmental influences. FEA models are generally based on idealized assumptions, material properties such as elastic modulus and Poisson's ratio are often treated as constants, and boundary conditions are simplified as perfectly fixed or pinned. These idealizations fail to capture the local variability in material behavior, residual stresses from processes like welding, and the actual flexibility or slight movements in supports found in physical experiments. As a result, the simulated responses may diverge from observed behavior (Bathe 2016; Dassault Systèmes 2013).

In practice, materials such as structural steel or aluminum exhibit inherent variability in their mechanical and thermal properties due to manufacturing variations and environmental exposure. Since FEA models typically use averaged nominal properties, they cannot fully represent this real-world variability, introducing further differences in predicted stresses and strains (Bartlett and Dexter 2001). Experimental uncertainties such as sensor calibration errors, installation quality, noise in measurement signals, and repeatability limitations also influence the data collected during tests. For example, strain gauges are sensitive to temperature fluctuations and the quality of adhesive bonding, while fiber optic sensors may suffer from signal attenuation or noise contamination (American Society of Civil Engineers 2017; Bao and Chen 2012).

Moreover, real experimental load applications may have minor eccentricities or uneven force distributions that do not align perfectly with the idealized, uniformly distributed loads applied in FEA models. Experimental support conditions may also exhibit compliance or slight movements instead of the rigid constraints assumed in the numerical model, which affects the local structural responses (Cook et al. 2001).

Environmental factors such as temperature and humidity variations can significantly affect both sensor readings and material behavior, yet these effects are often not included in numerical models. For example, thermal expansion mismatches between aluminum components and steel girders can notably influence strain measurements (ASM International 1990; Svendsen et al. 2022).

Geometric imperfections and residual stresses present in fabricated specimens, such as hand-made or welded parts like pi-brackets, further compound discrepancies. These stress concentrations and

irregularities are typically not modeled in FEA, which assumes perfect geometry and initial stress-free states (ASM International 1990).

Finally, numerical factors, including the choice of element types, mesh density, and solver algorithms, impact FEA accuracy. Limitations on mesh refinement, particularly in academic or simplified software environments, may reduce resolution in critical zones such as stress concentrations, leading to less precise strain predictions (Bathe, 2016; Dassault Systèmes 2013).

Together, these factors from modeling idealizations, material property variability, experimental uncertainties, loading and support differences, environmental effects, geometric imperfections, and numerical modeling limitations collectively explain why FEA results can differ from experimental observations. Understanding and addressing these discrepancies is essential for validating FEA models and improving their reliability in structural analysis and health monitoring applications.

5.6.2. Advantages of the Pi-bracket Sensor System

The pi-bracket sensor system offers significant improvements over traditional SHM methods, particularly in areas near stiffeners that are typically challenging to assess. By strategically positioning the pi-bracket adjacent to these critical regions, the system enhances the accuracy of crack detection where conventional sensors often fail due to bending limitations and installation difficulties.

Furthermore, the pi-bracket functions as a mechanical protective harness for the continuous FOS, safeguarding it from potential damage. This design facilitates uninterrupted and direct strain measurement along the full length of the girder, including critical zones near stiffeners, thereby eliminating the need to leave sensor segments unattached.

In addition to these practical benefits, the use of BOTDA technology streamlines the data acquisition process and supports the effective validation of computational models. The strong correlation between experimental measurements and FEA predictions attests to the reliability of the system, highlighting its promise as a tool for proactive and efficient bridge maintenance strategies.

5.6.3. Applicability, Limitations, and Capabilities

The results demonstrate the potential of the pi-bracket sensor system field applications in bridges. Recognizing the limitations of existing inspection protocols (Raeisi et al. 2018, Ettouney and Alampalli 2012), which primarily rely on periodic manual assessments, this system is proposed as a continuous, real-time monitoring solution. This approach would enable the immediate detection of cracks and the generation of automated alerts, thereby facilitating the timely deployment of bridge inspectors for detailed visual examinations and the initiation of necessary repair measures. Regarding the spatial resolution and differentiation of closely spaced cracks, the current system is designed to detect strain changes indicative of crack formation within the influence zone of the pi-bracket. This system is intended to detect the presence of cracks. Although it may not distinguish whether a single crack or multiple close cracks have formed in the bridge girder, it enables prompt action by signaling the need for an inspector to visually assess the affected area. This limitation highlights a valuable direction for future research.

Adapting the system is recommended for both new bridge construction and retrofitting existing structures to enable targeted monitoring of high-risk areas near vertical stiffeners. Its localized measurement capability allows targeted deployment in areas prone to cracking, while the pi-bracket itself provides a protective harness for the FOS.

It should be emphasized, however, that the author does not recommend the use of this system for monitoring existing cracks. Given the higher cost of FOS compared to conventional methods such as strain gauges, it is not cost-effective for short-term monitoring where the sensor would be installed, then removed during crack repair, and replaced afterward. Instead, this system is best suited for long-term, continuous monitoring, where the FOS is permanently attached to the surface of the girder. This makes it particularly advantageous for bridges that are approaching or have exceeded their intended service life, especially in cases where service life of the structure is being maximized, perhaps beyond it designed service life. Furthermore, the system is well-suited for deployment immediately following crack repair, to monitor the repaired region and prevent recurrence.

While the pi-bracket sensor system demonstrates clear advantages for crack detection and structural health monitoring, several limitations must be considered. One significant limitation is the complexity of installation. Unlike traditional methods, installing the pi-bracket requires precise

alignment and secure bonding to the girder, which can increase the time and expertise needed for successful deployment. This complexity may present challenges, particularly in field applications or when scaling up to larger structures.

Environmental factors also pose a critical limitation. Variations in temperature and moisture levels can influence sensor readings, potentially leading to inaccurate assessments if not properly compensated for. Developing robust strategies to mitigate these environmental effects is essential to ensure reliable system performance under real-world conditions (Svendsen et al. 2022).

The initial cost of the pi-bracket sensor system is another important consideration. Although the upfront investment is generally higher than that of conventional visual inspection techniques, the long-term benefits, such as continuous monitoring and early crack detection, may offset these initial expenses by reducing maintenance costs and improving structural safety. This proactive approach helps extend the service life of bridges by preventing severe damage and delaying costly retrofits or replacements. Additionally, continuous monitoring reduces the need for frequent manual inspections, lowering maintenance costs and minimizing traffic disruptions. The protective design of the pi-bracket also improves sensor longevity, reducing replacement frequency.

A particularly critical limitation lies in the scope of experimental validation. In this study, the primary purpose of the laboratory experiment was to validate the FEA model. The results showed good agreement between the experimental data and the FEA simulations, supporting the accuracy of the model. This successful validation suggests that further studies, including those based solely on simulations, can be used to explore more realistic scenarios and a broader range of conditions. However, it is important to note that the current validation was limited to a single beam under controlled laboratory settings. To fully assess the system's performance and durability, additional testing on larger structures and under actual environmental conditions is warranted.

Despite certain limitations, the pi-bracket system brings a range of strengths that significantly enhance crack detection in bridge structures. One of its key advantages is its ability to deliver accurate and reliable crack detection, even in complex areas near stiffeners where traditional methods may struggle. In addition to identifying the presence of cracks, the system provides quantitative strain measurements, offering valuable data to assess crack severity and predict how cracks may propagate over time.

Another important benefit is the capability for remote monitoring. By enabling continuous oversight of bridge health without the need for frequent manual inspections, the system can reduce both operational costs and the time required for maintenance activities. The pi-bracket system also integrates effectively with FEA models, allowing for a more comprehensive evaluation of structural integrity and supporting the development of predictive maintenance strategies.

Furthermore, the robust, protective design of the pi-bracket contributes to FOS durability. This increased durability extends the operational lifespan of the monitoring system and minimizes the frequency of sensor replacements, which is particularly advantageous for long-term infrastructure management. Collectively, these capabilities position the pi-bracket system as a valuable tool for advancing the effectiveness and efficiency of bridge crack detection and SHM.

To address the challenges of fatigue loading and load variations in real-world bridge environments, future implementations of this system could leverage frequent data acquisition (e.g., every 5 minutes). By subtracting consecutive strain measurements, the system might isolate strain changes primarily attributable to crack formation, potentially minimizing the influence of dynamic bridge response or environmental factors. However, the effectiveness of this differential approach in accurately isolating crack-related strain changes, particularly in the presence of complex loading scenarios, requires further investigation and validation through both numerical simulations and experimental studies. The influence of temperature and appropriate averaging time should be investigated to obtain the best results.

5.7. CONCLUSIONS

The findings presented in this chapter highlight the promising performance of the pi-bracket sensor system for detecting cracks near stiffeners in bridge girders. The system demonstrated reliable detection capabilities for crack openings as small as 0.2 mm. Notably, a strain of 129 με was recorded by the FOS distributed over the pi-bracket at this crack width, underscoring the system's sensitivity even when the sensor is not directly bonded to the cracked area.

A comparative analysis between FEA and laboratory experiments revealed discrepancies of 12.8% and 7% for the maximum strain values at crack openings of 0.1 mm and 0.2 mm, respectively. Specifically, for the 0.1 mm crack, FEA predicted a maximum strain of 69.5 με, while the

experimental measurement was 60.6 με. For the 0.2 mm crack, FEA predicted a maximum strain of 139 με, compared to an experimentally measured strain of 129 με. These results collectively validate the FEA model, demonstrating strong agreement between simulated and observed strain values across different crack widths. This validation supports the use of FEA modeling to simulate more complex situations that may be difficult to reproduce in laboratory settings, thereby extending the applicability of the modeling approach for further research and design optimization.

The pi-bracket configuration also effectively addresses the challenges associated with monitoring areas near vertical stiffeners, which are traditionally difficult to access. It enables continuous strain measurement along the length of the beam without interruption, while also protecting the FOS from mechanical damage.

Furthermore, the integration of BOTDA technology facilitated reliable, distributed strain measurements along the beam. This integration ensures comprehensive structural assessment and enhances the efficiency of data acquisition.

To fully leverage the resolution capabilities of the pi-bracket sensor system, it is essential that the spatial resolution of the FOS is significantly smaller than the dimension of the pi-bracket itself. This requirement ensures precise localization of strain changes and maximizes the effectiveness of crack detection.

Overall, these results confirm that the pi-bracket sensor system is a practical and effective solution for structural health monitoring in bridge girders, particularly in critical regions near stiffeners that are prone to fatigue cracking. The successful validation of the FEA model further enables the use of advanced simulations to explore a wider range of structural scenarios and optimize sensor deployment strategies.

CHAPTER 6: FEA-BASED SIMULATION OF CRACK DETECTION IN A MEDIUM SPAN BRIDGE GIRDER

6.1. INTRODUCTION

This chapter presents a comparative analysis of girder strain profiles obtained from FEA simulations using Abaqus, focusing on the performance of the pi-bracket sensor system in detecting strain variations induced by cracks under simulated loading conditions. The primary objective is to isolate and quantify the strain variations attributable solely to crack formation.

In the laboratory experiment (Chapter 5), the baseline condition corresponded to the state with no load applied. Upon applying the load, the strain profile measured under this unloaded baseline was subtracted from the strain profiles corresponding to crack openings of 0.1 mm and 0.2 mm.

For the current FEA analysis, the strain profile of the cracked girder under loading conditions that produce crack openings of 0.1 mm and 0.2 mm is compared to the strain profile of an uncracked girder subjected to the same loading. The strain profile of the uncracked girder serves as the baseline and is subtracted from that of the cracked girder, effectively isolating the strain specifically attributable to crack formation. This method removes the influence of other loads, such as temperature, allowing for a clear identification of strain changes caused by the crack.

The study examines two loading conditions resulting in crack openings of 0.1 mm and 0.2 mm, representing early-stage and more advanced crack scenarios, respectively. By isolating crack-induced strain variations through the subtraction method described above, this chapter evaluates how cracks alter strain distribution along the girder length and assesses how the pi-bracket sensor system would perform in detecting these changes under simulated conditions.

Unlike the laboratory experiments conducted in Chapter 5, which involved a 3.2 m-long beam, the girder modeled in this simulation is significantly larger, with an overall length of 29.3 m and supports spaced at 28.8 m. This larger-scale model allows for a more realistic evaluation of the pi-bracket system's capabilities when applied to full-scale bridge girders.

The findings presented in this chapter build upon those discussed in Chapter 5, which validated the effectiveness of the pi-bracket sensor system for detecting localized strain changes near

stiffeners. While Chapter 5 dealt with laboratory experiments and comparisons with FEA predictions for localized crack detection, this chapter employs the strain subtraction methodology to systematically isolate and quantify crack-induced strain variations, focusing on how cracks impact the performance of the pi-bracket system under simulated conditions on a significantly larger girder model.

To ensure accuracy and reliability, both uncracked and cracked FEA models are validated through theoretical calculations. The findings offer additional perspectives that may guide future improvements in the design and practical implementation of the pi-bracket sensor system for structural health monitoring.

6.2. METHODOLOGY

This section describes the methodology used to evaluate the strain profiles of cracked and uncracked girders through FEA simulations conducted in Abaqus. The primary aim of these simulations was to isolate strain variations resulting exclusively from crack formation and to assess the ability of the pi-bracket sensor system to detect these changes. Building on modeling principles established in earlier chapters, a similar approach was adopted, with modifications to accommodate a substantially larger girder length of 29.3 meters, compared to the 3.2-meter beam used previously, thereby simulating full-scale bridge conditions.

Two distinct FEA models were created, both subjected to the applied loads: one representing an uncracked girder and the other incorporating cracks with opening widths of 0.1 mm and 0.2 mm. Each model included the steel girder, the aluminum pi-bracket, and the steel stiffener, all modeled as deformable planar shell elements.

The methodology involved several critical steps. First, both cracked and uncracked girder models were subjected to identical displacement-controlled loading conditions designed to produce crack openings of 0.1 mm and 0.2 mm. Next, strain profiles were extracted from each model under these applied loads. The strain profile of the uncracked girder serves as the baseline and is subtracted from that of the cracked girder under the same loading conditions. This subtraction isolated the strain variations exclusively attributable to crack formation by removing the effects of normal loading, including other loads such as dead load.

This approach differentiates strains induced by crack presence from those caused by the applied forces alone, allowing a clear identification of crack-specific strain changes. The isolated strain magnitudes were analyzed to determine whether they fall within the detection capabilities of the pi-bracket sensor system.

Theoretical calculations will be performed as part of this study to validate both uncracked and cracked FEA models, ensuring consistency with established mechanics principles for structural analysis.

6.2.1. Girder and Pi-bracket Geometry

For this simulation, a full-scale single-span steel girder from a bridge in Manitoba was modeled in Abaqus. The geometry, including critical components such as the pi-bracket, crack, and stiffener, was derived from real-world dimensions to ensure accurate representation of structural behavior. Key geometric features of the girder are illustrated in Figure 6.1 and Figure 6.2.

Two conditions were modeled: one with a crack and one without. Both models were similar, with the sole exception that the cracked girder model incorporated the crack. To avoid redundancy, only the cracked model's full configuration is shown, as the uncracked model is visually similar apart from the absence of the crack.

This geometry served as the foundation for both the uncracked and cracked FEA models, ensuring consistency in subsequent analyses of strain distribution and sensor system performance.

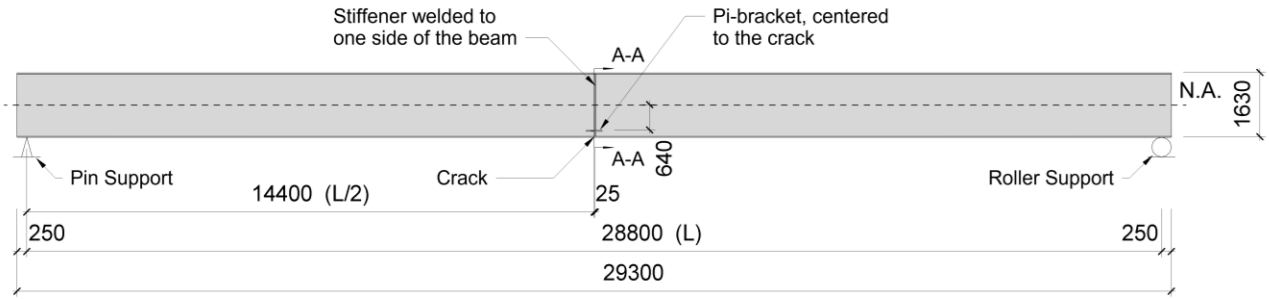

Figure 6.1: Girder – front elevation

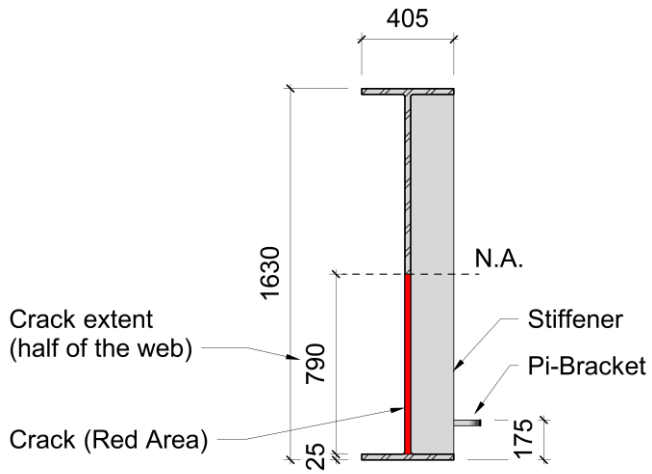

Figure 6.2: Girder – section A-A

Given the significant increase in girder dimensions from the 3.2m laboratory experiments (Chapter 5) to this full-scale simulation, the pi-bracket was designed as a 12" component to ensure adequate fit over the stiffener. The detailed geometry of the pi-bracket is presented in Figure 6.3.

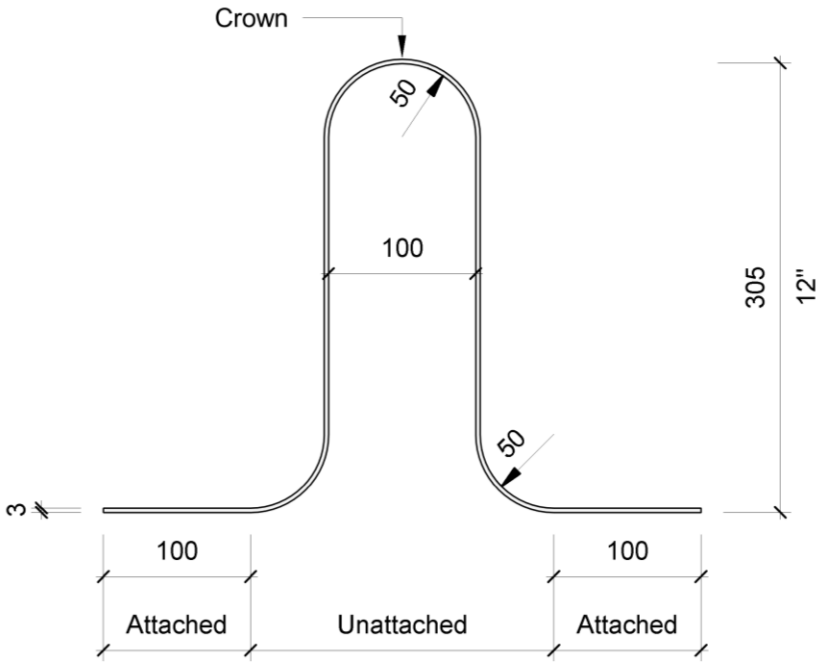

Figure 6.3: 12” Pi-bracket

Figure 6.3 also clearly indicates the areas of the pi-bracket that are attached and unattached to the girder, distinguishing between regions in contact and those not in contact with the girder. This visual distinction is critical for understanding the mechanical behavior and strain transfer mechanisms across both attached and unattached areas of the pi-bracket within the simulation.

6.2.2. FEA Model

Two similar FEA models were developed in Abaqus to simulate the behavior of a full-scale, simply supported steel girder under realistic loading conditions. The first model represents the uncracked girder and serves as a baseline, while the second model represents the cracked girder, created by modifying the first model to include a predefined crack. Both models consist of three primary components: the steel girder, aluminum pi-bracket, and steel stiffener, all modeled as deformable planar shell elements with thicknesses representative of typical bridge girder configurations. The girder length was set to 29.3 meters, with supports positioned 0.25 meters from each end and spaced 28.8 meters apart. This scale significantly exceeds the 3.2-meter beam used in previous chapters, enabling realistic assessment of the pi-bracket system's performance in detecting strain variations on a full-scale bridge girder.

The FEA model consisted of several major components, including a steel girder web modeled as 15 mm thick, steel girder flanges and stiffener at 25 mm thick, and an aluminum pi-bracket at 3.175 mm thick. The model incorporated two distinct material properties: steel, with a Young's modulus of 210,000 MPa and a Poisson's ratio of 0.3, and aluminum (for the pi-bracket), with a Young's modulus of 69,000 MPa and a Poisson's ratio of 0.33. The simulations focused on linear elastic material behavior within the elastic region of the elastic-plastic relationship, consistent with assumptions from prior chapters.

To replicate a simply supported girder, boundary conditions were applied at locations 250mm from each end: a pinned support at one end restricted U1 (translation along X), U2 (translation along Y), U3 (translation along Z), UR1 (rotation about X), and UR2 (rotation about Y); a roller support at the other end allowed axial displacement along X (U1) while restricting U2 (translation along Y) and U3 (translation along Z), with all rotations (UR1, UR2, UR3) remaining free.

The loading configuration was displacement-controlled, applying concentrated forces at midspan to replicate realistic loading conditions. Selection of the applied loads was performed iteratively: the process began with an initial estimate, after which successive simulations were analyzed for the resulting displacement under the pi-bracket corresponding to the crack width. The applied force was then incrementally adjusted until the desired crack opening was achieved. Ultimately, these finalized loads corresponded to those used in the cracked girder model and were sufficient to induce crack opening widths of 0.1 mm and 0.2 mm in the cracked girder, representing applied loads of 92.5 kN and 185 kN, respectively. Both the cracked and uncracked models were subjected to these identical loading conditions. Although the uncracked model had no crack present, applying these forces ensured comparability between numerical and experimental results in prior studies, establishing consistent baseline loading conditions for strain subtraction analysis. The dead load is expected to exceed the magnitudes used in the simulations, which were specifically selected to induce crack openings of 0.1 mm and 0.2 mm. Dead loads may vary considerably due to the unique design characteristics, dimensions, and site-specific conditions of each bridge, and as such, they can be several times greater than the applied loads used in simulations.

To evaluate the effects of crack formation on strain distribution and assess the pi-bracket sensor system's ability to detect these variations, the cracked girder model was developed by modifying the uncracked girder model described above. The same model configuration was used as for the uncracked girder, with the addition of a predefined crack to simulate localized structural damage. This approach ensured consistency and allowed for direct comparison between cracked and uncracked girder strain profiles.

A stationary crack was explicitly modeled as a geometric discontinuity in the web of the steel girder at midspan, where strain concentrations are typically highest under loading. The crack originated at the bottom edge of the web and propagated vertically to a length equal to half of the web height. Given the web height of 1.63 meters, the crack extended 790 mm vertically into the web thickness.

To accurately model this crack and evaluate fracture parameters, Abaqus' contour integral method was employed. The contour integral is a numerical technique used in elasticity and fracture mechanics to compute path-independent integrals around the crack tip, such as the J-integral, which represents the energy release rate driving crack growth. In Abaqus, the crack tip and

extension direction are defined by specified vectors known as q-vectors, which represent the virtual crack extension direction in the elastic field. These vectors are crucial for directing the contour integral evaluation along a physical crack propagation path (Dassault Systèmes 2012).

In Abaqus, modeling the crack tip singularity accurately requires a specialized meshing technique called "collapsed element sides with a single node." This approach involves modifying higher-order elements near the crack tip so that one side of the element "collapses" into a single node, concentrating the mesh and better capturing the stress and strain singularity that occurs at the crack tip. To enhance this, the mid-side nodes (in quadratic elements) are moved closer to the crack tip, controlled by a parameter typically set around 0.25 to 0.3. This parameter defines the relative position of the mid-side node along the element edge, moving the mid-side node closer to the crack tip improves the element's ability to represent the square-root singularity characteristic of linear elastic fracture mechanics. The mid-side node parameter in Abaqus is typically set to around 0.25 because this positions the mid-side nodes one quarter of the element edge length from the crack tip, which closely approximates the square-root singularity in the stress and strain fields characteristic of linear elastic fracture mechanics. Setting the parameter slightly higher, such as 0.3, moves the mid-side node slightly further away but can help improve mesh quality or convergence in specific geometries or numerical settings. The slight variation from 0.25 to 0.3 is often a balance between accurately representing the mathematical singularity and practical mesh considerations, such as element shape, distortion, and solver stability. Thus, 0.3 is chosen as an effective compromise to capture the crack tip singularity while maintaining numerical robustness in Abaqus simulations (Dassault Systèmes 2012). Using this technique, Abaqus transforms standard elements into wedge-shaped elements with collapsed edges near the crack tip, creating a more accurate representation of the steep gradients in stress and strain without requiring excessive mesh refinement. This method is essential for precise contour integral evaluations, such as calculating the J-integral, which is path-independent and fundamental for fracture mechanics assessment.

This combination of explicit crack geometry, contour integral evaluation, and q-vector definition allows accurate simulation and assessment of crack behavior under applied loads.

The crack was modeled only in the bottom half of the web, while the bottom flange remained uncracked as shown in Figure 6.5. This approach was adopted to represent a crack fully developed

to the specified dimensions within the structure, aligning with the primary objective of this research, which emphasizes the detection of cracks rather than the analysis of crack propagation. Two crack opening widths, 0.1 mm and 0.2 mm, were investigated as representatives of early-stage and more advanced cracking scenarios, respectively.

Figures 6.4 and 6.5 provide detailed views of the pi-bracket area in the uncracked and cracked FEA models, respectively, highlighting the crack's integration into the web geometry.

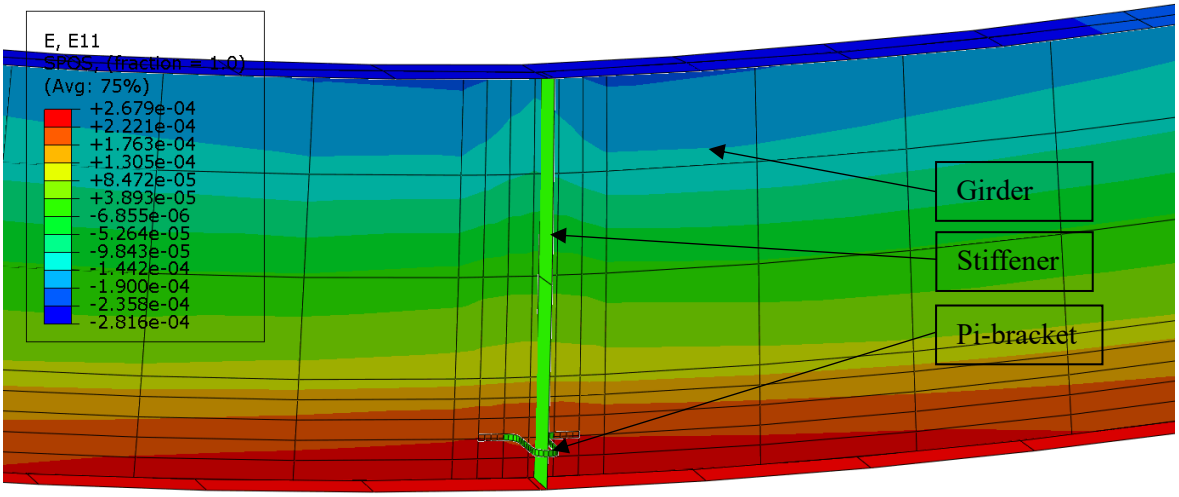

Figure 6.4: Detailed view of the Pi-bracket area in uncracked FEA Model

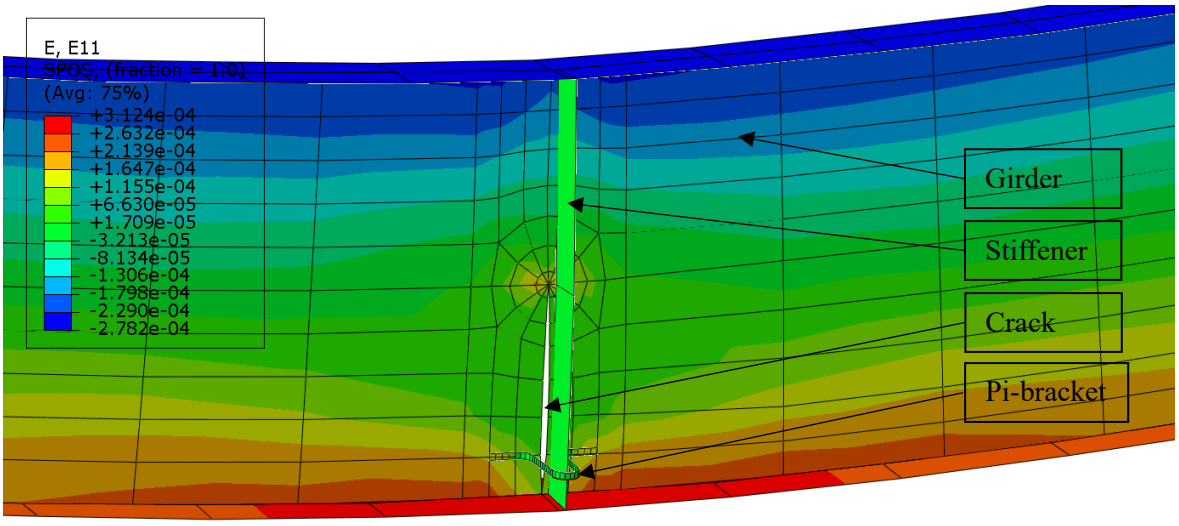

Figure 6.5: Detailed view of the Pi-bracket area in cracked FEA Model

For the cracked girder model, a refined meshing strategy was implemented to accurately capture localized stress and strain concentrations near the crack tip, using predominantly four-node quadrilateral shell elements (S4R) throughout most of the girder due to their robustness in handling large strains and deformations, with three-node triangular shell elements (S3) near the crack tip to resolve geometric complexities. In contrast, the uncracked model employed a structured mesh primarily composed of these four-node quadrilateral shell elements (S4R) across the entire girder length. This mesh was locally refined near stiffeners and the pi-bracket to ensure an accurate representation of localized strain gradients while maintaining computational efficiency.

Strain profiles obtained from the cracked model under each loading condition were compared against those from the uncracked model by subtracting corresponding strain values point by point along the girder length. This strain subtraction methodology effectively isolated variations solely attributable to crack formation, eliminating contributions from baseline loading conditions.

This comprehensive FEA modeling approach enabled detailed analysis of how cracks influence strain distribution throughout a full-scale girder, particularly around critical regions such as the pi-bracket and stiffeners. The study evaluated the pi-bracket sensor system's ability to identify strain fluctuations by determining whether the isolated strain variations exceeded its detection limits, thereby advancing structural health monitoring applications.

6.2.3. Theoretical Calculation

To validate the reliability of the FEA models (both uncracked and cracked), theoretical calculations were performed using classical beam theory. These calculations provided a benchmark for assessing the numerical results obtained from the simulations and ensuring consistency with established structural analysis methods. Specifically for the uncracked girder model, theoretical calculations were performed at 50 mm intervals along the full length of the girder for both applied load cases (92.5 kN and 185 kN). The focus was to determine strain values at the installation height of the pi-bracket, 150 mm above the top of the bottom flange, allowing direct comparison with the FEA model outputs. A free body diagram of the simply supported girder with its loading conditions is provided in Figure 6.6.

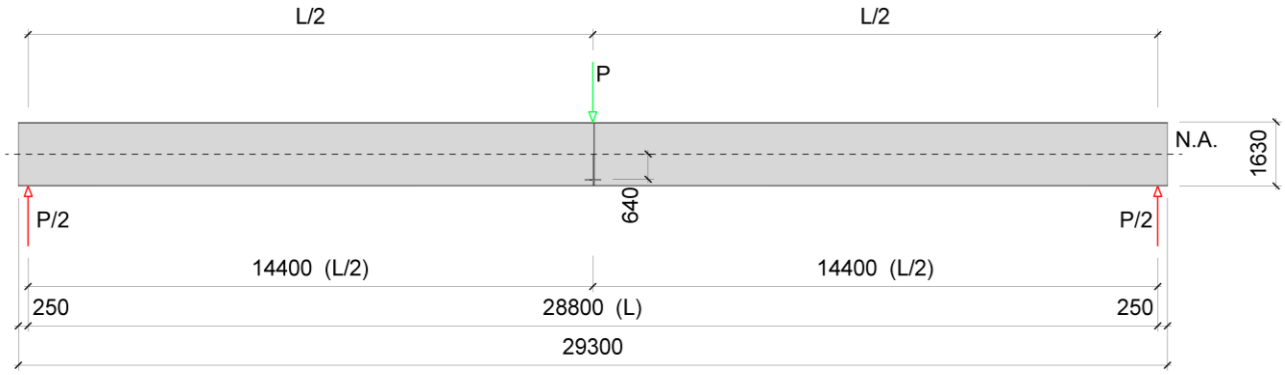

Figure 6.6: Girder free body diagram

For the uncracked girder, calculations assumed linear elastic behavior under bending and followed these steps:

Moment Calculation (*M*):

The bending moment was calculated every 50mm along the length of the beam, using the applied midspan concentrated forces of 92.5kN (for 0.1mm crack opening) and 185kN (for 0.2mm crack opening).

The formula used was:

$$M(x) = \frac{P}{2} \times x \text{ ; for } 0 \leq x \leq \frac{L}{2}$$

where P is the applied force (92.5kN or 185kN), L is the span length (28.8m), and x is the distance from the support.

Bending Stress (σ):

The bending stress was calculated at the height of the pi-bracket placement (150mm above the top of the bottom flange) using:

$$\sigma = \frac{M\,y}{I}$$

where *M(x)* is the bending moment at a specific location *x* along the beam, *y* is the distance from the neutral axis to the point of interest (150mm above the top of the bottom flange, where pi-bracket was installed and created path in Abaqus to simulate FOS placement), and *I* is the second moment of area for the girder cross-section.

Strain (ε):

The strain corresponding to bending stress was determined using Hooke's Law:

$$\varepsilon = \frac{\sigma}{E}$$

where *E* is Young's modulus for steel (210000 MPa).

These theoretical calculations for stress and strain distributions in the uncracked girder model were then directly compared to the FEA results for validation and consistency. Full details and sample calculations are provided in Appendix D.

6.3. RESULTS

6.3.1. Uncracked Girder

The strain profile for the uncracked girder was obtained for the loading conditions of 92500N and 185000N. Longitudinal strain profiles were extracted from the finite element model along a path simulating the position of the fiber optic sensor that passes over the pi-bracket, with sampling nodes positioned 150 mm above the top of the bottom flange. Figure 6.7 displays these strain profiles for the uncracked girder, providing the baseline distribution in the absence of cracks and serving as a reference for comparison with the cracked girder model. Green dashed vertical lines mark the position of the pi-bracket along the strain profile, consistent with previous chapters to maintain consistency. As the strain is measured along the sensor, not directly along the beam, the 400 mm width of the pi-bracket translates to an approximately 925 mm long strain profile along the sensor path. This is because the unattached segment of the pi-bracket, which is about 200 mm wide in the longitudinal direction, corresponds to a perimeter length of roughly 725 mm due to the bracket's geometry. Consequently, this 725 mm perimeter length effectively extends the length of

the unattached portion along the sensor path, increasing the actual length represented in the strain measurement beyond the physical 200 mm width.

From the figure can be observed that the strain increases as expected when the fiber optic sensor is directly attached to the beam, up to the green vertical lines that highlight the location of the pi-bracket. In the regions where the pi-bracket is physically attached to the beam, strain continues to rise, as strain is effectively transferred from the beam to the pi-bracket through ideal bonding conditions. When transitioning from attached to unattached parts of the pi-bracket, however, the strain drops significantly to just a few microstrains. Although the strain profile itself remains continuous and physically consistent, this mechanical discontinuity due to the unattached section causes a pronounced local reduction in measured strain near the top of the bracket.

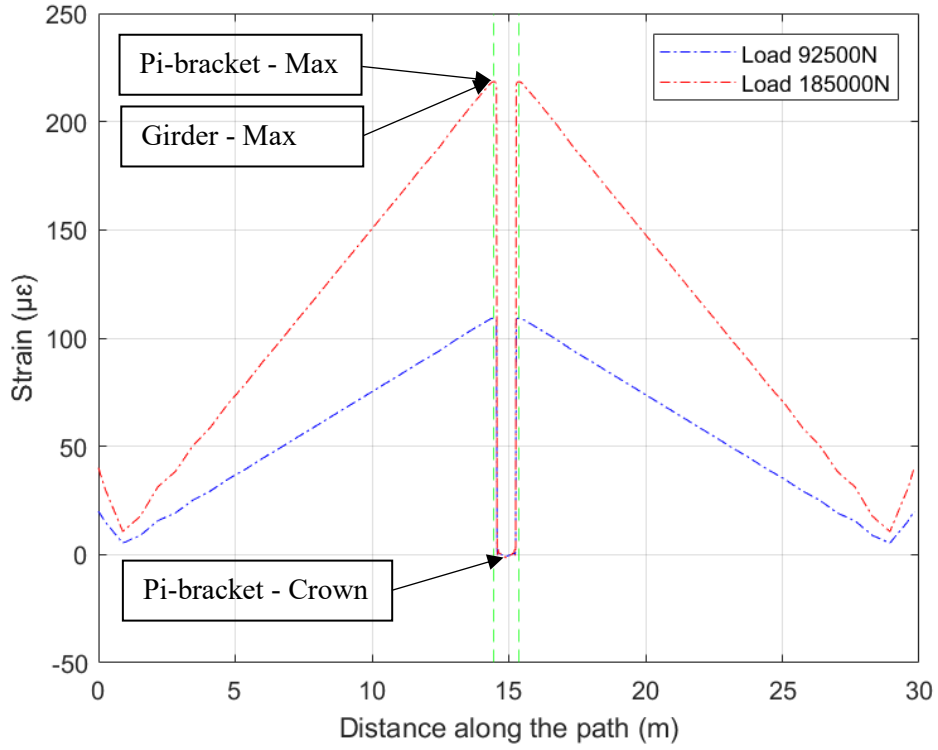

Figure 6.7: Strain profiles for uncracked girder - baseline

By establishing this baseline, it becomes possible to clearly identify and quantify strain variations that arise purely due to the presence of a crack. For the condition corresponding to a crack opening

displacement of 0.1 mm and a load of 92,500 N, the maximum recorded strain along the sensor path was 109.23 με. At the higher load of 185,000 N, corresponding to a 0.2 mm crack opening displacement, the maximum strain measured was 218.47 με.

In addition to the path measurements, strain values were also evaluated at specific points on the pi-bracket, as shown in Figure 6.3. With a 0.1 mm crack opening displacement (92,500 N), the strain at the crown of the pi-bracket was -0.72 με, while the maximum strain observed where the bracket contacts the girder was 109.23 με. For the larger 0.2 mm displacement (185,000 N), these values were -1.44 με at the crown and 218.47 με at the contact point. Notably, the maximum strain values for both the girder path and the pi-bracket contact point were the same, highlighting the effective transfer and capture of strain by the pi-bracket sensor system at the load levels studied.

These measured strains illustrate the elastic behavior of the uncracked girder under the applied loads, with smooth and continuous profiles along its length. No localized peaks or abrupt changes were found, indicating the absence of stress concentrations or structural damage. This comprehensive baseline is essential for understanding the strain behavior of a pristine girder, evaluating the influence of cracks on strain distribution, and assessing the sensitivity of the pi-bracket sensor system to subsequent damage detection analyses.

6.3.2. Cracked Girder

The strain profile for the cracked girder was obtained by subjecting the model to concentrated midspan loads that produced crack opening displacements of 0.1 mm and 0.2 mm. Specifically, these displacements were achieved using forces of 92,500 N and 185,000 N, respectively. Longitudinal train profiles were extracted from the FEA uncracked model along a path simulating the position of the FOS over the pi-bracket. The selected nodes for this path were located 150mm above the top of the bottom flange. Figure 6.8 depicts the resulting strain distributions for the cracked girder, clearly illustrating the effect of the introduced crack at midspan in an otherwise identical model to the uncracked girder.

The profiles reveal that, for a 0.1 mm crack opening (corresponding to a 92,500 N load), the maximum strain along the measurement path reached 98.76 με, while for a 0.2 mm crack opening (185,000 N load), the maximum was 197.52 με. Examination of the strain at specific points on the

pi-bracket further highlights the impact of cracking. For a 0.1 mm opening, the strain at the crown of the pi-bracket was -3.12 με, and the maximum strain at the interface between the pi-bracket and the girder was 77.11 με. At a 0.2 mm opening, the values shifted to -6.24 με at the crown and 154.22 με at the interface. The maximum strain in the girder and the pi-bracket differ due to the presence of the crack, with the strain in the girder culminating before the pi-bracket location, illustrating how cracking alters strain distribution.

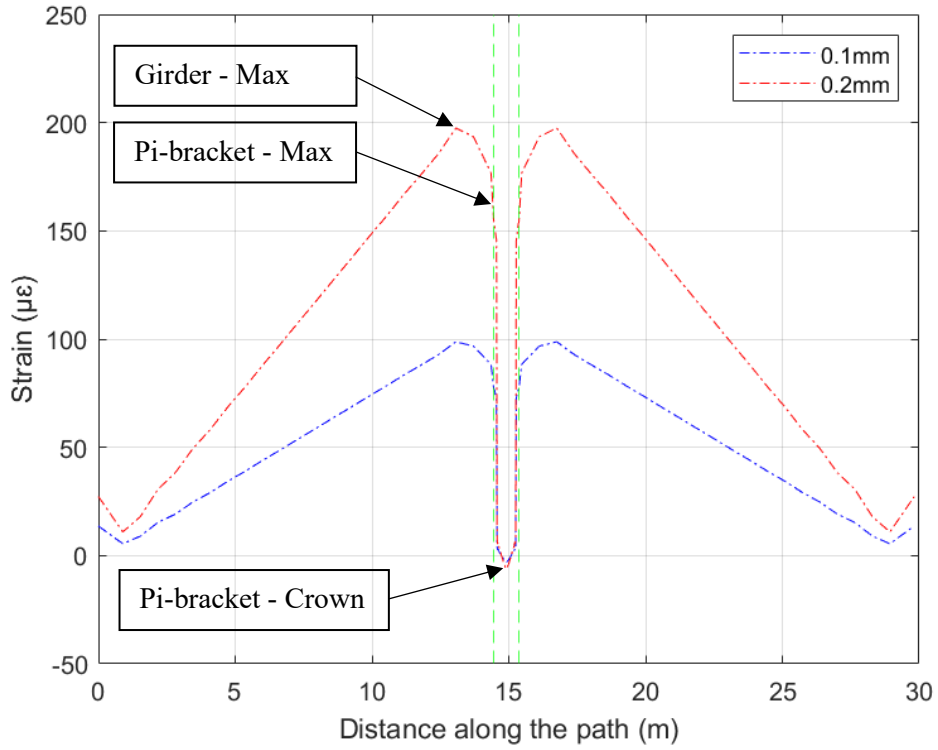

Figure 6.8: Strain profiles for cracked girder

Similar to the uncracked girder, strain still drops significantly when the measurement path transitions from the attached regions of the pi-bracket to the unattached portion. However, the pi-bracket at its crown now senses slightly higher values compared to the undamaged scenario, although these remain in the range of a few microstrains. Notably, the overall increasing trend in strain begins to decline prior to reaching the pi-bracket, a direct result of the localized strain reduction induced by the crack.

Furthermore, in current practice without the pi-bracket, when the FOS is left unattached near stiffeners or any obstacles, the strain in these critical regions becomes undetectable. This absence of effective attachment results in a lack of strain transfer to the sensor, making it difficult or impossible to monitor localized strain variations near stiffeners, highlighting the advantage of the pi-bracket system in ensuring continuous and reliable strain measurement in challenging areas.

As with the uncracked model, strain in the cracked girder is measured along the sensor path rather than directly along the beam. The 400 mm width of the pi-bracket therefore translates into an approximately 925 mm long strain profile along the sensor path because the unattached segment of the bracket, about 200 mm wide in the longitudinal direction, corresponds to a perimeter length of around 725 mm due to its geometry. As a result, the unattached region appears much longer in the sensor profile than its actual physical width.

Compared to the uncracked condition, these results demonstrate notable changes in the strain profile, particularly around the pi-bracket, confirming the influence of the crack. The local reductions and fluctuations in strain associated with the crack's location underline the sensitivity and effectiveness of the pi-bracket sensor system for detecting structural damage.

Sensor readings capture strain along the combined path of the girder and the pi-bracket. When a crack forms, the strain distribution changes. The maximum strain and the point where strain begins decreasing in the girder shift away from the crack. If the FOS were attached directly to the girder, a localized spike in strain would be expected at the crack. However, the shape of the pi-bracket redistributes this expected spike along its length, resulting in a smaller overall change in strain. The strain profile of the cracked girder is compared with the uncracked condition by subtracting the two, isolating the strain difference due to the crack. Results are provided in later sections to further explore these effects.

Given the significant increase in girder size from the 3.2 m laboratory experiments (Chapter 5) to this full-scale simulation, the pi-bracket was designed as a 12" component to ensure proper fit over the stiffener. Figure 6.3 presents the detailed geometry of the pi-bracket and indicates attached and unattached areas, clearly distinguishing regions in contact and non-contact with the girder. This detail aids in understanding strain transfer and interpreting subsequent strain profiles.

6.3.3. Comparison

This section presents a comparative analysis of the girder strain profiles obtained from the FEA simulations for the uncracked and cracked girders. The overall behaviour of these simulations is also compared and to the theoretical calculations. The analysis focuses on assessing the global structural behavior and strain changes in the vicinity of the pi-bracket sensor system, with a particular interest in understanding the expected strain levels if a real crack were to occur.

The primary objective is to isolate and quantify the strain variations attributable solely to crack formation. This is achieved by subtracting the strain profile of the uncracked girder from that of the cracked girder under identical loading conditions. This approach effectively eliminates the influence of the applied load, revealing the strain signature specific to the presence and severity of the crack. Once the strains due to crack formation are isolated, their magnitudes are analyzed to determine if they fall within the detection capabilities of the pi-bracket system.

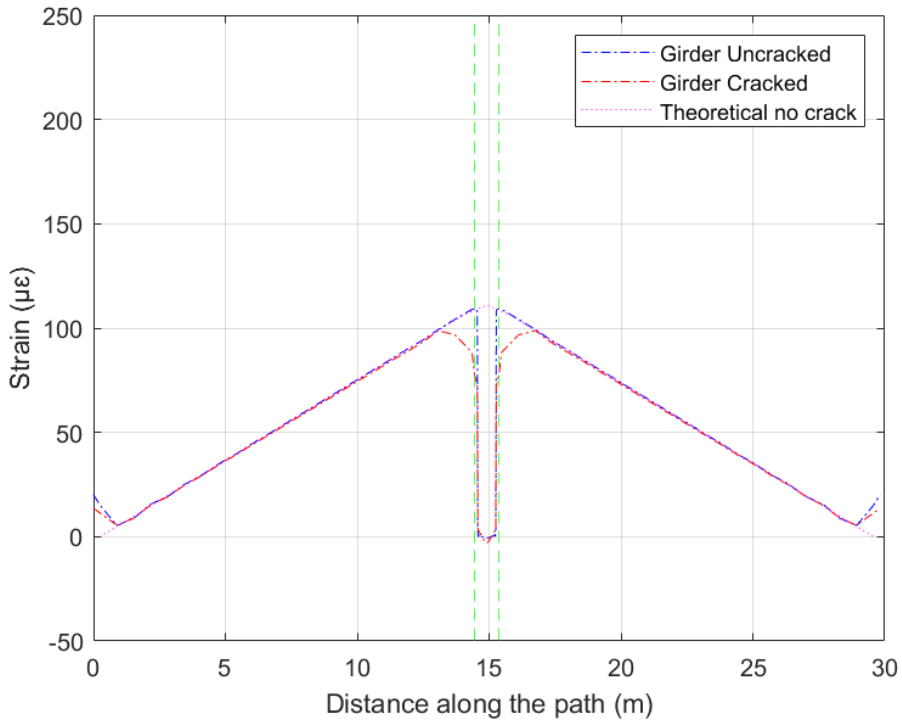

Figure 6.9: Strain profiles comparison 0.1mm

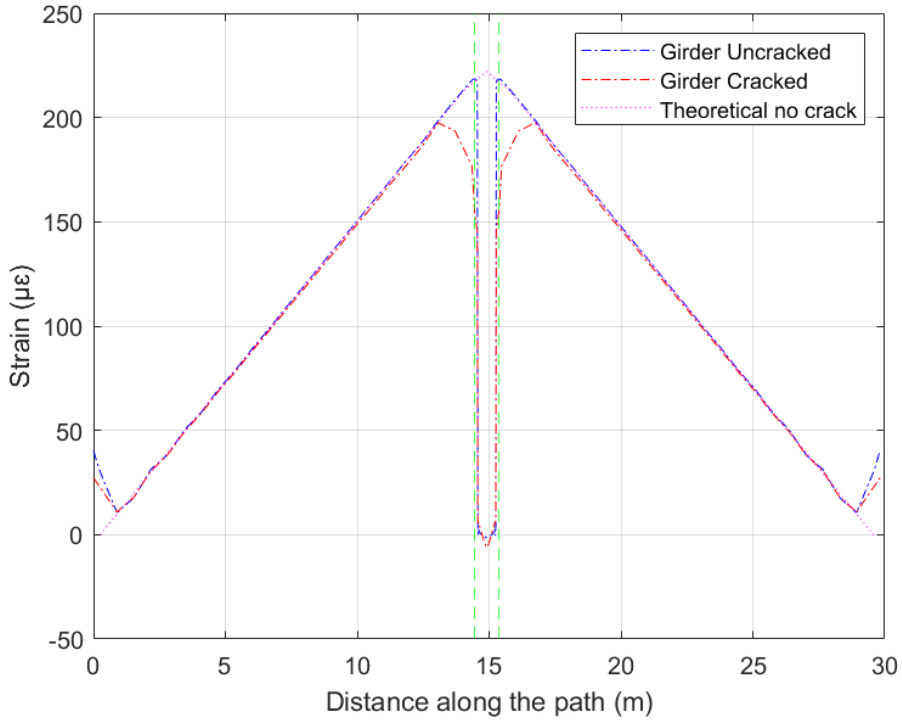

Figure 6.10: Strain profiles comparison 0.2mm

Figures 6.9 and 6.10 present a visual comparison of the overall strain profiles obtained from the FEA simulation of the uncracked and cracked girders, along with the corresponding theoretical strain profiles, for crack opening widths of 0.1mm (induced by a load of 92.5kN) and 0.2mm (induced by a load of 185kN).

A direct comparison between the theoretical strain calculations at the location x = 14.1 m and those derived from the FEA model is presented in Table 6.1.

Table 6.1: Comparison of FEA results and theoretical calculation

Load (kN)	FEA Strain (με)	Theoretical Strain (με)	Percent Error (%)
92.5	109.23	112.48	2.89
185	218.47	224.96	2.88

At an applied load of 92.5 kN, the FEA predicted a strain of 109.23 με, while the theoretical approach yielded 112.48 με, corresponding to a percent error of only 2.89%. For the 185 kN case, the FEA and theoretical strains were 218.47 με and 224.96 με, respectively, with a percent error of 2.88%.

These small discrepancies, all under 3%, confirm very good agreement between the classical beam theory and the numerical FEA results, substantiating the validity and accuracy of the FEA model for the uncracked girder.

In examining the uncracked girder, the simulations revealed the following strain characteristics: The peak strain along the measurement path reached 109.23με under the 92.5kN load (0.1mm crack opening) and 218.47με when subjected to the 185kN load (0.2mm crack opening). Focusing on the pi-bracket itself, the strain at its crown registered -0.72με for the smaller crack opening and -1.44με for the larger. The point of maximum strain on the pi-bracket was observed at the attached areas where the pi-bracket interfaces directly with the girder. This maximum strain reached values of 109.23με and 218.47με for the 0.1 mm and 0.2 mm crack opening cases, respectively. This clearly indicates that the highest strain concentration occurs in the sections of the pi-bracket physically bonded to the girder, where effective strain transfer takes place as shown in the Figure 6.3. For context, the theoretical maximum strains were 112.48με (0.1mm) and 224.96με (0.2mm). All these values are summarized in Table 6.2.

Table 6.2: Results summary

Load [kN]	Crack Opening [mm]	Strain - Theoretical Max [με]	FEA Girder - Uncracked			FEA Girder - Cracked			Strain Difference	
			Strain -Girder Max. [με]	Strain - Pi-bracket Crown [με]	Strain - Pi-bracket Max. [με]	Strain - Girder Max. [με]	Strain - Pi-bracket Crown [με]	Strain - Pi-bracket Max. [με]	Strain - Pi-bracket Crown [με]	Strain - Pi-bracket Max. [με]
92.5	0.1	112.48	109.23	-0.72	109.23	98.76	-3.12	77.11	-2.4	-35.64
185	0.2	224.96	218.47	-1.44	218.47	197.52	-6.24	154.22	-4.8	-71.28

Conversely, the cracked girder exhibited a different strain profile: The maximum strain along the path was 98.76με (0.1mm crack opening) and 197.52με (0.2mm crack opening). At the pi-bracket, the crown experienced strains of -3.12με (0.1mm) and -6.24με (0.2mm), while the maximum strain at the contact point with the girder reached 77.11με and 154.22με for the two crack opening scenarios.

The strain isolation process is illustrated in Figure 6.11, which shows the resulting strain profiles after subtracting the uncracked strain from the cracked strain. This approach eliminated contributions from normal loading, enabling differentiation between strains induced by applied forces and those caused by crack formation. The analysis reveals a maximum strain for the 0.1mm crack opening of 35.64 με and a maximum strain of 71.28 με for the 0.2mm crack opening after the subtraction. Given the successful detection of similar strain magnitudes in previous laboratory experiments, the isolated strain levels suggest that the proposed pi-bracket sensor system is well-suited for effective crack detection.

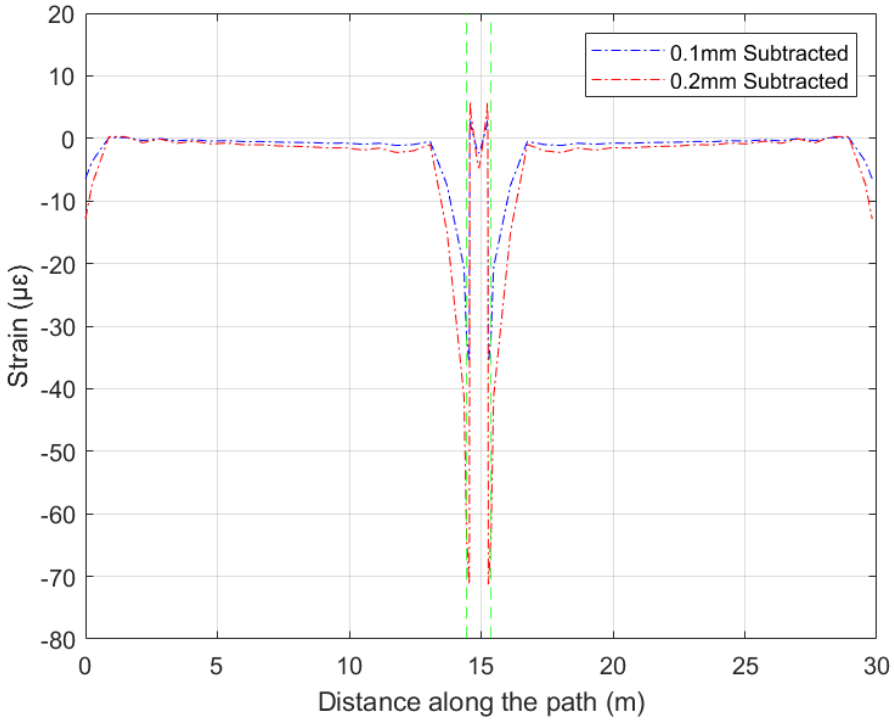

Figure 6.11: Change in strain relative to baseline

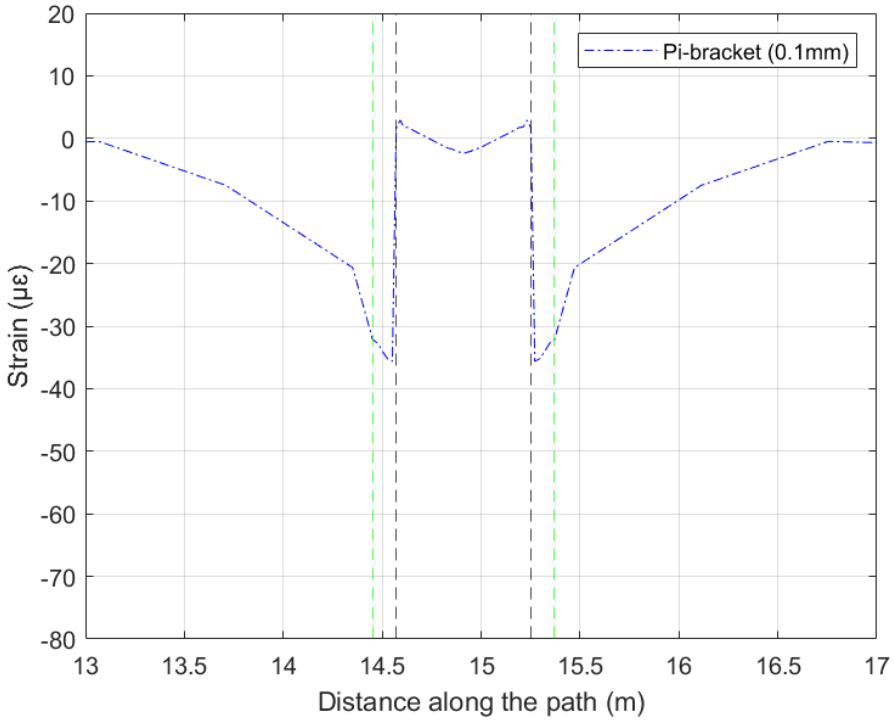

Figure 6.12: Change in strain in the vicinity of the Pi-bracket - 0.1mm

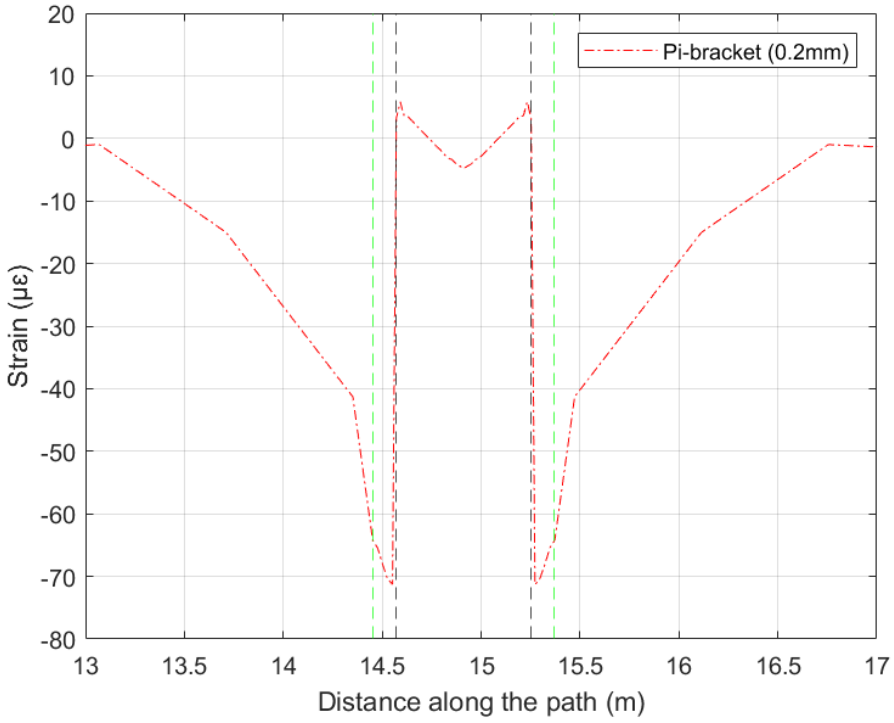

Figure 6.13: Change in strain in the vicinity of the Pi-bracket - 0.2mm

Figures 6.12 and 6.13 provide a more detailed examination of the strain profiles in the immediate vicinity of the pi-bracket for crack openings of 0.1mm and 0.2mm, respectively. These figures enable a closer inspection of the strain distribution within the critical sensing region of the pi-bracket. In addition to green dashed vertical lines marking the pi-bracket's overall position, black dashed vertical lines delineate the attached and unattached portions of the pi-bracket relative to the beam, facilitating clearer interpretation of the strain profiles. This visualization effectively demonstrates how strain is transferred from the girder to the pi-bracket.

Notably, the pi-bracket regions in direct contact with the girder consistently exhibit the highest strain levels, indicating efficient strain transfer. In contrast, the regions of the pi-bracket that are not in direct contact with the beam exhibit minimum strains. Researchers initially expected to observe higher strains in these unattached regions when formulating their hypothesis. However, the results revealed that the areas of the pi-bracket in contact with the girder are where most of the strain difference, resulting from the presence of a crack, is observable. These localized strain concentrations are readily detected by the pi-bracket, confirming its capability to serve as an effective intermediary for capturing and relaying strain data from the girder to the sensor, even when the sensor is not positioned directly above the crack. It is evident that the areas of the pi-bracket in contact with the girder are critical to strain detection.

The subtracted strain values were then averaged to simulate different DAQ settings to match various sampling and averaging resolutions (5SR-10AR, 5SR-20AR, 10SR-20AR, 10SR-50AR and 10SR-100AR), where SR represents the sampling resolution and AR represents the averaging resolution. Figures 6.14 and 6.15 depict the DAQ settings for the 0.1mm and 0.2mm crack openings, respectively.

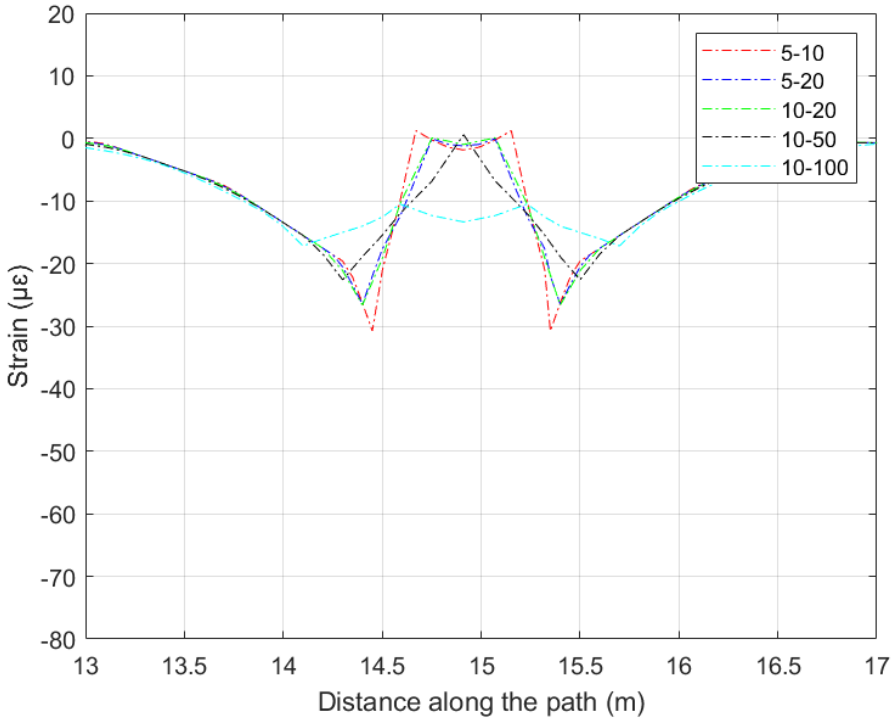

Figure 6.14: Effect of DAQ settings on strain profile for 0.1mm crack opening

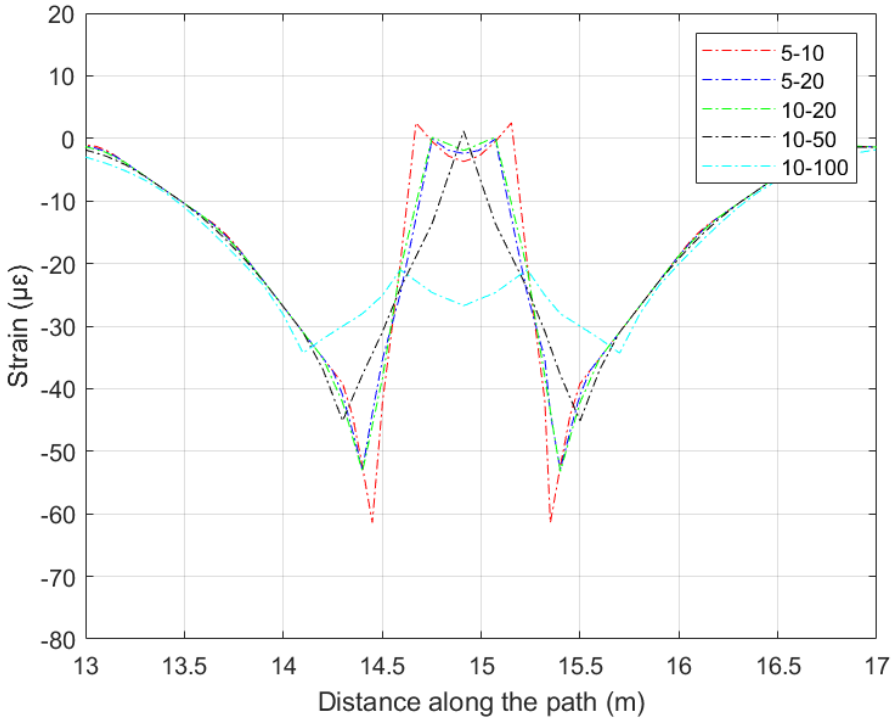

Figure 6.15: Effect of DAQ settings on strain profile for 0.2mm crack opening

Examination of these figures reveals that the strain profile is influenced by the selected DAQ settings. As anticipated, the 5SR-10AR setting exhibits the highest resolution, a consequence of possessing the most sampling values averaged over the shortest spatial interval. Although the 10SR-100AR setting demonstrated a comparatively lower resolution, the resultant strain magnitudes remain sufficiently distinct for reliable detection.

Analyzing the data from Table 6.2, for a 0.1mm crack opening, the maximum strain on the girder was 109.23με for the uncracked girder and 98.76με for the cracked girder, demonstrating a reduction of 10.47με, which is approximately 9.6%. For the 0.2mm crack opening, the maximum strain was 218.47με for the uncracked girder and 197.52με for the cracked girder, demonstrating a reduction of 20.95με, also showing a reduction of approximately 9.6%.

It was hypothesized that the change in strain at the crown of the pi-bracket would be used to detect cracks. However, while we observe some change in strain at the crown, the magnitudes are so minimal that they would be indistinguishable from noise. In contrast, the results revealed that the strains captured by the regions of the pi-bracket attached to the girders exhibit significantly higher changes due to the presence of the crack.

This is reflected in the data: for the 0.1 mm crack opening, the strain at the pi-bracket crown was -0.72με for the uncracked girder and -3.12με for the cracked girder, resulting in a difference of only -2.4με. For the 0.2 mm crack opening, the difference increased to -4.8με (-1.44με uncracked versus -6.24με cracked). These small differences at the crown of the pi-bracket contrast with much larger strain changes observed in the attached regions, highlighting why the attached areas are more reliable indicators for crack detection.

The maximum strain on the pi-bracket (at the contact point) was 109.23με for the 0.1mm crack opening in the uncracked girder and 77.11με in the cracked girder, representing a reduction of 32.12με, which is approximately 29.4%. Similarly, for the 0.2mm crack opening, the maximum strain was 218.47με in the uncracked girder and 154.22με in the cracked girder, demonstrating a reduction of 64.25με, also showing a reduction of approximately 29.4%.

The observed differences in strain between the uncracked and cracked girders indicate a redistribution of stresses caused by the presence of the crack, which affects the strain magnitudes measured at the pi-bracket. The strains measured for the cracked girder are considerably smaller

than those in the uncracked girder. However, the change in strain is still large enough to detect the presence of the crack. This behavior suggests that the numerical model is capable of accurately predicting the strain response of the pi-bracket under the applied loading conditions. The strain results exhibit trends similar to those observed in laboratory experiments, although some discrepancies may exist due to previously discussed factors.

The FEA results show good agreement with theoretical calculations, reinforcing the validity of the numerical approach. Furthermore, the isolated strain levels align with values successfully detected in prior laboratory testing, indicating that the proposed pi-bracket sensor system is well-suited for effective crack detection.

In terms of strain redistribution, the maximum strain on the cracked girder decreases by approximately 9.6%, whereas the maximum strain on the pi-bracket at the contact point experiences a larger reduction of about 29.4% due to the crack. Specifically, the strain difference at the pi-bracket crown is -2.4 με for a 0.1 mm crack opening and -4.8 με for a 0.2 mm crack opening. At the critical contact point between the pi-bracket and the girder, the strain differences are -35.64 με and -71.28 με for the respective crack openings. These isolated strain values are directly attributable to crack formation and provide essential information for evaluating the performance of the pi-bracket in detecting structural damage.

6.4. DISCUSSION

This chapter presented a comparative analysis of girder strain profiles obtained from FEA simulations, focusing on the performance of the pi-bracket sensor system in detecting strain variations induced by cracks under simulated loading conditions. Two conditions were compared: the uncracked girder, serving as a baseline, and the cracked girder. The study employed the strain subtraction methodology to isolate and quantify crack-induced strain variations. This strategic emphasis has helped to illustrate how cracks might specifically influence the performance of the pi-bracket system, as examined on a larger girder compared to Chapter 's laboratory experiment.

6.4.1. Impact of Cracks on Strain Distribution

By isolating strain variations attributable solely to crack formation, we were able to identify critical patterns in how cracks impact the pi-bracket's strain response. This section focuses specifically on the strain differences observed at the pi-bracket as a result of the crack. Analyzing the data from the last two columns of Table 6.2, which represent the strain differences after subtracting the uncracked girder's strain profile, several key observations emerge.

At the pi-bracket crown, the strain difference was -2.4 με for a 0.1 mm crack opening and -4.8 με for a 0.2 mm crack opening. These values denote the change in strain experienced solely due to the crack. Additionally, at the critical contact point where the pi-bracket interfaces with the girder, the strain difference was -35.64 με for the 0.1 mm crack opening and -71.28 με for the 0.2 mm crack opening.

These isolated strain differences are particularly important because they represent the pure signal that the pi-bracket sensor would need to detect in order to identify the presence of a crack. The fact that these strain differences are non-zero suggests that the pi-bracket is indeed capable of capturing a discernible signal related to crack formation.

Given the successful detection of similar strain magnitudes in previous laboratory experiments, the isolated strain levels suggest that the proposed pi-bracket sensor system is well-suited for effective crack detection.

6.4.2. Validation against Experiment Results

The findings presented in this chapter build upon those discussed in Chapter 5, which validated the effectiveness of the pi-bracket sensor system for detecting localized strain changes near stiffeners. The simulation in this chapter showed comparable behavior to what it is theoretically calculated. Despite the discrepancies for reasons discussed in previous chapter, the strains behavior and results have similar trends to what it was captured with laboratory experiments. Given the successful detection of similar strain magnitudes in previous laboratory experiments, the isolated strain levels suggest that the proposed pi-bracket sensor system is well-suited for effective crack

detection. The values demonstrate that even with a larger girder model, the system retains its ability to identify and measure crack-induced strain variations.

The simulation results suggest the numerical model can adequately predict the strain behavior of the pi-bracket under the applied loading conditions.

6.4.3. Effects of Girder Boundary Conditions in Steel Bridge Behaviour

In this study, the finite element models of the full-scale steel girder assumed traditional simply supported boundary conditions, simplifying the supports to pinned and roller restraints that allow expected longitudinal displacement and rotation. While these assumptions are common in FEA modeling and useful to simplify the problem, actual bridges often differ due to bearing restraint effects at the supports. For example, the North Muskoka River Bridge case, as reported by Bakht and Mufti (2015), showed that elastomeric bearings, designed to permit free longitudinal girder movement, actually impose substantial restraint forces. These bearing restraints led to the bridge behaving approximately 20% stiffer in dynamic testing and reduced mid-span deflections by about 12% in static tests compared to traditional simple support predictions. Furthermore, bearing stiffness can vary with temperature, becoming stiffer in cold conditions and less stiff in warmer conditions, which further influences bridge behavior.

It is important to highlight that the central focus of this research is to determine whether cracks forming directly under the pi-bracket sensor can be effectively detected using distributed FOS. While boundary conditions such as bearing restraints can influence overall strain and deflection results, this study mitigates such effects by focusing on differential strains, obtained by subtracting the baseline (uncracked) condition from the cracked one under identical loading and boundary conditions. Since the boundary conditions are consistently modeled in the same way for both scenarios, their impact on the resulting strain differences is minimal and thus negligible. This differential approach isolates the strain changes caused purely by crack formation, allowing for an accurate evaluation of the pi-bracket sensor system's crack detection capabilities despite potential limitations in the absolute modeling of boundary conditions.

Nevertheless, future modeling efforts will benefit from explicitly including the force-displacement characteristics of real bearing systems to more accurately capture the complex boundary conditions

observed in practice. Doing so will improve the simulative representation of real bridge behavior, refining predictions of strain fields and structural response. This will, in turn, enhance the reliability and practical application of structural health monitoring approaches, such as the pi-bracket sensor system, in full-scale bridge environments.

6.5. CONCLUSIONS

Based on the FEA simulations conducted and the comparative analysis of cracked and uncracked girder models, which were validated by the theoretical calculations, the following conclusions can be drawn regarding the pi-bracket sensor system.

The FEA simulations, which were confirmed by the theoretical approach, demonstrate that the appearance of a crack causes a measurable redistribution of strain, especially in the region surrounding the pi-bracket. By applying a strain subtraction methodology, the simulations isolated strain variations attributable solely to crack formation, enabling a targeted assessment of the pi-bracket's detection capabilities.

The isolated strain values measured at both the crown of the pi-bracket and at the contact point with the girder indicate that the pi-bracket is capable of capturing a discernible signal specifically related to crack development. Quantitatively, the strain difference at the pi-bracket crown was found to be -2.4 με for a 0.1 mm crack opening and -4.8 με for a 0.2 mm crack opening. At the point of direct contact between the pi-bracket and the girder, the strain differences were -35.64 με for the 0.1 mm crack and -71.28 με for the 0.2 mm crack. These values confirm the sensitivity of the pi-bracket to changes induced by cracking.

Overall, the FEA results indicate that the simulation framework can adequately predict the strain behavior of the pi-bracket, thus supporting its applicability for structural health monitoring purposes. Furthermore, the results and analysis presented in this chapter enhance and reinforce the findings reported in Chapter 5, demonstrating that the pi-bracket can successfully capture strain changes associated with crack formation.

These conclusions support the potential of the pi-bracket sensor system as a viable tool for SHM, particularly for crack detection in bridge girders.

CHAPTER 7: CASE STUDY – BRIDGE IN MANITOBA, CANADA

7.1. INTRODUCTION

The integration of innovative sensor systems into SHM requires rigorous validation beyond laboratory and numerical studies. While experiments and FEA provide essential information for understanding sensor design and behavior under controlled conditions, they cannot fully capture the complexities of field environment. Field validation thus serves as the critical link between theoretical development and practical deployment. It reveals how sensors perform amidst unpredictable operational conditions, environmental influences, and installation challenges. This stage is especially crucial for fatigue crack detection in steel bridge girders, where early identification near welds and vertical stiffeners is vital to prevent catastrophic failures.

The pi-bracket sensor system combines engineered geometric features with distributed fiber optic sensing technology, aiming for reliable crack detection in difficult-to-monitor regions. Comprehensive field trials are essential to demonstrate the system's robustness, sensitivity, and in situ applicability.

This chapter presents a case study of the instrumentation of a steel girder bridge located in Manitoba, Canada, using the pi-bracket sensor system integrated with FOS. The selected bridge is a common medium-span steel girder bridges with welded vertical stiffeners.

Although no cracks were detected during the observation phase, the instrumentation provided invaluable data. These data validated sensor installation methods, assessed signal quality amid cyclic loads and temperature fluctuations, and refined protocols for data interpretation. This "quiet" monitoring stage establishes foundational reference thresholds for future crack detection and alarm settings. Advanced algorithms were incorporated into these thresholds to enhance signal processing and anomaly identification, providing a context that calibrates FEA predictions and laboratory findings with field observations. Discussion of the rationale and methodology for defining strain thresholds, including the integration of predictive findings from simulation and experimental data, is an important component of this chapter.

The primary objective of the instrumentation is twofold: to establish accurate baseline strain profiles under uncracked conditions, and to enable sensitive detection of subtle strain variations indicative of crack initiation and propagation near critical regions, such as vertical stiffeners. Baseline measurements account for effects due to vehicle and environmental loads, thus providing a reliable reference against which changes in strains can be evaluated. The system collects strain data at frequent intervals, facilitating early crack identification through differential strain analysis. By comparing sequential strain profiles and applying validated FEA-based thresholds, the monitoring system generates timely, reliable alerts to help maintenance personnel prioritize inspections and interventions. Emphasis is placed on detecting strain changes on the order of tens of microstrains localized to small spatial extents, consistent with fatigue crack formation signatures. This proactive approach supports improved safety, cost-efficiency, and extension of bridge service life.

7.2. BRIDGE INSTRUMENTATION

The instrumentation of the Manitoba bridge demonstrates the real-world application of the pi-bracket sensor system integrated with distributed fiber optic sensing technology. The bridge consists of seven East-West spans, each supported by eight steel girders carrying a 260 mm thick composite concrete deck slab. The girders are connected by multiple transverse diaphragms and feature welded vertical stiffeners, which are typical locations susceptible to fatigue cracking. Instrumentation concentrated on a single girder, where strategically placed pi-brackets served as harnesses for distributed fiber optic sensors. These harnesses enabled the fiber optic cables to traverse vertical stiffeners.

The installation was carried out over six weeks, employing materials and methods designed to withstand Manitoba's extreme temperature range (−40°C to +40°C). This setup facilitates continuous structural health monitoring by collecting real-time strain data and allows comprehensive assessment and validation of sensor performance under realistic loading and environmental conditions.

7.2.1. Bridge Description and Monitoring Significance

The monitored bridge is a representative asset within Manitoba's transportation network, reflecting typical design and material conditions of mid-20th century steel girder bridges requiring fracture-critical monitoring. The composite structure, with steel girders and concrete deck slab, is subjected to cyclic traffic loads and environmental stresses that induce fatigue cracking, especially near welded stiffeners where stress concentrations often develop (Raeisi et al. 2019).

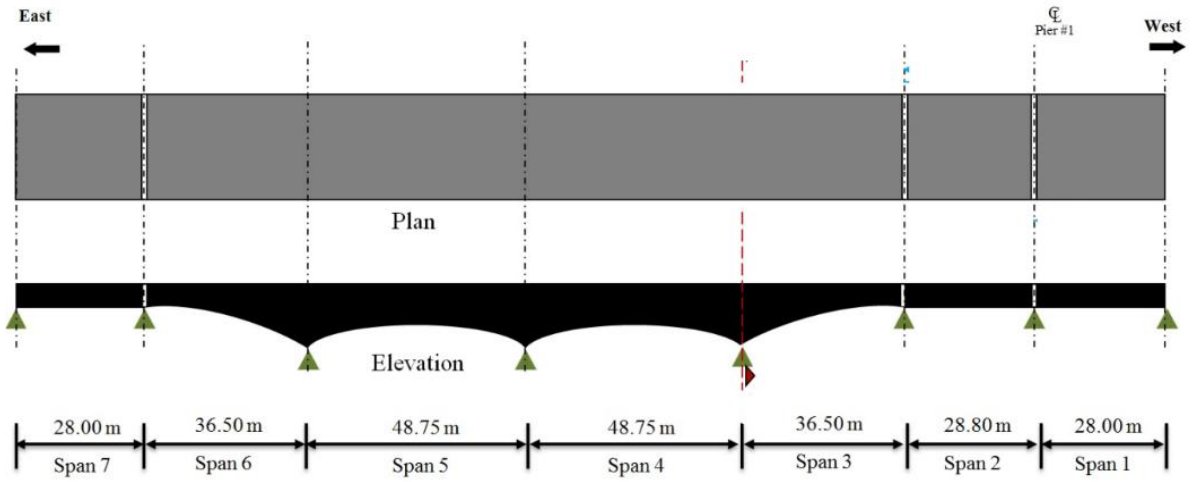

Figure 7.1: Bridge in Manitoba - plan and elevation

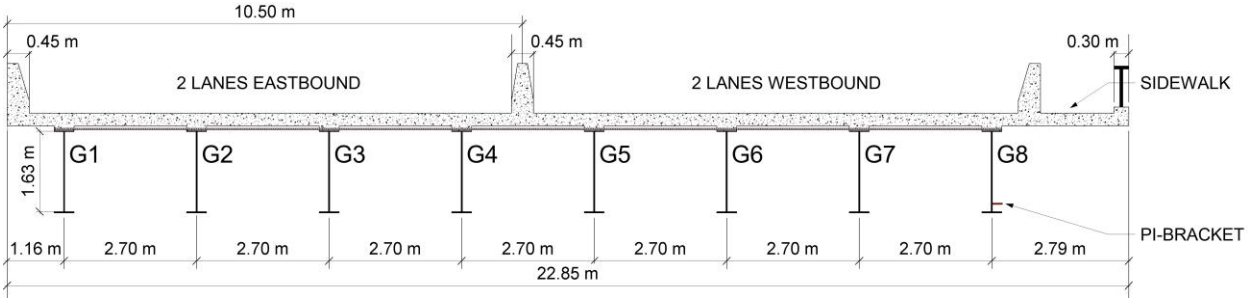

Figure 7.2: Bridge in Manitoba - cross-section

Figure 7.1 illustrates the bridge instrumented with FOS. To enable comprehensive monitoring, one girder was instrumented with distributed FOS. Eight sensor loops were installed on girder G8, covering both simply supported and continuous spans. Integration of the pi-bracket sensor system with DiTest SMARTape II utilizing BOTDA technology for distributed sensing, enables

continuous, high-resolution strain monitoring throughout the girder length. Cross section of the bridge, identifying instrumented girder is shown in Figure 7.2.

The pi-brackets serves as mechanical harnesses, allowing the FOS to traverse vertical stiffeners. This configuration ensures seamless strain transmission in the FOS and physically protects sensors from mechanical damage in critical areas.

The FOS technology offers exceptional immunity to electromagnetic interference, distributed sensing capability over several kilometers, and microstrain-level sensitivity suitable for detecting early-stage fatigue cracks (Roctest, n.d.). The DAQ system remotely collect and process strain measurements in near real-time. This integrated instrumentation strategy is expected to support scalable SHM, bridging laboratory validation and field deployment for infrastructure management.

Instrumenting this bridge provides an opportunity for systematic evaluation of advanced SHM's effectiveness for early crack detection, assessing potential for preventative maintenance before crack growth jeopardizes structural integrity. It is anticipated that the bridge's exposure to harsh climates will help validate sensor durability and data accuracy. The installation of pi-bracket harnesses coupled with distributed FOS is designed to address critical shortcomings in conventional monitoring by securing sensor continuity and mechanical protection over stiffened girder regions, thereby enhancing confidence in strain-based crack detection.

7.2.2. Instrumentation Procedure

The instrumentation procedure followed a systematic approach for installing FOS integrated with pi-brackets on the steel girders, particularly focusing on areas near vertical stiffeners. This approach ensures continuous SHM through distributed fiber optic sensing combined with the pi-bracket system.

Site preparation involved cleaning and surface conditioning of steel girders and pi-brackets to optimize sensor bonding. Laboratory protocols for sanding and cleaning were followed to promote strong adhesive attachment of FOS.

Aluminum pi-brackets (Figure 7.3) were adhered to the steel girder over the vertical stiffeners using Araldite 2021-1, a specialized adhesive engineered to endure Manitoba's annual temperature

variations from -40°C to +40°C. These pi-brackets enable continuous bonding of FOS along the girder, ensuring uninterrupted sensor coverage and mechanical protection in the stiffened regions.

Figure 7.3: Pi-bracket over a vertical stiffener

Four loops of FOS covered the bridge spans, with pi-brackets routing and protecting fiber optic sensors over vertical stiffeners to enable continuous strain measurements even where bending restrictions would otherwise prevent sensor placement. DiTest SMARTape II strain sensors were mounted on prepared girder surfaces and pi-brackets using high-strength adhesives, firmly securing the sensors to steel. After installation, the SMARTape sensors were covered with aluminum foil tape to protect against mechanical damage during field operation. The pi-brackets guided and shielded the sensors, preventing signal loss caused by bending or damage. Cabling included carefully fusion-spliced optical fiber extensions, which were connected to the DAQ system to maintain sensor integrity and minimize attenuation.

Each of the four strain sensor loops was paired with a parallel temperature sensor (Figure 7.4) to enable compensation of temperature effects on strain readings. It is noted that the temperature sensors were not used in this study. Figure 7.5 shows one of the fiber optic sensor loops on a girder.

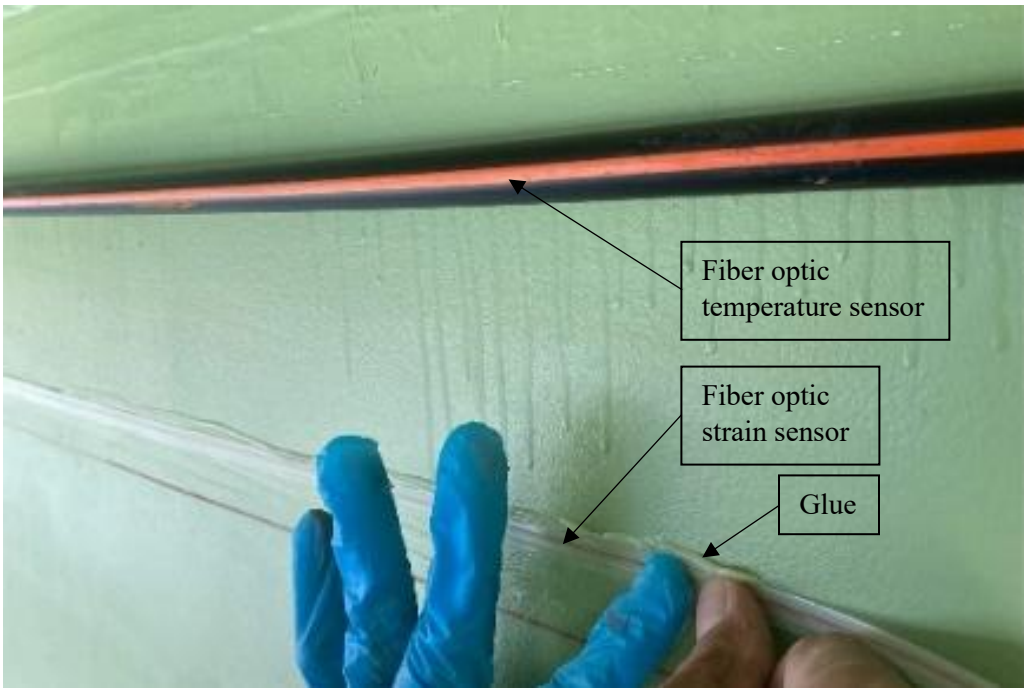

Figure 7.4: Installation of the FOS strain and temperature sensors

Figure 7.5: A girder of the bridge showing installed sensors

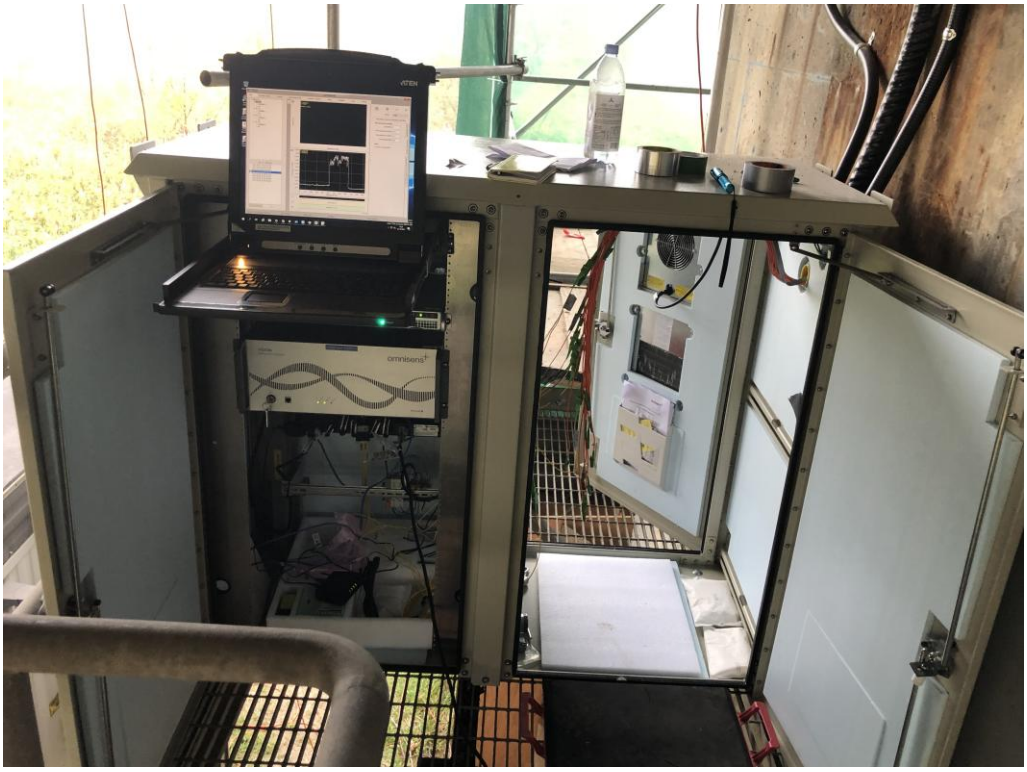

Figure 7.6: The DAQ system

Figure 7.7: Thermal localization of start and end points of each FOS sensor loop

The DAQ system, based on BOTDA technology and shown in Figure 7.6, was configured for real-time monitoring, acquiring distributed strain measurements along FOS loops with high sampling resolution of 5 cm, averaged to an effective spatial resolution of 1 meter, and strain resolution at microstrain level. On-site calibration employed thermal localization method, where a heat gun was used to selectively heat sections of the sensor, clearly identifying sensor start and end points (Figure 7.7). This process enables accurate mapping of strain data to specific girder locations.

A custom software package collects and manages strain data from the bridge. Figure 7.8 shows the installed loops and the DAQ program interface. This software processes the data, performing strain signal interpretation and automated crack detection, providing actionable infrastructure management information.

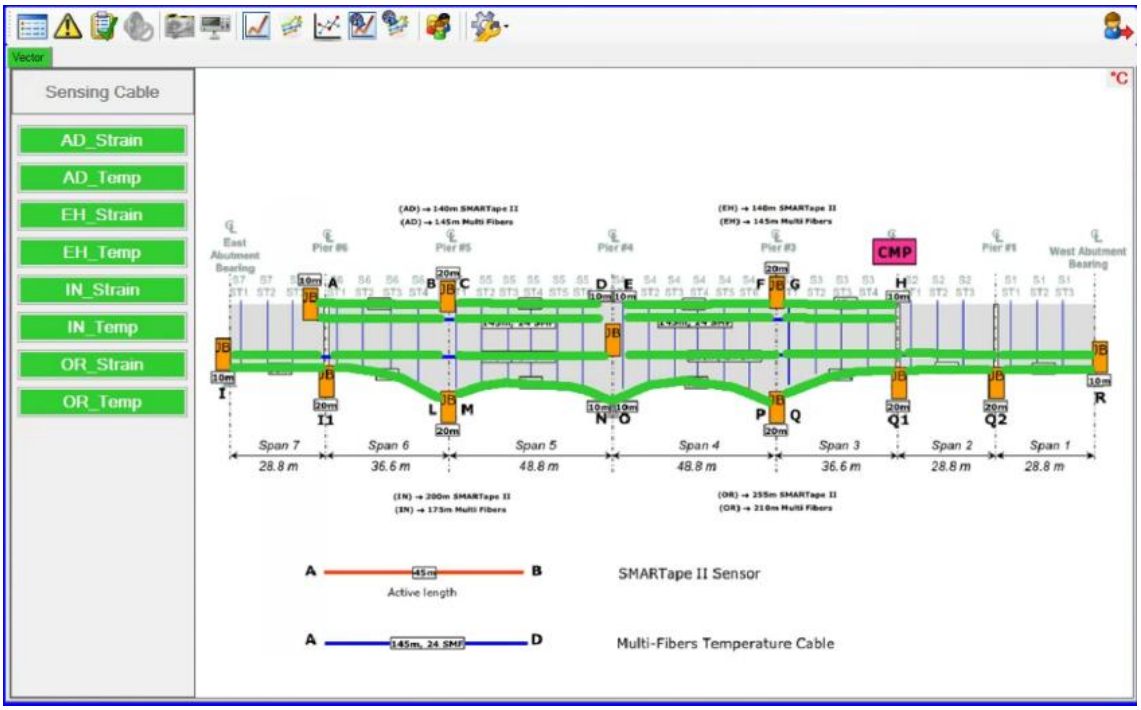

Figure 7.8: FOS loops and DAQ program interface

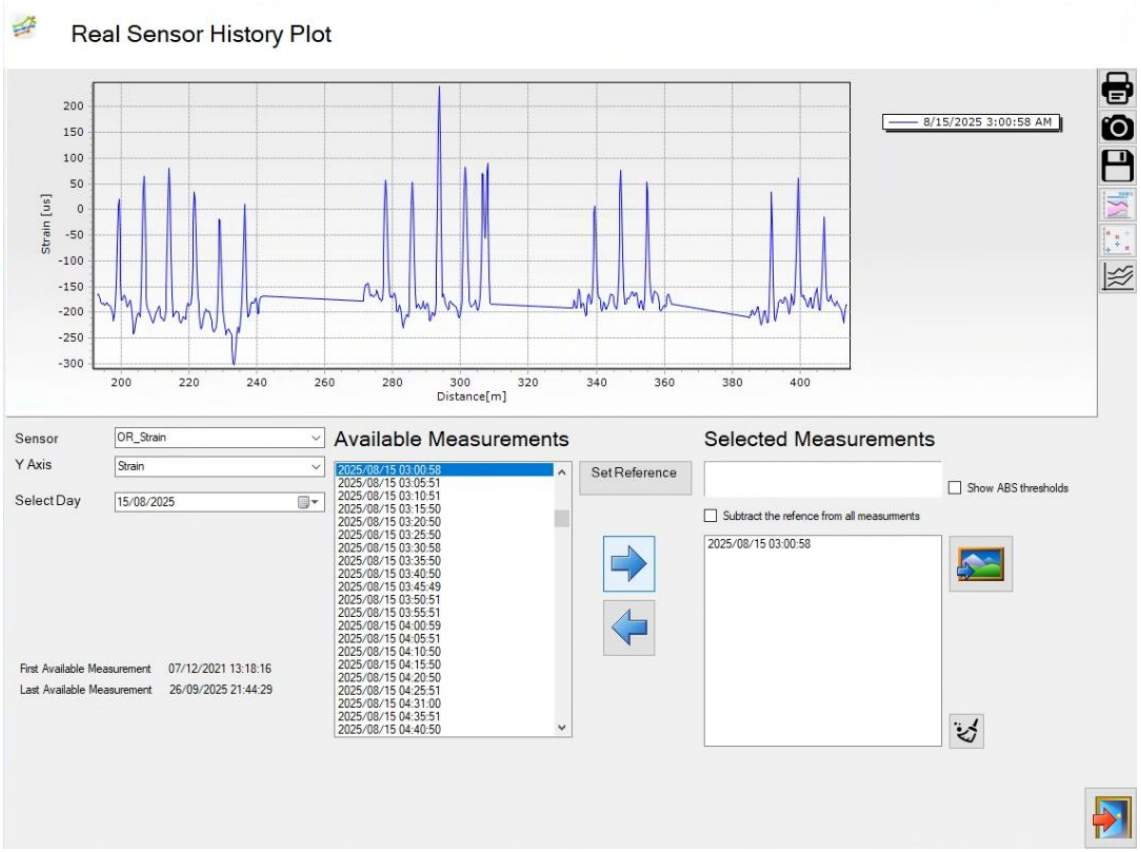

Figure 7.9: Raw strain profile recorded by a representative FOS loop – single measurement

Data are collected at five-minute intervals and transmitted for subsequent processing. Figures 7.9 and 7.10 present representative strain readings from a single sensor (O-R), with the data collected on August 15, 2025, between 03:00 AM and 05:00 AM. Figure 7.9 shows a raw single strain profile, while Figure 7.10 illustrates the temporal variation of strain readings at the same sensor over the two-hour period between 03:00 AM and 05:00 AM.

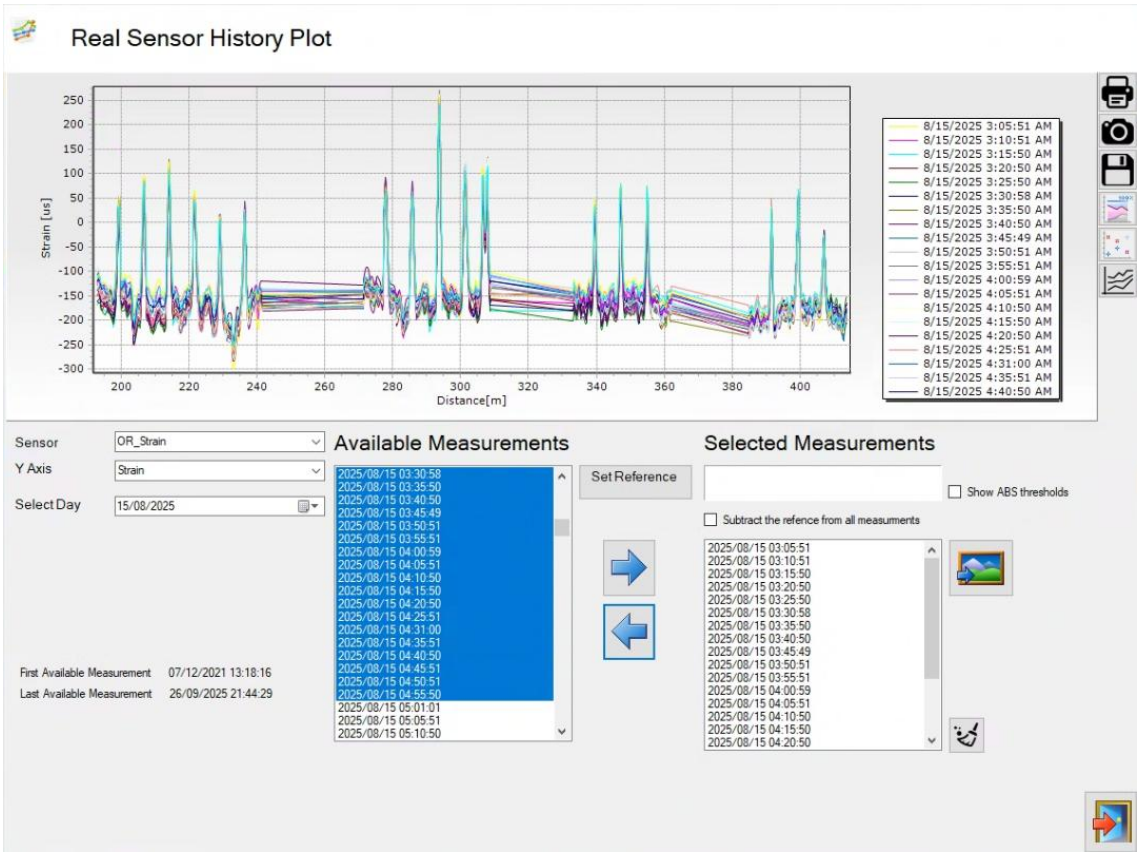

Figure 7.10: Raw strain profiles recorded by a representative FOS loop – temporal sequence

The strain profiles clearly reflect fluctuations in response to temperature changes, which are visually represented through color variations. Notably, sharp localized variations in strain occur at the pi-bracket locations due to the differences in mechanical properties and thermal expansion coefficients between the steel girder and the aluminum pi-brackets. These material differences induce strain discontinuities, resulting in distinct strain spikes in those regions, as clearly observed in Figure 7.10.

7.3. CRACK DETECTION METHODOLOGY

The mechanical behavior of the pi-bracket in the presence of cracks has been examined through a series of controlled experiments and FEA simulations. Building upon this foundation, the present section proposes an automated crack detection methodology by comparing strain data acquired

from field measurements with reference strain profiles simulated using FEA. This section presents techniques for processing distributed fiber optic sensor data collected from the pi-bracket system, aiming to reliably isolate crack-induced strain anomalies and to define criteria for sensor performance and detection limits applicable to real-world monitoring.

7.3.1. Controlled Environment Repeatability Assessment and Threshold Calibration

As shown in Figure 7.10, strain readings recorded over a two-hour interval clearly reveal significant influence of temperature fluctuations on strain measurements. To establish a robust detection threshold that is independent of such environmental effects, calibration was performed in a controlled environment using a small-scale experimental apparatus.

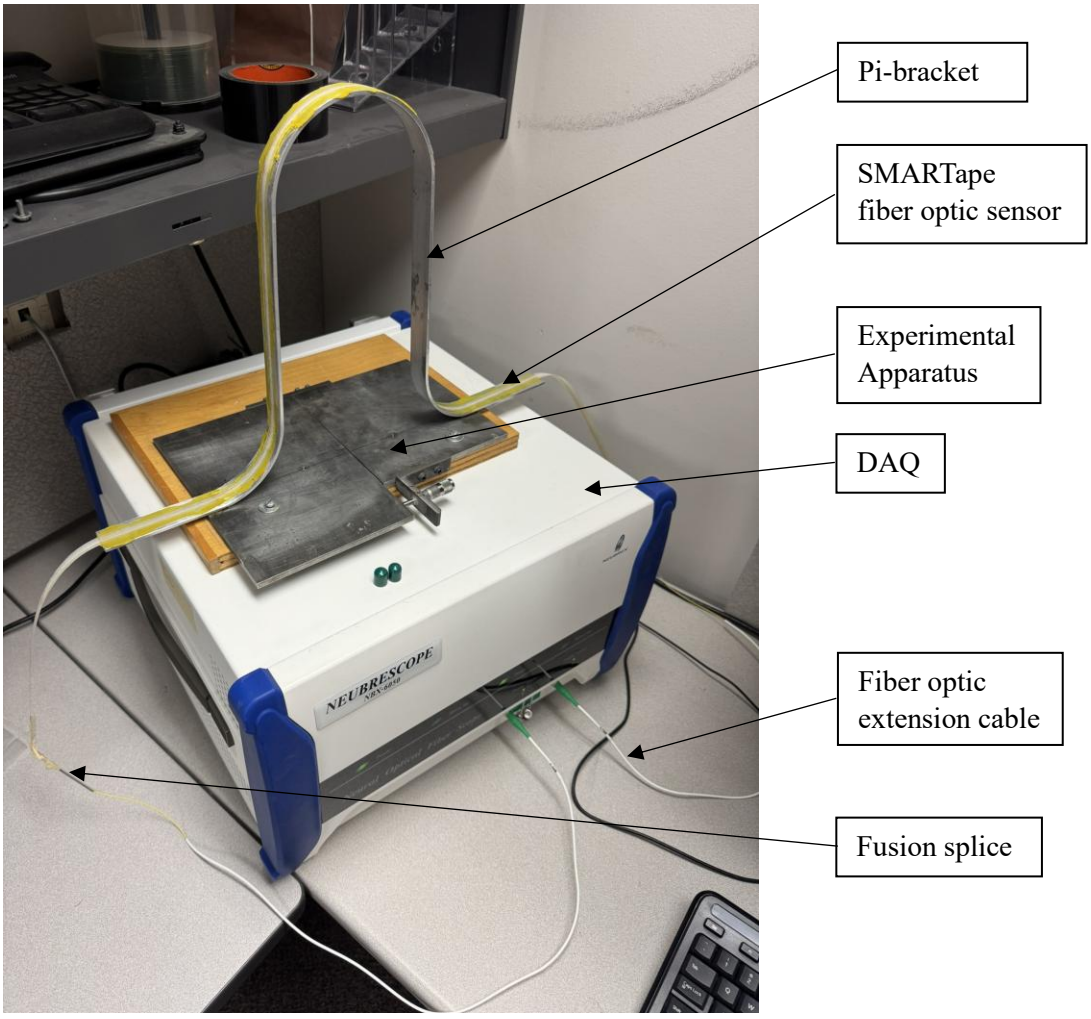

Figure 7.11: Experimental Setup

This is the same apparatus previously described in Chapter 3, used for DAQ settings optimization. Figure 7.11 shows the experimental apparatus setup adopted for the threshold calibration.

7.3.2. Experimental Procedure

The experimental apparatus instrumented for prior DAQ optimization was utilized without modification for threshold calibration. Detailed instrumentation and setup descriptions are provided in Chapter 3. Multiple measurements were recorded under stable conditions to assess repeatability of the FOS system, quantify measurement noise, and define a detection threshold. The DAQ reading unit configuration is presented in Appendix E.

The initial measurement served as a baseline, as presented in Figure 7.12.

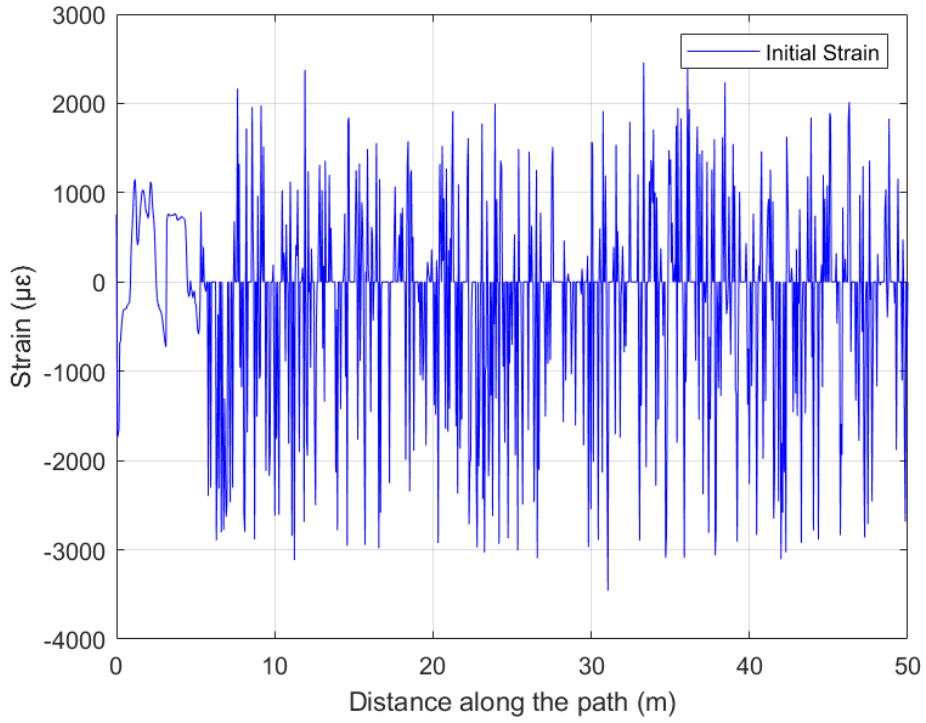

Figure 7.12: Initial strain measurement

The Neubrescope NBX-6050 was configured with a minimum sensor length of 50 meters, so that, any data recorded beyond the actual sensor length, approximately 3.5 meters including the

extension cables, represent electronic noise and do not constitute valid strain measurements. To enhance clarity in data presentation, Figure 7.13 shows strain profiles limited to the first 5 meters, thereby excluding electronic noise beyond this range from the analysis. In Figure 7.13, vertical magenta dashed lines indicate the location of the SMARTape fiber optic sensor along the path, while vertical green dashed lines identify the location of the pi-bracket.

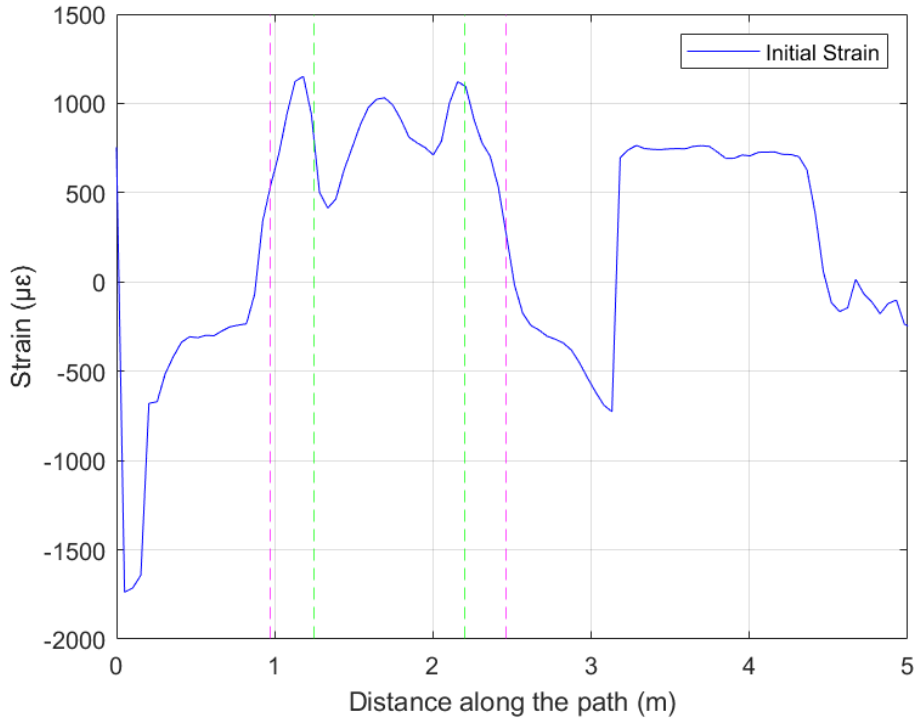

Figure 7.13: Initial strain measurement - close up detail to first 5m

For repeatability assessment, the SMARTape fiber optic sensor included spliced extension fibers at both ends. Because the extension cables may exhibit physical or sensing characteristics that differ from those of the primary sensor, only the SMARTape segment between 0.95 m and 2.45 m was considered in the evaluation. This segment includes the pi-bracket located between 1.25 m and 2.25 m along the path of the sensor.

Subsequently, ten consecutive measurements were acquired in a short time, without altering the setup, to ensure unchanged environmental conditions, as shown in Figure 7.14.

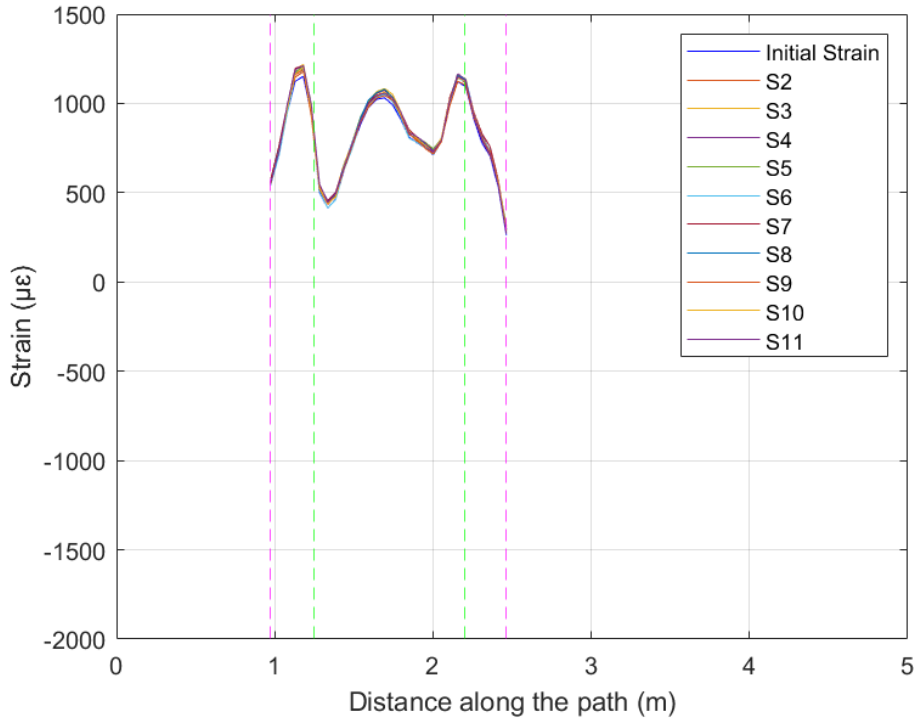

Figure 7.14: Raw strains for SMARTape FOS segment

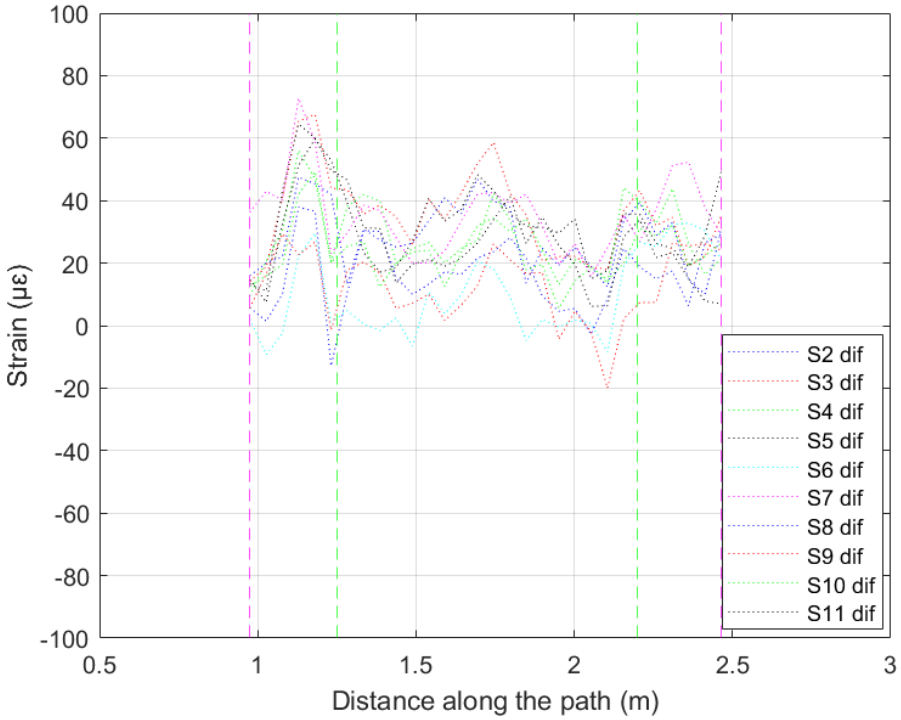

Figure 7.15: Differential strains for SMARTape FOS segment after baseline subtracted

Figure 7.14 presents data exclusively for the SMARTape segment between 0.95 m and 2.45 m along the sensor, since only this portion is considered in the evaluation. Each of the ten measurements was baseline-corrected by subtracting the initial measurement to determine the differential strain attributable to system noise, as shown in Figure 7.15.

7.3.3. Results

Standard deviations of differential strains at each spatial point within the SMARTape segment were obtained to characterize typical system noise. The detection threshold was conservatively set at three times the average standard deviation, calculated 37 με and indicated by a horizontal red line in Figure 7.16.

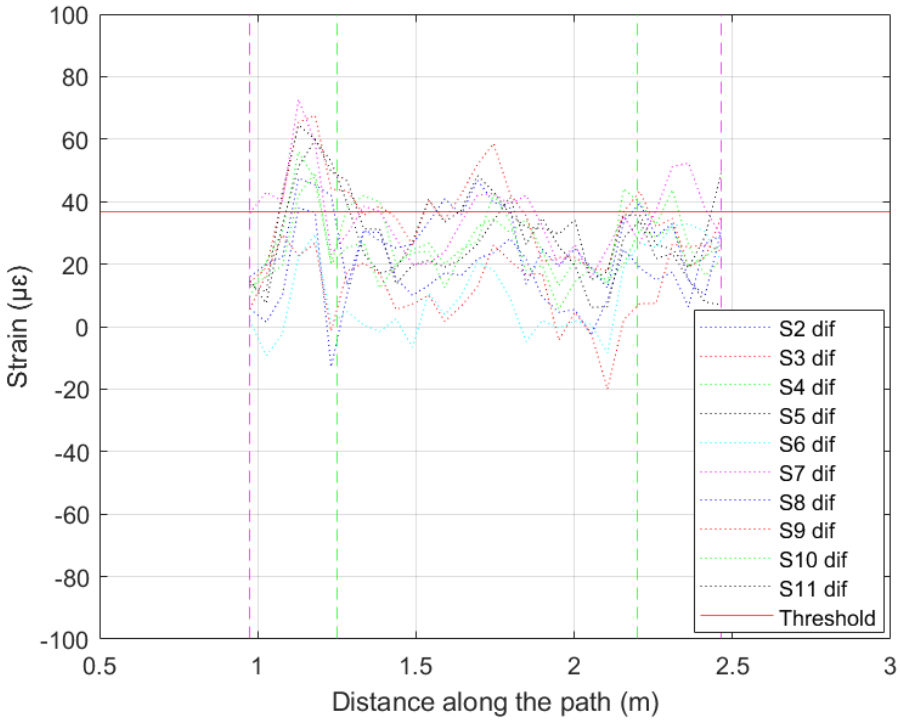

Figure 7.16: Threshold level for strain detection

The computed false positive rate from this calibration data was 20%, reflecting the frequency of erroneous detections under this threshold for the 5SR-10AR DAQ configuration. Variation in DAQ

setup that effects on threshold performance will be discussed in Section 7.3.4. Despite the relatively high false positive rate, the threshold remains at 37 με to prioritize early detection and prevention of structural damage that could lead to catastrophic failure.

If a crack develops where the FOS is directly attached to the girder, a substantial strain increase exceeding the threshold will be observed, triggering an immediate alert. In contrast, cracks occurring near the stiffeners display a distinct strain pattern (see Chapter 6), for which pattern recognition will be employed to mitigate false alarms.

Establishing a detection threshold using repeatability data from controlled laboratory conditions, rather than from field measurements, is essential to accurately differentiate true measurement noise from genuine structural changes. In a controlled environment, external variables such as traffic, wind, temperature fluctuations, and operational loads are minimized or held constant. This isolation allows for quantification of the sensor system's intrinsic noise characteristics, those attributed strictly to the sensor hardware, installation, and DAQ electronics, absent the unpredictable disturbances encountered in the field (Rodrigues, Inaudi, and Glisic 2013).

If threshold calibration were conducted using field-acquired data, the resulting noise estimate would be confounded by ambient environmental and operational influences. These additional sources of variation would inflate the noise estimate, leading to overly conservative thresholds that could mask subtle crack-induced strain events and reduce the sensitivity of the crack detection system. Conversely, laboratory-derived noise thresholds offer a robust and repeatable benchmark that is independent of site conditions. By setting the detection threshold at three times the standard deviation, the system achieves high confidence that any strain excursion exceeding this level is unlikely to be noise and is instead indicative of a real structural change.

This methodology not only ensures the reliability of crack detection by minimizing false positives and negatives but also allows for subsequent adaptation and refinement of the threshold as field-specific noise trends are better understood during long-term deployment (Rodrigues, Inaudi, and Glisic 2013).

7.3.4. DAQ Configuration Effect on Crack Detection

Two crack scenarios are investigated: one where the crack occurs in the girder area under direct FOS attachment and the other near a vertical stiffener. Building upon Chapters 5 and 6, this section evaluates DAQ setting influences on crack detectability. We can now analyze how different DAQ configurations affect the detectability of such cracks using the established detection threshold. This evaluation helps to clarify which DAQ settings optimize sensitivity to potential cracks in these critical bridge locations.

The DAQ used in the experiment was configured with a 5 cm sampling interval (SR) and 10 cm spatial resolution (AR), meaning that strain measurements were taken every 5 cm along the sensor, and each measurement represents an average strain value over a 10 cm segment. As presented in Chapter 5, if a crack develops in the area where the FOS is directly attached to the girder, the resulting strain change will be significant, easily exceeding the established threshold, which is shown as horizontal red lines, without need for further clarification. Such an event would trigger an immediate notification to the bridge owner for intervention.

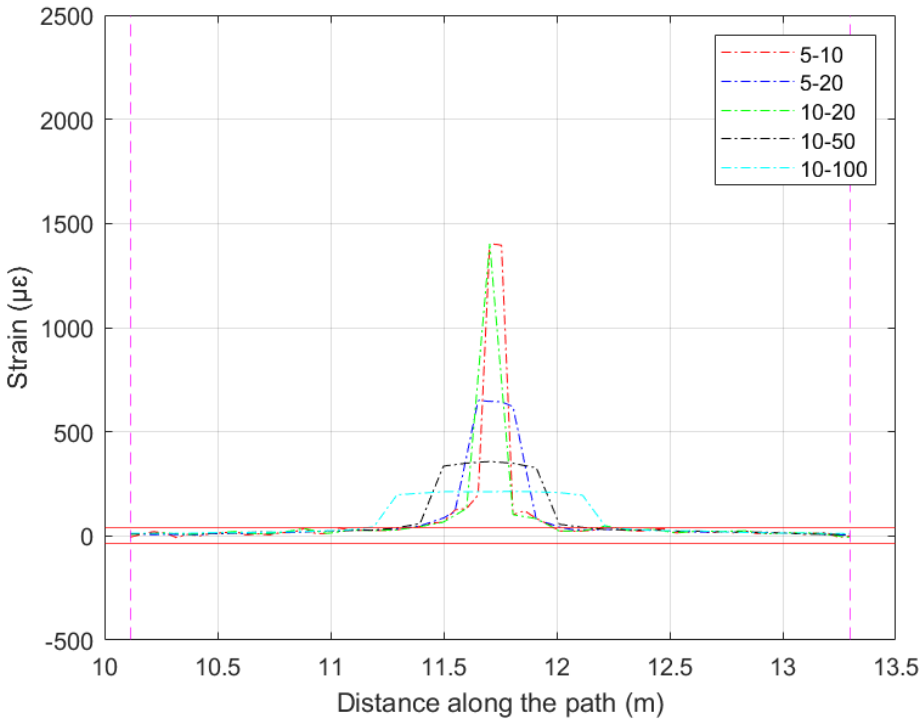

Figure 7.17: Strain profiles for 0.1mm crack at girder under different DAQ configurations

Figure 7.17 presents strain profiles as observed during the laboratory testing presented in Chapter 5 for a 0.1 mm crack opening in the region of the girder where the FOS is directly attached. While Chapter 5 primarily presents the strain under the one DAQ configuration (5SR-10AR), the current figure additionally illustrates the strain profiles averaged according to various DAQ configurations, thereby elucidating the influence of these configurations on the measured strain response.

Figure 7.18 shows the corresponding profiles for a 0.2 mm crack opening, also illustrating the influence of varying DAQ configurations.

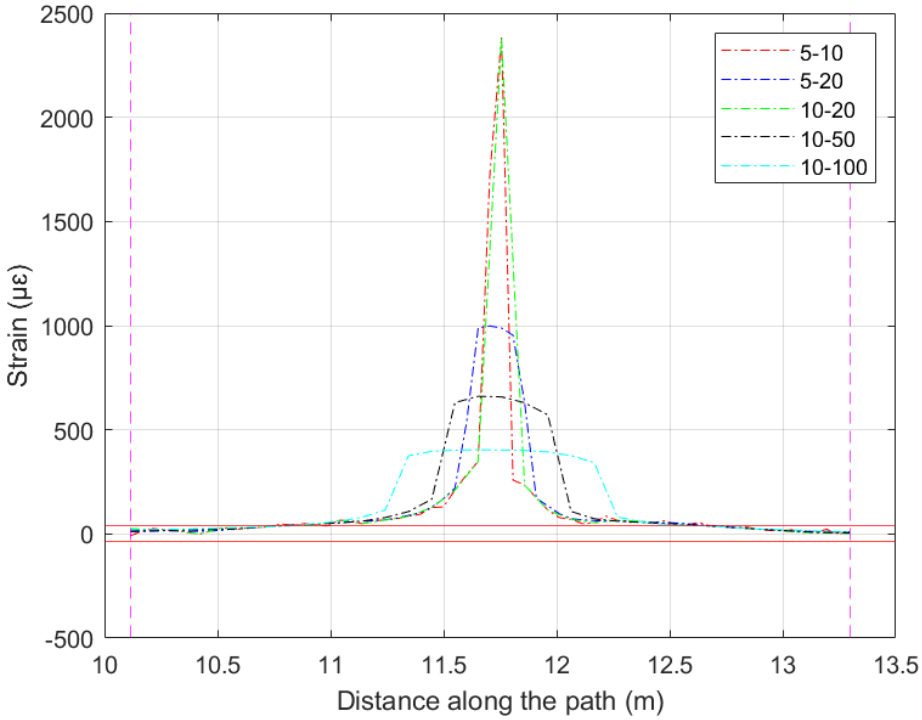

Figure 7.18: Strain profiles for 0.2mm crack at girder under different DAQ configurations

In contrast, if a crack develops near a vertical stiffener, the strain profile exhibits a unique pattern due to the shape of the pi-bracket, as discussed in Chapter 6.

The influence of DAQ configuration on the strain profile critically determines whether the observed strain change is sufficient to surpass the threshold and be distinguished from noise. Figure 7.19 presents results from FEA simulations for a 0.1 mm crack opening near stiffener,

illustrating how different DAQ configurations perform against the established threshold. None of the strain profiles under the investigated DAQ configurations exceed the established threshold level, indicating that a 0.1 mm crack would likely go undetected using the current procedure.

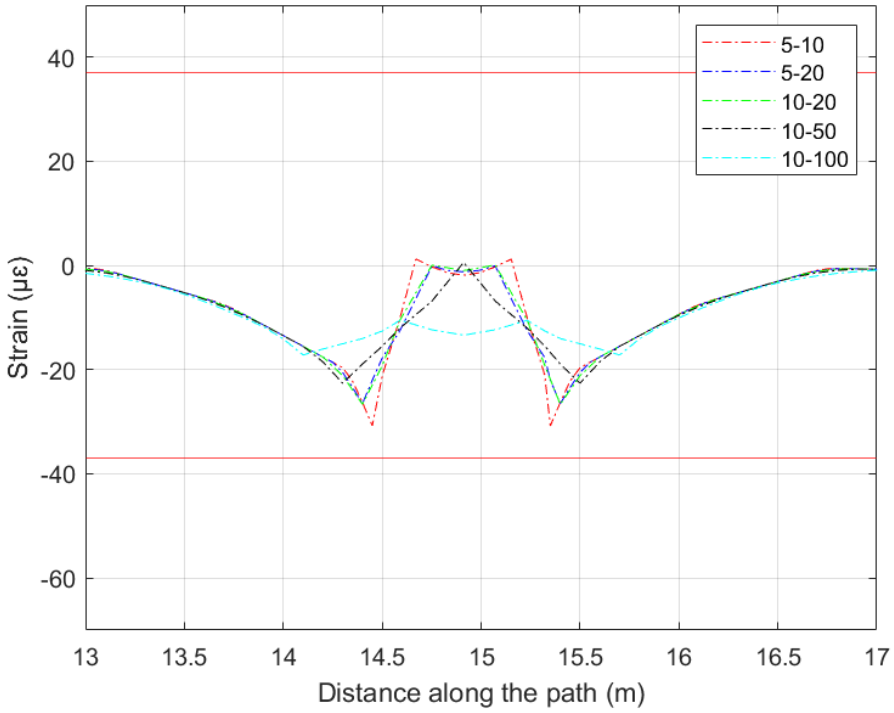

Figure 7.19: Strain profiles for 0.1mm crack near a vertical stiffener under different DAQ configurations

Figure 7.20 presents similar results for a 0.2 mm crack developed near the pi-bracket. The configurations 5SR-10AR, 5SR-20AR, and 10SR-20AR perform best in terms of crack detection, with strain changes exceeding the threshold. The 10SR-50AR configuration still barely surpasses the threshold and based on the similarity between 5SR-20AR and 10SR-20SR, it is expected that 5SR-50AR will behave similarly to 10SR-50AR. Conversely, under the 10SR-100AR configuration, the crack would not be detected, with expectations that 5SR-100AR would likely go undetected too.

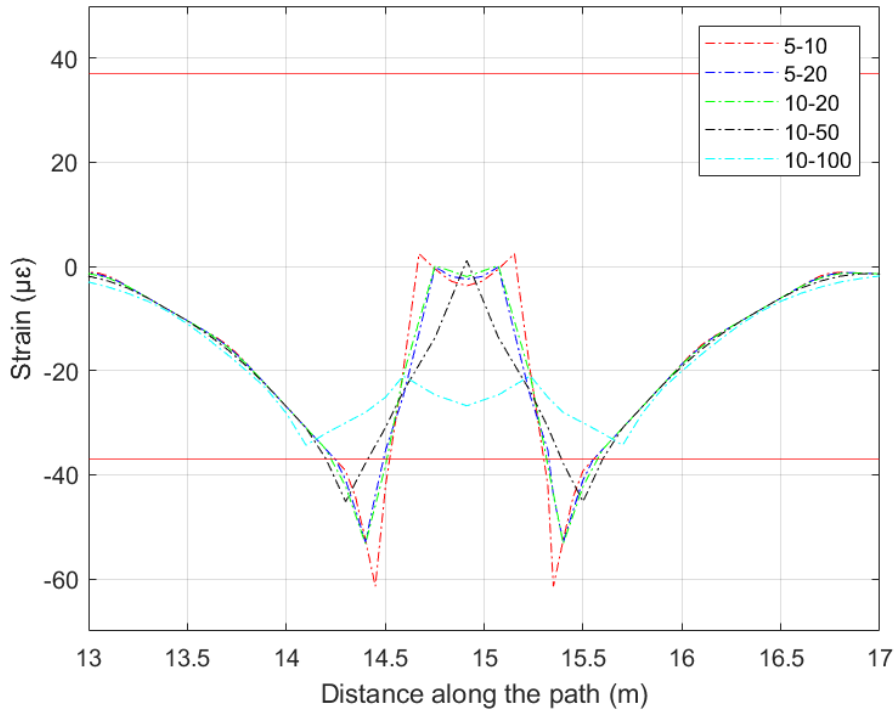

Figure 7.20: Strain profiles for 0.2mm crack near a vertical stiffener under different DAQ configurations

7.3.5. Proposed Crack Detection Procedure

The crack detection procedure consists of the following steps:

1. Establish baseline strain profiles under uncracked conditions to account for environmental and operational effect.
2. Acquire strain profiles continuously at fixed intervals during field monitoring.
3. Compute strain differential profiles by subtracting the baseline measurement from the current measurement to isolate temporal changes.
4. Compare these differential profiles to DAQ-adjusted FEA-simulated strain patterns corresponding to known crack sizes (0.1mm and 0.2mm openings).
5. Apply alarm threshold for crack indication: Any localized strain anomaly exceeding 37 με (corresponding to three standard deviations of the RMS noise in the fiber optic sensor system) is flagged as significant.

6. Employ advanced signal processing (spatial averaging, anomaly detection algorithms) to reduce false positives and enhance detection reliability.

This threshold-based approach targets significant strain events by flagging any localized strain anomaly exceeding 37 με, allowing for timely intervention and supporting proactive bridge management regardless of crack severity. It ensures robust differentiation between true crack-induced signals and noise, enabling reliable automated detection of early crack formation.

7.3.6. Validation of the Proposed Crack Detection Procedure

The data used in this validation are described in Section 7.2.2. These data were collected at five-minute intervals and transmitted for subsequent processing. Figures 7.9 and 7.10 present representative strain readings from a single sensor (O-R), with the data collected on August 15, 2025, between 03:00 AM and 05:00 AM. Figure 7.8 shows a raw single strain profile, while Figure 7.10 illustrates the temporal variation of strain readings at the same sensor over the two-hour period.

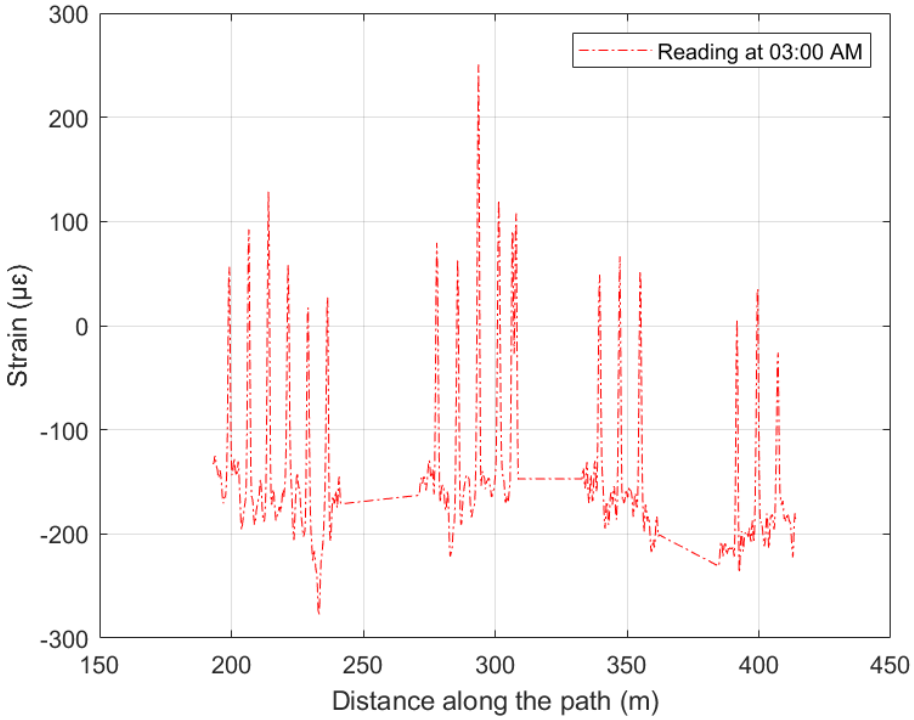

Figure 7.21: Initial raw strain reading

For validation purposes, the first reading at 03:00 AM is considered as the baseline measurement (Figure 7.21). Subsequent readings at 04:00 AM and 05:00 AM, as shown in Figure 7.22, are used to validate the proposed crack detection procedure. It is important to note that these strain measurements are raw data and have not yet been compensated for temperature-induced effects.

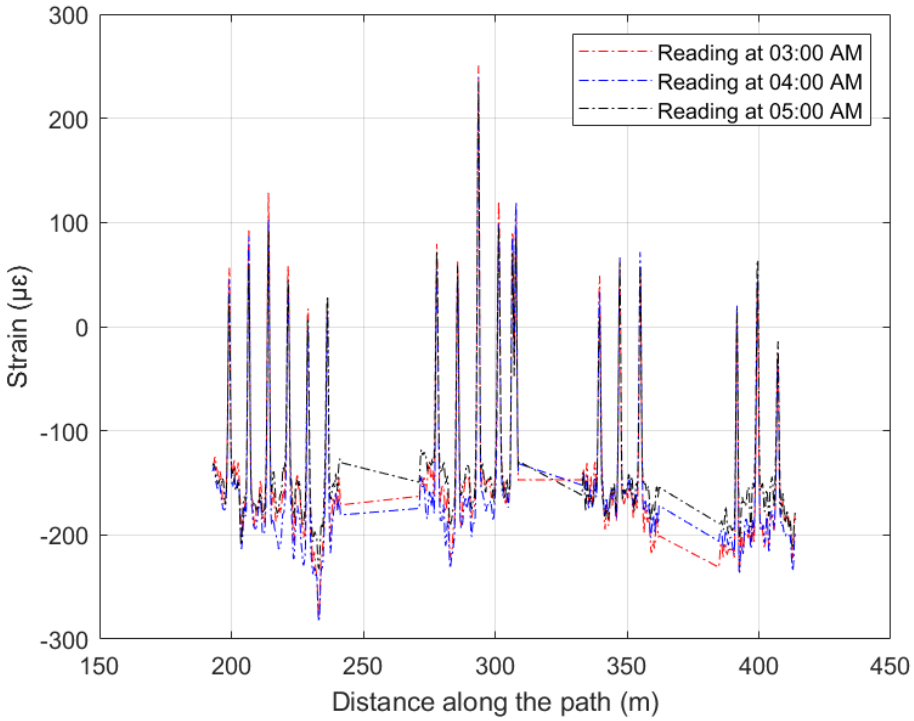

Figure 7.22: Three raw strain readings

To isolate temporal changes, all measurements were baseline-corrected by subtracting the initial reading at 03:00 AM. The differential strain for the 04:00 AM reading is presented in Figure 7.23, where horizontal red lines indicate the crack detection threshold. The differential strain generally remains within the threshold, with a few exceptions. As discussed in the previous section, if any strain exceeds the threshold, two scenarios would be investigated. The first considers crack formation in the girder, which would produce significant strain variations, not observed here. Instead, strain exceedances occur at a limited number of sampling points, suggesting potential crack development near stiffeners monitored with pi-brackets. Pi-bracket locations were established during initial sensor mapping, thus, spatial correlation between threshold exceedances

and pi-bracket positions allows for targeted pattern recognition. Since no corresponding pattern is evident, it can be concluded that these few exceedances do not indicate crack formation.

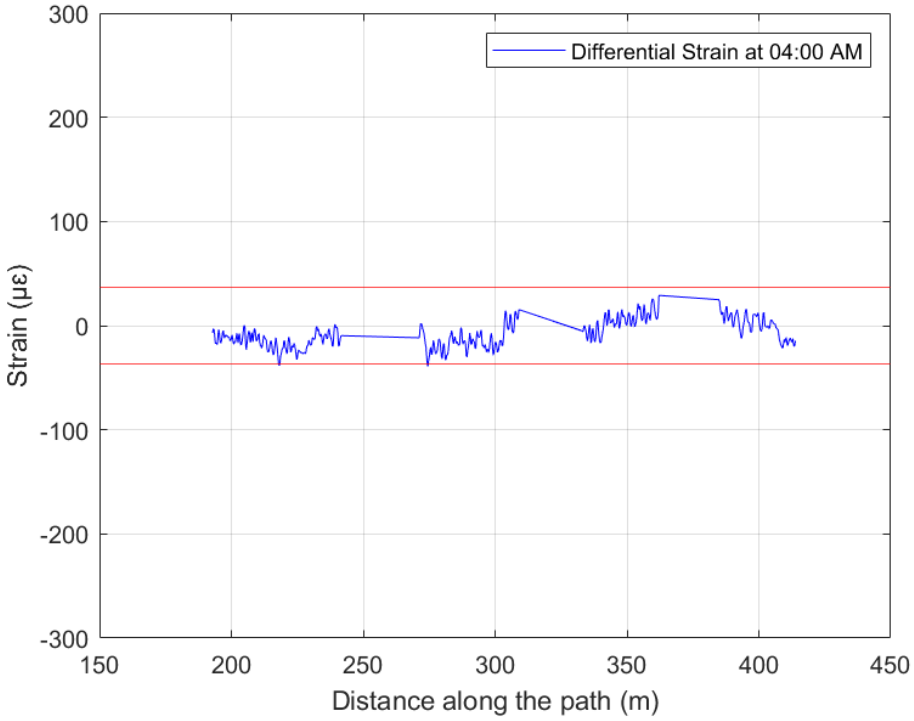

Figure 7.23: Differential strains at 04:00 AM

During signal processing, temperature data from the DAQ system is used to compensate for strain caused by temperature changes, ensuring accurate assessment of strain variations related to structural behavior. Figure 7.24 shows how the sampling point varies with temperature. It shows that the temperature at 03:00 AM is almost the same as at 04:00 AM, indicating that no temperature compensation is necessary in this instance. As noted earlier, fiber optic temperature sensors were installed alongside the strain sensors, but they are not yet used for automatic temperature compensation. Instead, temperature differences needed for compensation can be derived directly from the recorded data.

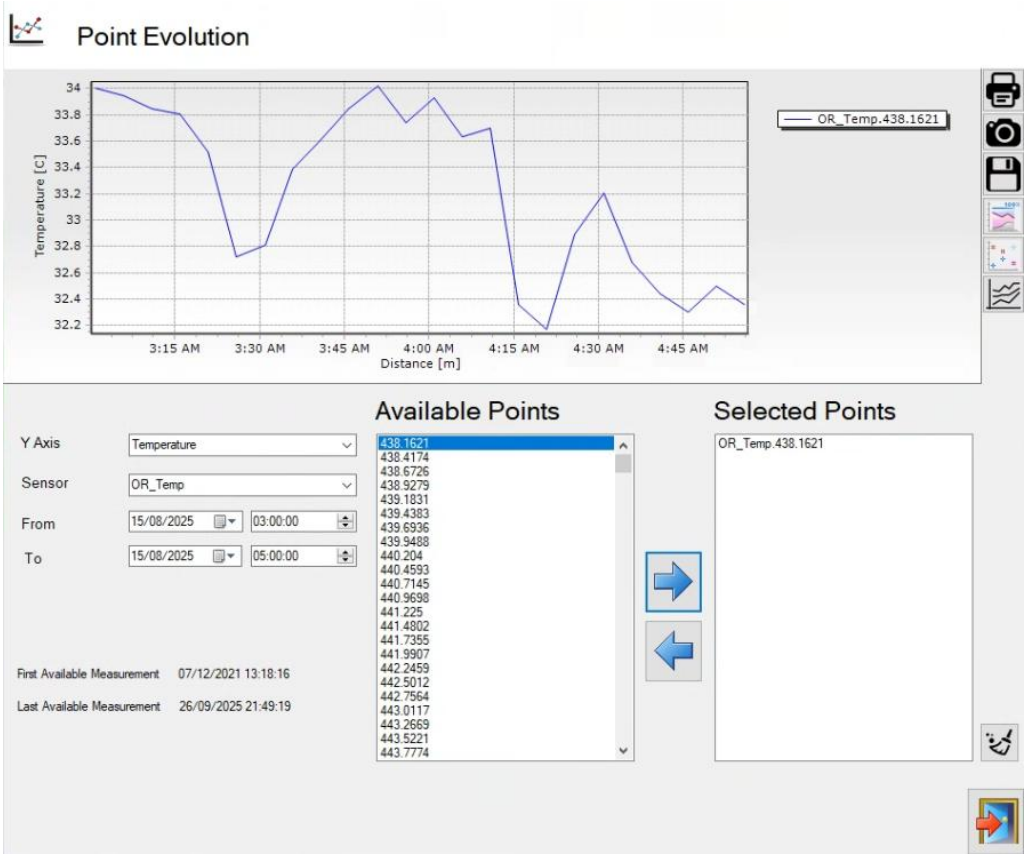

Figure 7.24: Temperature evolution of a single sampling point

Figure 7.25 presents the differential strain for the 05:00 AM reading. It is evident that significantly more strain values exceed the crack detection threshold at this time. Referring back to Figure 7.24, it can be observed that the temperature decreased by approximately 1.6 °C between 03:00 AM and 05:00 AM. This temperature drop has a considerable effect on the strain profile, as the fiber optic sensor measures total strain, which includes thermal strain.

Thermal strain ($\varepsilon_{thermal}$) is proportional to the temperature difference (ΔT) and the material's coefficient of thermal expansion (α), and can be expressed as:

$$\varepsilon_{thermal} = \alpha \times \Delta T$$

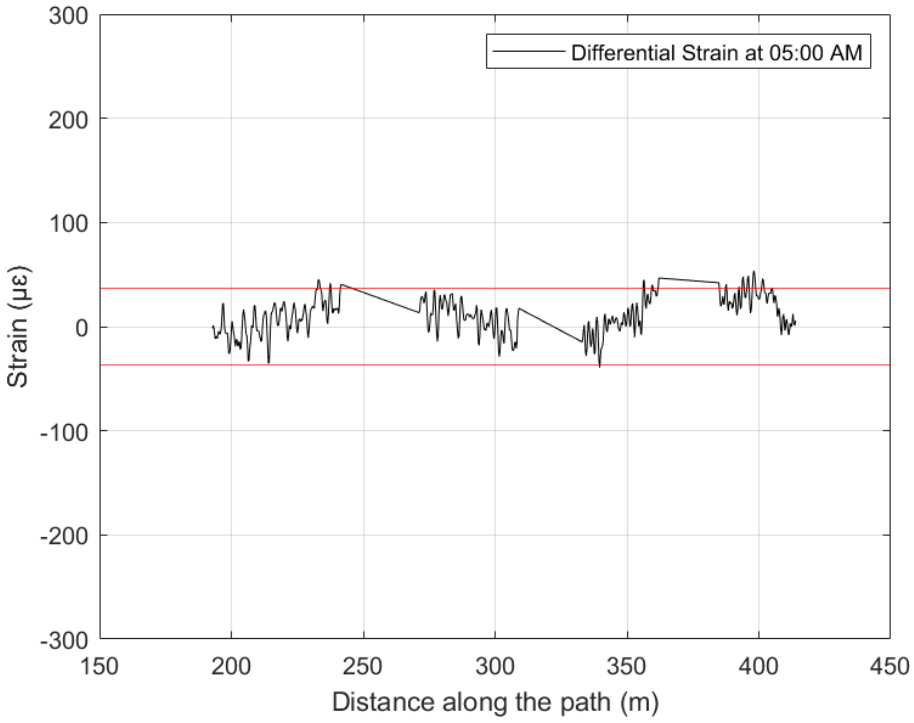

Figure 7.25: Differential strains at 05:00 AM

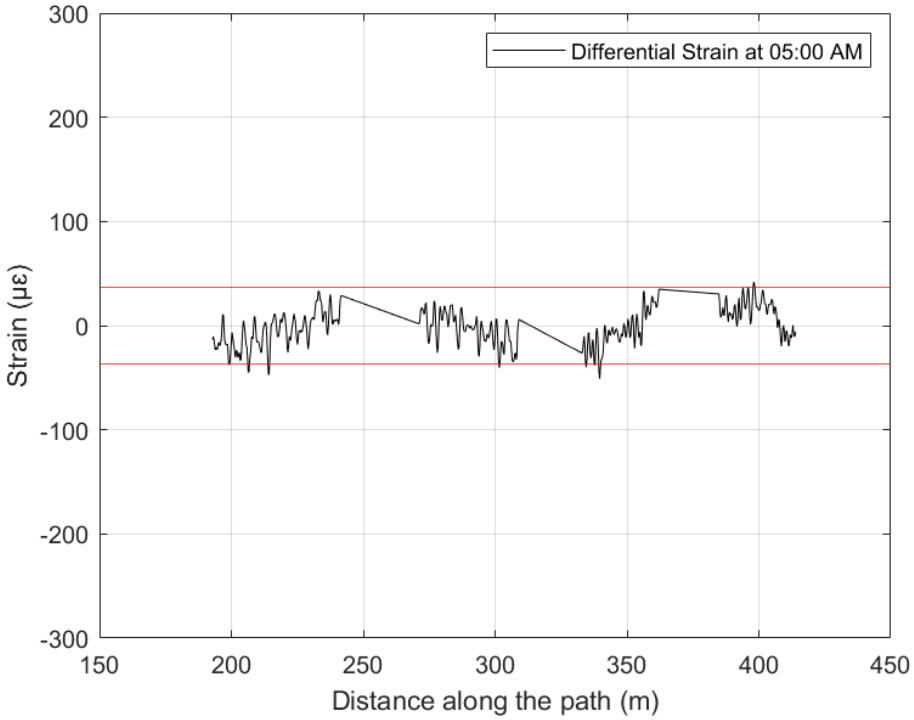

Figure 7.26: Differential strains at 05:00 AM – temperature compensated

The coefficient of thermal expansion for steel is 11.7με/°C, while for aluminum it is 23.4με/°C. Previous experiments have shown that the largest strain values are observed along the steel girder, whereas strains on the aluminum parts of the pi-bracket are minimal. Therefore, only the steel's coefficient of thermal expansion is considered in the signal processing.

Given the 1.6 °C temperature difference, the thermal strain adjustment amounts to approximately 18.72με. Figure 7.26 presents the temperature-compensated differential strain for the 05:00 AM reading. After the compensation, the strain profile lies more consistently within the threshold boundaries. Although some strain values still exceed the threshold, further examination indicates these are not attributable to crack formation.

This preliminary validation assesses the effectiveness of the proposed crack detection procedure when applied to real bridge data without any cracks, providing an evaluation of the procedure's performance under actual field conditions, however, validation under conditions involving an actual crack would be beneficial for confirmation

7.3.7. Discussion

7.3.7.1. Signal Processing

Automated crack detection in steel girders relies heavily on signal processing techniques to extract meaningful information from the raw strain data collected by distributed FOS. The methodology discussed in this chapter, involving detailed finite element simulations of full-scale girders with and without crack, provides a foundation for understanding how crack-induced strain variations manifest along the girder length. These simulations generate strain profiles that serve as numerical baselines and reference conditions, critical for distinguishing normal structural responses from crack-induced variations.

In field monitoring, strain measurements are collected at regular intervals. To detect crack formation or progression, each new strain reading is compared against an initial baseline profile by computing a strain difference profile. This difference aims to isolate changes specifically attributable to crack development while filtering out static influences such as dead load, or previously discussed boundary conditions. However, strain variations are caused not only by

temperature but also by other environmental and operational factors including traffic loads, humidity, wind, and installation-related influences (Svendsen et al. 2022).

The field-obtained strain differentials are compared with simulation-based profiles adjusted for the spatial and sampling resolution of the DAQ. Averaged differential strain profiles from finite element analysis represent signature patterns for cracks of defined sizes under specific loading, providing benchmarks for field data interpretation. By comparing the measured strain differentials from the field to these DAQ-matched simulation profiles, the automated detection system can accurately assess the presence and estimate the severity of cracks developing in the steel girder.

To reliably detect cracks, it is crucial to assess the repeatability and noise characteristics of the sensing system in a controlled environment prior to field deployment. Controlled validations involve subjecting test samples or specimen girders to known loading and thermal cycles in a laboratory or sheltered setting, where external disturbances can be minimized or systematically varied. This process enables characterization of the measurement noise floor and identification of threshold levels above which observed strain changes can be confidently attributed to structural damage rather than measurement variability (Bao and Chen 2012).

Measurement noise arises from multiple sources: sensor intrinsic noise, installation variability, optical signal loss or attenuation, data acquisition system resolution limits, and environmental disturbances (Inaudi et al. 2001; Barrias et al. 2016).

Thresholds for crack detection are then set at levels exceeding the quantified noise, ensuring a high signal-to-noise ratio. Experimental and field studies report that strain increments on the order of a few microstrains, when spatially localized, correspond reliably to crack initiation and propagation. Signal enhancement techniques including spatial averaging over sensor segments and anomaly detection algorithms improve detection sensitivity and specificity. Averaging reduces random measurement fluctuations, while algorithms utilize pattern recognition to discriminate structural changes from noise. By integrating simulation-based strain signatures with empirically derived noise thresholds, the automated monitoring system achieves reliable early warning capability. This approach facilitates preventive maintenance interventions, reducing risk and extending bridge service life (Richter et al. 2024; Mikhailov et al. 2023).

7.3.7.2. Sensor Performance Criteria and Detection Limits

The practical success of the pi-bracket sensor system in crack detection is influenced by factors such as spatial resolution and strain resolution. Current distributed FOS technologies achieve spatial resolution on the order of centimeters and strain resolution in the microstrain range, enabling detection of early-stage cracks with openings around 0.1 mm or smaller (Richter et al. 2024).

The design of the pi-bracket facilitates effective mechanical coupling between the optical fiber sensor and the steel girder, particularly across vertical stiffeners where cracks frequently develop. This coupling ensures efficient strain transfer, enhancing detection capability. External factors such as environmental noise, installation quality, and operational conditions can impact detection limits, but careful sensor design and robust data processing methodologies mitigate these effects.

Integration with finite element modeling allows prediction and interpretation of strain patterns, supporting the optimization of sensor placement and configuration. This combined approach strengthens confidence in early crack detection and provides valuable insights for structural health monitoring and maintenance planning.

7.3.7.3. Temperature Effects on Sensor Signal

Accurate crack detection using FOS in bridge girders is influenced not only by mechanical strain but also significantly by temperature variations. Temperature fluctuations induce thermal expansion or contraction in both the fiber optic sensor and the host structure, leading to changes in strain readings that are unrelated to structural damage. Understanding and addressing these temperature effects is critical to prevent misinterpretation of sensor data and ensure reliable SHM. This section explores the influence of temperature on fiber optic strain measurements, the challenges posed by temperature-strain cross-sensitivity, and effective approaches for temperature compensation to enhance sensor accuracy and reliability in diverse environmental conditions.

Fiber optic sensors operate by measuring changes in light properties such as Brillouin frequency shift, which are affected by both mechanical strain and temperature. Temperature variations induce physical changes in the fiber optic material and its surrounding environment, resulting in

measurable frequency shifts that can mask or mimic strain signals from structural deformation. In bridge structures subjected to wide temperature ranges, often spanning from sub-zero winters to warm summers, these thermal influences can lead to significant signal deviations. For example, aluminum components exhibit higher coefficients of thermal expansion and conductivity compared to steel girders, resulting in differential thermal strain that complicates interpretation. Therefore, temperature-induced strain variations must be properly understood and accounted for to avoid false positives or negatives in crack detection.

One intrinsic challenge of fiber optic sensing technology is temperature-strain cross-sensitivity. Because both temperature and mechanical strain affect the optical signals similarly, disentangling the two influences becomes complex. This cross-sensitivity can lead to measurement errors where temperature changes are incorrectly identified as strain, or genuine strain signals are obscured. In structural health monitoring, such errors can undermine the accuracy of crack detection and condition assessment, leading to inappropriate maintenance actions or overlooked damage. Environmental factors such as diurnal temperature cycles, seasonal shifts, and transient thermal loads further exacerbate this issue. Additional complexities arise from differential thermal responses between sensor materials, adhesives, and the host structure, causing localized inaccuracies.

To overcome temperature-strain cross-sensitivity issues, several compensation and mitigation strategies have been developed and integrated into SHM systems. These include the use of co-located temperature sensors alongside strain sensors to measure ambient temperature independently, enabling mathematical subtraction of temperature effects from strain data. Advanced signal processing algorithms and baseline correction techniques further isolate mechanical strain components. Proper sensor installation methods, such as bonding protocols that minimize thermal mismatches and selecting materials with compatible thermal expansion properties, reduce induced thermal strain. Moreover, the application of dual-parameter sensing techniques, leveraging the distinct temperature and strain sensitivities of multiple optical phenomena, enhances the ability to differentiate between temperature and strain signals. These comprehensive approaches ensure that sensor outputs reflect true structural responses rather than environmental artefacts.

Integrated temperature monitoring is essential for achieving reliable and accurate SHM using fiber optic sensors. By deploying dedicated temperature sensors in close proximity to strain sensors, the system can continuously monitor and compensate for temperature variations affecting the optical signals. This integration is especially important in bridge applications where infrastructure experiences extreme and rapid temperature changes, which can significantly influence sensor readings. The data from temperature sensors provide the foundational reference for calibration, baseline subtraction, and real-time correction of strain measurements. Additionally, including temperature measurements aids in understanding the structural thermal behavior influencing fatigue crack initiation and propagation. Therefore, embedded temperature monitoring not only improves data fidelity and detection confidence but also supports holistic infrastructure health assessment under varying environmental conditions (Omnisens 2009).

7.4. CONCLUSIONS

This chapter has provided a detailed case study of applying the pi-bracket sensor system integrated with distributed fiber optic sensing technology for structural health monitoring of a steel bridge in Manitoba, Canada. The study affirmed the system's capability for continuous, high-resolution strain measurement, especially across challenging stiffened girder regions where fatigue cracks are prone to initiate. Critical to the methodology is the establishment and use of a conservative detection threshold set at 37με, derived from controlled laboratory repeatability tests and validated through extensive field instrumentation.

The proposed crack detection procedure, grounded in finite element simulations and supported by signal processing techniques to compensate for temperature effects and environmental noise, was successfully validated against real-world bridge data. While no cracks were present in the monitored bridge during the study period, the validation demonstrated the system's sensitivity and robustness in distinguishing strain signals that could indicate crack formation from normal structural and environmental variations.

The integration of predictive strain signatures from simulations with reliable noise thresholds and temperature compensation protocols ensures high confidence in early crack detection. Moreover,

the mechanical design of the pi-bracket facilitates efficient strain transfer and sensor protection over stiffeners, overcoming common limitations seen in traditional fiber optic sensor installations.

Although the bridge condition during this study did not involve active cracks, the findings establish a solid foundation for future monitoring environments where crack initiation and propagation may occur. Validating the procedure on live field data without cracks offers critical insight into baseline variability and system reliability under actual operating conditions, an essential step toward widespread deployment.

In summary, this chapter illustrates that combining rigorous laboratory validation, robust simulation-based methodologies, and comprehensive field instrumentation enables effective, automated detection of fatigue cracks in steel bridge girders. The demonstrated 37με threshold serves as a key parameter underpinning the detection reliability, and with future validation under crack-containing conditions, the approach promises to significantly enhance structural safety, maintenance prioritization, and long-term durability of bridge infrastructure.

CHAPTER 8: CONCLUSIONS AND RECOMMENDATIONS

8.1. CONCLUSIONS

This research has investigated the performance of the pi-bracket sensor system for SHM in steel girders of bridges to detect cracks formed near vertical stiffeners, combining experimental testing, FEA, and theoretical validation. The following conclusions are drawn from the findings of each chapter:

Chapter 3: Pi-Bracket Design and Sensor Integration

1. The pi-bracket configuration was successfully designed to address challenges associated with monitoring difficult-to-access areas near vertical stiffeners in bridge girders.
2. The integration of BOTDA technology enabled distributed strain measurements while protecting FOS from mechanical damage.
3. The pi-bracket design ensures continuous strain monitoring along the beam length without interruptions, making it suitable for SHM applications.

Chapter 4: Pi-Bracket Optimization

1. The Pi-bracket was identified as the optimal design due to its high strain sensitivity and low displacement among evaluated concepts.
2. The smaller 8-inch bracket showed higher strain measurements than the 12-inch version and was selected for laboratory testing.
3. Increased bracket thickness correlates with higher strain values while displacement remains consistent.
4. Aluminum prototypes were used for ease of fabrication, though steel is recommended for long-term use due to better thermal compatibility and durability.

Chapter 5: Laboratory Experiments

1. The pi-bracket sensor system demonstrated reliable detection of crack openings as small as 0.2mm during laboratory experiments.

2. Strain measurements of 60.6 με and 129 με were recorded by the fiber optic sensor distributed over the pi-bracket at crack openings of 0.1 mm and 0.2 mm, respectively, demonstrating the system's sensitivity to crack-induced strains.
3. The system effectively captured localized strain changes near vertical stiffeners, confirming its suitability for fatigue crack monitoring in critical areas of steel girders.

Chapter 5: Validation of Experimental and FEA Results

1. Comparative analysis between FEA and laboratory experiments revealed discrepancies of 12.8% and 7% for the maximum strain values at crack openings of 0.1 mm and 0.2 mm, respectively. Specifically, for the 0.1 mm crack, FEA predicted a maximum strain of 69.5 με, while the experimental measurement was 60.6 με. For the 0.2 mm crack, FEA predicted a maximum strain of 139 με, compared to an experimentally measured strain of 129 με
2. This agreement validated the system's effectiveness and reliability, as well as the robustness of the modeling approach used for design optimization.
3. The strain subtraction methodology effectively isolated crack-induced strain variations, enabling targeted assessments of sensor performance.

Chapter 6: FEA Simulations on Full-Scale Girder Models

1. FEA simulations demonstrated that cracks lead to measurable redistribution of strain, particularly in the vicinity of the pi-bracket.
2. By employing a strain subtraction methodology, the simulations isolated strain variations attributable solely to crack formation:
    - Pi-bracket crown: -2.4με (0.1mm crack opening) and -4.8με (0.2mm crack opening).
    - Pi-bracket-girder contact point: -35.64με (0.1mm crack opening) and -71.28με (0.2mm crack opening).
3. The simulations confirmed that the pi-bracket sensor is capable of detecting localized strain changes caused by cracks in larger girder models.
4. The results reinforced the scalability of the pi-bracket system for field SHM applications, demonstrating its ability to monitor fatigue-prone areas in bridge girders effectively.

Chapter 7: Case Study - Crack Detection Methodology

1. The pi-bracket sensor system demonstrated effective high-resolution strain monitoring on a Manitoba steel girder bridge, particularly in regions prone to fatigue cracks near stiffeners.
2. A conservative crack detection threshold of 37 με was established from laboratory tests and was validated with field data, providing a reliable standard for early crack identification.
3. Validation using FEA simulations and signal processing techniques ensured robust detection by compensating for temperature and environmental effects.
4. While no cracks were detected during the study, the system's sensitivity to distinguish crack-related signals establishes a solid baseline for future crack monitoring.
5. This integrated approach combining laboratory, simulation, and field data supports effective automated crack detection, promoting improved bridge safety and maintenance efficiency.

These conclusions collectively validate the pi-bracket sensor's performance with experimental and numerical investigations, confirming its potential for practical applications in SHM.

8.2. RECOMMENDATIONS

While this study successfully demonstrated the reliability of the pi-bracket sensor system for crack detection, several areas warrant further investigation to enhance its performance and applicability:

1. Refinement of FEA Models:
    - Improve mesh density in FEA simulations to capture more accurate strain distributions around cracks and pi-brackets.
    - Develop FEA models incorporating crack propagation to investigate strain evolution during crack growth.

2. Validation Under Dynamic Loading Conditions:
    - Conduct experiments and simulations under dynamic loading scenarios to evaluate how the pi-bracket performs under fluctuating stresses typical of bridge environments.
    - Investigate its sensitivity to high-cycle fatigue cracking caused by repeated loading over time.
3. Optimization of Sensor Placement:
    - Optimize sensor placement along girders to ensure maximum coverage of critical areas prone to fatigue cracking while minimizing costs.
    - Investigate whether alternative configurations improve signal clarity or reduce installation complexity.
4. Development of Predictive Models:
    - Use data collected from laboratory experiments and field tests to develop predictive models for crack propagation based on strain measurements.
    - These models could help engineers anticipate potential failure points before they occur.
5. Application to Truss Bridges:
    - Investigate the adaptability of the pi-bracket sensor system for tension chords of truss bridges, which present distinct structural configurations and stress distributions compared to girder bridges.
    - Assess whether the strain subtraction methodology and BOTDA integration remain effective in detecting cracks at truss joints or under complex multi-directional loading.
6. Temporary FOS Bonding Techniques:
    - Explore methods for temporary bonding and debonding of FOS without damaging the substrate or compromising measurement accuracy.

- Develop reusable or non-invasive attachment mechanisms (e.g., magnetic clamps, adhesive tapes with controlled release) to enable flexible sensor deployment for short-term monitoring.

By addressing these recommendations, future research can further enhance the reliability, scalability, and practicality of the pi-bracket sensor system for SHM applications in bridge girders.

REFERENCES

Abruzzese, D., Micheletti, A., Tiero, A., Cosentino, M., Forconi, D., Grizzi, G., Scarano, G., Vuth, S., and Abiuso, P. (2024). “IoT sensors for modern structural health monitoring: A new frontier.” Journal of Structural Engineering, 150(11).

American Society of Civil Engineers. (2017). Minimum design loads and associated criteria for buildings and other structures (ASCE/SEI 7-16), ASCE, Reston, VA.

ANSYS, Inc. (2023). ANSYS: Engineering simulation and 3D design software, ANSYS, Inc. Accessed December 23, 2024. https://www.ansys.com/

ASM International. (1990). "Properties and Selection: Nonferrous Alloys and Special-Purpose Materials." ASM Handbook, Vol. 2, ASM International, Materials Park, OH.

Atamturktur, S., Aydinoglu, M.N., and Kucukdemirci, A. (2014). “Structural Health Monitoring for Sustainable and Resilient Infrastructure Management.” Journal of Civil Engineering, 18(1), 1-12.

Autodesk. (2023). Revit: BIM software for architects, engineers, and contractors, Autodesk. Accessed December 23, 2024. https://www.autodesk.com/products/revit/overview

Azimi, M., Eslamlou, A. D., and Pekcan, G. (2020). “Data-driven structural health monitoring and damage detection through deep learning: State-of-the-art review.” Sensors, 20(10).

Bakht, B., and Mufti, A. (2015). *Bridges: Analysis, Design, Structural Health Monitoring, and Rehabilitation*, 2nd ed., Springer International Publishing, Switzerland.

Balageas, D., Fritzen, C. P., and Güemes, A. (2006). Structural health monitoring. ISTE Ltd., London.

Bao, X., and Chen, L. (2012). “Recent progress in distributed fiber optic sensors.” *Sensors*, 12(7), 8601–8639.

Barrias, A., Casas, J. R., and Villalba, S. (2016). "A Review of Recent Distributed Optical Fiber Sensors for Civil Engineering Applications." Sensors, 16(5).

Bartlett, F. M., and Dexter, R. J. (2001). "Updating standard shape material properties database for design and reliability." Research Report No. 3062, American Institute of Steel Construction, Chicago, IL.

Bathe, K. J. (2016). Finite element procedures, 2nd Ed., Prentice Hall, Watertown, MA.

Belytschko, T., Liu, W. K., and Moran, B. (2000). Nonlinear finite elements for continua and structures, Wiley, Chichester, UK.

Bentley Systems. (2023). STAAD.Pro: Structural analysis and design software, Bentley Systems, Inc., Accessed December 23, 2024. https://www.bentley.com/wp-content/uploads/PDS-STAADPro-CONNECT-LTR-EN-HR.pdf

Brownjohn, J. M. W. (2007). “Structural health monitoring of civil infrastructure.” Philos. Trans. R. Soc. A., 365(1851), 589-622.

Chopra, A. K. (2017). Dynamics of structures: Theory and applications to earthquake engineering, Pearson, London, UK.

Computers and Structures, Inc. (2023). ETABS: Integrated building design software, Computers and Structures, Inc. Accessed December 23, 2024. https://www.csiamerica.com/products/etabs

Computers and Structures, Inc. (2023). SAP2000: Integrated software for structural analysis and design, Computers and Structures, Inc. Accessed December 23, 2024. https://www.csiamerica.com/products/sap2000

Cook, R. D., Malkus, D. S., Plesha, M. E., and Witt, R. J. (2001). Concepts and applications of finite element analysis, 4th Ed., John Wiley & Sons, Hoboken, NJ.

CSA (Canadian Standards Association). (2014). "Canadian highway bridge design code." CSA S6-14, Mississauga, ON, Canada.

CSA (Canadian Standards Association). (2019). "Canadian highway bridge design code." CSA S6-19, Toronto, ON, Canada.

Dassault Systèmes. (2012). "Abaqus 6.12 CAE/User's manual." Dassault Systèmes Simulia Corp., Providence, RI.

Dassault Systèmes. (2023). Abaqus Unified FEA: Complete solutions for realistic simulation, Dassault Systèmes. Accessed December 23, 2024. https://www.3ds.com/products/simulia/abaqus

Diler, E., Peltier, F., Becker, J., and Thierry, D. (2021). "Real-time corrosion monitoring of aluminium alloys under chloride-contaminated atmospheric conditions." Materials and Corrosion, 72(5), 764-776.

Encardio Rite. (2024). “Renewable Energy in Structural Health Monitoring - Sustainable Infrastructure.” Accessed December 20, 2024. https://www.encardio.com/blog/renewable-energy-structural-health-monitoring-sustainable-infrastructure

Eastman, C., Teicholz, P., Sacks, R., and Liston, K. (2011). BIM handbook: A guide to building information modeling for owners, managers, designers, engineers and contractors, John Wiley & Sons, Hoboken, NJ.

Ettouney, M. M., and Alampalli, S. (2012). Infrastructure health in civil engineering: Theory and components. Springer, New York.

Farrar, C. R., and Lieven, N. A. J. (2007). “Damage prognosis: The future of structural health monitoring.” Philos. Trans. R. Soc. A., 365(1851), 623-632.

Farrar, C. R., and Worden, K. (2006). “An introduction to structural health monitoring.” Philos. Trans. R. Soc. A., 365(1851), 303-315.

Farrar, C. R., and Worden, K. (2013). Structural health monitoring: A machine learning perspective. John Wiley & Sons, Chichester, UK.

Federal Highway Administration (FHWA). (2012). *Steel bridge design handbook: Design for fatigue and fracture*, FHWA-IF-12-052, Vol. 12, U.S. Department of Transportation, Washington, DC.

Glisic, B., Inaudi, D., Lau, J. M., and Fong, C. C. (2013). "Ten-year monitoring of high-rise building columns using long-gauge fiber optic sensors." Smart Mater. Struct., 22(5), 055030.

Glisic, B. (2022). “Concise historic overview of strain sensors used in the monitoring of civil structures: The first one hundred years.” Sensors, 22(7).

Inaudi, D., and Glisic, B. (2006). “Distributed fiber optic strain and temperature sensing for structural health monitoring.” Proc., 3rd Int. Conf. on Bridge Maintenance, Safety and Management (IABMAS’06), Porto, Portugal, 16–19 July.

Inaudi, D., Casanova, N., and Glisic, B. (2001). “Lessons learned in the use of fiber optic sensor for civil structural monitoring.” *International Journal for Restoration of Buildings and Monuments*, 7(3-4), 301–320.

ISIS Canada. (2001). Guidelines for structural health monitoring. ISIS Canada, Winnipeg, Manitoba.

Khaloo, A., Lattanzi, D., Cunningham, K., Dell'Andrea, R., and Riley, M. (2018). “Unmanned aerial vehicle inspection of the Placer River Trail Bridge through image-based 3D modelling.” Struct. Infrastruct. Eng., 14(1), 124-136.

Kim, Y. J., Murison, E., and Mufti, A. (2010). Structural health monitoring: A Canadian perspective. Proc. Inst. Civ. Eng. Struct. Build., 163(4), 185–191.

Kralovec, C., and Schagerl, M. (2020). "Review of structural health monitoring methods regarding a multi-sensor approach for damage assessment of metal and composite structures." Sensors, 20(3), 826.

Lai, X., Yang, L., He, X., Pang, Y., Song, X., and Sun, W. (2023). “Digital twin-based structural health monitoring by combining measurement and computational data: An aircraft wing example.” Ind. Manuf. Eng., 8(1), 1-15.

Limongelli, M.P., Previtali, M., Cantini, L., Carosio, S., Matos, J.C., Isoird, J.M., Wenzel, H., and Pellegrino, C. (2019). “Lifecycle Management, Monitoring and Assessment for Safe Large-Scale Infrastructures: Challenges and Needs.” ISPRS Archives, XLII-2/W11, 727-734.

Liu, G. R., and Quek, S. S. (2014). The finite element method: A practical course, 2nd Ed., Butterworth-Heinemann, Oxford, UK.

Lynch, J. P., and Loh, K. J. (2006). “A summary review of wireless sensors and sensor networks for structural health monitoring.” Shock Vib. Dig., 38(2), 91-130.

Mazhandu, F. (2024). “How IoT is enhancing structural health monitoring (SHM).” Accessed December 18, 2024. https://www.iotforall.com/how-iot-is-improving-structural-health-monitoring-shm

Mikhailov, S., van Wittenberghe, J., Luyckx, G., Thibaux, P., Geernaert, T., Berghmans, F. (2023). “Fatigue weld crack detection using distributed fiber optic strain sensing.” *International Journal of Fatigue*, Volume 176, Article 107851, November 2023.

Mufti, A. A. (2002). "Structural health monitoring of innovative Canadian civil engineering structures." Struct. Health Monit., 1(1), 89-103.

Mufti, A. A., Bakht, B., Raeisi, F., Algohi, B., and Faraz, S. (2018). “A case for adding an inspection level related to SHM for bridge evaluation by CHBDC.” Proc., 9th Int. Conf. on Structural Health Monitoring of Intelligent Infrastructure, SHMII-9, St. Louis.

Mufti, A. A., and Thomson, D.J. (2024). “Role of Civionics in the Civil Structural Health Monitoring System.” Infrastructures, 9(3), 57.

Mufti, A. A., Thomson, D. J., Inaudi, D., Vogel, H. M., and McMahon, D. (2011). “Crack detection of steel girders using Brillouin optical time domain analysis.” J. Civil Struct. Health Monit., 1(1), 66-68.

Muttillo, M., Stornelli, V., Alaggio, R., Paolucci, R., Di Battista, L., de Rubeis, T., and Ferri, G. (2020). “Structural health monitoring: An IoT sensor system for structural damage indicator evaluation.” Sensors, 20(17).

National Instruments. (2024). “New Technologies for Structural Testing and Health Monitoring.” Accessed December 18, 2024. https://link.springer.com/article/10.1007/s44285-024-00031-2

Neubrex. (2023). “NBX Series Version 7.25.0 user’s manual.” Neubrex Co., Ltd., Kobe, Japan.

Nikles, M., Thevenaz, L., and Robert, P. (1997). “Brillouin gain spectrum characterization in single-mode optical fibers.” J. Lightwave Technol., 15(10), 1842–1851.

Omnisens SA. (2009). DITEST STA-R™ Fibre Optic Distributed Temperature and Strain Analyzer User Manual, Version 2-0-b. Riond Bosson 3, 1110 Morges, Switzerland: Omnisens SA.

Presno Vélez, A., Fernández Muñiz, M. Z., and Fernández Martínez, J. L. (2024). “Enhancing structural health monitoring with machine learning for accurate prediction of retrofitting effects.” AIMS Mathematics, 9(11), 30493-30514.

Pulse IoT Technologies. (2024). “The Future of Structural Health Monitoring: Emerging Trends and Technologies.” Accessed December 19, 2024. https://pulseiot.tech/2024/08/29/the-future-of-structural-health-monitoring-emerging-trends-and-technologies/

Raeisi, F., Algohi, B., Mufti, A., and Thomson, D. J. (2021). “Reducing carbon dioxide emissions through structural health monitoring of bridges.” Journal of Civil Structural Health Monitoring, 11(3), 679–689.

Raeisi, F., Mufti, A., and Thomson, D. J. (2018). “A finite-element model and experimental investigation of the influence of pre-straining of wire on the sensitivity of binary crack sensors.” J. Civil Struct. Health Monit., 8(4), 673-687.

Raeisi, F., Mufti, A., Algohi, B., and Thomson, D. J. (2019). “Placement of distributed crack sensor on I-shaped steel girders of medium-span bridges, using available field data.” Struct. Control Health Monit., 26(2).

Rakha, T., and Gorodetsky, A. (2018). “Review of unmanned aerial system applications in the built environment: Towards automated building inspection procedures using drones.” Autom. Constr., 93, 252-264.

Richter, B., Herbers, M., Marx, S. (2024). “Crack monitoring on concrete structures with distributed fiber optic sensors—Toward automated data evaluation and assessment.” *Struct. Control Health Monit.*, 30(11), e3285.

Roctest. (n.d.). “DiTeSt SMARTape II Strain Sensor.” Accessed December 10, 2024. https://roctest.com/en/product/ditest-smartape-ii-strain-sensor/

Rodrigues, C., Inaudi, D., and Glišić, B. (2013). "Long-gauge fibre optic sensors: performance comparison and applications." *J. Struct. Eng.*, 147(6), 04021075.

Russo, F. M., Mertz, D. R., Frank, K. H., and Wilson, K. E. (2016). Design and Evaluation of Steel Bridges for Fatigue and Fracture – Reference Manual, Report No. FHWA-NHI-16-016, U.S. Department of Transportation, Federal Highway Administration, National Highway Institute, Washington, DC.

Rytter, A. (1993). “Vibrational based inspection of civil engineering structures.” Ph.D. thesis, Dept. of Building Technology and Structural Engineering, Aalborg Univ., Denmark.

Scuro, C., Sciammarella, P. F., Lamonaca, F. and Olivito, R. S. (2023). “IoT for structural health monitoring.” Sensors, 23(9).

Seo, J., Hu, J. W., and Lee, J. (2016). “Summary review of structural health monitoring applications for highway bridges.” J. Perform. Constr. Facil., 30(4), 04015072.

Siemens. (2023). Simcenter Femap: Advanced simulation pre- and post-processor, Siemens. Accessed December 23, 2024. https://plm.sw.siemens.com/en-US/simcenter/mechanical-simulation/femap/

Smart Structures. (2024). “Innovations in Structural Health Monitoring (SHM).” Accessed December 20, 2024. https://smart-structures.com/innovations-in-structural-health-monitoring-shm/

Sohn, H., Farrar, C. R., Hemez, F. M., Shunk, D. D., Stinemates, D. W., Nadler, B. R., and Czarnecki, J. J. (2003). A review of structural health monitoring literature: 1996-2001. Rep. No. LA-13976-MS, Los Alamos National Laboratory, NM.

Svendsen, B. T., Øiseth, O., and Rønnquist, A. (2022). "A hybrid structural health monitoring approach for damage detection in steel bridges under simulated environmental conditions using numerical and experimental data." Structural Health Monitoring, 22(1).

Telehanic, B., Mufti, A., Thomson, D., Algohi, B., and Belli, R. (2022). "Pi-bracket sensor for crack detection near stiffeners for steel girder bridges." Proc., 11th Int. Conf. on Structural Health Monitoring of Intelligent Infrastructure (SHMII-11), Montreal, QC, Canada.

Tokyo Electric Power Services Co., Ltd. (2021). “Deterioration diagnosis technology for PC road bridges: Measurement using strain gauge and pi shaped displacement gauge.” Tokyo Electric Power Services Co., Ltd., Tokyo, Japan. https://www.tepsco.co.jp/english/pcroadassesment/

Tokyo Measuring Instruments Laboratory Co., Ltd. (TML). (2019). “Pi shape displacement transducer (PI series).” Tokyo Measuring Instruments Laboratory Co., Ltd., Tokyo, Japan. https://tml.jp/e/product/transducers/pi.html

Tokyo Measuring Instruments Laboratory Co., Ltd. (2025). *TML Transducers 2025–2026: Load cells, displacement transducers, pressure transducers, acceleration transducers*. Tokyo Measuring Instruments Laboratory Co., Ltd., Tokyo, Japan.

Tokyo Sokki Kenkyujo Co., Ltd. (TML). (2024). Pi Gauge for Crack Width Measurement: PI-5-100, PI-5-200. https://www.tml.jp/english/products/pi_gauge/index.html

Trimble. (2023). Tekla Structures: Building Information Modeling (BIM) software, Trimble. Accessed December 23, 2024. https://www.tekla.com/products/tekla-structures

Wang, H., Guo, J.-K., Mo, H., Zhou, X., and Han, Y. (2023). “Fiber optic sensing technology and vision sensing technology for structural health monitoring.” Sensors, 23(9), 4334.

Worden, K., and Manson, G. (2007). “The application of machine learning to structural health monitoring.” Philos. Trans. R. Soc. A., 365(1851), 515-537.

Ye, X. W., Su, Y. H., and Han, J. P. (2014). “Structural health monitoring of civil infrastructure using optical fiber sensing technology: A comprehensive review.” Sci. World J., 2014.

Yoon, J.-H., Lee, J., Kim, G., Park, J., and Ryu, S. (2022). “Deep neural network-based structural health monitoring technique for real-time crack detection and localization using strain gauge sensors.” Sci. Rep., 12(1), 20204.

Zhang, S., Liu, B., and He, J. (2019). “Pipeline deformation monitoring using distributed fiber optical sensor.” Measurement, 138, 467-471.

Zhu, H.-H., Shi, B., Yan, J.-F., Zhang, J., and Wang, J. (2015). “Investigation of the evolutionary process of a reinforced model slope using a fiber-optic monitoring network.” Eng. Geol., 186, 34-43.

Zienkiewicz, O. C., Taylor, R. L., and Fox, D. D. (2014). The finite element method for solid and structural mechanics, Butterworth-Heinemann, Oxford, UK.

Zienkiewicz, O. C., Taylor, R. L., and Zhu, J. Z. (2013). The finite element method: Its basis and fundamentals, Butterworth-Heinemann, Oxford, UK.

APPENDIX A

SIMULATION TOOL SELECTION

9.1. INTRODUCTION

In the rapidly evolving field of civil engineering, software tools have become indispensable for design, analysis, research and SHM. These tools range from basic computer-aided design (CAD) software to sophisticated FEA programs, each serving specific purposes in the engineering workflow (Eastman et al. 2011). By leveraging these technologies, engineers can address increasingly complex challenges with improved accuracy, efficiency, and productivity (Zienkiewicz et al. 2013). This section aims to provide a comprehensive overview of civil engineering software, with a particular focus on comparing Abaqus and SAP2000 in the context of structural engineering research and SHM field applications.

We will begin by categorizing civil engineering software into three main types, providing examples and brief descriptions for each. Following this, we will delve into a detailed comparison of Abaqus and SAP2000, examining their features, strengths, limitations, and appropriate use cases in research and SHM contexts. This comparison will be valuable for students, early researchers, and young professionals in the field of structural engineering with or without focus on SHM, who are seeking to choose the most suitable software for their specific needs (Cook et al., 2001).

9.2. CATEGORIZATION OF CIVIL ENGINEERING SOFTWARE

Civil engineering software can be broadly categorized into three main types:

- Design Software
- Structural Analysis Software
- FEA Software

Each of those serving distinct yet interconnected roles in the engineering process.

9.2.1. Design Software

Design software focuses on the creation and detailing of structural elements according to specific codes and standards (American Society of Civil Engineers 2017). These tools are essential in the initial stages of a project, allowing to create detailed models and generate construction documents.

One widely used example is REVIT, a Building Information Modeling (BIM) software that supports the development of intricate 3D models with integrated structural components (Autodesk 2023). TEKLA STRUCTURES is another specialized tool tailored for structural engineering, offering advanced features for the detailing of both steel and concrete elements (Trimble 2023). STAAD.Pro is an integrated platform that facilitates 3D model generation, structural analysis and design, as well as result visualization (Bentley Systems 2023).

These software packages typically provide robust 3D modeling capabilities, automated drawing generation, and material quantity takeoffs. They are designed to integrate seamlessly with structural analysis software and include automated checks to ensure that designs adhere to relevant codes and standards. By streamlining the design process and supporting code compliance, these tools enhance both the efficiency and accuracy of structural engineering projects.

9.2.2. Structural Analysis Software

Structural analysis software is specialized for analyzing the behavior of structures under various loads. These programs are significant for predicting how structures will perform under different conditions and ensuring they meet safety and performance requirements (Chopra 2017). These programs allow engineers to model and analyze complex structural systems, assessing their behavior under different scenarios to identify potential issues before construction begins.

Among the most widely used structural analysis software is SAP2000, a versatile platform capable of analyzing and designing a wide range of structural systems (Computers and Structures, Inc. 2023). ETABS is another prominent example, tailored for the analysis and design of buildings, especially high-rise structures, providing specialized tools for this application (Computers and Structures, Inc. 2023). STAAD.Pro also offers comprehensive analysis and design capabilities, accommodating various types of structures and engineering requirements (Bentley Systems 2023).

These software solutions typically feature both linear and nonlinear analysis capabilities, allowing for the assessment of structural behavior under routine and extreme conditions. They support static and dynamic analysis, including tools for seismic evaluation, and are integrated with relevant design codes and standards to ensure regulatory compliance. Visualization tools are also provided, enabling users to interpret analysis results through graphical representations, which aids in understanding structural performance and communicating findings effectively.

9.2.3. FEA Software

FEA software offers advanced capabilities for detailed analysis of complex structural behaviors, material responses, and multi-physics problems. These tools are essential for research and advanced engineering applications where standard structural analysis software may be insufficient (Zienkiewicz et al. 2014).

Among the leading FEA software solutions is ABAQUS, a robust suite of engineering simulation tools built on the finite element method, widely recognized for its versatility and accuracy in modeling challenging engineering problems (Dassault Systèmes 2023). ANSYS is another comprehensive platform, offering a broad spectrum of engineering simulation solutions that cater to various industries and analysis needs (ANSYS, Inc. 2023). FE MAP, developed by Siemens, is

known for its advanced finite element modeling and analysis capabilities, supporting a range of engineering disciplines (Siemens 2023).

These FEA software packages typically feature advanced nonlinear analysis capabilities, allowing users to simulate large deformations, complex contact interactions, and material nonlinearities. They provide detailed material modeling options to accurately represent the behavior of different materials under various loading conditions. Multi-physics simulation capabilities enable the analysis of coupled phenomena, such as thermal, structural, and fluid interactions. High-performance computing options are available to handle large and computationally intensive models, and users can further customize analyses through scripting or programming interfaces. This combination of features makes FEA software an essential tool for tackling sophisticated engineering challenges and pushing the boundaries of structural analysis.

A detailed comparison of software will be conducted in the subsequent Chapter, focusing specifically on SAP2000 and Abaqus. This analysis will evaluate their respective capabilities, strengths, and limitations in the context of structural analysis and finite element modeling. By examining the features and performance of these tools, the most appropriate software for this research will be selected. This decision will depend on the specific requirements of the project, ensuring that the chosen software effectively meets the analytical needs and enhances the overall quality of the research.

9.2.4. Fundamentals of FEA

FEA is a powerful computational technique widely used in structural engineering to simulate and analyze complex structures under various loading conditions. FEA works by discretizing a continuous structure into smaller, simpler parts called finite elements, which are interconnected at nodes (Bathe 2016). This process, known as meshing, allows engineers to transform complex geometries into manageable mathematical models.

The typical FEA workflow in structural simulations consists of three main stages. The pre-processing stage involves defining the geometry of the structure, specifying material properties, setting boundary conditions, and applying loads. During the analysis stage, the system of equations governing the structure is solved to determine nodal displacements and element stresses. Finally,

the post-processing stage focuses on interpreting and visualizing the results, often using color-coded plots to display stress or displacement distributions.

FEA software packages offer various material models to represent the behavior of different materials under load. These models range from simple linear elastic to complex nonlinear models that account for plasticity, viscoelasticity, and other material-specific behaviors (Zienkiewicz et al. 2014). The accuracy of FEA results is heavily influenced by the meshing technique used. Common element types include one-dimensional elements for beams and trusses, two-dimensional elements for shells and plates, and three-dimensional elements such as tetrahedra and hexahedra. The selection of element type and mesh density plays a critical role in balancing solution accuracy with computational efficiency (Liu and Quek 2014).

FEA can be applied to several types of analyses, including static analysis, which evaluates structural response under constant loads and assumes no time-dependent effects, and dynamic analysis, which considers time-dependent loads and inertial effects, essential for studying vibrations and impacts (Chopra 2017). Linear analysis assumes minor structural changes and linear material behavior, providing quick solutions for many engineering problems. In contrast, nonlinear analysis considers large deformations, material nonlinearities, and contact interactions, yielding more accurate results for complex scenarios but at a higher computational cost (Belytschko et al. 2014).

While linear static analysis remains the most common type due to its simplicity and efficiency, engineers must carefully consider the appropriateness of analysis type based on the specific problem and desired accuracy (Cook et al. 2001).

9.3. DETAILED COMPARISON OF ABAQUS AND SAP2000

Both Abaqus and SAP2000 are powerful tools widely used in structural engineering and SHM, each representing a distinct category of software with its own set of capabilities and strengths. Abaqus, as a representative of FEA Software, offers advanced capabilities for detailed and complex simulations, which are particularly valuable in SHM for modelling intricate structural behaviours and predicting responses to various conditions. SAP2000, on the other hand, exemplifies Structural Analysis Software, providing specialized tools for analyzing and designing

civil engineering structures, with features that are well-suited for implementing SHM strategies in large-scale infrastructure projects. In the context of SHM, Abaqus excels in detailed component analysis and advanced material modeling, making it ideal for investigating localized damage and complex material degradation processes. Its multi-physics capabilities allow for the simulation of various environmental effects on structures, fundamental for comprehensive SHM programs. SAP2000, with its user-friendly interface and efficient handling of large structural models, is particularly adept at integrating real-time monitoring data and performing rapid structural assessments, essential for ongoing SHM of bridges, buildings, and other civil infrastructure. While other software packages within each category may offer similar functionalities, this comparison focuses specifically on Abaqus and SAP2000 due to the author's direct experience with these tools in their research and SHM applications. This section provides a detailed comparison of these two software packages, highlighting their unique features, strengths, and limitations in the context of structural engineering research and SHM implementation. The comparison will explore how each software can be leveraged for different aspects of SHM, from sensor data integration and model updating to damage detection and long-term performance prediction.

9.3.1. SAP2000

SAP2000, developed by Computers and Structures, Inc., has been an industry standard for structural analysis and design for over 45 years (Computers and Structures, Inc. 2023). It is designed specifically for structural engineering applications and is widely used in both professional practice and academic research, including SHM.

9.3.1.1. Key Features for SHM

SAP2000 is equipped with several key features that make it well-suited for SHM applications. The software provides a unified interface that integrates modeling, analysis, design, and reporting within a single user environment, streamlining the workflow for structural engineers. At its core is the SAPFire Analysis Engine, which supports multiple 64-bit solvers, enabling efficient analysis of large and complex structural models.

Advanced graphics capabilities, powered by DirectX, facilitate fast 2D and 3D drafting and intuitive model navigation, enhancing both user experience and productivity. SAP2000 includes sophisticated meshing techniques that allow for the accurate representation of complex geometries, which is critical for detailed structural analysis.

The software supports code-based design for a variety of materials, including steel, concrete, aluminum, and timber, ensuring compliance with relevant standards (American Society of Civil Engineers 2017). It offers comprehensive tools for both linear and nonlinear dynamic analysis, such as time history and response spectrum analysis, which are essential for evaluating structural performance under dynamic loading conditions.

Specialized modules are available for bridge design and analysis, including features for moving load analysis and cable-stayed bridge analysis, making SAP2000 particularly valuable for infrastructure projects. The program can also integrate field-measured monitoring data directly into the analysis model, allowing for real-time assessment and calibration. Additionally, SAP2000 provides tools for damage detection by identifying and assessing changes in dynamic properties, which supports early identification of structural issues and enhances overall SHM effectiveness

9.3.1.2. Advantages for SHM

SAP2000 offers several advantages that make it particularly effective for SHM applications. Its user-friendly interface is designed with structural engineers in mind, making it intuitive and straightforward to learn for professionals in the field. The software incorporates built-in design code checks for a range of international standards, ensuring that structural designs comply with regulatory requirements.

SAP2000 is highly efficient when analyzing common civil engineering structures such as frames, shells, and plates, providing rapid and reliable results. It also includes specialized tools for seismic analysis, bridge design, and other specific structural engineering tasks, supporting a wide array of SHM scenarios.

The program integrates seamlessly with other software in the CSI suite, such as ETABS and SAFE, facilitating smooth workflows in building design and analysis projects. Additionally, SAP2000 can

incorporate field-measured monitoring data directly into its analysis models, enhancing its utility for real-time assessment and calibration in SHM applications (Farrar and Worden 2013).

9.3.1.3. Limitations for SHM

Despite its many advantages, SAP2000 does have certain limitations when applied to SHM. One notable constraint is its limited capacity for advanced material modeling. While SAP2000 is adequate for most standard structural engineering applications, it may not be suitable for analyzing complex material behaviors often encountered in advanced SHM scenarios, especially when compared to specialized FEA software.

Additionally, although SAP2000 includes nonlinear analysis capabilities, these options are not as comprehensive or robust as those offered by dedicated FEA programs. This can be a drawback when detailed nonlinear behavior and intricate interactions need to be captured for accurate SHM assessments.

Customization is another area where SAP2000 falls short. While the software does provide some options for user customization, it is generally less flexible than general-purpose FEA platforms when it comes to implementing novel SHM algorithms or integrating cutting-edge monitoring techniques. As a result, engineers seeking highly specialized or experimental SHM solutions may find SAP2000 somewhat restrictive in comparison to more advanced FEA tools.

9.3.1.4. Student Version Limitations

The student version of SAP2000 comes with several limitations compared to the full commercial release. Model size is typically restricted, meaning users can only work with smaller or less complex structures. Certain advanced analysis types may be unavailable, limiting the range of simulations that can be performed. Outputs generated from the student version often include watermarks, and export capabilities may be limited, which can affect the presentation and sharing of results. Additionally, the student version is intended solely for academic and non-commercial use, prohibiting its application in professional or revenue-generating projects. These restrictions

are designed to differentiate the educational offering from the full-featured commercial product while still providing valuable learning opportunities for students.

9.3.2. Abaqus

Abaqus, part of Dassault Systèmes' SIMULIA product line, is a collection of advanced engineering simulation tools utilizing the finite element method. It's designed for more advanced and complex analyses across various engineering disciplines and can offer advanced capabilities that can be leveraged for sophisticated SHM applications (Dassault Systemes 2023).

9.3.2.1. Key Features for SHM

Abaqus offers a robust suite of features that make it particularly well-suited for SHM applications. Its comprehensive analysis capabilities allow users to tackle a wide range of problems, from straightforward linear analyses to highly complex nonlinear simulations (Zienkiewicz et al. 2013). This advanced nonlinear analysis functionality is essential for accurately modeling the real-world behavior of structures under diverse loading and environmental conditions.

The software boasts an extensive element library, enabling the modeling of virtually any geometry encountered in engineering practice. Abaqus also provides a wide array of material models, accommodating metals, polymers, composites, and geotechnical materials, which allows for detailed and realistic representation of complex material behaviors in monitored structures.

Abaqus excels in multi-physics simulation, making it possible to couple structural analysis with other physical phenomena relevant to SHM, such as thermal effects and fluid-structure interactions (Balageas et al. 2006). For researchers and advanced users, the software offers extensive customization through user subroutines, supporting the implementation of novel material models, specialized analysis procedures, or custom SHM algorithms.

High-performance computing support is another key feature, as Abaqus can leverage parallel processing to efficiently solve large-scale, computationally intensive problems. The integrated Abaqus/CAE environment further enhances usability by providing a consistent platform for model creation, simulation submission, monitoring, and results evaluation, streamlining the entire SHM workflow.

9.3.2.2. Advantages for SHM

Abaqus offers several notable advantages for SHM applications. One of its key strengths is its advanced nonlinear analysis capabilities, which enable the software to effectively handle complex scenarios involving large deformations, contact interactions, and material nonlinearities (Cook et al. 2001). This makes Abaqus especially effective for conducting detailed analyses of critical structural components, enabling engineers to develop a thorough understanding of the behavior and performance of monitored structures.

The software's extensive material modeling options further enhance its utility, providing the ability to accurately represent a wide variety of complex material behaviors. This versatility makes Abaqus applicable to a broad spectrum of structures and materials commonly encountered in SHM projects, as well as in other engineering disciplines.

Abaqus is also highly regarded in research settings, thanks to its advanced features and extensive customization options. Researchers can develop and test new SHM methodologies, implement novel algorithms, and tailor simulations to specific investigative needs. Comprehensive documentation and robust support resources are available, making it easier for users to leverage the software's full capabilities in both practical and research-oriented SHM applications.

9.3.2.3. Limitations for SHM

Abaqus presents several limitations when applied to SHM. The software has a steeper learning curve compared to standard structural analysis programs, particularly for users without a background in FEA, making it more challenging to be used effectively in SHM applications.

Additionally, the full version of Abaqus is generally more costly than specialized structural analysis software, which can be a barrier for some organizations.

In terms of efficiency, Abaqus may be less suitable for routine structural analysis tasks, as it is optimized for advanced simulations rather than standard applications. Another limitation is its integration with monitoring systems; incorporating real-time monitoring data into Abaqus often requires additional effort and customization, making it less seamless compared to software designed specifically for SHM workflows.

9.3.2.4. Student Version Limitations

The Abaqus Student Edition comes with several notable restrictions compared to the full commercial version. Model size is limited to a maximum of 1,000 nodes, which constrains the complexity and scale of simulations that can be performed. The student version is intended strictly for academic purposes and cannot be used for commercial or professional projects. Additionally, some advanced features available in the full version may be disabled, further limiting the scope of analyses students can conduct. These constraints are designed to provide a learning platform while distinguishing the student edition from the comprehensive capabilities of the full Abaqus software.

9.4. CHOOSING BETWEEN ABAQUS AND SAP2000 FOR SHM APPLICATIONS

The choice between Abaqus and SAP2000 for SHM should be guided by the specific objectives of the research project. Here, we outline scenarios where each software would be more appropriate.

9.4.1. When to Choose SAP2000

SAP2000 is particularly well-suited for research projects dealing with structural analysis of buildings, bridges, and other civil engineering structures. It excels in long-term monitoring of large-scale structures, such as bridges, high-rise buildings, or extensive infrastructure networks, due to its efficiency in managing large and complex models. The software is ideal when the

primary objective is to assess monitored structures for compliance with current design codes, ensuring regulatory standards are met (American Society of Civil Engineers 2017).

SAP2000 is also advantageous for operational modal analysis, making it a strong choice for projects that involve identifying modal parameters from ambient vibration data. For bridge health monitoring, the specialized bridge module provides comprehensive tools tailored to the unique requirements of bridge SHM programs. These capabilities make SAP2000 a preferred option for projects focused on practical, code-based assessment and continuous monitoring of critical infrastructure.

9.4.2. When to Choose Abaqus

Abaqus is the preferred software for research projects that demand advanced finite element analysis, particularly when the focus is on complex material behaviors, multi-physics problems, or in-depth component analysis. It is especially suitable for advanced damage detection and prognosis, where sophisticated material models are required to accurately predict the progression of structural damage. Abaqus excels in multi-physics SHM applications, making it ideal for projects that involve the interaction of structural behavior with other physical phenomena, such as offshore structures exposed to wave loading.

The software’s robust customization capabilities support the development and testing of novel SHM algorithms, allowing researchers to implement and refine new methodologies. Additionally, Abaqus is well-suited for detailed fatigue analysis, making it a strong choice for SHM projects that focus on assessing the fatigue life of critical structural components. These strengths make Abaqus the optimal tool for research that goes beyond standard structural analysis and requires a high level of modeling sophistication and flexibility.

9.5. COMPARATIVE ANALYSIS IN RESEARCH APPLICATIONS

To further illustrate the differences between SAP2000 and Abaqus in general and SHM research contexts, let's consider some specific research scenarios:

9.5.1. Performance of Bridge (General Research)

For general research focused on the overall performance of bridges, SAP2000 is typically the preferred choice. Its specialized bridge module, efficient handling of large and complex structural models, and integration with a wide range of design codes make it particularly well-suited for studying bridge behavior under various loading conditions, including moving loads, wind, and seismic forces. SAP2000's advanced analysis engine and dedicated features for bridge modeling and assessment streamline the process of evaluating global bridge performance, supporting both routine and sophisticated engineering studies (Computers and Structures, Inc. 2023).

While Abaqus can perform similar analyses, it is generally less efficient for large-scale, global bridge studies due to its focus on detailed finite element modeling and advanced material behavior. However, Abaqus can complement SAP2000 by providing in-depth analysis of critical bridge components identified during the global assessment, such as investigating complex joint behavior or local stress concentrations that require more sophisticated modeling techniques (Dassault Systemes 2023).

In summary, SAP2000 is ideally suited for comprehensive bridge performance research, while Abaqus is best reserved for detailed component-level studies that demand advanced finite element capabilities.

9.5.2. Fracture Mechanics in Steel Structures (General Research)

For general research in fracture mechanics of steel structures, Abaqus is the superior choice. Its advanced material modeling capabilities and specialized tools for simulating crack initiation and propagation, such as the Extended Finite Element Method (XFEM) and Cohesive Zone Modeling, make it ideal for detailed studies of fracture behavior under various loading and environmental conditions. Abaqus allows for accurate analysis of complex scenarios, including the evolution of cracks in steel components, welds, and composite materials, and provides robust post-processing tools to interpret results such as stress intensity factors, energy release rates, and crack growth trajectories. (Dassault Systemes 2023).

In contrast, while SAP2000 can perform nonlinear analysis of steel structures, it lacks the dedicated features required for in-depth fracture mechanics studies. SAP2000 does not offer the same level of sophistication in modeling crack propagation or detailed failure mechanisms, making it less suitable for research that demands precise fracture analysis (Computers and Structures, Inc. 2023).

Therefore, for research centered on fracture mechanics in steel structures, Abaqus is the preferred platform because of its robust fracture simulation capabilities and its capacity to provide actionable understanding for optimizing material use and enhancing structural safety.

9.5.3. Performance-Based Seismic Design (General Research)

For general research in performance-based seismic design, SAP2000 is particularly well-suited due to its seamless integration of analysis and design features. The software offers efficient nonlinear analysis capabilities, enabling researchers to evaluate structural performance under seismic loading and to assess compliance with relevant design codes. This makes SAP2000 an effective tool for the iterative processes involved in performance-based seismic design, where rapid modeling, analysis, and code-based assessment are essential.

Abaqus, while capable of providing highly detailed analysis of specific structural components or behaviors, is generally less efficient for the overall performance-based design workflow. It is best utilized for in-depth investigation of particular aspects identified during the broader analysis, such as localized nonlinear responses or complex failure mechanisms. However, for comprehensive performance-based seismic design studies, SAP2000 remains the preferred choice due to its integrated features and streamlined processes.

9.5.4. Thermal Effects on Bridge Structures (General Research, SHM Research)

For research on the thermal effects on bridge structures, including both general and SHM studies, SAP2000 offers practical capabilities. Its dedicated bridge module and integrated thermal analysis tools enable users to assess how temperature variations influence overall bridge performance,

making it suitable for evaluating global thermal responses and ensuring code compliance (Computers and Structures, Inc. 2023).

Abaqus, on the other hand, is better equipped for detailed investigations of thermal stresses and strains, particularly when dealing with complex bridge geometries or advanced material behaviors. Its advanced finite element modeling and multi-physics simulation capabilities allow for in-depth analysis of localized thermal effects, such as differential expansion, stress concentrations, and the interaction of thermal and mechanical loads (Dassault Systèmes 2023).

In summary, SAP2000 is effective for broad thermal performance studies of bridges, while Abaqus excels in detailed, component-level thermal analysis, especially in research requiring high modeling precision and complexity.

9.5.5. Monitoring of a Bridge Structures (SHM Research)

For SHM research focused on bridge structures, SAP2000 is generally the preferred software. Its ability to efficiently handle large-scale models, combined with specialized features for bridge analysis, makes it well-suited for ongoing monitoring of bridge performance. SAP2000 can effectively incorporate field-measured monitoring data, enabling users to update the structural model and assess changes in performance over time. This integration supports continuous evaluation and helps in identifying potential issues as they develop.

Abaqus, while capable of detailed structural analysis, is less efficient for long-term, large-scale monitoring tasks typical in SHM of bridges. However, it serves as a valuable complement to SAP2000 by providing in-depth analysis of specific components identified as critical through the broader SAP2000 model. This targeted approach allows for advanced investigation of localized phenomena, such as crack propagation or complex material behavior, when higher modeling precision is required.

9.5.6. Performance of Bridge Components (General Research, SHM Research)

When researching the performance of bridge components, whether for general studies or structural health monitoring (SHM), SAP2000 and Abaqus offer complementary strengths. SAP2000 is well-

suited for analyzing the overall performance of bridge components within the context of the complete structure. Its bridge module enables efficient modeling and assessment of standard bridge elements, making it effective for evaluating how individual components contribute to the global behavior and integrity of the bridge (Computers and Structures, Inc. 2023).

Abaqus, in contrast, excels at detailed analysis of specific bridge components, particularly those with complex geometries or advanced material behaviors. It is especially valuable for investigating localized effects, such as stress concentrations in connections or nonlinear material responses in critical elements. This level of detail is key for understanding the behavior of components that may be prone to issues like cracking or fatigue, supporting targeted SHM efforts and advanced research (Dassault Systemes 2023).

9.6. SHM APPLICATIONS

9.6.1. SHM Applications on Bridges

In Manitoba, Canada, several bridges have been instrumented with advanced SHM systems to ensure the ongoing safety and performance of critical infrastructure. These field applications serve as practical examples of SHM implementation in regions facing challenging environmental conditions, such as extreme temperature fluctuations and the risk of flooding (Mufti 2001; Telehanic et al. 2022).

Typical SHM systems installed on these bridges employ a range of sensor technologies. Fiber optic sensors are embedded within bridge decks and girders to measure strain and temperature distributions, providing continuous insight into the structural response. Accelerometers are strategically placed to capture vibrations and detect changes in the bridges' dynamic properties, which can indicate the onset of structural issues. Tiltmeters monitor shifts in alignment or settlement, while environmental sensors track ambient temperature, humidity, and wind speed, allowing engineers to correlate environmental factors with structural behavior.

Centralized data acquisition systems collect and process information from all sensors in real time, and remote monitoring capabilities enable engineers to access data and receive alerts from any location. This comprehensive approach allows for early detection of deterioration or damage, often before it becomes visible during routine inspections, and supports the validation and refinement of theoretical models using real-world performance data. By integrating SHM data with FEM software, researchers and engineers can predict long-term structural performance, optimize maintenance schedules, and assess the impact of extreme events such as earthquakes or floods.

The use of SHM systems on Manitoba's bridges highlights the value of combining sensor technologies and advanced analytical tools to enhance infrastructure resilience and safety, particularly in demanding environments.

Research by Dr. Mufti has significantly contributed to this field. Mufti (2001) demonstrated the effectiveness of integrating SHM systems with FEM models for innovative Canadian civil engineering structures, including bridges. His work showcased how real-time data from FOS could be used to validate and refine FEM models, leading to more accurate assessments of structural health.

By leveraging the strengths of both SAP2000 and Abaqus, researchers can develop comprehensive SHM strategies that combine efficient large-scale modeling with detailed analysis of critical components. This approach enhances our ability to maintain and extend the lifespan of bridge infrastructure, ensuring both safety and cost-effectiveness in the long term.

9.6.2. SHM Applications on Infrastructures

Beyond bridges, SHM systems are increasingly being applied to various types of infrastructure, showcasing their adaptability and value in safeguarding critical assets. In buildings, particularly high-rise structures, stadiums, and essential facilities, SHM systems are deployed to continuously monitor structural integrity, which is especially important in seismically active regions. Dams benefit from SHM technologies that track water levels, structural deformations, and seepage, providing early warning of potential issues in these massive structures.

Tunnels are equipped with sensors to monitor convergence, rock mass deformation, and water ingress, ensuring the stability and safety of underground passages. In the renewable energy sector, wind turbines, both onshore and offshore, use SHM systems to assess blade integrity, tower vibrations, and foundation stability, helping to maintain reliable energy production. Pipelines, particularly those transporting oil and gas, utilize fiber optic sensing systems to detect leaks, monitor ground movements, and identify third-party interference, enhancing operational safety and environmental protection.

These varied applications demonstrate the versatility of SHM technologies in improving the safety, performance, and longevity of infrastructure assets (Brownjohn 2007). In practice, engineers often analyze SHM data using software such as SAP2000 for assessing overall structural behavior and ensuring compliance with design codes. For more detailed investigations of specific components or complex environmental interactions, Abaqus is frequently employed. This combination of SHM systems and advanced analytical tools illustrates how real-world infrastructure projects benefit from tailored monitoring solutions and sophisticated data analysis techniques.

9.7. IMPACT ON ENGINEERING PRODUCTIVITY

The choice between Abaqus and SAP2000, or indeed any structural analysis software, has significant implications for the productivity of both professional engineers and research engineers.

9.7.1. Professional Engineering Productivity

For professional engineers working in design firms or consultancies, productivity is typically evaluated by how quickly projects are completed, the accuracy of analytical results, and the efficiency with which client requirements are met. In this professional context, SAP2000 often stands out as the more productive choice for standard structural engineering tasks. Its intuitive interface, seamless integration with a wide range of design codes, and specialized modules tailored for common structures, such as buildings and bridges, enable engineers to rapidly set up, analyze, and design projects that meet regulatory standards. This streamlined workflow significantly

reduces the time and effort required for routine design activities, allowing firms to deliver projects faster and with greater confidence in code compliance (Computers and Structures, Inc. 2023).

In contrast, Abaqus, while offering powerful simulation capabilities, can present challenges for day-to-day productivity in typical structural engineering applications. Its steeper learning curve and more complex setup process may slow down routine tasks, making it less efficient for standard design work (Dassault Systèmes 2023). However, for specialized projects that demand advanced analysis, such as those involving complex material behaviors or nonlinear phenomena, the initial investment in mastering Abaqus can yield substantial benefits. In these cases, Abaqus provides the depth and accuracy needed for comprehensive and innovative engineering solutions (Belytschko et al. 2000).

Ultimately, the choice of software can directly influence the productivity of professional engineers, with SAP2000 excelling in routine, code-based design tasks and Abaqus offering advantages for complex, research-driven projects.

9.7.2. Research Engineering Productivity

For research engineers in academia, productivity is frequently measured by their capacity to produce original, in-depth understanding and to tackle complex, interdisciplinary problems. In this research context, Abaqus frequently enhances productivity by enabling the modeling and analysis of phenomena that go beyond the reach of standard structural analysis tools. Its advanced material modeling and multi-physics simulation capabilities allow researchers to investigate cutting-edge topics, develop new methodologies, and contribute original findings to the field (Zienkiewicz et al. 2013).

While SAP2000 is less versatile for highly advanced research, it can significantly boost productivity in projects focused on practical applications within structural engineering. Its efficient management of large-scale structures and seamless integration with design codes make it especially valuable for research aimed at improving structural design practices or evaluating the

real-world performance of structural systems (Chopra 2017). This efficiency allows researchers to quickly implement and validate ideas, facilitating impactful contributions to engineering practice.

9.7.3. Balancing Software Capabilities and Project Needs

Maximizing engineering productivity requires carefully balancing the capabilities of structural analysis software with the specific needs of each project. Time efficiency plays a critical role, as the duration needed for model setup, analysis, and post-processing can vary significantly between programs. For routine structural engineering tasks, SAP2000 often provides faster turnaround times due to its intuitive interface and streamlined workflows, making it well-suited for projects where speed is essential.

Accuracy requirements also influence software choice. Projects demanding highly precise modeling of complex phenomena, such as nonlinear material behavior or multi-physics interactions, may justify the additional time and expertise needed to use Abaqus. Its advanced simulation capabilities enable more detailed and comprehensive results, which are particularly valuable in research or specialized engineering applications.

The learning curve is another important consideration. The ease with which team members can become proficient with the software affects overall productivity. SAP2000's user-friendly design and widespread industry adoption make it accessible to teams with varying experience levels, thereby reducing training time and lowering barriers to effective use.

Collaboration is enhanced when models and results can be easily shared among team members and clients. SAP2000's broad use in the industry and standardized output formats often facilitate smoother communication and integration within multidisciplinary teams.

Finally, future project demands should be considered. Investing time in mastering advanced software like Abaqus can lead to long-term productivity gains, especially for engineers anticipating work on increasingly complex or interdisciplinary projects. Proficiency in such tools opens opportunities to tackle sophisticated research questions and innovative engineering challenges.

By considering factors such as time efficiency, accuracy, learning curve, collaboration, and future needs, engineers can select the structural analysis software that best aligns with their productivity

goals, whether focused on rapid project delivery in professional practice or generating novel understanding in research environments.

9.8. CONCLUSIONS

Both Abaqus and SAP2000 offer valuable capabilities for SHM applications, each with its own strengths and limitations. SAP2000 excels in general structural analysis and design-oriented research, particularly for building and bridge structures. Its user-friendly interface and integration with design codes make it an excellent choice for a wide range of civil engineering applications (Computers and Structures, Inc. 2023).

Abaqus, on the other hand, offers superior capabilities in advanced material modeling, nonlinear analysis, and multi-physics simulations. It's particularly valuable for research involving complex material behaviors, detailed component analysis, or interdisciplinary studies that go beyond traditional structural engineering (Dassault Systemes 2023).

The choice between these software packages should be guided by the specific requirements of the SHM project, the complexity of the analysis required, and the expertise of the research team. In many cases, a complementary approach using both software packages may yield the most comprehensive results.

For students and early-career researchers, gaining proficiency in both software packages can be highly beneficial. This dual expertise allows for a more comprehensive approach to structural engineering problems and prepares researchers to tackle a wide range of challenges in both academic and professional settings.

As the field of SHM continues to evolve, the ability to effectively utilize and integrate these powerful software tools will remain pivotal for researchers and practitioners alike. By recognizing the advantages and limitations of each, engineers can select the most appropriate tool for their specific SHM needs, ultimately contributing to safer and more resilient infrastructure (Zienkiewicz et al. 2013; Cook et al. 2001; Chopra 2017).

For further research, Abaqus emerges as the superior software choice. Its advanced capabilities in material modeling, nonlinear analysis, and multi-physics simulations provide a more

comprehensive approach to detailed component investigation. Unlike SAP2000, which excels in general structural analysis, Abaqus offers sophisticated tools for modeling complex material behaviors, precise geometrical interactions, and environmental factor influences. The software's flexibility in element types, robust contact analysis, and ability to incorporate user-defined material models make it particularly well-suited for intricate sensor component research. By enabling detailed, nuanced simulations that go beyond traditional structural engineering approaches, Abaqus will provide more accurate and insightful results for Bracket Crack Sensor study, ultimately supporting a more comprehensive understanding of the sensor's performance and characteristic.

APPENDIX B

Apparatus Experiment with Strain Gauges - Results

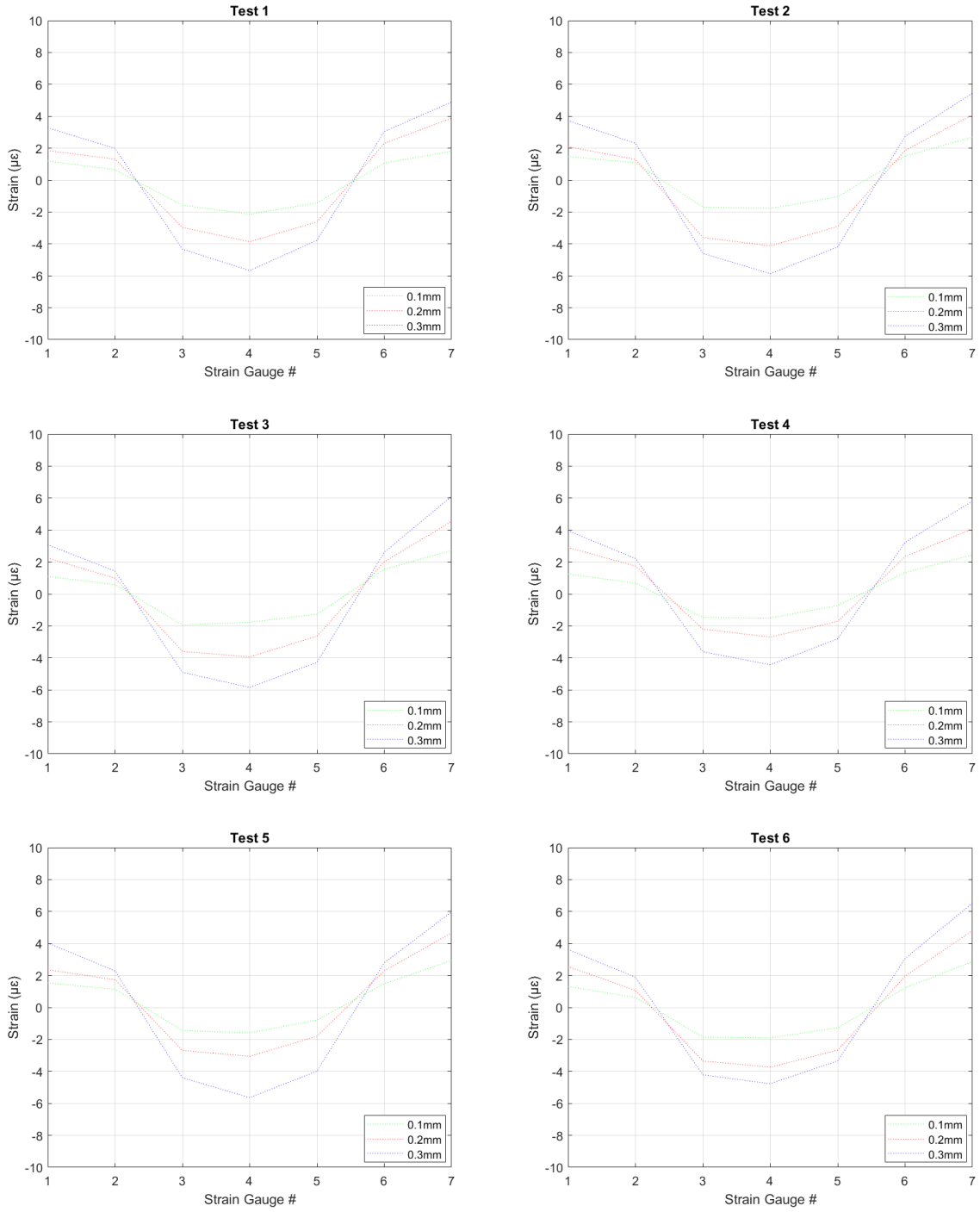

Figure B.1: Apparatus Experiment with Strain Gauges – Test 1 - Test 6

DAQ Optimization Results

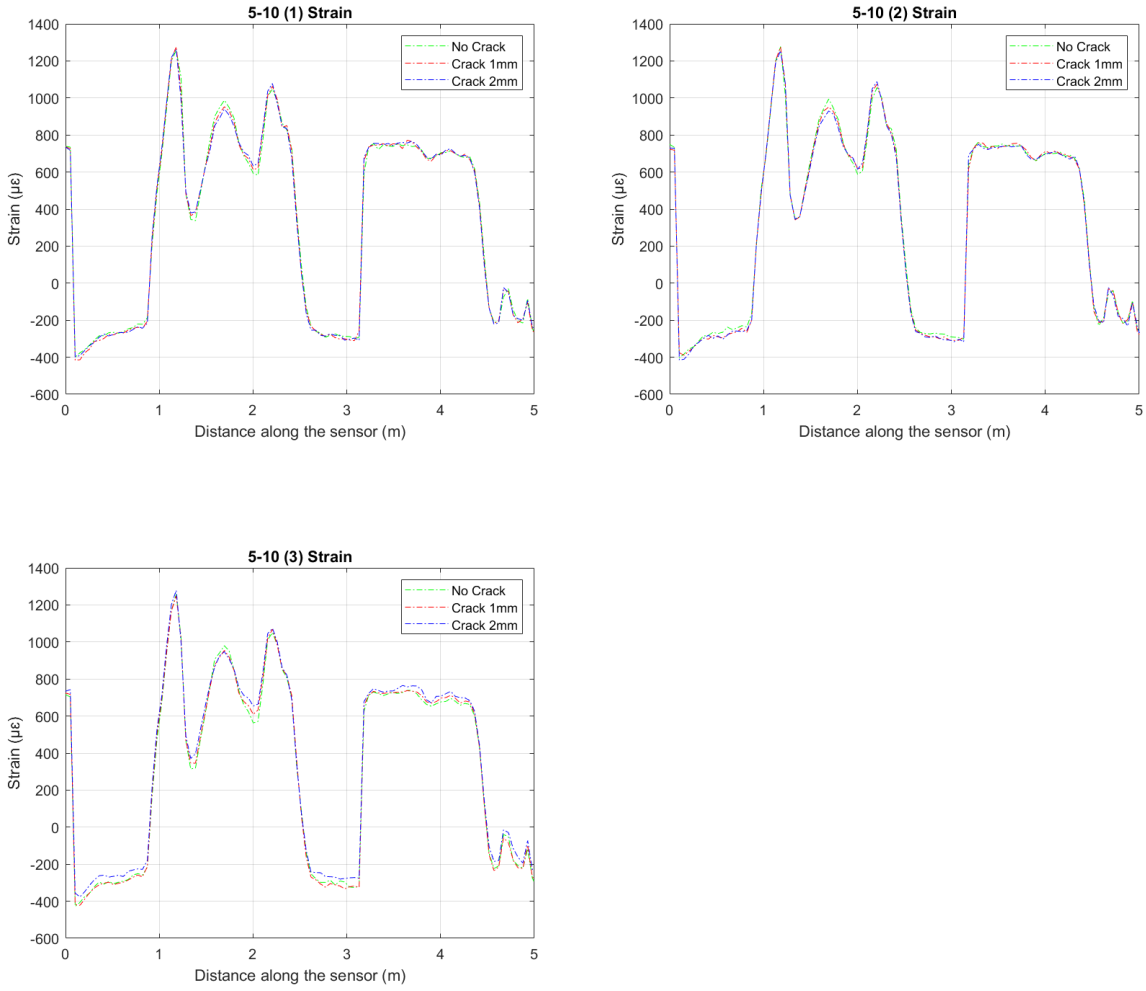

Figure B.2: Strain profiles for 5-10 DAQ settings

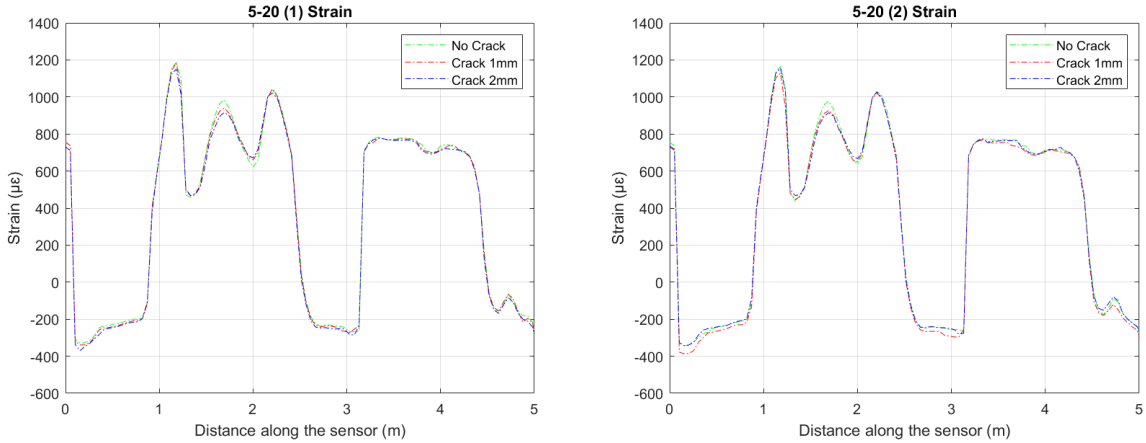

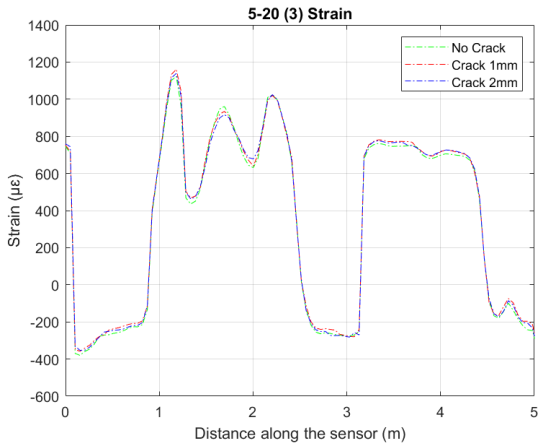

Figure B.3: Strain profiles for 5-20 DAQ settings

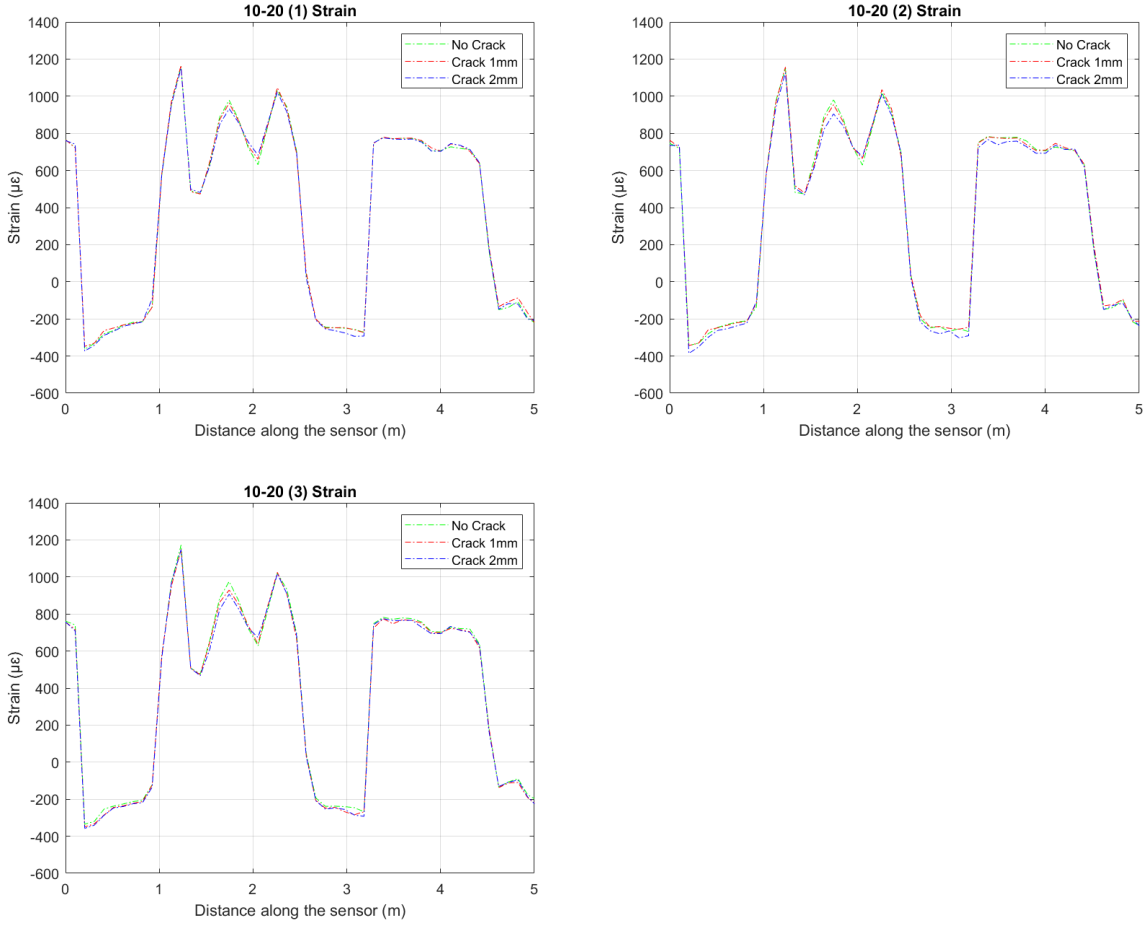

Figure B.4: Strain profiles for 10-20 DAQ settings

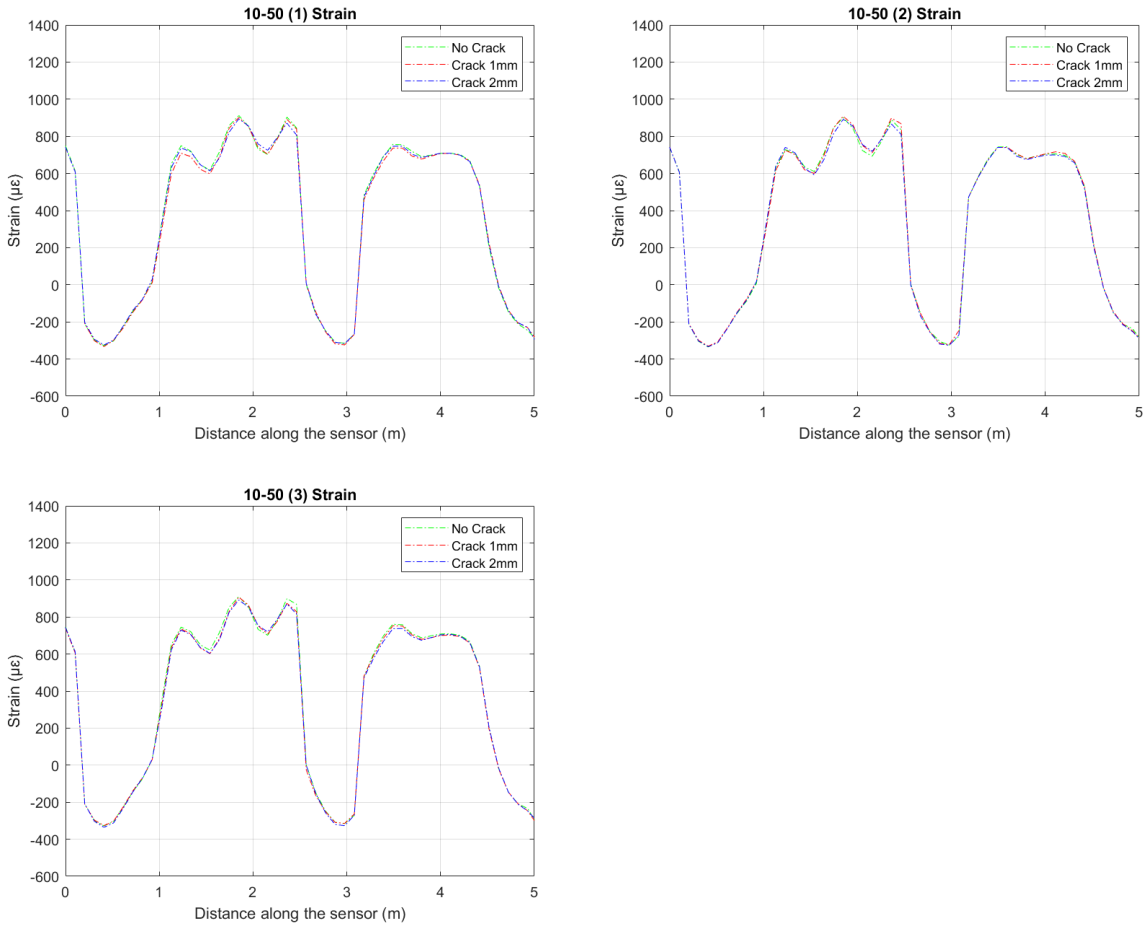

Figure B.5: Strain profiles for 10-50 DAQ settings

APPENDIX C

Bar Modelling Procedure

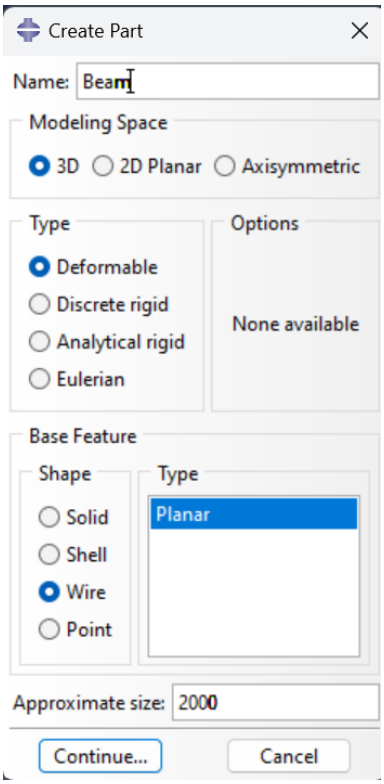

Figure C.1: Part creation: Defining Part

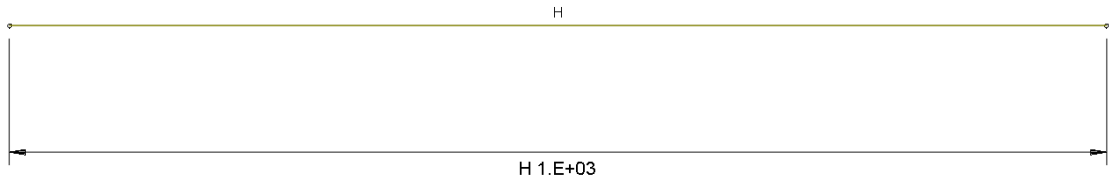

Figure C.2: Part creation: 1000mm long wire

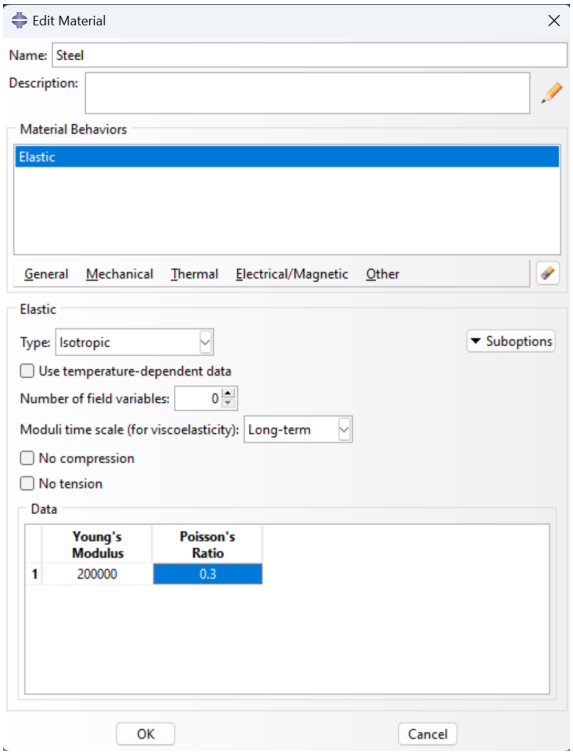

Figure C.3: Material creation - Steel

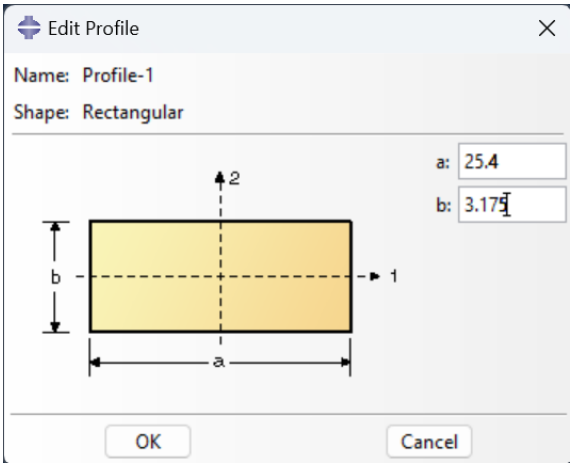

Figure C.4: Profile creation

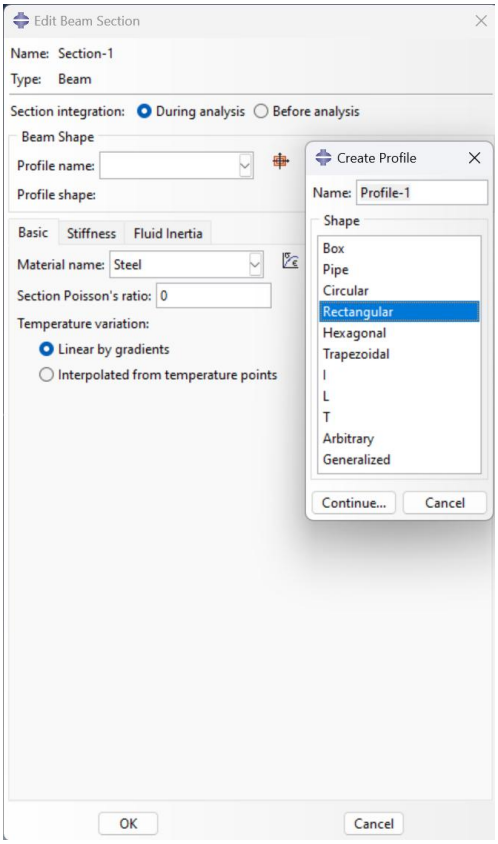

Figure C.5: Section creation

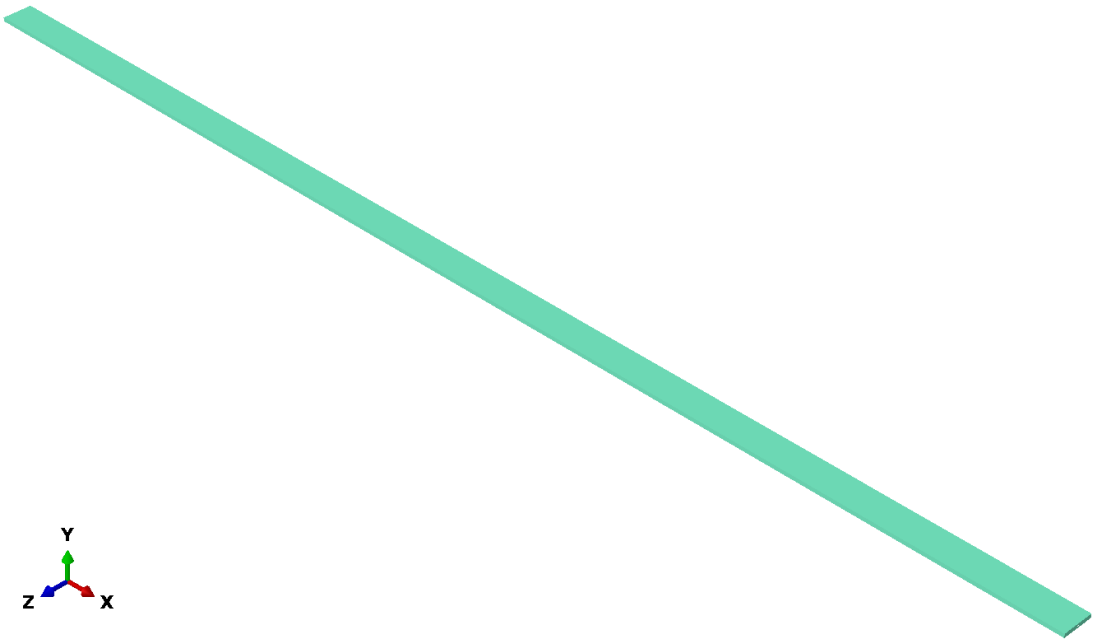

Figure C.6: Bar

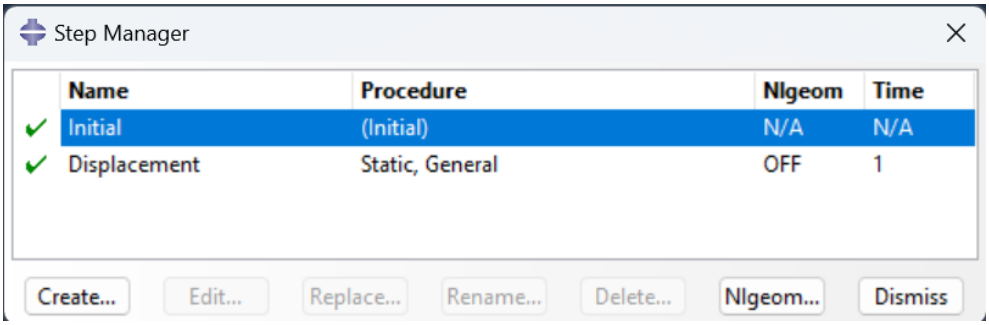

Figure C.7: Step creation - Displacement

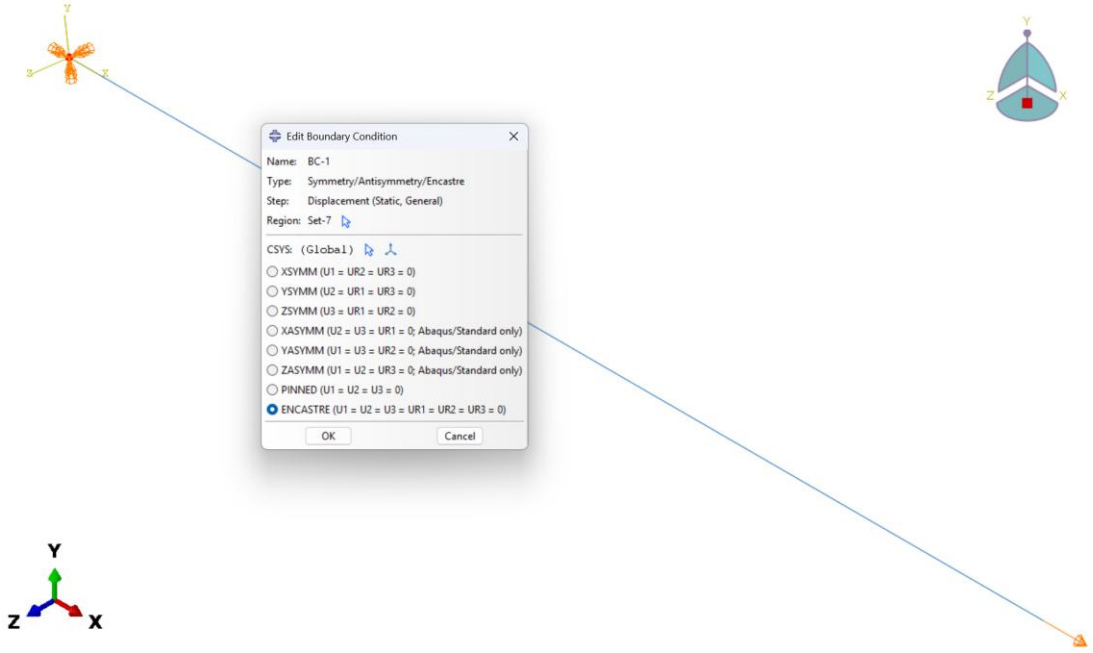

Figure C.8: Boundary conditions: Fixed end

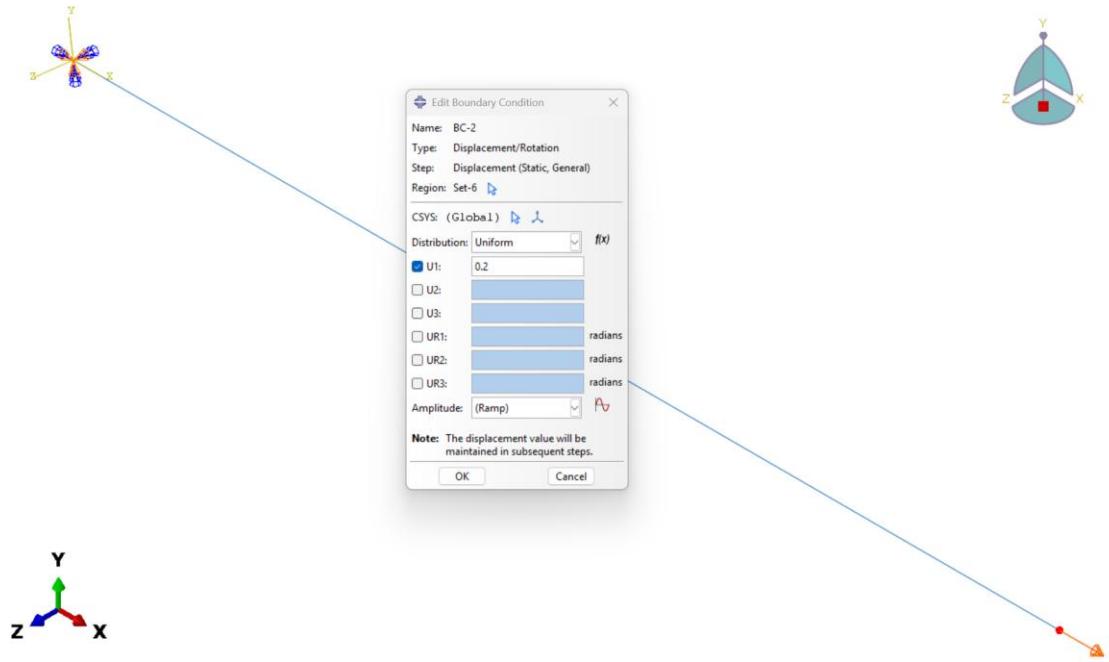

Figure C.9: Boundary conditions: Load defined as displacement

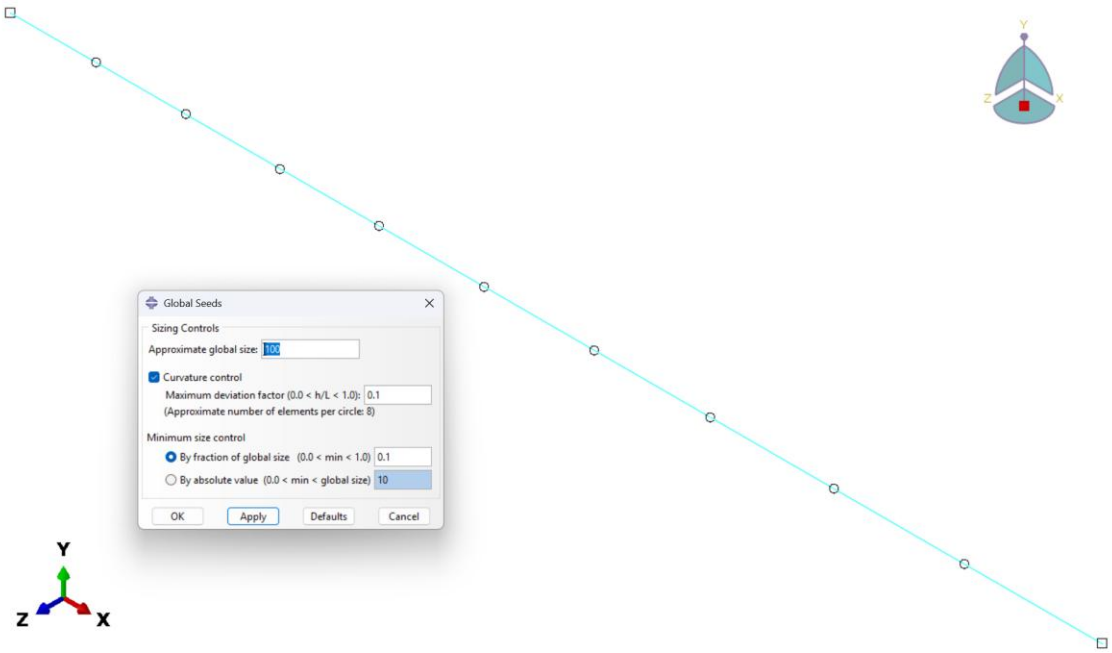

Figure C.10: Meshing

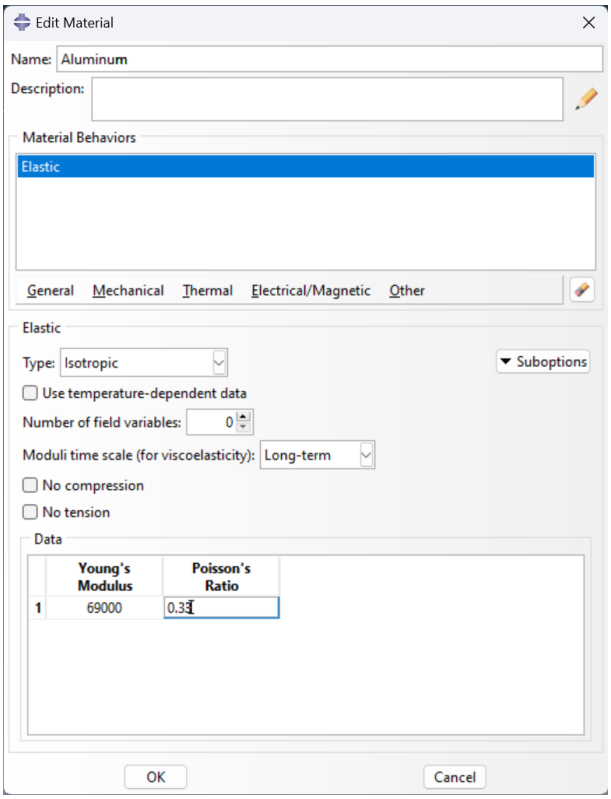

Figure C.11: Material creation - Aluminum

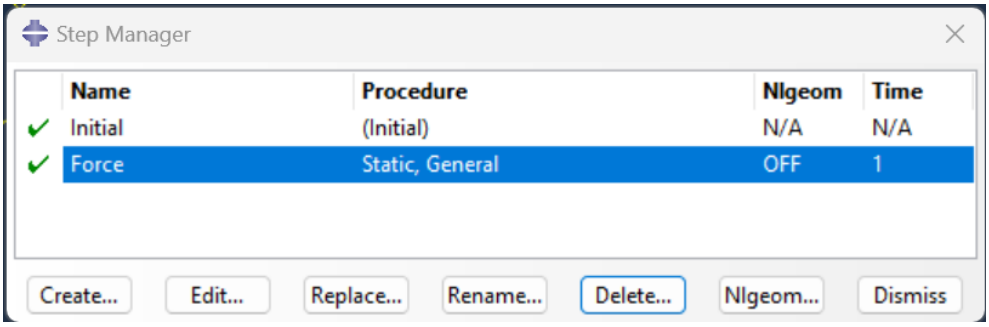

Figure C.12: Step creation - Force

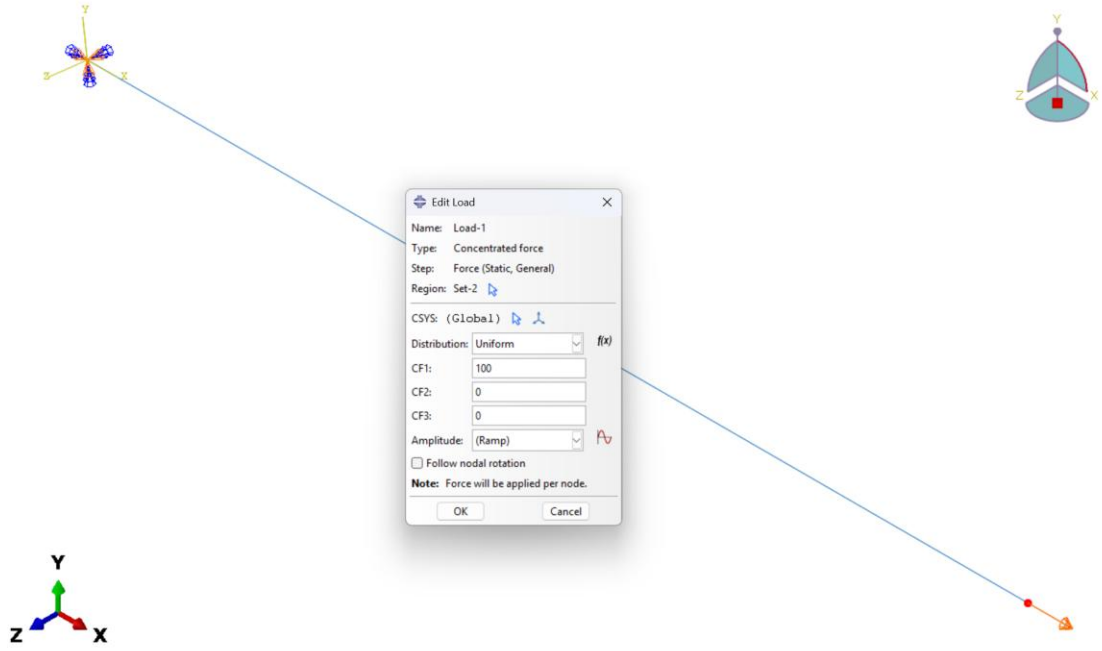

Figure C.13: Boundary conditions: Concentrated load

Displacement-Controlled Results

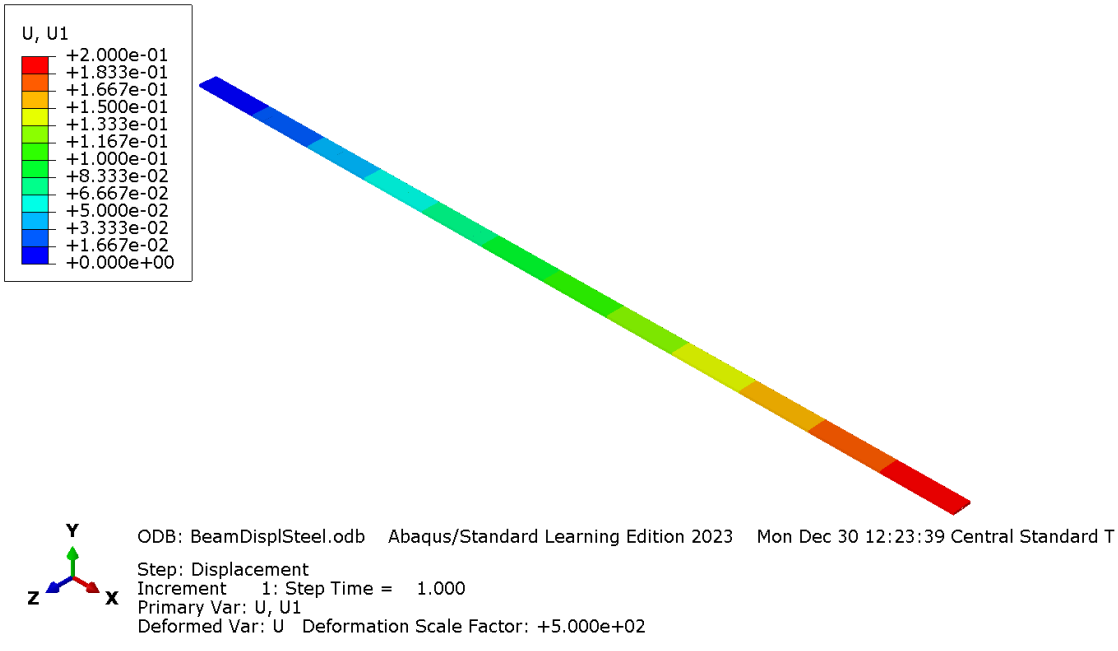

Figure C.14: Displacement-Controlled Simulation - Displacement - Steel

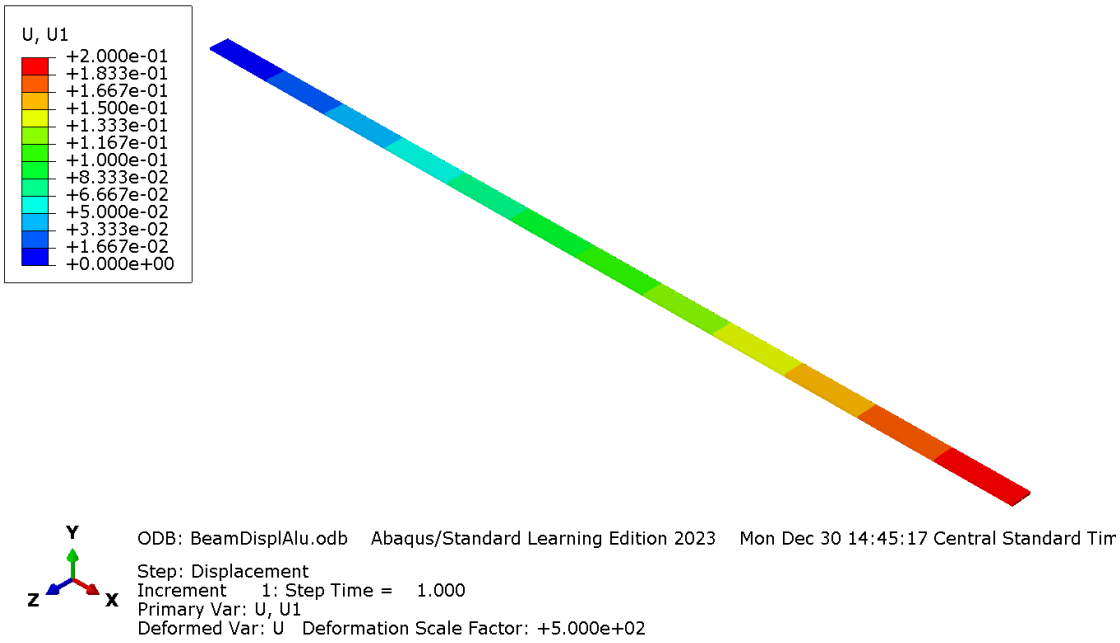

Figure C.15: Displacement-Controlled Simulation - Displacement - Aluminum

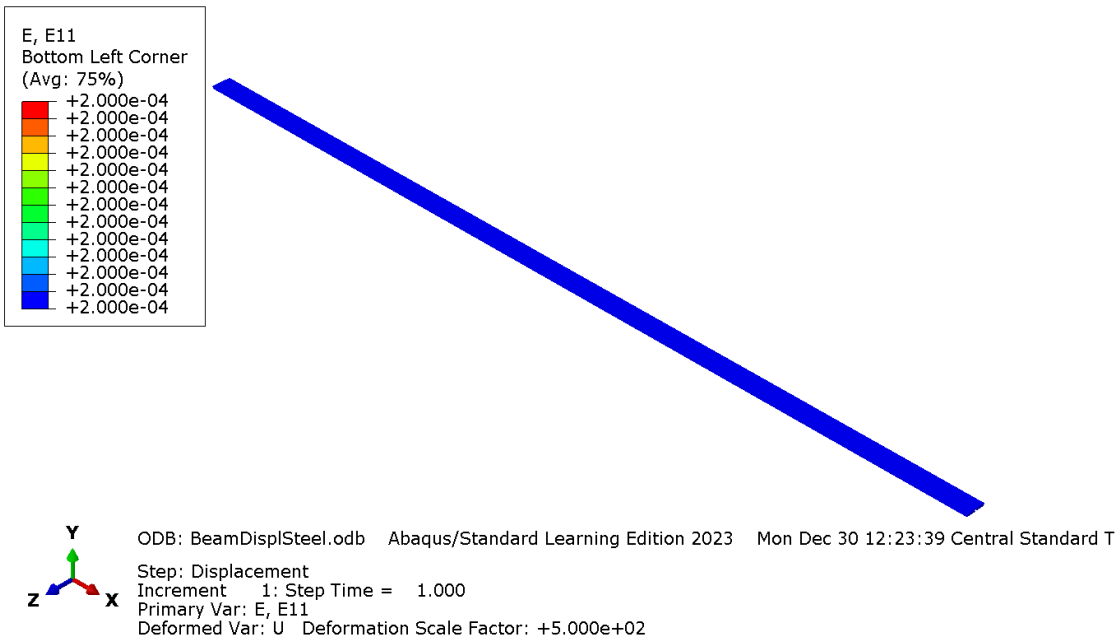

Figure C.16: Displacement-Controlled Simulation - Strain - Steel

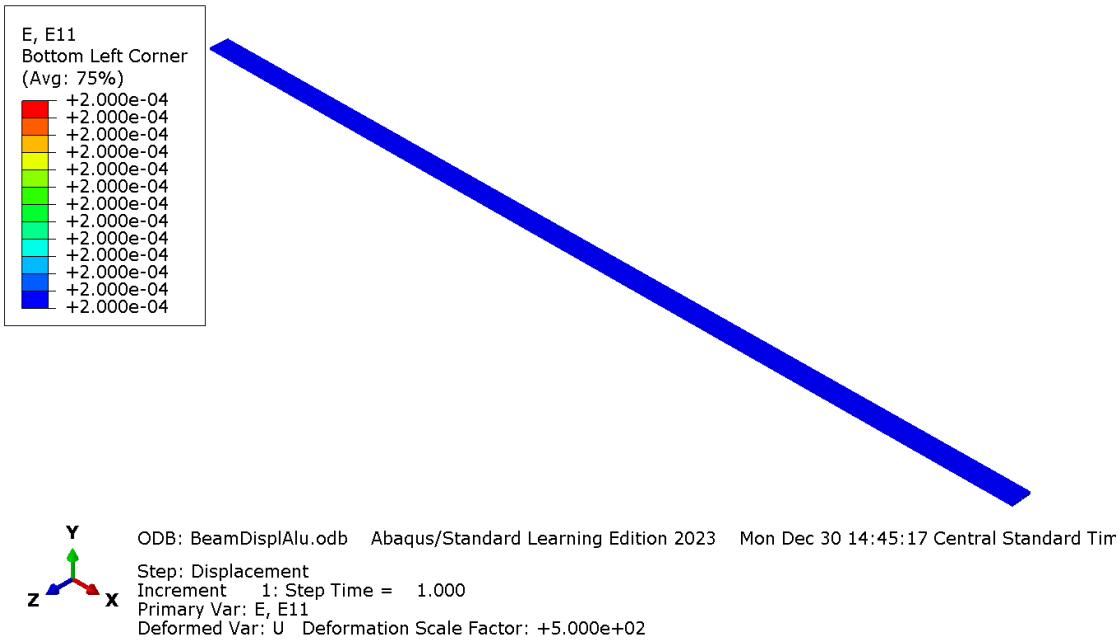

Figure C.17: Displacement-Controlled Simulation - Strain - Aluminum

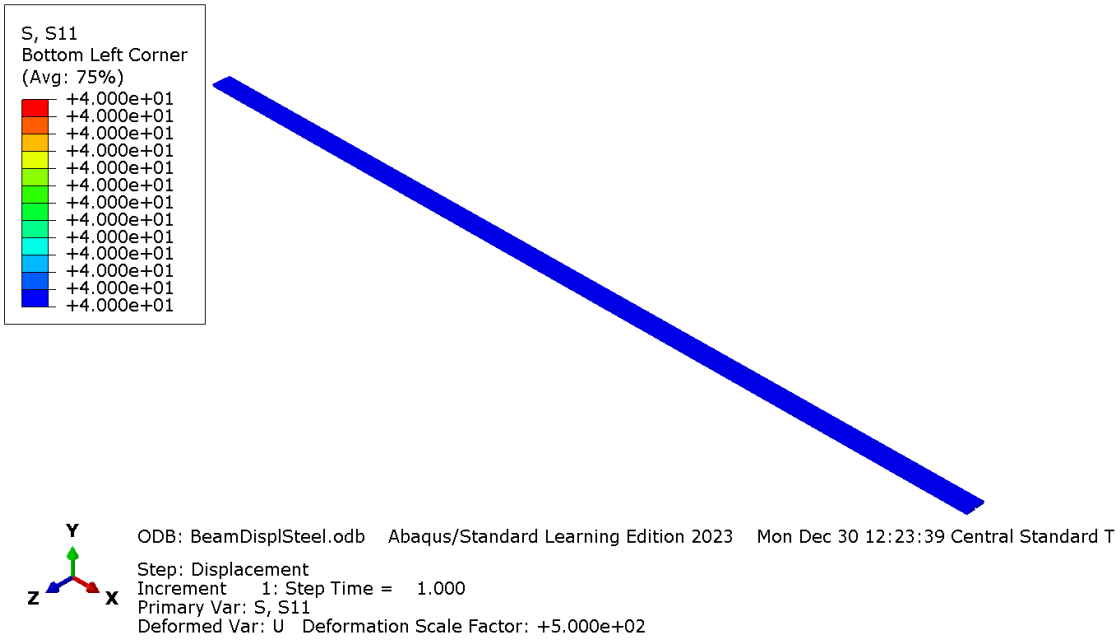

Figure C.18: Displacement-Controlled Simulation - Stress - Steel

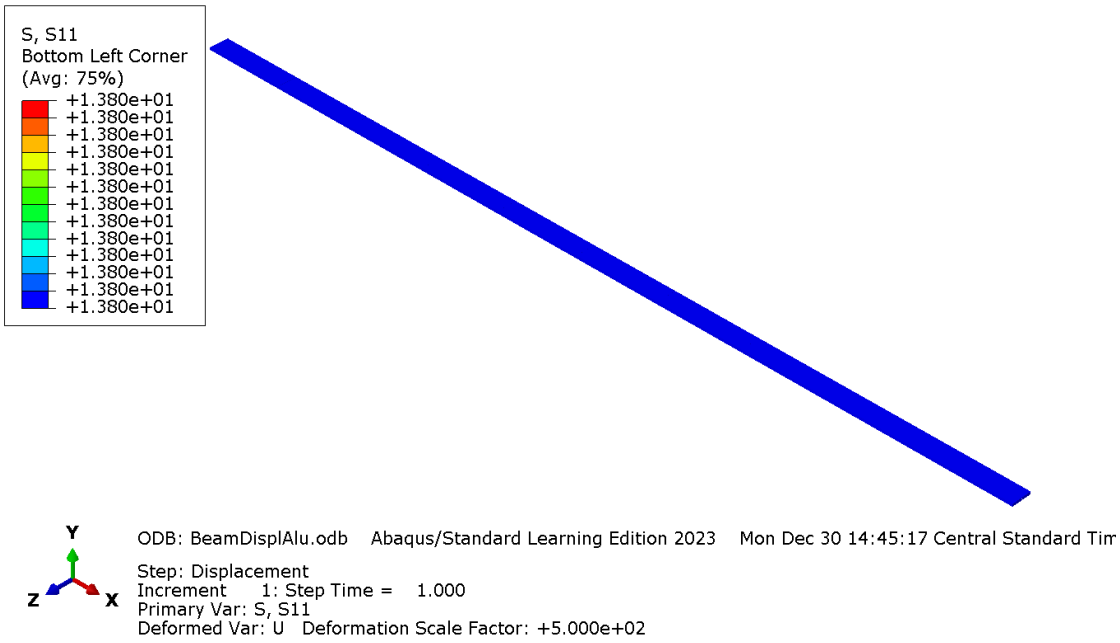

Figure C.19: Displacement-Controlled Simulation - Stress – Aluminum

Force-Controlled Results

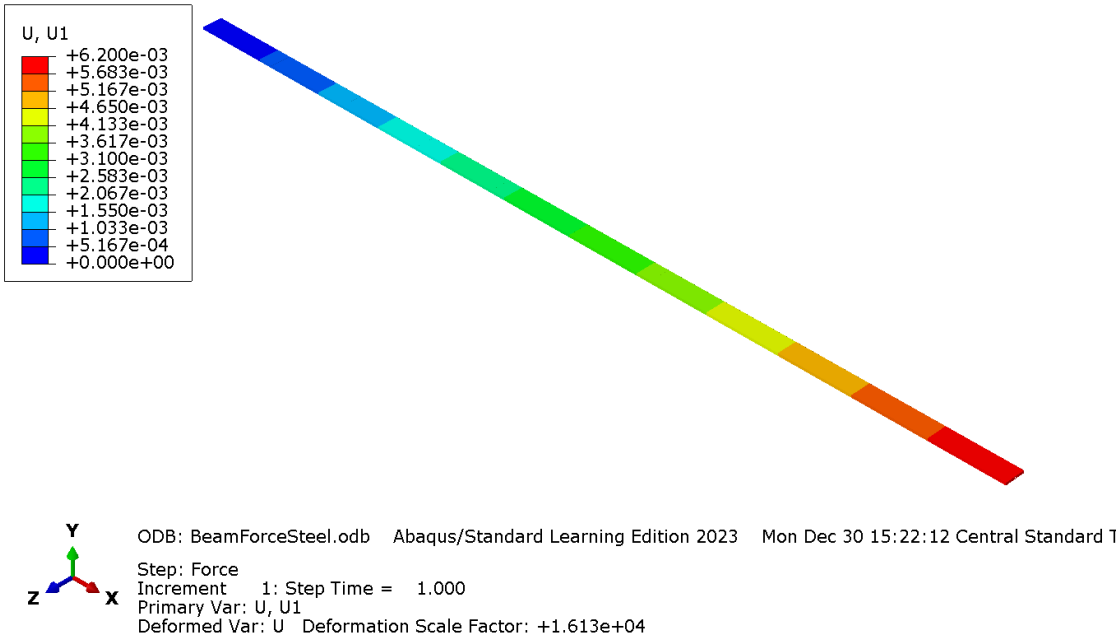

Figure C.20: Force-Controlled Simulation - Displacement - Steel

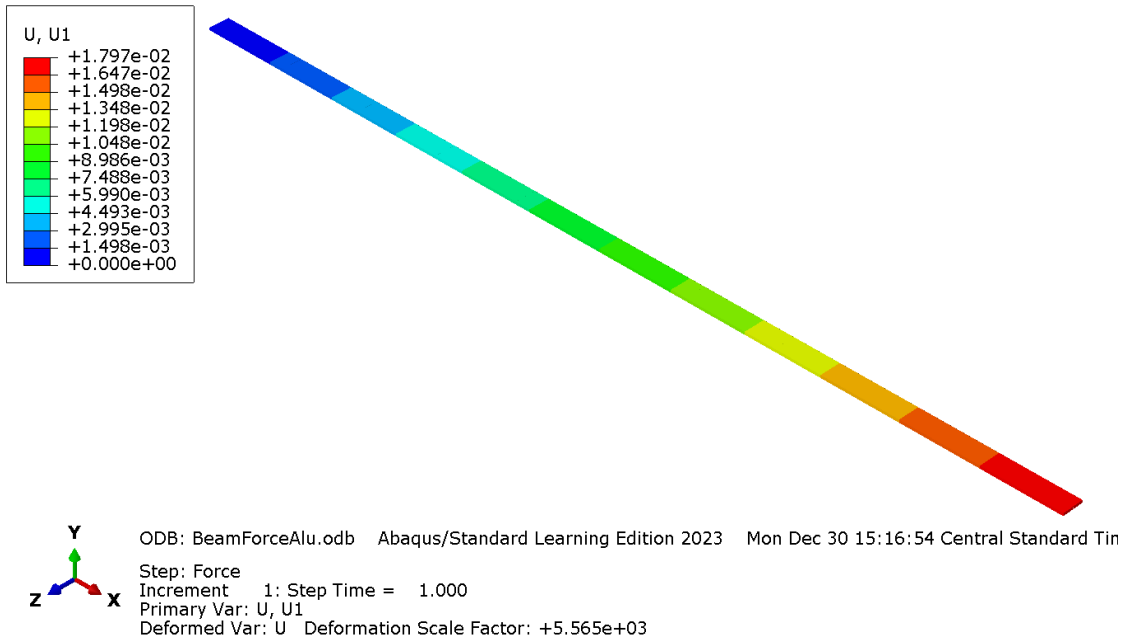

Figure C.21: Force-Controlled Simulation - Displacement - Aluminum

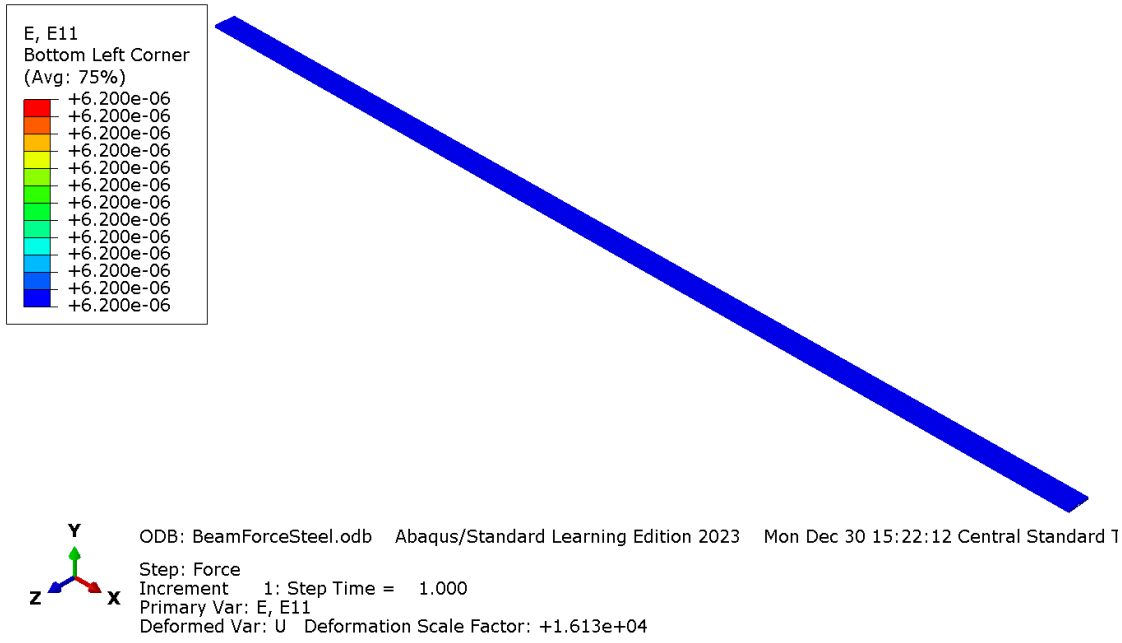

Figure C.22: Force-Controlled Simulation - Strain - Steel

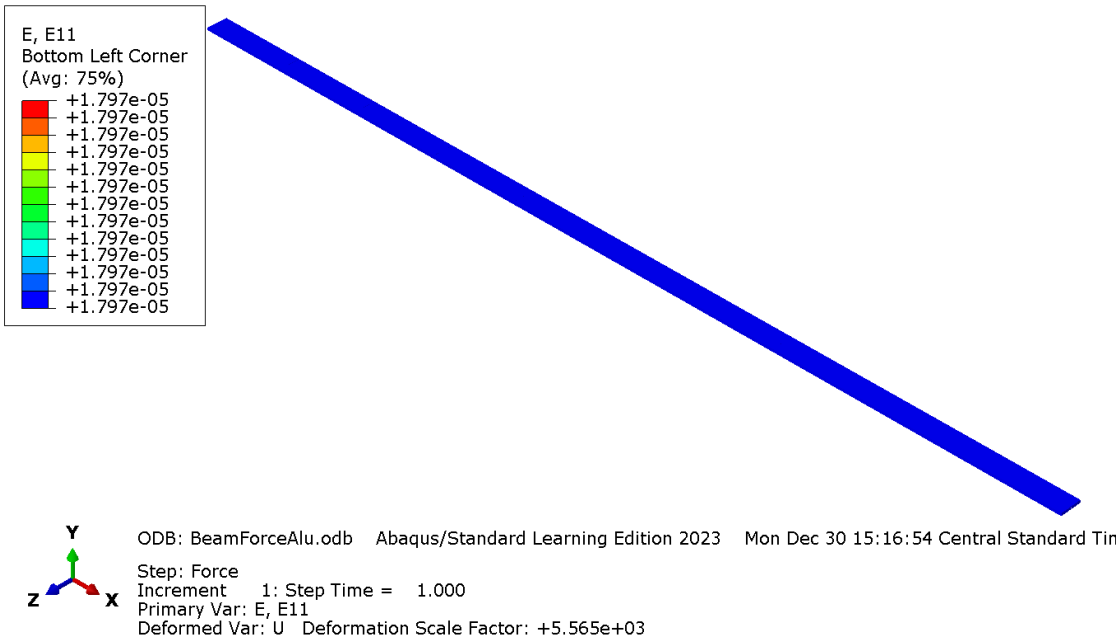

Figure C.23: Force-Controlled Simulation - Strain - Aluminum

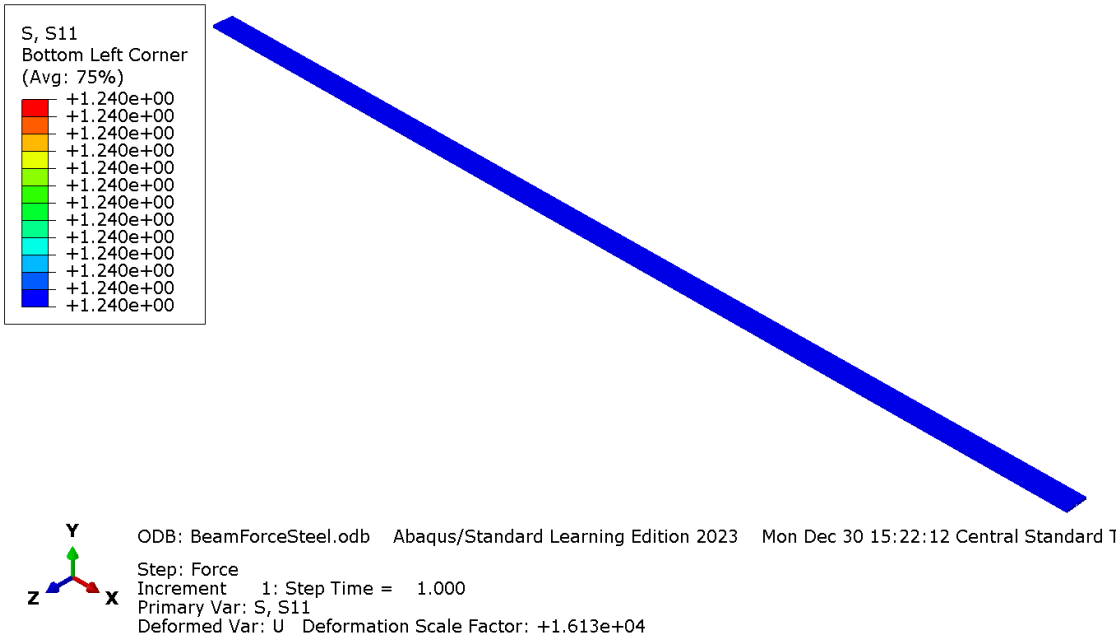

Figure C.24: Force-Controlled Simulation - Stress - Steel

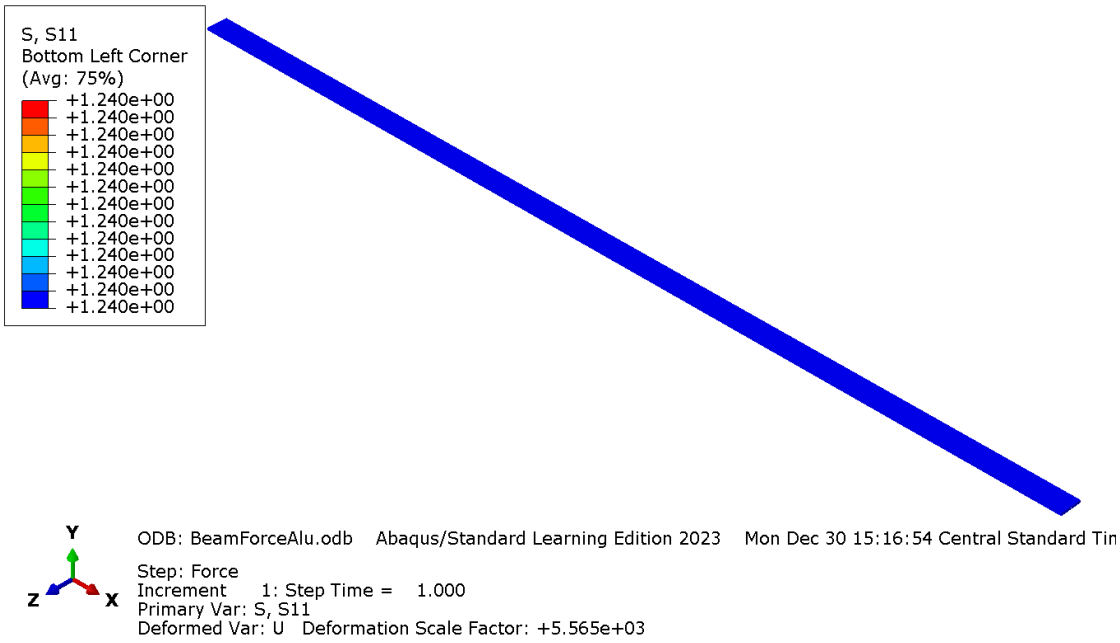

Figure C.25: Force-Controlled Simulation - Stress - Aluminum

APPENDIX D

Theoretical Calculations

This section presents sample calculations carried out to validate the FEA results for the uncracked girder model using principles of classical beam theory. Calculations were performed at 50 mm intervals along the girder for applied load cases of 92.5 kN and 185 kN. The main objective is to determine the strain values at the pi-bracket installation height (150 mm above the top of the bottom flange) for direct comparison with FEA-derived strain results. A free body diagram of the simply supported girder and its loading conditions is provided in *Figure D.1*.

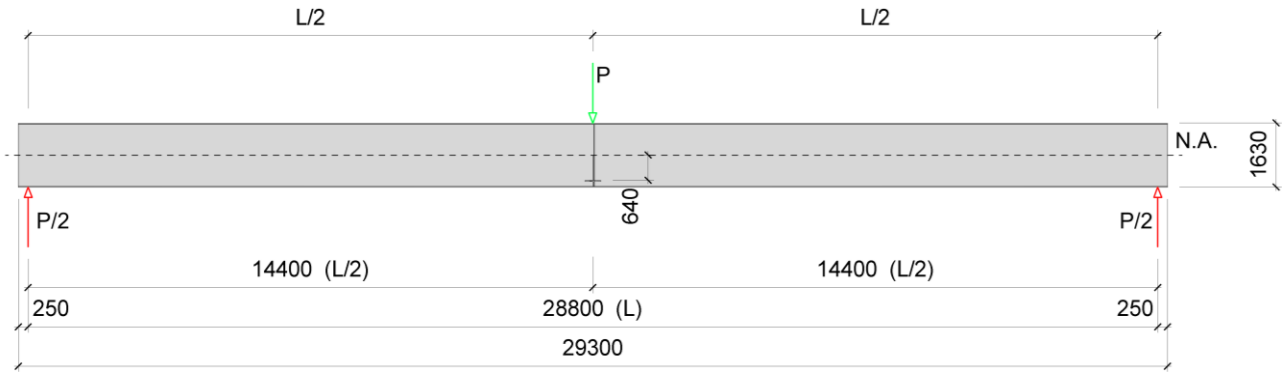

Figure D.1: Girder free body diagram

The analysis began by computing the bending moment at each position along the girder. The bending moment *M(x)* at any point *x* along the girder ($0 \leq x \leq \frac{L}{2}$) is given by:

$$M(x) = \frac{P}{2} \times x$$

Where P = Applied load (92500N or 185000N), x = Distance from the support (mm) and L = Girder span (28800mm).

For a concentrated midspan load, the bending moment equation used was expressed in terms of the applied load, span length, and distance from the support. As an example, for a load of 92,500 N applied at midspan, the moment at x = 14,100 mm from the support was evaluated.

$$M(x) = \frac{P}{2} \times x = \frac{92500}{2} \times 14100 = 652125000\ Nmm$$

The next step involved calculating the bending stress at the height of the pi-bracket. Bending stress σ at the pi-bracket height is calculated using the classic flexure formula:

$$\sigma = \frac{M\,y}{I}$$

where M is the bending moment at the location of interest, y is the perpendicular distance from the neutral axis to the point of interest, and I is the second moment of area (area moment of inertia) of the girder's cross-section.

For this application, y specifically represents the vertical distance from the neutral axis to the center of the FOS, which is mounted over the pi-bracket and positioned 150 mm above the top of the bottom flange. The neutral axis of the girder is situated 815 mm from the bottom, at mid-height of the 1,630 mm-deep girder. The height of the pi-bracket location, measured from the bottom, is 175 mm, accounting for the 25 mm flange thickness plus the 150 mm to the top of the bracket.

y = 815 mm (neutral axis) – 175mm (pi-bracket height) = 640mm

However, since the FOS is centered over the pi-bracket and has an approximate height of 10 mm, the final effective height from the neutral axis to the sensor is:

y = 640 mm + 10 mm = 650 mm

The second moment of area for the girder, I, is calculated based on the contributions from each component of the cross-section:

$$I = I_1 + I_2 + I_3 = 17.94 \text{ x } 10^9 \text{mm}^4$$

where:

I_1 – Moment of Inertia of the Top Flange; $I = \frac{b\,d^3}{12} + Ah^2$

I_2 – Moment of Inertia of the Web; $I = \frac{b\,d^3}{12}$

I_3 – Moment of Inertia of the Bottom Flange; $I = \frac{b\,d^3}{12} + Ah^2$

As an example, at the location x = 14100 mm along the girder, the bending stress was calculated as:

$$\sigma = \frac{M\,y}{I} = \frac{652125000\,x\,650}{17.94x10^9} = 23.62\text{MPa}$$

Hooke's Law was then used to convert the calculated bending stress into strain by dividing by the Young's modulus (E = 210,000 MPa). For example, at the midspan location and an applied load of 92,500 N, the calculated strain was found to be 112.48 με.

$$\varepsilon = \frac{\sigma}{E} = \frac{23.62}{210000} = 112.48\mu\varepsilon$$

APPENDIX E

The DAQ reading unit was configured to following settings:

Distance Range:	50m
Sampling Interval:	5cm
Spatial Resolution:	10cm
Averaging Count:	2^16 (65536)
Frequency Range Start:	10.650 GHz
Frequency Range Stop:	10.950 GHz
Step:	3 MHz
Span - Count:	101
Puls Adjustment:	On
Auto Frequency Adjustment:	On
Measurement Mode:	Progressive